Effect of Polymer Additives on Transitioning and Turbulent Boundary Layers

by

Yash Hemant Shah

A thesis
presented to the University of Waterloo
in fulfillment of the
thesis requirement for the degree of
Doctor of Philosophy
in
Mechanical and Mechatronics Engineering

Waterloo, Ontario, Canada, 2021

Examining Committee Membership

The following served on the Examining Committee for this thesis. The decision of the Examining Committee is by majority vote.

External Examiner	Dr. B. Elbing Associate Professor Mechanical and Aerospace Engineering Oklahoma State University , USA
Supervisor	Prof. S. Yarusevych Professor Dept. of Mechanical and Mechatronics Engineering University of Waterloo
Internal Members	Dr. J. P. Hickey Assistant Professor Dept. of Mechanical and Mechatronics Engineering University of Waterloo
	Dr. Z. Pan Assistant Professor Dept. of Mechanical and Mechatronics Engineering University of Waterloo
Internal-External Member	Prof. K. Lamb Professor Dept. of Applied Mathematics University of Waterloo

Author's Declarations

I hereby declare that I am the sole author of this thesis. This is a true copy of the thesis, including any required final revisions, as accepted by my examiners.

I understand that my thesis may be made electronically available to the public.

Abstract

Injection of small quantities of polymer solutions in various internal and external turbulent flows can produce a substantial reduction of skin friction drag. This phenomenon, known as Toms phenomenon, has been actively studied in the past few decades and applied in various industrial flows to increase efficiency, decrease operating costs, and reduce emissions. A number of previous numerical studies have hypothesized that the long chains of polymer molecules interact with various turbulent motions thereby decreasing the turbulent fluctuations and reducing skin friction. The experimental investigations conducted in the present work provide a comprehensive understanding of the development of a polymer drag reduced boundary layer flow while providing critical insights into the polymer-turbulence interactions in both turbulent and bypass transitioning boundary layers. The outcomes are particularly applicable for the practical implementation of this flow control strategy on marine vehicles.

The experiments are conducted in a specialized water tunnel facility by means of particle image velocimetry (PIV) and planar laser-induced fluorescence (PLIF) in a flat-plate boundary layer injected with polymer solutions via a tangentially inclined two-dimensional slot. The drag reducing effect of the heterogeneously distributed polymers on the flow development is characterized by contrasting the results against the baseline flow of water in each case. Critical questions with regards to the effect of the polymer concentration on the drag reduction performance in turbulent boundary layers are first addressed by considering three different concentrations of polyethylene oxide (PEO) covering a wide range of the drag reduction regime. The analysis of velocity and concentration measurements provides a link between the local polymer concentration, flow development, and achieved drag reduction. The changes in the slope of the logarithmic region of the velocity profiles are associated with various sub-regimes of drag reduction providing insights into the dominance of the viscous and inertial effects within the respective sub-regimes, which are important for the understanding of the ultimate limit of drag reduction.

Further investigations are conducted using three-dimensional PIV measurements in the buffer and lower log regions of a drag reduced boundary layer, which elucidate the effect of polymer injection on various coherent structures in this region. The polymers are noted to dampen the turbulence producing motions, such as ejections and sweeps, which is illustrated through conditionally averaged flow fields. Accordingly, the Reynolds shear stress, a measure of turbulence production, is observed to be reduced in both cores of the structures and around the quasi-streamwise vortices, presenting an effect expected due to various viscoelastic mechanisms. The same trend is also observed to varying degrees within other frequently occurring coherent structures which

are associated with the low-speed streaks, such as hairpin-like vortices, meandered streaks, and the precursors of streak breakdown events, confirming the importance of the polymer-turbulence interactions in turbulence control with this technique.

The detailed planar and tomographic PIV measurements are further utilized for the characterization of extreme skin friction events which are largely associated with the low and high-speed streaks. Conditional averaged flow fields corresponding to the extreme events elucidate the polymer effect on the associated topology of the near-wall flow surrounding these events while signifying the dampening of large structures of Reynolds shear stress formed within the buffer layer. Further, a scale decomposition based analysis elucidates the effect of polymers on various length scales which are directly associated with the reduction in the Reynolds shear stress. The scale-decomposed conditional flow fields are further utilized to establish a quantitative measure of the association of the near-wall Reynolds shear stress with the skin friction, highlighting the effect of polymer injection on the phase differences between these quantities.

Considering the substantial effects of the polymers particularly on the turbulence producing coherent structures, the effect of polymers on the transitional-turbulent motions within a bypass transitioning boundary layer are investigated using both planar PIV and PLIF. The effect of polymer injection is observed to accelerate the transition process in comparison to the baseline Newtonian flow depending on the location of injection with respect to a trip-wire. The acceleration of the transition process is observed via the increase in the amplification of velocity perturbations in the early transition stages which are dominated by Kelvin-Helmholtz instabilities. Characterization of the resulting flow development illustrates important differences in the trends of flow statistics and skin friction, highlighting the advantages and drawbacks of polymer injection within the transitional regime of the boundary layer.

Acknowledgements

I extend my deepest gratitude to my supervisor and mentor, Prof. Serhiy Yarusevych, for providing me with this wonderful opportunity to pursue a Ph.D., and for the constant motivation and guidance which proved to be crucial for the attempts made in this thesis towards the understanding of a challenging topic like turbulence. I am also deeply thankful to you for involving me in various other projects such as the development of the water flume and the COVID-19 project, and for the trust shown in me when things became difficult during the development of the flume.

I also thank Dr. Sina Ghaemi for making this collaboration a success and imparting his expertise along with the best-practices for experimentation and analysis. I thoroughly enjoyed our experimental campaign in Jan. 2019 and the following discussions. The impeccable balance of calmness and critique you showed in going through the analysis amazed me.

I thank all the committee members, Prof. Lamb, Dr. Elbing, Dr. Hickey, and Dr. Pan, for taking the time and effort to go through the thesis in detail and providing an excellent feedback and discussion during the defence.

Many thanks to Dr. Sean Peterson and Dr. John Kurelek for an excellent cooperation during the COVID-19 project and for their extraordinary efforts in making this project a success. Your commitment to research and perfection are truly inspiring for me. I also thank my collaborators on the water flume project: graduate students - Jeff McClure, Mark Istvan, Qihang Yuan, Nikhilesh Tumuluru, undergraduate interns - Elise Belakebi, Mike Pfeifer, Jeremy Newton, technical/support staff - Jason Benninger, Karl Janzen, Richard Gordon, Robert Wagner, James Merli, Neil Griffett, Terry Ridgway, and Juan, for an excellent cooperation in the development of this facility. Without your efforts, none of this would be possible.

Thanks to all my colleagues at the Fluid Mechanics Research Lab - Jeff, John, Xueqing (Caddie), Supun, Dallyn, Mark, Amitvikram, Eric, Qihang, Nikhilesh, Connor, Kieran, and Kaycee for all the help and support through the past four years and making a friendly environment in the office. I also thank my friends and roommates, Dr. Pranav Agrawal, Abhinav Dahiya, Naman Gupta, Sunidhi Taneja, and Prarthana Bhattacharyya for being there and understanding me during all the difficult times, for all the nerdy, yet fun-filled discussions on the dinner table, and for all the exciting outings, which I will cherish forever. Special mention to Caddie who provided me with the much-needed support to cope with the challenges of the Ph.D.

Lastly, and most importantly, I extend my deepest gratitude to my parents, Mr. Hemant Shah and Mrs. Manasi Shah, for encouraging me to pursue higher studies despite the difficulties in terms of health and finances. I sincerely appreciate your selfless efforts in helping me succeed in my goals and I can only hope to become as loving and caring as you are.

Dedication

To my parents,
for their endless love, support, and encouragement.

Contents

List of Figures

List of Tables

List of Abbreviations

DR	Drag Reduction
PDR	Polymer Drag Reduction
PEO	Polyethylene Oxide
PAM	Polyacrylamide
RSS	Reynolds Shear Stress
VLSM	Very Large Scale Motion
DNS	Direct Numerical Simulations
MDR	Maximum Drag Reduction
HDR	High Drag Reduction
LDR	Low Drag Reduction
PIV	Particle Image Velocimetry
LDV	Laser Doppler Velocimetry
FOV	Field of View
PLIF	Planar Laser-Induced Fluorescence
PDF	Probability Density Function
JPDF	Joint Probability Density Function
CDF	Cumulative Density Function
K-H	Kelvin-Helmholtz
PC-ABS	Polycarbonate-Acrylonitrile Butadiene Styrene

List of Symbols

Accents and Subscripts

Example	Description
$\langle a \rangle$	time-averaged quantity
$\overline{a}$	spatially-averaged quantity
$\overline{a}\|_{y_1-y_2}$	spatially-averaged quantity within the range [y_1, y_2]; y_1 and y_2 in inner coordinates
$\widetilde{a}$	conditionally-averaged quantity
$\widetilde{\widetilde{a}}$	fluctuation of conditionally sampled quantity
a'	fluctuating quantity of a signal
a_{rms}	root-mean-square of a quantity
a^+	quantity in inner scaling
a_N	quantity corresponding to Newtonian flow
a_0	quantity corresponding to the baseline Newtonian flow
a_P	quantity corresponding to polymer flow
a_w, $a\|_w$	quantity at the wall (*i.e.,* at $y = 0$)
a_i	quantity corresponding to the i^{th} spatial component
a_{tr}	quantity at the location of the trip (*i.e.,* at $x = x_{\text{trip}}$)
a_c	quantity corresponding to the centre of a conditional domain
a_M	maximum of a quantity
$C_{a_1 a_2}$	two-point correlation coefficient of signals a_1 and a_2
a_l	large scale component of a quantity
a_s	small scale component of a quantity

Dimensionless Quantities

Symbol	Description	Definition
Re_x	Reynolds number based on x coordinate	xU_∞/ν
Re_r	Reynolds number based on trip height r	rU_r/ν
Re_θ	Reynolds number based on momentum thickness	$U_\infty\theta/\nu$
Re_{δ^*}	Reynolds number based on displacement thickness	$U_\infty\delta^*/\nu$
Re_τ	Frictional Reynolds number	$u_\tau\delta/\nu$ or δ/λ
Wi	Weissenberg number	$t_{\text{rel}}\dot{\gamma}$
H	Shape factor	δ^*/θ
C_f	Skin friction coefficient	$\tau_w/(0.5\rho U_\infty^2)$

Greek Symbols

Symbol	Description	Units
λ	viscous unit ν/u_τ	m
ρ	density	kg m^{-3}
ν	kinematic viscosity	m s^{-2}
μ	dynamic viscosity	kg m^{-1} s^{-1}
δ	boundary layer thickness	m
δ^*	displacement thickness	m
θ	momentum thickness	m
δ_{slot}	boundary layer thickness at injection slot	m
Γ	circulation	m^2 s^{-1}
τ_w	wall shear stress $\mu\frac{d\langle u\rangle}{dy}\|_{y=0}$	kg m^{-1} s^{-2}
τ_{total}	total shear stress	kg m^{-1} s^{-2}
τ	stress	kg m^{-1} s^{-2}
κ	von Kármán constant	-
ω	vorticity	s^{-1}
$\dot{\gamma}$	characteristic shear rate	s^{-1}
ϵ	relative uncertainty with 95% confidence	[%]

Roman Symbols

Symbol	Description	Units
x	streamwise coordinate	m
y	wall-normal coordinate	m
z	spanwise coordinate	m
u	streamwise velocity component	m s^{-1}
U	streamwise velocity component	m s^{-1}
v	wall-normal velocity component	m s^{-1}
w	spanwise velocity component	m s^{-1}
u_τ	frictional velocity; $\sqrt{\tau_w/\rho}$	m s^{-1}
DR	drag reduction	[%]
L	length of flat-plate	m
c	local concentration	kg m^{-3}
c_o	local concentration in the outer layer	kg m^{-3}
c_{inj}	injection concentration	kg m^{-3}
Q_{inj}	injection flow rate	m^3 s^{-1}
u_{inj}	injection velocity	m s^{-1}
x_{inj}	injection location	m
x_{trip}	location of trip	m
x_{VO}	location of the virtual origin	m
r	height of trip	m
U_∞	freestream velocity	m s^{-1}
K	polymer flux parameter	m
k	slope of logarithmic layer in inner coordinates	-
t_{rel}	relaxation time of polymer molecule	s
D	diffusion coefficient	m^2 s^{-1}
Q	Q-criterion for vortex identification	s^{-1}
Tu, TI	Turbulence intensity; u_{rms}/U_∞	[%]
d	slot width of the injector	m
$\overline{V}$	mean outlet velocity in characterization of injector	m s^{-1}
$\overline{\overline{V}}$	spatially averaged mean outlet velocity in characterization of injector	m s^{-1}

Chapter 1

Introduction

The phenomenon of polymer drag reduction is introduced and its relevance is highlighted in the backdrop of the current efforts of the marine industry to increase ship's efficiency to minimize carbon emissions. Challenges in the fundamental understanding of polymer drag reduction are identified and specific research objectives are formulated.

The maritime industry, which is responsible for more than 75% of the total freight transportation in the world, currently accounts for approximately 3% of the total anthropogenic emission of CO_2 and other greenhouse gases (GHG) according to the reports from a number of international organizations [1, 2]. Although shipping is the most energy-efficient form of transportation for cargo, the direct GHG emissions from ships are projected to grow by 50% - 250% by 2050 [3], leading to a global contribution of nearly 17% of total GHG emissions [4]. While in accordance with the guidelines provided by the Paris Agreement [5] for the reduction in GHG emissions, the current proposals for switching to alternate low-carbon and bio-fuels [3, 6], reduction in ship operating speeds, and improved hull coatings [7] are unlikely to be adopted at the required scales by 2050 due to high costs according to the recent projections of the International Energy Agency [3]. In light of these projections, technologies such as polymer drag reduction (PDR) aimed at the reduction of frictional drag on a ship have gained increased significance. Based on the current international marine bunker statistics Cho *et al.* [8] suggest that a 10% reduction in the drag of a ship would result in 4.7 billion US$/year in savings. Considering that PDR can result in drag reductions of more than 50% [9], development of this technology could serve the current efforts towards reducing GHG emissions while providing the much needed time for transition to alternate fuels.

The drag on a ship is mainly composed of the resistances due to pressure, wave, and friction, of which the frictional resistance arising at the contact surface accounts for nearly 80% of the total drag in cargo ships [10]. Given the large scale of operation, resulting in Reynolds numbers which are some of the highest in engineering applications [11], the boundary at the contact surface is highly turbulent which causes the high frictional resistance on the ship. While a number of passive (*e.g.,* riblets [12], compliant coatings [13]) and active flow control (*e.g.,* air/bubble injection [14–16], surfactant injection [17]) technologies exist to mitigate the adverse effects of the turbulent boundary layer, polymer based drag reduction [18–20] has attracted significant research interest due to its fundamental nature and commercial utility, with skin friction reductions of up to 80% reported in various turbulent flows [21].

The phenomenon of drag reduction by introducing dilute polymer solutions in wall-bounded turbulent flows has been actively explored and implemented since its discovery in 1948 by Toms [18] and the first patent in 1949 by Mysels [19]. The practical utility of this phenomenon covers a wide range of applications, including the oil industry for enhancing oil recovery [22, 23] and decreasing pressure losses in pipelines [24–29], marine industry for enhancing the efficiency or speed of ships and underwater vehicles [30–34], fire-fighting [35], jet cutting [36, 37], sewers [38–40] and irrigation [41], and even bio-medical field for the treatment of atherogenesis [21, 42–45]. While a number of commercial applications have utilized synthetic polymers, such as polyethylene oxide (PEO) and polyacrylamide (PAM), which has raised significant environmental concerns, contemporary research has also focused on the assessment of bio-polymers

as drag reducing agents [46, 47].

Significant insights into the working mechanisms of PDR have been gained through a number of experimental [48–52] and numerical [53–56] studies which have highlighted the effect of viscoelasticity of the polymer on various turbulent motions within the turbulent boundary layer. The polymer molecules have been shown to reduce turbulent production by interacting with near-wall coherent structures and reducing their strengths [55–57]. Attenuation of near-wall vortices through viscoelastic mechanisms highlighted by Min *et al.* [54] is accompanied by a reduction in wall-normal velocity fluctuations and Reynolds shear stress [49, 58, 59], increased spanwise spacing of near-wall streaks [50, 51], and decreased magnitudes of ejections and sweeps [60, 61]. Further, several studies have highlighted the role of polymer macromolecules in dampening of small-scale motions thereby disrupting the turbulent energy cascade [62–64]. Along with these insights, a number of competing theories [53, 65] describing the mechanisms of polymer drag reduction have been propounded, leading to a long-standing and ongoing debate in the research community.

1.1 Motivation and Objectives

Despite their successful implementation in internal flows, significant challenges exist in the application of drag reducing polymers in external flow scenarios and motivate the present work. These challenges primarily pertain to, but are not limited to, the reduction of polymer concentration close to the wall due to the transport of the polymer away from it, chain scission which leads to a decreased drag reduction efficiency [66], identification of suitable injection parameters and injector designs to minimize the wastage of polymer, and optimization of injection points within the boundary layer flow to maximize drag reduction. While these challenges are of engineering nature, a fundamental understanding of the mechanisms of polymer drag reduction, which is still lacking as evidenced by the aforementioned debated theories, is likely to offer better solutions to these challenges and open up newer avenues for the implementation of this flow control technique. Thus, the present work is focused on the evaluation of the performance of the polymer solutions and elucidating various mechanisms of polymer drag reduction through experimental investigations. In addition, considering the profound effect of polymers on turbulence, an underlying goal of this study is to accord fundamental insights into the nature of turbulence. The following research questions are raised with the aim to understand the key parameters and relations which control the polymer performance in the turbulent boundary layer:

1. What is the effect of polymer injection concentration on the development of a drag-reduced turbulent boundary layer, and how does the diffusion of polymer away from the wall relate to the drag reduction performance?

2. Which types of turbulent motions and coherent structures are affected by polymer injection, and how do they get affected?

3. Is there a relation between drag reduction and suppression of turbulent motions?

4. How does the polymer affect various turbulent scales in the turbulent boundary layer?

5. Can polymer injection be effective in delaying laminar-turbulent transition in a bypass-transitioning boundary layer?

In light of these research questions, detailed optical measurements of a zero-pressure gradient boundary layer developing over a flat-plate model are conducted in a water tunnel facility. Both transitional and fully developed turbulent boundary layers are investigated with the polymer-injection conducted via a spanwise oriented tangential slot in the flat-plate model, and the results are contrasted against the baseline flow of water. Further, in order to decouple the effect of momentum injection at the slot, a case with benign injection of water through the slot with the same injection parameters is considered in all the investigations. The following objectives are pursued to answer the above research questions:

1. Characterize the streamwise evolution of a polymer-injected turbulent boundary layer and identify the role of polymer concentration on its development.

2. Identify the critical streamwise and wall-normal locations where polymer effect is presented in maximum capacity.

3. Characterize the three-dimensional flow-field at the identified location to elucidate the polymer effect on three-dimensional coherent structures and various turbulent motions.

4. Evaluate the skin friction in conjunction with various turbulent motions in a polymer-injected boundary layer and contrast them against the Newtonian flow of water.

5. Evaluate the effect of polymer on various scales in the boundary layer and identify mechanisms which may explain the effect.

6. Characterize the streamwise evolution of a bypass-transitioning boundary layer and evaluate the effect of polymer injection on the boundary layer parameters.

1.2 Outline of the thesis

This thesis is organized as follows. Chapter 2 presents a review of the current understanding of the Newtonian and drag reduced boundary layer flows. Here, pertinent results from studies in drag reduced internal flows and the underlying concepts of polymer-turbulence interactions are discussed with an extension to their applications in drag reduced external flows. Chapter 3 describes the methodology of experimentation, including brief descriptions of the water tunnel facility and the various optical techniques used throughout the thesis.

The main results from this work are presented in Chapters 4 - 7. Each of these chapters is organized to answer specific research questions outlined above by first providing a relevant background and identifying additional research gaps. Thereafter, description of the experimental setups and analysis techniques used for data collection and reduction is provided with a detailed discussion on the results. Finally, each chapter includes concluding remarks which highlight the specific insights into the considered research question(s).

The performance aspects of the polymer drag reduction in external turbulent boundary layers are first examined in Chapter 4 with a focus on its effect on various turbulent motions in a two-dimensional sense. Chapter 5 presents a three-dimensional characterization of the buffer and lower-log regions of a drag reduced turbulent boundary layer, and the effect of polymer on various coherent structures and Reynolds shear stresses is highlighted through conditional sampling techniques. The three-dimensional flow-fields are further utilized to examine the effect of the polymer on various scales of turbulent motions in Chapter 6. Here, the effect of the polymer on the relation between the Reynolds shear stresses and relatively large-scale skin friction events is of particular importance. Chapter 7 is dedicated to a novel attempt of investigating the effect of polymer injection in transitioning boundary layers which are bypassed into turbulence using a tripping round rod.

Finally, Chapter 8 combines the conclusions from the individual chapters and provides a holistic understanding gained from this thesis. In addition, some recommendations are provided for future directions of research in this area.

Chapter 2

Literature Review

A brief review of the relevant literature in Newtonian and polymer drag reduced boundary layer studies is provided with a focus on the fundamental concepts and well-accepted flow phenomena in each of the scenarios. Discussions on debated topics and other open questions are provided in the context of the current research objectives.

2.1 The flat-plate boundary layer

This section briefly describes the governing equations of a boundary layer and provides the mathematical framework for various boundary layer parameters used throughout this thesis. Thereafter, literature on Newtonian boundary layer flows is reviewed with a focus on the laminar-turbulent transition process, and the implications of the near-wall boundary layer dynamics and turbulence on skin friction.

2.1.1 Governing equations

Boundary layer flows are primarily governed by the conservation laws of mass and momentum in the absence of thermal effects, which is the case in the present work. These are described for a steady incompressible zero-pressure gradient boundary layer flow in 2D Cartesian coordinates as:

$$\frac{\partial u}{\partial x} + \frac{\partial v}{\partial y} + \frac{\partial w}{\partial z} = 0, \tag{2.1}$$

$$u\frac{\partial u}{\partial x} + v\frac{\partial u}{\partial y} + w\frac{\partial u}{\partial z} = \nu\frac{\partial^2 u}{\partial y^2}, \tag{2.2}$$

with the following boundary conditions

$$u = 0,\ v = 0,\ w = 0 \ \text{ at } \ y = 0;\ \ u = U_\infty \ \text{ at } \ y = \infty.$$

Detailed derivations for these equations may be found in Schlichting [67]. In a turbulent flow, the flow variables in Eqs. 2.1 and 2.2 are decomposed into their steady and fluctuating components using Reynolds decomposition:

$$u = \langle u \rangle + u';\ \ v = \langle v \rangle + v',\ \ w = \langle w \rangle + w'.$$

The steady terms are obtained by time-averaging of the signals, whereas the unsteady terms are obtained by subtracting the steady quantity from the original signal. This form of decomposition allows for the evaluation of Reynolds stresses ($\rho\langle u_i' u_j' \rangle$) which are essential in the description and quantification of turbulence in the boundary layer. For a fully developed turbulent boundary layer, the Reynolds shear stress ($\rho\langle u'v' \rangle$) is incorporated in the total stress as [68]:

$$\tau_{\text{total}} = \mu \frac{\mathrm{d}\langle u \rangle}{\mathrm{d}y} - \rho \langle u'v' \rangle. \tag{2.3}$$

In the context of polymer drag reduction, the Reynolds stresses and the total stress are of significant interest, and the influence of the polymer is modelled through an additional polymer stress, which is generated as a result of the interactions of polymer molecules with various turbulent motions, incorporated within Eq. 2.3 as shown in Eq. 2.4 [54, 58, 69]:

$$\tau_{\text{total}} = \mu \frac{\mathrm{d}\langle u \rangle}{\mathrm{d}y} - \rho \langle u'v' \rangle + \tau_{\text{P}}. \tag{2.4}$$

Therefore, a time-resolved, two-component, measurement is mandated to explore the effect of polymers on boundary layer turbulence, and forms the basis for the method of investigation (Chapter 3) used throughout this study.

2.1.2 Laminar-Turbulent Transition

The natural process of laminar-to-turbulent transition occurs in a boundary layer with low levels of external disturbances (Tu $\leq 0.1\%$, where Tu is the turbulence intensity) wherein the disturbances enter the boundary layer and amplify in the near-wall region through the well known Tollmien-Schlichting waves before the ensuing non-linear interactions lead to turbulent breakdown [70]. The initial stage of this process is well described by the linear stability theory [71–73] and has been documented in various scenarios through experimental studies [70, 74–76]. The transition process is said to be *bypassed* when the initial amplification of disturbances is rapid, and leads to a much earlier transition to turbulence [70, 77]. This form of transition is not as well understood and occurs in the presence of relatively high levels of external disturbances (Tu $> 0.5\%$) [78–80] and/or surface roughness among a number of other factors [81–84]. The bypass transition process is of practical significance for a number of engineering applications including flows over marine vehicles due to bio-fouling of the external surfaces [85, 86]. Thus, the effect of polymer injection in the transitioning flow region and the ensuing turbulent boundary layer development is of particular interest.

The bypass transition in the flat-plate boundary layer is characterized by low frequency oscillations in the streamwise velocity leading to the formation of low- and high-speed streaks [79, 87–89]. These streaky structures are also known to undergo various modes of instabilities and oscillate in the spanwise direction with peak-to-peak amplitudes on the order of the freestream velocity [90, 91]. The eventual intermittent appearance of turbulence spots has been

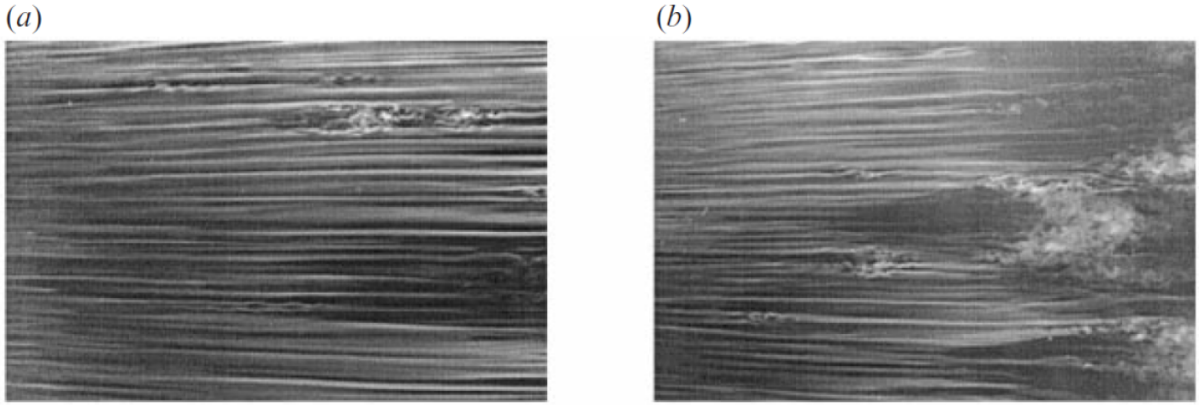

Figure 2.1: Smoke flow visualization of boundary layer in bypass transition highlighting (a) streaky structures (b) intermittent turbulent bursts. Figures adapted from Matsubara and Alfredsson [79] for air flow at a freestream turbulence intensity of 2.2%. Flow is from left to right.

attributed to the breakdown of the streaky structure due to secondary instabilities, adding to the complexity of the transition mechanism [79, 92–96]. Pioneering studies by Emmons [97], and Dhawan and Narasimha [98] illustrate the universality of the intermittency in the late transition stages in both classical and bypass transitioning boundary layers produced by various means, highlighting the similarity and dominance of the turbulence spots within these stages. More recent investigations provide a detailed account of the associated flow dynamics in the vicinity of such turbulent events [79, 92, 99]. A number of computational studies provided critical insights into the pre-transitional processes, such as receptivity mechanisms [100, 101], and turbulent spot generation [102–104], however, their success in describing the later stages of bypass transition, and therefore the transition point, has been limited due to the noted complexity in the intermittent phenomena [105].

Experimental studies have frequently exploited the relative efficiency of various surface roughness elements to trigger the transition process by using distributed surface roughness [106–108] and two- and three-dimensional surface protrusions [109–111]. The efficiency of the tripping device depends on its geometry as well as the Reynolds number based on the height (r) of the roughness element ($Re_r = rU_r/\nu$) [112]. The transition process in two- (*e.g.,* trip wires [113, 114]) and three-dimensional (*e.g.,* zigzag strips [115, 116], pins [109, 117]) surface elements is rather well understood and, hence, controllable for laboratory experiments. In contrast, the transitional flow induced by distributed roughness is not only more complex but also requires relatively long distances for the onset of turbulence [106], which make it a less favourable choice for small to moderate scale experimentation.

2.1.3 Coherent structures

Reviews of Robinson [118] and Dennis [119] provide an excellent and detailed account of the enormous body of work on this topic, and the discussion here concerns with the most pertinent studies for the present work. The near-wall region of a turbulent boundary layer presents a complex structure with an assortment of coherent motions [118–121] which include low- and high-speed streaks, ejection and sweep motions, quasi-streamwise vortices, and hairpin-like vortex structures. Previous studies employing flow visualization methods [122] as well as quantitative measurements [123] have confirmed the streaky structures to have an average spanwise spacing of approximately 100λ in the viscous sublayer (λ is the viscous unit), which increases approximately linearly with wall-normal distance in the buffer layer. The average streamwise extent of the near-wall streaks has been characterized via two-point correlations to be in the range 1000 -1500λ [124, 125], which is in agreement with that obtained using dye visualization techniques [126]. The low-speed streaks have been shown to undergo meandering due to various modes of instabilities [127] which eventually leads to the breakdown of the streaks [99, 128], and thus plays an important role in the self-sustenance of the turbulence cycle [128–130].

Willmarth and Lu [131] categorized near-wall flow motions into quadrants of the fluctuating streamwise (u') and wall-normal (v') velocity components, and introduced a systematic approach to conditionally sample them based on the corresponding Reynolds shear stress (RSS). A number of subsequent studies [121, 132, 133] conditionally sampled the coherent motions, and showed the presence of counter-rotating quasi-streamwise vortices responsible for the production of near-wall turbulent kinetic energy. The average streamwise lengths of these quasi-streamwise vortices is documented to be two orders of magnitude smaller than that of the low speed streaks [134]. These counter-rotating vortices form between the low- and high-speed streaks, and transfer streamwise momentum in the near-wall region through ejection (Q2) ($u' < 0, v' > 0$) and sweep (Q4) ($u' > 0, v' < 0$) events [133].

In addition to the quasi-streamwise vortices in the buffer layer, the low-speed streaks and other low-momentum zones in the upper regions are typically flanked by hairpin-like vortices [120, 135–138] which play a major role in the near-wall dynamics. Experimental verification of these hairpin-like structures was first provided by Adrian *et al.* [136] at low to moderate Reynolds numbers. Adrian *et al.* proposed that the hairpin-like vortices typically appear in the form of packets of multiple closely spaced hairpin structures in a nested hierarchy. These packets of hairpins have been confirmed by numerous studies [120, 139, 140]. The hairpin packets been shown to produce multiple large-scale ejections leading to production of Reynolds shear stresses that are at least an order of magnitude higher than the time-averaged RSS [139] and are typically associated with turbulent bursts [141]. The legs of the hairpins closely resemble the quasi-streamwise vortices in the buffer layer [138], and spanwise vortical heads are found

to appear throughout the log-region with a wide range of inclination angles dependent on their wall-normal distance from the wall [136].

Recent studies at higher Reynolds numbers [142–144] have shown the presence of very large-scale motions (VLSMs) in the log-layer which persist and meander over relatively long distances ($\sim 20\delta$, where δ is the boundary layer thickness) in the streamwise direction. Such large-scale motions in the log-layer have been shown to modulate the near-wall motions [145], further complicating the dynamics in the near-wall region.

2.1.4 Turbulence and skin friction

The wall-shear stress is of practical interest for engineering applications, such as prediction of performance and design optimization of marine vehicles. The wall-shear stress is dependent on the wall-normal gradient of the streamwise velocity at the wall which is significantly influenced by the dynamics of the coherent structures within the near-wall region. Although the effect of turbulence on skin-friction is still an open question, partly due to practical limitations on the achievable Reynolds numbers in experiments and simulations [11], some studies have attempted to associate the effect of the coherent structures in the buffer and log regions with the *footprint* of the wall shear stress [143, 146, 147]. These studies elicit the formation of elongated low- and high-shear stress regions that are reminiscent of the near-wall streak structure. Conditionally averaged three-dimensional flow fields produced by Sheng *et al.* [146] show that the extreme wall-shear stress events are observed within the cores of the corresponding low- and high-speed streaks. The local low and high shear stress regions are also accompanied by coherent wall-normal motions leading to ejections, and sweeps, respectively, and give rise to counter-rotating streamwise oriented vortices. The correlated and organized motion induced by these vortices above the low and high wall-shear stress regions produce large magnitudes of Reynolds shear stress (RSS) in the near-wall region within the immediate vicinity of these regions [146].

Several studies at moderate to high Reynolds numbers [143, 145, 148–150] have shown the influence of very large-scale motions (VLSMs) in the outer layer on the near-wall motions as well as on the wall-shear stress. The DNS simulations of Abe *et al.* [148] at $180 < Re_\tau < 640$ show a strong correlation between the outer layer VLSMs and the wall-shear stress. At the same time, Fukagata, Iwamoto & Kasagi (FIK) identity [151] based decomposition of the wall-shear stress by Deck *et al.* [11] shows that the Reynolds shear stress produced due to the large-scale structures ($> \delta$) accounts for nearly 50% of the wall-shear stress. Hutchins *et al.* [143] produced conditional large-scale low-momentum structures in the log-region extending up to 6δ in the streamwise direction by conditionally sampling the flow corresponding to large-scale low wall shear stress events. While these studies at high Reynolds numbers indicate the footprint of the

VLSMs on the fluctuating wall shear stress, Schlatter *et al.* [150] suggest that such a footprint is not distinguishable at lower Reynolds numbers ($Re_\theta < 1000$). Recently, Wang *et al.* [149] have also argued that the footprint of the superstructures/VLSMs is only mild in the range $400 < Re_\tau < 2900$, and the near-wall streaks are likely to have the most dominant effect on the wall shear stress.

2.2 Polymer drag reduction

This section first introduces some fundamental concepts of polymer drag reduction which are mainly derived from numerous studies in internal flows and have been generally accepted by the research community. Thereafter, a brief description of the results obtained from recent studies performed in external flow scenarios is given, followed by an overview of the debated theories of PDR which form the basis for the discussion of the current results.

2.2.1 Fundamentals of PDR

The majority of previous investigations of polymer-based drag reduction have been focused on internal turbulent flows. Comprehensive reviews of earlier and more contemporary research efforts in this category are provided by Virk [152], Lumley [65, 153], Sellin *et al.* [20], and White and Mungal [154]. They show that the extent of the viscous and buffer layers, encapsulating the dominant viscous effects, is increased in a drag reduced normalized velocity profile. The profile features an effective slip velocity over the Newtonian velocity profile in the same configuration. This results in a velocity defect structure known as the *Newtonian plug*, where the inertial layers, that encapsulate the regions of dominating inertial effects, are displaced farther away from the wall in a uniform manner.

Similar to the description in a Newtonian flow, the log-region of a drag reduced boundary layer is expressed as $\langle u \rangle^+ = \mathrm{A} \ln y^+ + \mathrm{B}$, where A and B are the best-fit coefficients to the semi-logarithmic velocity profile [152], with $\mathrm{A} = 2.44$ and $\mathrm{B} = 5.5$ being typical of a Newtonian flow [155]. Virk *et al.* [48] empirically derived the Maximum Drag Reduction (MDR) asymptote, also known as the *ultimate profile*,

$$\langle u \rangle^+ = 11.7 \ln y^+ - 17, \tag{2.5}$$

which represents the limiting velocity profile corresponding to the maximum drag reduction that can be realized. In a number of subsequent studies, it has been shown to be applicable in both

internal [156–161] and external [50, 59, 162] wall-bounded flows with typical drag reductions of up to 80%.

On the other hand, a limiting shear stress below which no drag reduction occurs is given by the *onset hypothesis* [163], which stems from the transition of the molecular configuration through a coil-stretch process [164]. Besides confirming the onset hypothesis, further studies have shown that the critical shear stress is dependent on the physical properties of the polymer, such as its molecular weight, as well as the polymer-solvent combination used [152, 165–168]. Moreover, from studies on several different polymers in pipe flows, it was established that polyethylene oxide (PEO) was the most effective in drag reduction on a weight basis due to its relatively flexible backbone [167, 169–172], and it is one of the most prominently used polymer for laboratory studies in this area.

2.2.2 Drag reduction in external flows

In comparison to the extensive body of work done on polymer-based drag reduction in internal flows, a limited number of previous investigations considered this technique for turbulent boundary layer control in external flows. Harder and Tiedermann [173] noted that the slope of the inertial layers increased with induced drag reduction in fully developed homogeneously distributed polymer flows, which was verified by recent studies [51, 60, 174, 175]. Some of the earlier works using visualization techniques in homogeneously distributed polymer flows in channels [52, 176, 177] showed that the near wall structure of the drag reduced turbulent boundary layers is altered significantly. Recent investigations using quantitative techniques [50, 51] confirmed that the spanwise spacing of the low-speed streaks is, indeed, increased, and the average rate of the passage of turbulent bursts arising from the appearance of turbulent spots is significantly attenuated in the drag reduced boundary layer.

Motivated by potential flow control applications, such as on marine vehicles, several studies considered the injection of polymer solutions through a spanwise oriented slot into a turbulent boundary layer. Petrie and Fontaine [49] showed the differences in the statistical quantities for a slot-injected boundary layer as compared to a homogeneously distributed channel. White *et al.* [50] performed near-wall PIV measurements at an effectively single streamwise station in multiple wall-parallel planes and found that the spacing of the low-speed streaks increased linearly with increasing drag reduction. They also showed that the strength of the quasi-streamwise vortical structures is reduced, weakening the dispersion of energy from the streamwise to spanwise directions. Warholic *et al.* [51] conducted PIV measurements in both wall-normal and wall-parallel planes and showed that Reynolds stresses are dampened significantly in a drag reduced boundary layer. Walker and Tiederman [178] analysed the quadrants of the velocity fluctuations

obtained using LDV measurements, revealing dampening in all quadrants, with more substantial effects seen in quadrants 2 and 4. However, in light of a minor increase in streamwise fluctuations (u') in the presence of the polymer, the overall decrease seen in the Reynolds shear stress was attributed to the notable reduction in wall-normal velocity fluctuations (v'). Furthermore, the correlation between the streamwise and wall-normal fluctuations was decreased, further reinforcing the argument of decreased dispersion of energy from streamwise to other directions. Similar observations were noted by Fontaine *et al.* [179].

The streamwise development of the drag reduced boundary layer was considered by Hou *et al.* [59] by conducting PIV measurements at multiple streamwise stations downstream of the injection slot. They showed that the injection concentration and the distance from the injector have a significant effect on the mean velocity profiles and the local drag reduction (DR). They also noted discrepancies in DR produced by different brands of the same polymer with slightly different molecular weights when MDR was not attained; however, the trends in statistical quantities remained similar. Polymer stress (τ_{P}), defined by Eq. 2.4 [54], was found to be significant only for $y/\delta < 0.3$, with a contribution of up to 25% of the wall shear stress estimated using a modified version of the FIK identity [151].

In contrast, the polymer stress evaluated for the study of Warholic *et al.* [58] on homogeneously distributed polymer flow in a fully developed channel results in a contribution in excess of 60% of the wall shear stress. Owing to a phase lag in the response of the polymer reaction to the boundary layer turbulence, Hou *et al.* [59] found that the streamwise development of the polymer stress and DR were not correlated.

The diffusion of the injected polymer solution downstream of the injection location has been considered by Walker and Tiederman [180], Somandepalli *et al.* [181], and Winkel *et al.* [182]. Depending on the injection concentration and the distance from the injection slot, Winkel *et al.* [182] observed three distinct regimes of the near-wall polymer flow. These were classified as the development, transitional mixing, and the depletion regimes, identifiable by the polymer flux parameter $K = Q_{\text{inj}} c_{\text{inj}} / \rho (x - x_{\text{inj}}) U_\infty$, where $x - x_{\text{inj}}$ is the distance from the injection slot. The regimes are dictated by the near wall polymer concentrations and its reduction due to diffusion and mixing which affect the polymer performance. The impact of these flow regimes on the DR was also considered by Hou *et al.* [59], who suggest that the relation between the parameter K and DR is independent of the type and the concentration of the injected polymer.

The topic of various drag reduction regimes in the polymeric region (DR $<$ MDR) has seen a great interest since its introduction by Warholic *et al.* [58], who found that the slope of the log-layer in terms of the von Kármán constant (κ) remains constant and matches the Newtonian value in the low drag reduction LDR regime (DR $< 35\%$), whereas κ decreases in the high drag reduction (HDR) regime. Subsequent studies [55, 162, 175, 183] indicate that the identified

threshold varies between $20\% \leq \text{DR} \leq 40\%$.

2.2.3 Mechanisms and theories of PDR

A number of theories have been proposed to describe the mechanism of PDR, particularly by early studies, including wall-adsorption and slip [184–187], shear thinning within the viscous sublayer [188], and polymer-turbulence interactions [53, 65]. While the theories based on wall effects were immediately refuted citing inconsistent observations through experiments [169, 189, 190], the viscoelastic mechanisms arising from the interactions of polymer molecules and turbulent motions are still at the heart of the ongoing research efforts in this area. These mechanisms are primarily classified into the viscous mechanism proposed by Lumley [65, 153] which postulates the disruption of the turbulent energy cascade caused by the increased extensional viscosity of the stretched polymer additives outside the viscous sublayer, and the elastic mechanism of Tabor and de Gennes [53] which assumes the same effect due to the storage of the turbulent energy within the partially stretched polymer molecules in the buffer layer.

Remarkably, both the proposed mechanisms have been subject to a number of investigations in the recent past through DNS simulations complemented with viscoelastic models, such as the Finitely Extensible Nonlinear Elastic - Peterlin (FENE-P) [191] and Oldroyd-B models, which have produced comparable descriptions of the flow dynamics despite the differences and limitations of the models [54, 56, 191, 192]. From the perspective of the elastic model, it is suggested that the polymer chains stretched by the mean shear in the near-wall regions are lifted up by the quasi-streamwise vortical structures into the lower log-layer where they release the stored elastic energy. This release of energy is shown to primarily occur in the streamwise direction resulting in the observed increase in the streamwise fluctuations in the lower-log region [49, 59–61]. In contrast, a recent investigation by Pereira *et al.* [56] has shown that, while the polymer stretching due to mean shear in the near-wall region is considerable, additional polymer stretching due to extensional turbulent motions ($u_i' u_i'$) in the buffer layer is necessary to fully explain the observed levels of polymer stretching outside the viscous sublayer.

The numerical studies have also underscored the importance of the Weissenberg number (Wi) on the flow characteristics and the obtained drag reduction by illustrating the role of elasticity in dampening near-wall vorticity and decreasing the RSS in the coherent structures [54,55,57,193]. It is proposed that the counter-torques responsible for this vortex damping are generated as a result of the polymer stretching in the quasi-streamwise vortices [57, 183, 193]. Furthermore, the dampening of the near-wall vorticity results in a significant reduction in the Reynolds shear stress leading to an expanded buffer layer. Li and Graham [194] noted that even with a strong enough viscoelasticity, a non-negligible instantaneous Reynolds shear stress [54, 195, 196] is

still observed, limiting the drag reduction by the so-called Maximum Drag Reduction (MDR) asymptote [48]. The asymptotic drag reduction limit has been shown to hold regardless of the polymer, or even the type of the drag reducer [17, 197].

Experimental investigations into the working mechanisms of PDR have been limited to statistical descriptions of the drag reduced flow (*e.g.,* [49–51, 59, 182]), possibly due to practical limitations and unavailability of highly resolved three-dimensional measurement techniques. Nevertheless, experiments in homogeneous channel flows conducted by Shaban *et al.* [60] demonstrate the effect of extensional viscosity of the polymer on the achieved drag reduction. Earlier, Tiederman *et al.* [52] observed that there was no drag reduction when the polymer molecules were contained within the viscous sublayer which led them to hypothesize that the polymers become active when subjected to the extensional motions in the buffer layer, and are relatively passive in the viscous sublayer. Other indirect evidences for the correlation between extensional viscosity and drag reduction have been obtained through capillary breakup extensional rheometry (CaBER) [161, 198]. On the other hand, the attribution of the reduced RSS to an accumulated polymer stress (τ_P) by Hou *et al.* [59], points to an elastic mechanism of PDR.

Chapter 3

Methodology

Descriptions of the testing facility, model, and polymer-injection method are given along with an overview of the setups used for the flow measurement using two different techniques and the related processing parameters.

3.1 Experimental Setup

3.1.1 Water tunnel facility

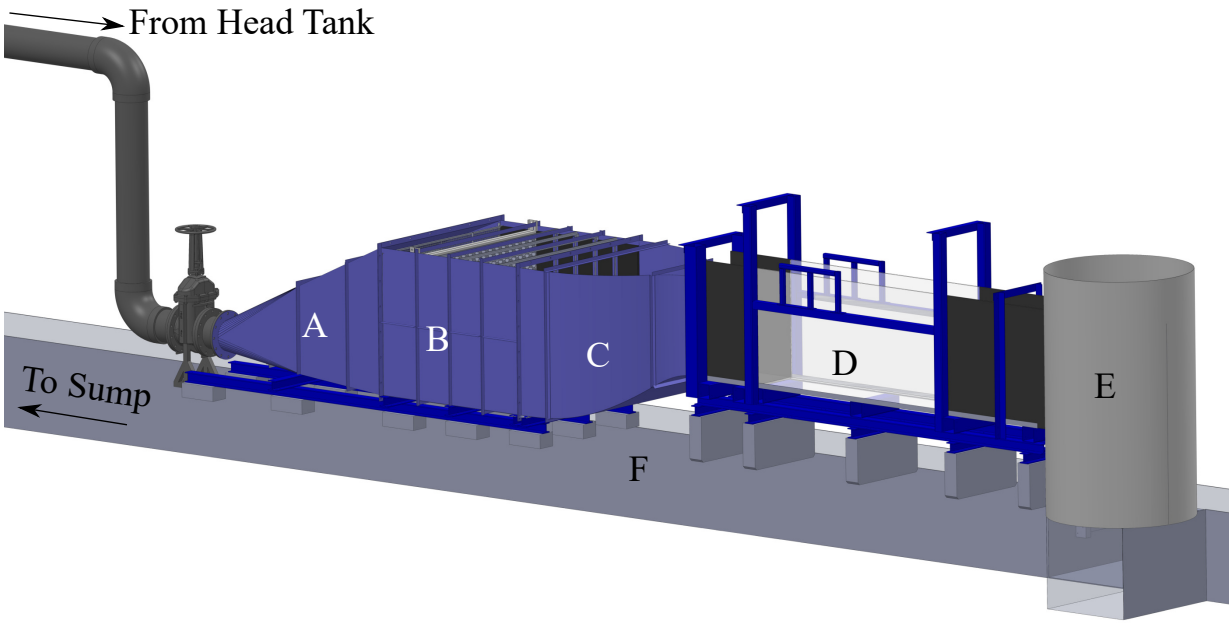

Figure 3.1: Water tunnel facility at University of Waterloo. A: diffuser , B: settling chamber, C: contraction, D: glass test section, E: outlet tank, and F: return channel to the sump.

The experiments were carried out in a closed-loop water tunnel facility at University of Waterloo shown in Fig. 3.1. The flow in the tunnel is driven by a constant head developed in the overhead tank, where water is supplied from the sump reservoir by two centrifugal pumps. A gate-valve is installed upstream of a wide-angled diffuser in order to control the flow rate in the tunnel. The settling chamber houses the flow conditioning elements which include a square grid (12.7 mm spacing), a honeycomb (12.7 mm cell), and four wire meshes, with all the elements following the design recommendations of Mehta and Bradshaw [199] and Derbunovich *et al.* [200]. The flow enters the test section through a contraction which has an area ratio of 5.9. An entrance length equivalent to the width of the contraction is allowed before the start of the glass test section. The 2.5 m long test-section is 0.5 m in width and is designed for a water height of 0.8 m. The flow velocity is set by a combination of the gate valve and a variable porosity backgate placed approximately 1 m downstream of the test-section. The water exits from the tunnel through the outlet tank that is placed directly above the return channel. For the designed oper-

ating water level, test-section velocities up to 0.5 m s^{-1} can be achieved. The flow uniformity in the vertical and spanwise directions is within 1% of the free stream velocity and the freestream turbulence intensity in the streamwise direction is within 1% for all the test cases considered in this investigation. The temperature of the water is verified to remain constant within 0.1 °C during all the experiments.

3.1.2 Flat-plate model

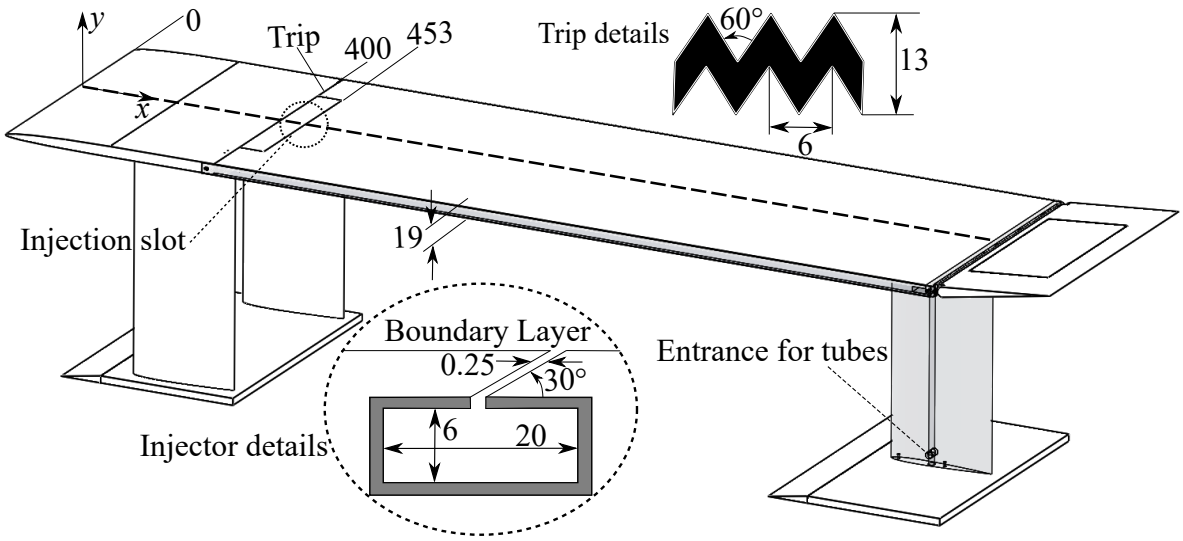

Figure 3.2: Sketch of the flat-plate model showing the coordinate system, details of the polymer injector and the zigzag trip. The zigzag trip is used for experiments reported in Chapters 4 - 6. All the dimensions shown are in mm but are not to scale.

The flat-plate model, shown in Fig. 3.2, is designed in a modular fashion consisting of a modified super-ellipse type leading edge [201], a flat middle section, and a movable trailing edge flap. The flat plate has a surface roughness (k_s) of 0.5 µm which corresponds to the surface roughness parameter (k_s^+) of less than 0.01. The coordinate system used for data presentation is shown in Fig. 3.2, with the origin located at the leading edge. The assembled plate model spans the entire width of the test section, and the flap was set to 5° to appropriately condition the location of the stagnation point. The total length of the plate model (L) is 2200 mm measured from the leading edge to the trailing edge with flap set to 0°. The elliptical portion of the leading edge extends up to $x/L = 0.1$, and the zero pressure gradient along the top surface begins at $x/L \approx 0.25$. The polymer injection slot is located at $x/L \approx 0.206$, or 453 mm downstream of

the leading edge. It is 0.25 mm wide, spans 300 mm, and is inclined at 30° with the streamwise direction to achieve nearly tangential injection. This injection angle is close to the optimum angle suggested by Walker *et al.* [202] and matches the one used in the study of Hou *et al.* [59]. The entire plate model is mounted on three supports that have a NACA 0012 cross section.

3.1.3 Polymer solution preparation and injection

Polyethylene oxide (PEO, Sigma-Aldrich Inc.) with an average molecular weight of 8 Million g/mol was used in all the experiments in this thesis. The viscosity of 1% solution in water at 25 °C is 10 000 - 15 000 mPa s. The polymer solutions were prepared using the following protocol. The mass of the polymer powder was measured using digital scales with a resolution of 0.01 g. The powder was mixed with distilled water using a stationary overhead mixer with a four-bladed impeller operated at 70 rpm for two hours and then allowed to stand for 12 h for degassing [203]. The polymer solutions were characterized using a standard rotor-bob viscometer (Model 35 - Fann Instrument Company) over a range of shear rates $1.5 \leq \dot{\gamma} \leq 1021$, where $\dot{\gamma}$ is the imposed shear rate in s^{-1}. The measurements were used to verify the consistency of the polymer solutions obtained using the described preparation protocol.

Polymer solution injection on the measurement surface of the flat-plate is achieved via a peristaltic pump (AOBL BT101S), which pumps the solutions at a constant flow rate into a 3D printed polymer injector located under a 0.25 mm wide injection slot, as shown in the detailed cross-sectional sketch in Fig. 3.2. The use of a peristaltic pump minimizes any potential for polymer degradation known to occur in rotary pumps [204]. The injector serves as a manifold with one inlet at each spanwise end. A metallic mesh is incorporated along the span within the injector body to improve the flow uniformity.

The injector was characterized in a stagnant pool of water with the same pressure head, and the outlet velocity from the manifold was verified to be uniform to $\pm$ 7.6% along 75% of the centre span. A detailed description of the injector design and outlet flow characterization is presented in Appendix B. It must be mentioned that the inclined slot above the outlet of the manifold is a duct of 50 slot widths in length, which provides further improvement of injection uniformity. A mean injection velocity (u_{inj}) of 0.025 m s^{-1} was used in all the cases investigated, which is less than 9% of the freestream velocities used in all the experiments (U_∞ = 0.28 - 0.3 m s^{-1}), corresponding to a normalized injection rate $Q_{\text{inj}}/Q_{\text{s}}$ = 0.086, where $Q_{\text{s}} = 67.3\nu$ is the discharge in the viscous sublayer ($y^+ < 11.6$) per unit width [205]. It should be noted that the employed injection velocity is considerably lower than those used in some of the previous studies, *e.g.,* 23% of the freestream velocity in the case of Hou *et al.* [59], which was done to minimize the effect of momentum injection on the boundary layer development. The injection flow rates

and concentrations were chosen to achieve similar polymer flux parameters (K) with previous studies [59, 182] and the universal curve identified by Hou *et al.* [59]. During the experimental campaigns with polymer injection, the total mass of injected polymer was monitored in order to maintain a homogeneous background concentration well below the limit of 1 ppm, as used in most of the previous studies [179, 182]. Based on the polymer injection rates used in the present experiments, a homogeneous background concentration of approximately 0.7 ppm may be expected, although the actual background polymer build-up is expected to be lesser, since the choice of PEO ensures significant mechanical degradation as the molecules pass through the centrifugal pumps [66].

3.2 Experimental Techniques

Particle Image Velocimetry

Planar and tomographic particle image velocimetry (PIV) measurements were employed for flow measurements in this study. These techniques allow for the measurement of local flow velocities through optical means and yield two- and three-dimensional velocity vector fields with two and three velocity components, respectively. The measurement setup involves one or more cameras and a high-power laser to illuminate the flow which is seeded with light-scattering micron scale particles. Given the optical nature of the technique, it is minimally intrusive for flow measurement which is critical for measurements in boundary layers. Detailed working of the techniques are provided by Raffel *et al.* [206].

3.2.1 Setup

The PIV parameters used in all the experiments reported in this thesis are presented in Table 3.1. The planar PIV measurements were conducted in all the experiments for baseline boundary layer characterization and investigation of benign and polymer-injection, and used hollow glass spheres (Sphericel, Potters Inc.) with a mean particle diameter of 10 µm for flow seeding. The tomographic PIV measurements were conducted for the investigation of the near-wall region of the turbulent boundary layer and required larger seeding particles with higher scattering intensities owing to the significant expansion of the laser beam. Thus, silver coated hollow glass spheres (SH400S20, Potters Inc.) with a mean particle diameter 16 µm were used. The particle slip velocities for both types of seeding particles were verified to be negligible based on the computed

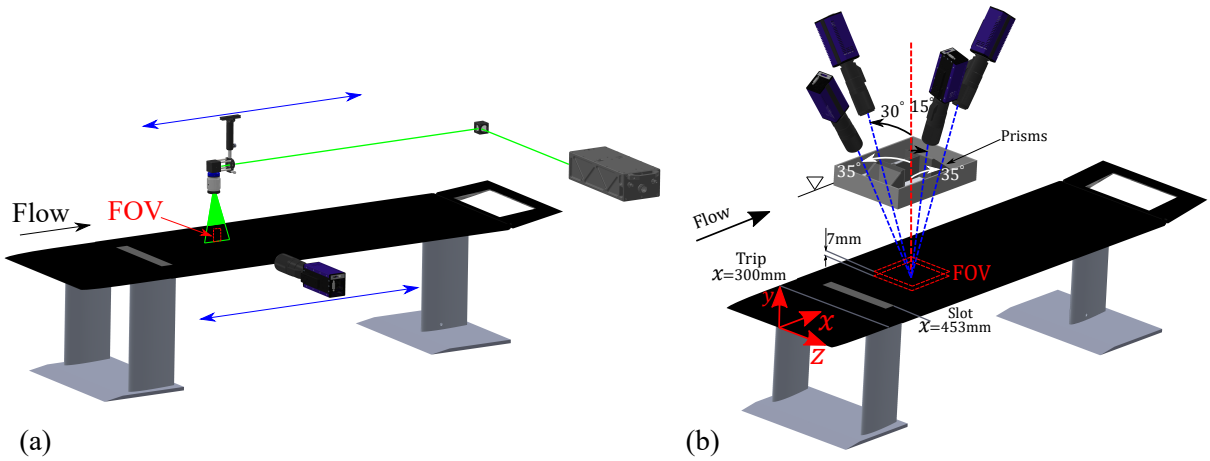

Figure 3.3: Schematic of the experimental setup for (a) planar PIV, and (b) tomographic PIV.

Stokes numbers [206]. In addition, the injected solutions were pre-seeded with the seeding concentrations matched to the concentration in the background flow to minimize any biases caused by inhomogeneous seeding.

The experiments used two types of cameras and lasers with their specifications given in Table 3.1. The schematics of the setups used in the planar and tomographic PIV measurements are shown in Figs. 3.3(a) and 3.3(b), respectively. The camera(s) were equipped with Nikkor macro lenses with a fixed focal length of 200 mm set to a numerical aperture $f_{\#} = 5.6$ and $f_{\#} = 22$ in planar and tomographic PIV measurements, respectively. For the tomographic PIV measurements, all four cameras were equipped with Scheimpflug adapters. Water-filled prisms were used for three cameras with large tomographic angles ($\geq 30°$), while no prism was necessary for the camera with 15° angle. All the PIV images were captured in double-frame mode and the laser and cameras were synchronized by a programmable timing unit and controlled via DaVis 8.4.0 and 10.1 softwares (LaVision GmbH). The time separation between the laser pulses, acquisition frequencies, and number of samples acquired are presented in the table. All the planar PIV measurements were conducted at multiple streamwise stations along the mid-span of the flat-plate model with the streamwise positioning of the camera and the laser sheet facilitated by two separate traversing systems, both with a resolution of 5 µm. The exact measurement locations and the corresponding boundary layer parameters are reported in the corresponding experimental setup sections in each of the result chapters.

PIV parameters							
Parameter	Ch. 4		Ch. 5 and 6			Ch. 7	
Measurement technique	Planar PIV		Planar PIV		Tomographic PIV	Planar PIV	
Laser	Quantel EverGreen 70		Photonics DM20				
Seeding particles	Sphericel - 10 µm				SH400S20 - 16 µm	Sphericel - 10 µm	
Camera(s) (px pitch, res.)	Imager Pro X (7.4 µm, 14 bit)		Imager sCMOS (6.5 µm, 16 bit)				
Sensor size (px)	701 × 1600		1800 × 2160		2560× 2160		
Lens focal length (mm)	200						
Numerical aperture ($f_\#$)	5.6				22	5.6	
Field of view	27.8 × 63.5 mm^2		40.6 × 48.7 mm^2		49.3 × 7.0 × 58.5 mm^3	38.4 × 32.4 mm^2	
Digital resolution (px/mm)	25.2		44.3		43.8	66.7	
Dataset	6000				1000	4500	
Acquisition frequency (Hz)	14		15				
Laser pulse separation (µs)	1600		1000				
Part. disp. in freestream (px)	11.5		13.0			20.8	
Velocity evaluation method	Seq.	Ens.	Seq.	Ens.	FFT - volume	Seq.	Ens.
Interrogation window (px/vox.)	24 × 24	4 × 4	24 × 24	4 × 4	48 × 48 × 48	24 × 24	4 × 4
Window overlap	75%	50%	75%	75%	75%	75%	50%
Vector pitch (µm)	238.0	79.4	135.4	22.5	274.0	89.9	30.0

Table 3.1: Parameters for PIV measurements used for experimental results presented in Chapters 4-7. Seq. and Ens. refer to the sequential and ensemble of correlation PIV processing algorithms, respectively.

3.2.2 Processing

The planar PIV particle images were pre-processed using a minimum intensity subtraction time-series filter with a kernel of 15 images to improve the signal-to-noise ratio. The images were then normalized with the ensemble average to mitigate the reflections at the wall and adjust for any variations in the illumination intensity within the field of view (FOV). The pre-processed image pairs were first processed with the ensemble of correlation algorithm [207, 208] to obtain a time-averaged velocity field. These results were used as an initial displacement predictor for a sequential-correlation algorithm which was employed with final window sizes and overlap factors given in Table 3.1. The associated uncertainty due to the random error in the measurement of instantaneous freestream velocity is estimated to be smaller than 0.5% of U_∞ in all the cases. In addition, the particle images were also processed using a single-pixel correlation algorithm [209, 210] for the most upstream location reported in Ch. 4 to improve the resolution in the near-wall region for the wall shear stress estimation.

In case of tomographic PIV, the images were pre-processed by employing an ensemble minimum subtraction for all images, sliding minimum subtraction over a kernel of 3×3 pixels for each image, and normalization of the images with a local average computed over a relatively large kernel of 90×90 pixels to adjust for any intensity variations within the image. All the images were normalized with the first frame in the sequence at each time instant to correct for any variations in the intensities between different cameras and pulses. Volume calibration using a third-order polynomial was performed through a perspective calibration based on a dual-plane calibration target. Then, the volume self-calibration procedure [211] was performed separately on each acquired data set until a residual disparity of less than 0.05 pixel was achieved. Reconstruction of particle intensities in 3D space was achieved using the combination of MLOS and SMART algorithms [212]. Velocity vectors in the 3D space were obtained using an iterative cross-correlation technique [213] with a final interrogation volume size of 48 × 48 × 48 voxels with 75% overlap. This resulted in a velocity vector field consisting of 197 × 26 × 204 vectors per snapshot corresponding to a vector pitch of 274 µm.

The average uncertainty in the particle displacements obtained from tomographic PIV based on the random error in both longitudinal and out-of-plane components is estimated to be approximately 0.4 pixels [214, 215] which corresponds to approximately 3.2% of U_∞. However, this uncertainty of the longitudinal component is expected to vary inversely with the distance from the wall from about 1.5 pixels close to the wall to 0.1 pixels in the freestream due to the strong velocity gradient near the wall [214]. Measurement accuracy of the velocity fluctuations from tomographic PIV was assessed by comparing tomographic and planar PIV data, and the results were found to be in agreement with the above uncertainty estimates. A higher relative error was observed in the out-of-plane component (v') at low velocity magnitudes, however, being

uncorrelated with the noise in the streamwise component, it leads to only a minor overestimation in the RSS. A detailed description of the procedure used for uncertainty estimation in PIV measurements is presented in Appendix C.

3.2.3 Planar Laser Induced Fluorescence

Planar laser-induced fluorescence (PLIF) measurements were conducted for the evaluation of the evolution of near-wall concentration of the injected solutions. The PLIF measurements were conducted in both turbulent (Ch. 4) and transitioning (Ch. 7) boundary layers for water and polymer with a concentration of $c_{\text{inj}} = 1000\,\text{ppm}$. For this purpose, the injected solutions were doped with Rhodamine-6G fluorescent dye. The flow field images were obtained in single-frame mode with same illumination and camera settings as those used for planar PIV. 200 images with a FOV of $57 \times 27\ \text{mm}^2$ were obtained in the turbulent boundary layer, whereas 1000 images with a FOV of $38.4 \times 32.4\ \text{mm}^2$ were obtained in the bypass-transitioning boundary layer. A yellow band-pass filter was used to isolate the fluorescent emission of the dye. A linear relationship between the local fluorescent intensity and concentration for the weakly excited dye [216] allows the evaluation of the time averaged local concentrations (c) relative to the injected concentrations at the slot (c_{inj}).

Chapter 4

Streamwise development of a drag-reduced turbulent boundary layer

The effect of local polymer solution injection on the evolution of a flat-plate turbulent boundary layer has been investigated experimentally. Polyethylene oxide (PEO) solutions were injected through an inclined slot. The influence of polymer injection on boundary layer development downstream of the slot is assessed at three different concentrations (100, 500, 1000 ppm) using planar velocity field and concentration measurements. Local drag reduction (DR) of up to 60% *was obtained in the vicinity of the slot. A systematic change observed in the inverse of the von Kármán constant (*$k = 1/\kappa$*) with increasing DR is used to define sub-regimes of the high drag reduction regime, and a linear relation between* k *and DR is shown to persist over a wide range of Reynolds numbers. The analysis of combined velocity and concentration measurements provides added insight into the associated changes in the boundary layer characteristics and the underlying flow physics.*

Parts of this chapter have been adapted from Y. Shah and S. Yarusevych, "Streamwise evolution of drag reduced turbulent boundary layer with polymer solutions," *Physics of Fluids*, vol. 32, no. 6, p. 065108, 2020.

4.1 Introduction

Sec. 2.2.1 discusses the expected trends in polymer based drag reduced internal flows, while their extensions to external flows were presented in Sec. 2.2.2. Previous investigations in both channel flows and external turbulent boundary layers have focused on the dynamics of drag reduced boundary layers and have illustrated the extended buffer layers and increased log-law slopes [59, 60, 173], decreased bursting rates [176, 177], and increased spanwise spacing of low and high speed streaks [50] leading to a significant attenuation of velocity fluctuations and Reynolds shear stresses [49, 51, 178, 179]. Furthermore, in an effort to investigate the control mechanism of polymer drag reduction, recent studies have illustrated the suppression of small eddies and quasi-streamwise vortices which lead to the decreased Reynolds stresses [50, 57], as discussed in Sec. 2.2.3.

The streamwise development of the drag reduced turbulent boundary layer considered by Hou *et al.* [59] elucidated the resulting stress deficit in the form of the polymer stress (τ_P) using Eq. 2.4. While their results suggest a contribution of the polymer stress of approximately 25% to the wall-shear stress, they highlighted some open questions that motivate the present study. Firstly, the reported mean streamwise velocity profiles in inner coordinates (normalized using the viscosity of water) show significant changes in the viscous sublayer ($y^+ \leq 10$), contrasting with the results of Koskie and Tiederman [217] and Tamano *et al.* [17]. Subsequent studies of Motozawa *et al.* [218, 219] and Elbing *et al.* [162] have not been able to resolve this issue due to the lack of data in the viscous sublayer. Secondly, the viscosity corrected velocity profiles in inner coordinates show a clear distinction between the near MDR cases and DR $<$ MDR cases within the inertial sublayers, but the underlying cause of this remains unclear. Finally, the skin friction determination assumes the validity of the $(1 - y/\delta)$ fitting technique [69] to the shear stress profiles in the polymer flow which is based on the FIK identity [151]. However, the results of the Reynolds shear stress profiles and the applicability of Eq. 2.4 throughout the boundary layer suggest that the polymer stress may be significant until the edge of the boundary layer, bringing into the question the validity of the FIK identity based approach in the case of inhomogeneous polymer flow.

Notwithstanding the pronounced focus on polymer based drag reduction in inhomogeneous external wall-bounded flows, as discussed in detail in Sec. 2.2, its underlying mechanism and its influence on the development of the turbulent boundary layer remain open research questions. This is reflected in the aforementioned discrepancies in some of the previously reported findings, often related to the experimental data in the near-wall region, or the validity of approximations employed in the analysis. Thus, the goal of the present study is to systematically examine the salient flow characteristics that accompany drag reduction in a spatially evolving turbulent boundary layer. This is achieved through detailed 2D-PIV and planar-laser induced flu-

orescence (PLIF) measurements conducted in a polymer drag reduced turbulent boundary layer downstream of a spanwise injection slot, allowing for a holistic interpretation of the turbulence statistics in the context of varying near-wall polymer concentrations.

4.2 Experimental Setup

Planar, two-component PIV measurements were conducted in the $x-y$ plane located at the mid-span of the plate model as described in Sec. 3.2.1, with the specifications of the measurement instrumentation outlined in Table 3.1. The boundary layer was tripped by placing a zigzag trip at $x/L \approx 0.18$ as shown in Fig. 3.2. A constant freestream velocity of $U_\infty = 0.28 \pm 0.003\,\mathrm{m\,s^{-1}}$ was used for the present investigation. The Reynolds number based on the height of the trip is approximately 575, which falls within the range suggested by Braslow and Knox [112]. The laminar boundary layer thickness at this location is $\delta_{\mathrm{tr}} \approx 6.3\,\mathrm{mm}$, and the effect of the trip on the boundary layer statistics is expected to be negligible beyond $15\delta_{\mathrm{tr}}$ [115], or by $x/L \approx 0.225$.

The measurements were performed in two different sets as shown in Table 4.1. The first set included one injected polymer concentration $c_{\mathrm{inj}} = 1000$ ppm and five downstream measurement locations in increments of $100\,\mathrm{mm}$, while the second set included tests with three different polymer concentrations c_{inj} = 100 ppm, 500 ppm, and 1000 ppm, and three downstream measurement locations. For the purpose of comparison with the Newtonian flow, baseline measurements without injection and measurements with water injection (c_{inj} = 0 ppm) were conducted. The consistency of the results and the effect of the polymer injection was also verified by repeating measurements for baseline flow and $c_{\mathrm{inj}} = 1000$ ppm.

The PIV measurements were performed using an Imager Pro X CCD camera with a cropped sensor size of 701×1600 pixel. The camera has a pixel pitch of $7.4\,\mu\mathrm{m}$ and a 14 bit resolution. It was equipped with a Nikkor macro lens with a fixed focal length of $200\,\mathrm{mm}$ set to a numerical aperture $f_\# = 5.6$. A green band-pass filter was mounted in front of the lens to minimize optical noise in the images. The camera imaged a field of view (FOV) of 27.8×63.5 mm^2 illuminated with a dual cavity $532\,\mathrm{nm}$ Nd:YAG laser (Quantel EverGreen 70). The arrangement of the main PIV system elements is depicted in Fig. 3.3(a). The laser and camera were synchronized by a programmable timing unit and controlled via LaVision DaVis 8.4.0 software. The sheet forming optics for the laser beam was mounted on an automated streamwise traverse with a resolution of $5\,\mu\mathrm{m}$ and a travel length of $1270\,\mathrm{mm}$. The camera was mounted on another automated streamwise traverse, allowing for the FOV position to be adjusted while maintaining the same relative position between the camera and the laser sheet. The flow was seeded with hollow glass spheres with a mean particle diameter of $10\,\mu\mathrm{m}$. For each set of experimental conditions (Table 4.1), 6000 image pairs were acquired in double-frame mode at $14\,\mathrm{Hz}$. The image pairs had a time

Experimental parameters					
PIV Set 1, $c_{\text{inj}} = 1000$ ppm, $U_\infty = 0.28\,\text{m}\,\text{s}^{-1}$					
x/L	$x - x_{\text{inj}}$	$Re_x \times 10^5$	Re_{θ_0}	δ_0	λ_0 (μm)
[0.248, 0.261]	[87, 114]	1.472	357	13.0	72
[0.291, 0.294]	[187, 214]	1.736	418	15.6	74
[0.339, 0.352]	[287, 314]	1.998	470	18.1	75
[0.385, 0.397]	[387, 414]	2.261	523	20.0	76
[0.430, 0.442]	[487. 514]	2.524	600	22.9	78
PIV Set 2, $c_{\text{inj}} = 0^\dagger$, 100, 500, 1000 ppm, $U_\infty = 0.28\,\text{m}\,\text{s}^{-1}$					
[0.248, 0.261]	[87, 114]	1.472	357	13.0	72
[0.430, 0.442]	[487, 514]	2.524	600	22.9	78
[0.567, 0.579]	[787, 814]	3.313	708	26.7	79
PLIF Set, $c_{\text{inj}} = 0^\dagger$, 1000 ppm, $U_\infty = 0.28\,\text{m}\,\text{s}^{-1}$					
[0.202, 0.228]	[-13, 44]	1.194	-	-	-
[0.248, 0.274]	[87, 144]	1.472	357	13.0	72
[0.291, 0.319]	[187, 244]	1.736	418	15.6	74
[0.339, 0.365]	[287, 344]	1.998	470	18.1	75
[0.384, 0.410]	[387, 444]	2.261	523	20.0	76
[0.430, 0.456]	[487, 544]	2.524	600	22.9	78
[0.475, 0.501]	[587, 644]	2.802	-	-	-

Table 4.1: Test matrix. Coordinate ranges identify the streamwise extent of each field of view and boundary layer parameters are given for the baseline case measured $3\,\text{mm}$ downstream of the upstream edge of each FOV. All the dimensions are in mm unless specified otherwise. †indicates water injection. $\lambda_0 = \nu/u_\tau$, where u_τ is the friction velocity.

separation of $\Delta t = 1600\,\mu\text{s}$ corresponding to a mean particle displacement of 11.5 pixels in the freestream, and an uncertainty in the measurement of instantaneous freestream velocity of $< 1\%$.

Particle images were pre-processed using a minimum intensity subtraction time-series filter

with a kernel of 15 images to improve the signal to noise ratio. Each image was then normalized with the ensemble average to mitigate the reflections at the wall and adjust for any minor variations in illumination intensity within the FOV and between pulses. The image pairs were first processed with ensemble of correlation algorithm [207, 208] to obtain a time-averaged velocity vector field, with a final window size of 4×4 pixel and an overlap of 50% resulting in a vector pitch of $79.4\,\mu\mathrm{m}$. In addition to providing mean velocity fields, the results were used as an initial displacement predictor for a sequential-correlation algorithm employed to obtain instantaneous velocity fields. The final interrogation window size in this case was 24×24 pixel with an adaptive weighting factor and 75% overlap, resulting in a vector pitch of $238\,\mu\mathrm{m}$. For the most upstream measurement location (Table 4.1), particle images were also processed using a single-pixel correlation algorithm [209, 210] to improve the resolution in the near-wall region for the wall shear stress estimation.

In addition to PIV measurements, PLIF measurements were conducted for a polymer concentration of $c_{\text{inj}} = 1000$ ppm to quantify the diffusion of polymer downstream of the injector (Table 4.1) using the procedure outlined in Sec. 3.2.3.

4.3 Results and Discussion

4.3.1 Characterization of polymer solutions

For the assessment and analysis of the polymer effect on boundary layer development, it is essential to quantify polymer characteristics in terms of their shear viscosity and stability. The results of multiple viscometer measurements conducted at free-stream temperature are presented in Fig. 4.1, where uncertainty limits incorporate measurement uncertainty as well as variability in properties between measurements performed on different batches of polymer solutions. The results illustrate the expected shear thinning behaviour characterized by decrease in the viscosity with increasing shear rates. The viscosity of water at the free-stream temperature is shown for comparison. It can be seen that, as expected, the shear thinning becomes progressively weaker at lower concentrations [60]. These measurements were performed with every batch of polymer solution to ensure consistent polymer characteristics.

4.3.2 Near wall polymer concentration

PLIF images of the turbulent boundary layer injected with dyed water (passive tracer) and polymer solution are presented in Figs. 7.2(a) and 7.2(b), respectively, to qualitatively illustrate

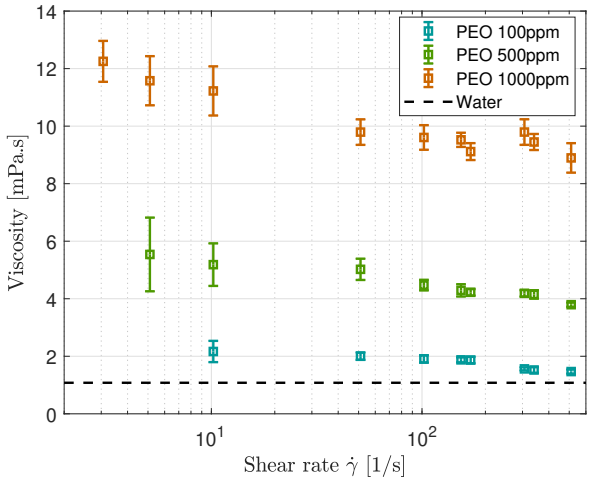

Figure 4.1: Measurements of shear viscosity of the polymer solutions with increasing shear rates on a semi-logarithmic plot.

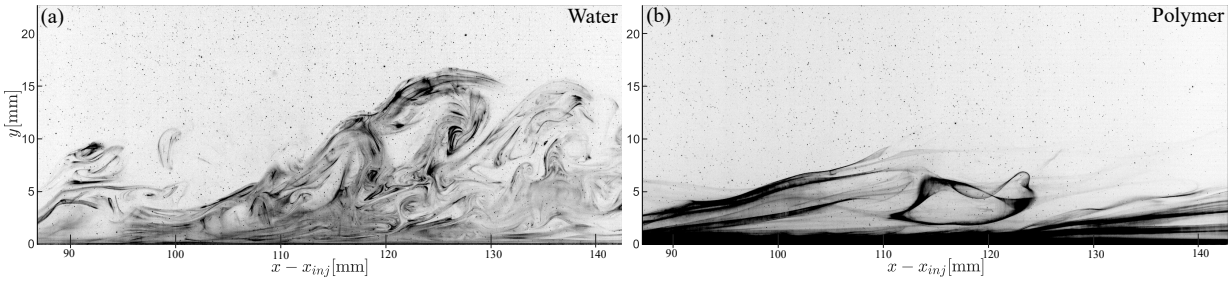

Figure 4.2: Instantaneous flow visualization images in a turbulent boundary layer with (a) water injection (passive tracer) and (b) polymer injection $c_{\text{inj}} = 1000$ ppm. Note that images are intended to qualitatively illustrate differences in the boundary layer development between the two cases due to passive/active nature of the visualization tracer.

boundary layer development. The flow development with water injection is representative of a typical turbulent boundary layer with large-scale eruptions from the wall and a range of smaller scales visualized in Fig. 7.2(a). The results in Fig. 7.2(b) visualize polymer filaments stretched in the streamwise direction, and, in contrast to Fig. 7.2(a), the boundary layer flow appears to be less chaotic. Although notable detachment of polymer filaments from the highly concentrated near wall layer indicate the presence of turbulent mixing, the extent of these eruptions in the wall-normal direction is reduced considerably in comparison with the Newtonian flow.

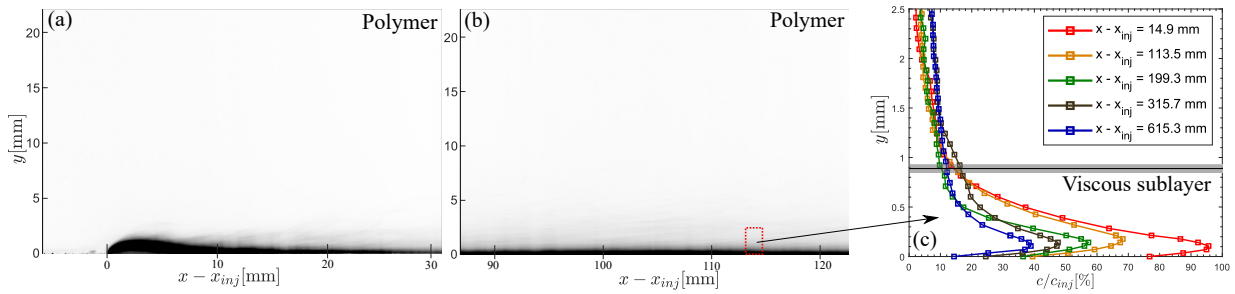

Figure 4.3: Time-averaged PLIF images with polymer injection $c_{\text{inj}} = 1000$ ppm at (a) the injection slot, (b) $x - x_{\text{inj}} = 87\,\text{mm}$. (c) Concentration profiles normalized by the concentration at the slot at various downstream distances from the slot. Edge of the local viscous sublayer ($y^+ = 11.6$) varies in the region shown in gray.

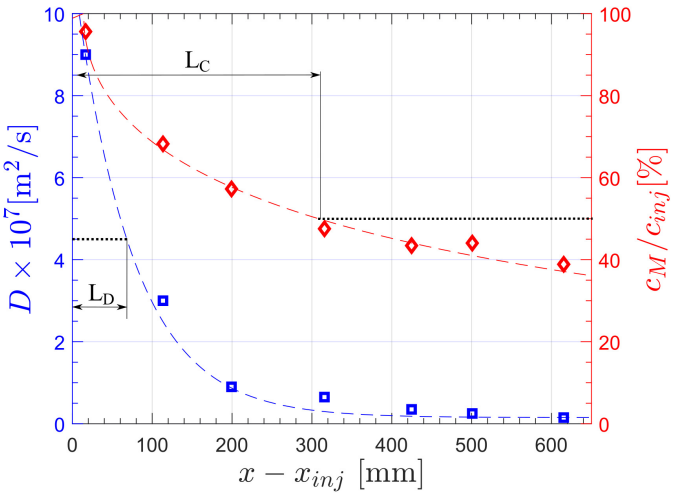

Figure 4.4: Variation of the diffusion coefficient D and the relative wall concentration c_M/c_{inj} with the distance from the slot. Dashed lines in blue and red depict equations 4.2 and 4.3 respectively.

The downstream development of injected polymer solution is examined through time-averaged images presented in Fig. 4.3. Time averaged visualization of polymer injection in Fig. 4.3(a) shows minor jet penetration owing to the low injection rate employed in the present study. Nevertheless, the injected polymer jet reorients within a relatively short downstream region and effectively reattaches to the wall by $x - x_{\text{inj}} \approx 10\,\text{mm}$, which is also evidenced by the downstream polymer solution tracer development in Fig. 4.3(b). Since it is essential for drag reduction to concentrate the polymer solution in the near-wall region, the results highlight the importance of

injection parameters in such a jet-in-cross-flow configuration with relatively high viscosity ratio. The time-average concentration (c/c_{inj}) profiles, presented in Fig. 4.3(c) for $c_{\text{inj}} = 1000$ ppm, confirm high polymer concentration in the viscous sublayer region demarcated in the figure. Similar to the observations reported in previous studies involving slot injection [179, 182, 220, 221], the polymer concentration profiles feature a peak near the wall, whose magnitude decreases with increasing distance from the injection location. It should be noted that the observed small wall-normal deviation of the peak concentration (c_M) from the wall ($y = 0$) can be attributed to the near-wall variation in the index of refraction in the presence of polymers [221], and thus the peak concentration location can be assigned at $y = 0$ for modelling purposes. The uncertainty associated with the peak concentration (c_M/c_{inj}) is estimated to be within $\pm 2.5\%$. It should be noted that, while the maximum near-wall concentrations exceed the overlap concentration for the current polymer ($c^* = 330$ ppm, estimated using the Mark-Houwink relationship [222]), the concentration profiles quickly decrease below this limit within the viscous sublayer.

The effectiveness of the polymer solutions is directly dependent on the near wall polymer concentrations, and hence polymer diffusion [49, 179, 220, 223, 224]. In the present study, the diffusion of the polymer is quantified by considering the concentration profiles normalized by the local maximum concentration. The diffusion coefficient (D) is estimated from the solution of one-dimensional Fick's problem (Ballufi *et al.* [225]) given by Eq. 4.1.

$$\frac{c(y,t^*)}{c_M} = 1 - (1 - \frac{c_o}{c_M})\text{erf}\left(\frac{y}{2\sqrt{Dt^*}}\right). \tag{4.1}$$

Here, in the range $c_o/c_M \leq c/c_M \leq 1$, $t^* = (x - x_{\text{inj}})/U_\infty$ is the characteristic time, maximum concentration is assigned to $y = 0$, and c_o is the concentration in the outer region evaluated at $y = 2.5\,\text{mm}$. The estimates of the diffusion coefficients obtained from fitting the measured concentration profiles using Eq. 4.1 are shown in Fig. 4.4. The results show an exponential decrease in diffusion coefficient with downstream distance, following the decrease in peak concentration. The exponential decay of the diffusion coefficient and the maximum concentration are confirmed by data fits (shown by dashed curves in Fig. 4.4) given by Eqs. 4.2 and 4.3, respectively.

$$D = c_1\text{exp}(-(x - x_{\text{inj}})/L_D + \beta) + c_2, \tag{4.2}$$

$$c_M/c_{\text{inj}}[\%] = 100 \times \text{exp}(-\alpha\sqrt{(x - x_{\text{inj}})/L_C)}). \tag{4.3}$$

In these expressions, constants c_1, c_2, α, and β are the fit constants (82×10^{-7} m^2/s, 1.5×10^{-7} m^2/s, 0.7, and 0.3, respectively), L_D is the length from the injection slot where D decreases to 50% of its value close to the slot, and L_C is the equivalent parameter for the peak concentration. The exponential decay in both diffusion and peak concentration with the downstream distance

are in accordance with the results of Vdovin and Smol'yakov [223], and Fontaine *et al.* [179]. Notably, equations 4.2 and 4.3 show a weaker dependence on the distance $(x-x_{\text{inj}})$ for the relative wall concentration c_M/c_{inj} as compared to the diffusion coefficient D. The rapid decrease in the diffusion coefficient is attributed to the progressive attenuation of the mixing in the drag reduced boundary layer, which allows to sustain a relatively high wall concentration farther downstream from the slot. This, in turn, aids in sustaining polymer performance over a longer streamwise distance compared to that expected from the diffusion of a passive tracer in turbulent boundary layer.

4.3.3 Turbulent flow statistics

The effects of polymer injection on boundary layer development are first quantified by the boundary layer parameters presented in Fig. 4.5. The baseline data show the expected variation of boundary layer parameters, with shape factors typical of those expected for turbulent boundary layers. This is contrasted with the results pertaining to the highest polymer concentration in Figs. 4.5(a) and 4.5(c). It can be seen that the polymer injection results in a thinner boundary layer, with notably higher shape factor. The effect of injection concentration is considered in Figs. 4.5(b) and 4.5(d). Higher injection concentration results in thinner boundary layer profiles and higher shape factors. However, the significance of the polymer injection effect is reduced progressively with streamwise distance from the injection slot, reflecting the decreasing wall concentrations of the polymer (Fig. 4.4).

The effect of the polymer additives on the mean velocity profiles is examined in Fig. 4.6, where the data are presented in inner coordinates. For the normalization of the coordinates, the wall shear stress was estimated directly from the slope of the linear sublayer [60, 175, 226] using the methodology briefly outlined here. Within the linear sublayer, where the near-wall law $\langle u\rangle^+ = y^+$ is expected, the wall-normal gradient of the streamwise velocity $d\langle u\rangle/dy$ is verified to remain constant for both Newtonian and polymer injected boundary layer profiles. The near-wall velocity data conforming to the linear trend are used to estimate the wall-normal velocity gradient at the wall $d\langle u\rangle/dy|_w$, yielding wall shear stress estimates at a given streamwise location. In order to reduce the measurement and methodological error propagation, the wall shear is computed using a sliding average operation on the local estimates over a window of $3\,\text{mm}$ (≈ 75 pixels). The results are verified in inner coordinates based on the near-wall law ($\langle u\rangle^+ = y^+$) within the range $y^+ \leq 6$, with fluid properties taken as those of water at the measured freestream temperature.

To aid the interpretation of the data, the results in Fig. 4.6 are complemented by dashed lines corresponding to the near-wall law, the log-law for Newtonian boundary layers, and Virk's

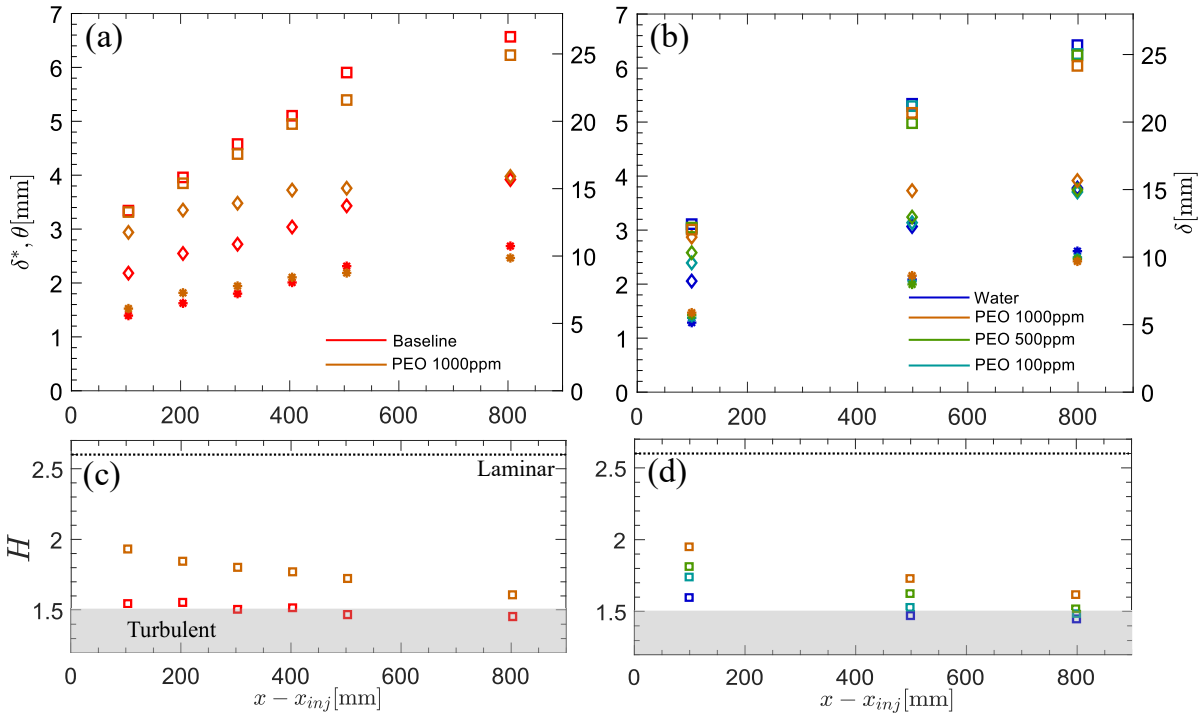

Figure 4.5: Variation of the boundary layer parameters with the distance from the injection slot. For sub-figures (a) and (b), □ represents the boundary layer thickness δ, ◊ represents the displacement thickness δ^*, and $*$ represents the momentum thickness θ for the cases shown in the respective sub-figures. Shape factor $H = \delta^*/\theta$ is shown in sub-figures (c) and (d) for the corresponding cases. Typical values of H for laminar and turbulent boundary layers are indicated.

ultimate profile (Eq. 2.5) for maximum drag reduction [48]. The profiles for the Newtonian flows (i.e. the baseline and water injection) follow the classical trends expected at comparable Reynolds numbers ($180 < Re_\tau < 340$) [227–229]. Fig. 4.6(a) shows the presence of a subtle wake region in the outer layer, which is attributed to a mild adverse pressure gradient on the model at that station. The pressure gradient becomes negligible farther downstream.

The effect of polymer injection in the near-wall region ($y^+ \leq 10$) is clearly absent in all data presented, as the profiles for all injected concentrations are in excellent agreement with the near-wall law $\langle u \rangle^+ = y^+$. This is in contrast to the results of Hou *et al.* [59], which is likely attributed to the use of a much higher injection velocity in their study. This is substantiated by the distorted shape of velocity profiles in the near-wall region corresponding to the water injection cases in their study (see their Fig. 2(a)), with a similar feature apparent in the results

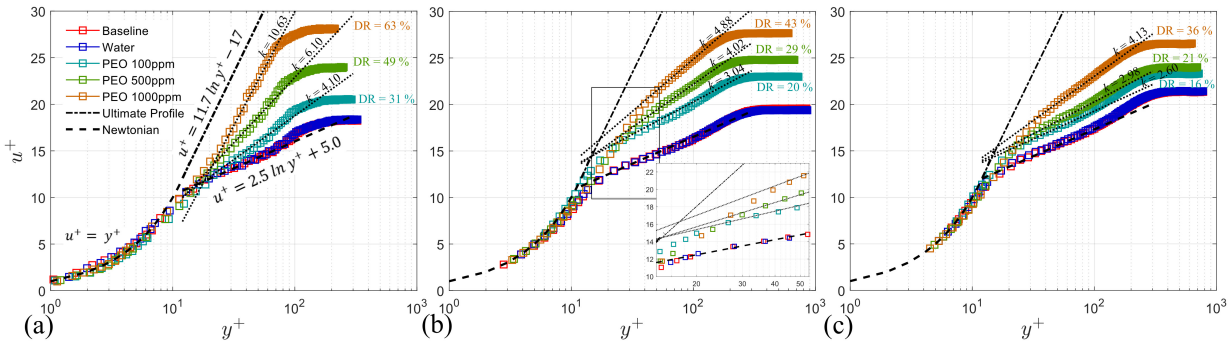

Figure 4.6: Mean streamwise velocity profiles in inner coordinates showing effect of injected polymer concentration at locations (a) $x - x_{\text{inj}} = 90\,\text{mm}$, (b) $x - x_{\text{inj}} = 490\,\text{mm}$ and (c) $x - x_{\text{inj}} = 810\,\text{mm}$. Dotted lines show the best logarithmic fit to the log-layer with the slope denoted by k.

of Somandepalli and Mungal [220] (see their Fig. 4-2(a)) who used an experimental set up and injection velocity similar to that of Hou *et al.* [59]. Thus, the usage of an apparently variable viscosity in the viscous sublayer region to correct the velocity profiles [59] is not found to be applicable based on the results of the present study. Instead, it is argued that such a variation in the apparent viscosity is merely an artefact of fitting the near-wall law $\langle u \rangle^+ = y^+$ in a boundary layer flow disturbed by relatively high momentum injection. Further it should be pointed out that higher injection velocities result in higher polymer deposition outside the buffer layer, thereby decreasing the drag reduction efficiency [202, 230, 231].

The results in Fig. 4.6 show that mean velocity profiles begin to deviate from the near-wall law at $y^+ \approx 10$ in all the cases, which marks the edge of the viscous sublayer. The effect of the injection concentration is clearly seen on the extent of the buffer layer ($y^+ > 10$, inset plot in Fig. 4.6(b)). The extent of the buffer layer increases with increasing injection concentration of the polymer, which is similar to the trend reported earlier for internal flows with polymer additives [152, 153]. The extent of the buffer layer is also seen to depend on the distance from the injection slot. Fig. 4.6(b) shows that the inflection point that separates the inertial and buffer layers is displaced farther away from the wall owing to the extension of the buffer layer with increasing polymer concentration. For the case of the highest injection concentration near the injection slot (Fig. 4.6(a)), the aforementioned inflection point is found to be absent in the region $y^+ \leq 80$, indicating that the inertial sublayer is relatively inconsequential at near MDR conditions. The buffer layer spans nearly the entire boundary layer thickness, following a logarithmic relation. A detailed explanation of this phenomenon that occurs at near MDR conditions is given by Lumley [153] in the context of internal flows, and is evident in the near MDR external flow case studied here. Such observations are also apparent in the viscosity corrected results of Hou *et*

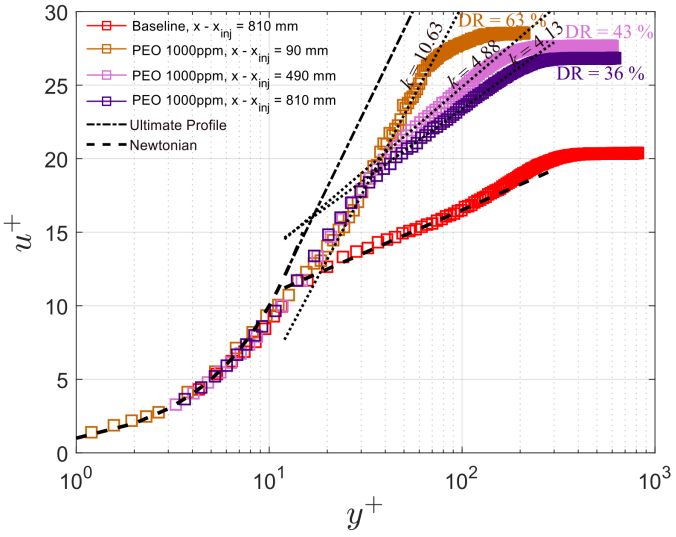

Figure 4.7: Mean streamwise velocity profiles in inner coordinates showing the effect of the distance from injection location. Dotted lines show the best logarithmic fit to the log-layer.

al. [59] for near MDR cases.

Due to the observed similarity in the relationship followed by the extended buffer layer in the initial region close to the slot and that by the typical inertial sublayer farther away from the slot, the slope of the logarithmic relations corresponding to these sublayers are termed as k. The slope k in the context of inertial sublayer is defined as the inverse of the von Kármán constant (κ). These slopes are observed to increase with the polymer concentration, as indicated by the k values in Fig. 4.6. Agreeing with previous results in the drag reduced external flow cases [17, 59, 175, 220, 232], this highlights a notable difference with the drag reduced internal flow cases [152, 153] where the inertial sublayers are observed to be parallel to the Newtonian profiles leading to a so-called 'Newtonian plug'.

The evolution of the mean velocity profiles with the streamwise distance from the injection slot is exemplified in Fig. 4.7. Characteristics of both buffer, and inertial sublayers are seen to change with the streamwise distance. The extent of the buffer layer is observed to decrease with the streamwise distance, as the inertial sublayer moves closer to the wall. The slopes of the logarithmic fits (k) are also seen to decrease with the distance from the injection slot (Fig. 4.7), which is attributed to the decrease in the near wall concentration of the polymer.

Noting the intrinsic dependence of the polymer performance on its distribution in the boundary layer, the streamwise variation of the spatially averaged relative concentrations inside the viscous sublayer ($y^+ \leq 11.6$) and the buffer layer ($11.6 < y^+ \leq 100$) are shown in Fig. 4.8.

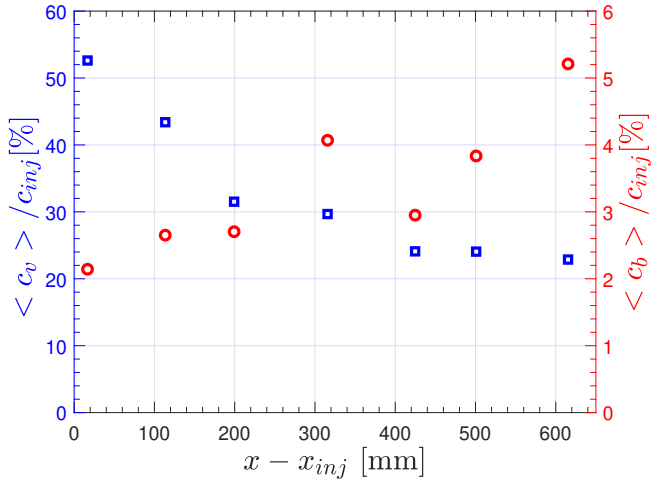

Figure 4.8: Variation of the average polymer concentration within the viscous sublayer $\overline{\langle c_v \rangle}$ ($y^+ \leq 11.6$) and buffer layer $\overline{\langle c_b \rangle}$ ($11.6 < y^+ \leq 100$) represented by $\square$ and $\circ$, respectively.

Consistent with the methodology employed for wall shear stress estimation, the spatially averaged concentrations are subjected to a sliding average operation over a window of 3 mm (≈ 85 pixels). The latter region is associated with significant extensional motions which are considered to activate the polymer macromolecules [52, 179, 230, 231, 233]. The results show that the average polymer concentration within the viscous sublayer ($\overline{\langle c_v \rangle}$) decreases sharply with streamwise distance, attributed to high near-wall diffusion near the injection slot (Fig. 4.4). As the near-wall diffusion decreases exponentially farther downstream, the rate of decrease of the polymer content within the sublayer is also reduced. On the other hand, the average polymer concentration through the buffer layer ($\overline{\langle c_b \rangle}$) is observed to progressively increase indicating an increase in polymer accumulation in the extensional region. This process is driven by the diffusion of the polymer from the viscous sublayer, and is expected to be eventually checked by the diffusion into the log layer as the flow develops farther downstream.

The drag reduction (DR) due to polymer injection is evaluated from the time-averaged velocity fields using the relation given by Eq. 4.4,

$$\text{DR}[\%] = \left(1 - \frac{\tau_{w,P}}{\tau_{w,N}}\right) \times 100, \tag{4.4}$$

where $\tau_{w,N}$ is the local wall shear stress evaluated for the baseline Newtonian case and $\tau_{w,P}$ is that for the respective polymer injection cases. The results are presented in Fig. 4.9(a) for all the

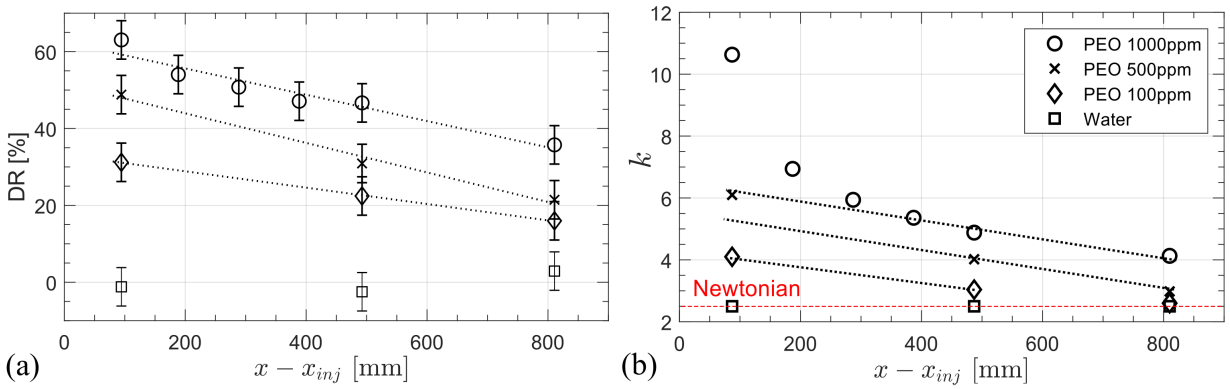

Figure 4.9: Streamwise evolution of (a) drag reduction DR% (b) k for different injection concentrations with distance from the injection slot. Dotted lines depict the trend lines for the respective parameters with $x - x_{\text{inj}}$. Dashed line in red represents the slope of the log-layer for typical Newtonian flows ($k = 2.5$).

cases studied. The uncertainty in estimating DR[%] is estimated to be within $\pm 5\%$. For water injection, the observed drag reduction is found to be within the uncertainty of the measurement at all the locations. With polymer injection, drag reduction is observed in all the cases, being more pronounced at higher injection concentrations. The DR is also observed to decrease from the injection location for all the cases, as indicated by the corresponding linear fits. The observed decrease in DR correlates with the decrease in average polymer concentration in the viscous sublayer (Fig. 4.8), accompanied by the polymer flux into buffer layer. The role of the increased number of activated polymer macromolecules in the extensional region ($11.6 \leq y^+ \leq 100$) is credited for sustaining a relatively high DR over substantial streamwise distances.

Given the notable changes in the velocity profiles within the inertial sublayer with both the injection concentration and downstream distance from the slot (Figs. 4.6 and 4.7), it is of interest to explore a possible correlation between the inertial sublayer characteristics and the drag reduction. To this end, Fig. 4.9(b) presents the streamwise variation of k for all the cases examined. The results illustrate a nearly linear decay in k for the values removed from the near MDR conditions achieved at high polymer concentrations near the slot (e.g., for $c_{\text{inj}} = 1000$ ppm) and prior to asymptotic return to Newtonian behaviour (e.g., for $c_{\text{inj}} = 100$ ppm at $x - x_{\text{inj}} > 500$ mm).

The results in Fig. 4.9 suggest a correlation between DR and log layer slope. It has been explored in some previous studies [175, 217] in terms of the relation between DR and the von Kármán constant (κ). The relation between DR and κ is examined in Fig. 4.10(a) where the results from the present study are complemented by the data from previous investigations in external flows involving different polymers [50,51,58,59,175,220] and even a surfactant solution

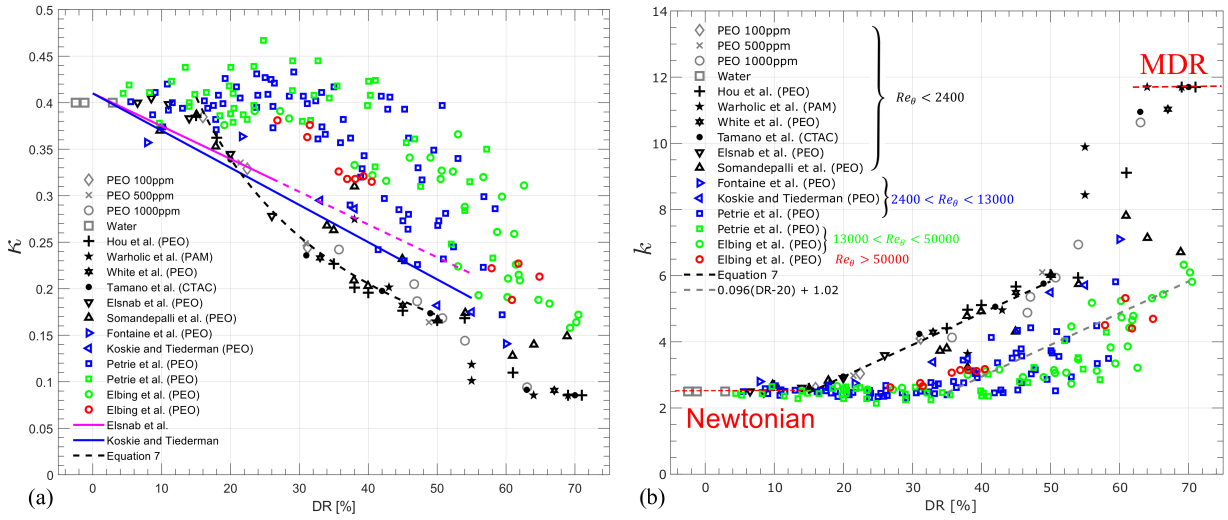

Figure 4.10: (a) Variation of the von Kármán constant with DR. The results from several previous studies [17, 50, 51, 58, 59, 162, 175, 179, 217, 220, 234] are presented for comparison. Solid lines show previously proposed correlations in their respective validity ranges. Pink dashed line indicates extrapolated estimates of κ using the correlation of Elsnab *et al.* [175]. (b) Variation of $k(1/\kappa)$ with DR. Dashed lines in red represent the slope of the log-layer for typical Newtonian flows ($k = 2.5$), and at MDR conditions ($k = 11.7$). Black and gray symbols correspond to $Re_\theta \leq 2400$, blue symbols correspond to $2400 < Re_\theta \leq 13000$, green symbols correspond to $13000 < Re_\theta \leq 50000$, and red symbols correspond to $Re_\theta > 50000$.

[17] at comparable Reynolds numbers ($Re_\theta < 2400$). Data at higher Reynolds numbers [162, 179, 217, 234] are also shown for comparison of the general trends. Despite a notable data scatter, particularly at higher Reynolds numbers, some important trends can be identified. At low DR values, the von Kármán constant remains essentially constant which has been termed as the *low drag reduction regime* in some previous studies [58, 183, 235]. As DR increases, κ eventually begins to decrease from the Newtonian value. The region was identified as the *high drag reduction regime* [58, 183, 235], which has been shown to extend from DR $\approx 35\%$ to the MDR condition in the classical definition [58]. However, a comparative analysis of the results in Fig. 4.10(a) suggests, that on average the critical DR associated with the onset of this regime tends to increase at higher Reynolds numbers and the saturation of κ to MDR values is not universal.

Koskie and Tiederman [217] and Elsnab *et al.* [175] proposed linear correlations between the von Kármán constant (κ) and DR (Fig.4.10(a)). Despite being forced to produce Newtonian κ at DR $= 0\%$, the proposed correlations provided a reasonable approximation of the results in

their respective studies ($R^2 = 0.84$ for Koskie and Tiederman [217], and $R^2 = 0.70$ for Elsnab *et al.* [175] for their respective data). However, when assessed in relation to the results from other investigations in Fig. 4.10(a), the fidelity of the proposed relations diminishes significantly. Considering that these correlations do not account for the region of constancy of κ, a linear correlation in an appropriate DR range can be better suited to represent the aforementioned trend at low Reynolds numbers. Nevertheless, such a linear correlation will still prove to be inconsistent at the boundaries of such a DR range due to the observed non-linearity in the variation of κ within $15\% < \text{DR}[\%] < 50\%$ at low Reynolds numbers.

As expected, the results in Fig. 4.10(b) capture the same general trends as those observed in Fig. 4.10(a). In particular, an asymptotic behavior towards the Newtonian k values is seen at lower DR values representative of *low drag reduction regime*, retaining the same physics as in the original definition by Warholic *et al.* [58]. Velocity profiles for the flows in this regime have been shown to retain Newtonian characteristics, with a velocity defect structure similar to the internal flow cases and the upward shift in the inertial sublayer indicative of the reduction in turbulence production [236]. A monotonic increase in k at higher DR values is seen to closely follow a linear trend for the results pertaining to $Re_\theta \leq 2400$ within $15\% < \text{DR}[\%] < 50\%$. The fit to all the low Reynolds number data sets (black and gray symbols) is shown by a black dashed line, given by the following correlation

$$k = 0.096 \times \text{DR}[\%] + 1.02. \tag{4.5}$$

Within the identified DR range, the proposed correlation has a significantly higher goodness of fit ($R^2 = 0.94$) than those evaluated for previous correlations [175, 217], which can also be seen from the corresponding fit shown in Fig. 4.10(a) for comparison. It is interesting to note that the data obtained with surfactant solutions [17] involving different drag reduction physics also closely follow the correlation, suggesting possible extensions to other drag reduction strategies at comparable Reynolds numbers.

It can be deduced from Fig. 4.10(b) that the intercept of the proposed correlation based on the low Reynolds data changes at higher Reynolds numbers, for which the onset of k increase takes place at higher DR values. Although the relatively high data scatter of the high Reynolds numbers hinders quantitative analysis of the Reynolds number effect, it can be seen that the results at higher Reynolds number closely follow the linear slope of Eq. 4.5, which is illustrated by a dashed gray line of the same slope. This indicates that the proposed linear relation between k and DR can be extended to higher Reynolds numbers once the variability in the bounds between low and high drag reduction regime is accounted for. Related to the latter, the results in Fig. 4.10 suggest the existence of two sub regimes for the classical high drag reduction regime at lower Reynolds numbers. In particular, as the mean velocity profiles progressively approach MDR

conditions (DR $\gtrsim 50\%$), further drag reduction is attained, but the correlation with inertial sublayer characteristics is no longer justified given the significance of viscous effects in the entire inner layer at such conditions. For the high Reynolds number cases ($Re_\theta > 2400$), a generally linearly increasing trend is observed within $35\% <$ DR$[\%] < 70\%$, with k reaching $k \approx 6$ at DR levels typically associated with MDR. The maximum k value matches that reached by the low Reynolds data at the maximum end of the linear trend (DR $\approx 50\%$), which is followed by a steep increase in k to MDR values. This takes place due to the continual growth of the buffer layer eventually leading to the differences of the log layer at sufficiently high DR values (Fig. 4.7). As the relative extent of the log layer increases with increasing Reynolds number, such a condition is expected to occur at higher DR values and is not reached at sufficiently high Re. Thus, the high drag reduction regime at lower Reynolds numbers can be subdivided into the inertial sub regime ($15\% <$ DR $< 50\%$), where the slope of the shrinking log layer follows a linear relation with DR, and viscous sub regime (DR $> 50\%$), where the log layer is no longer observed and k represents the slope of the significantly expanded buffer layer.

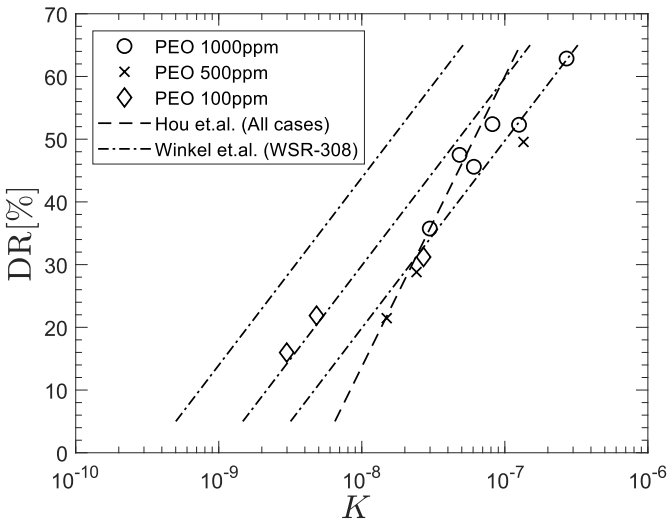

Figure 4.11: Semi-logarithmic plot showing variation of DR [%] with parameter K. Trends corresponding to the steady-state regime from the results of Hou *et al.* [59] and Winkel *et al.* [182] are also plotted for reference.

Fig. 4.11 illustrates the relation between DR and polymer flux parameter *K*, defined earlier, which provides a coarse approximation of the effective local concentrations based on the injection concentration, flow rate and the distance from the slot [223, 224]. The results suggest a power law relation between DR and K and feature a reasonable collapse of the data in the steady-state regime pertaining to different injection concentrations and other studies [59,182] employing

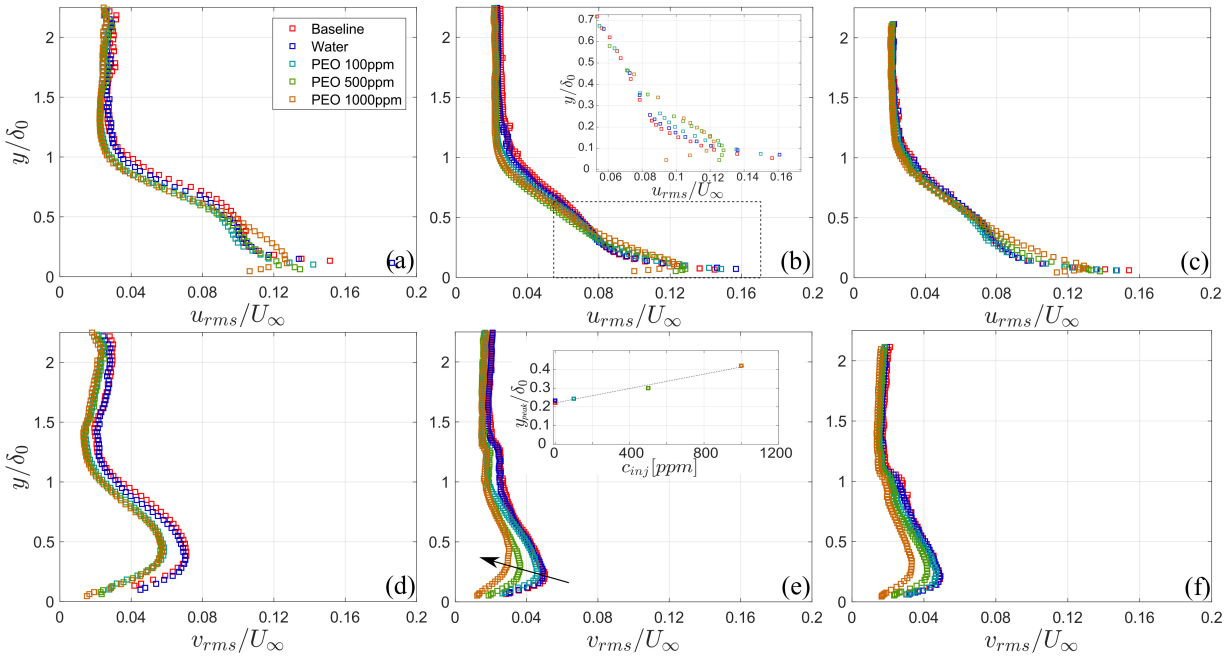

Figure 4.12: Profiles of velocity fluctuations (top row: u_{rms}/U_∞, bottom row: v_{rms}/U_∞) with injected polymer concentration at distances (a, d) $x - x_{\text{inj}} = 90\,\text{mm}$, (b, e) $x - x_{\text{inj}} = 490\,\text{mm}$, and (c, f) $x - x_{\text{inj}} = 810\,\text{mm}$. Inset plot in (b) shows a zoomed-in view of the highlighted region. Inset plot in (e) shows the variation of the wall-normal location y_{peak}/δ_0 of the peak v_{rms} with injection concentration c_{inj} and the dotted line shows the trend.

polymers with similar backbone chain structure. Near the injection slot, where K is large, the DR saturates with increasing K, which is indicative of near MDR conditions at high injection concentrations. This suggests that a further increase in the value of K, either by increasing the flow rate or the injection concentration, closer to the injection slot will not yield additional gains in performance at these locations. Thus, parameter K serves as an approximate performance prediction and optimization tool for injection parameters and a given spanwise extent of the surface downstream of a single injection site.

To gain further insight into the effect of polymer additives on the boundary layer development, it is of interest to consider the velocity fluctuation profiles, which are presented in Fig. 4.12 in outer coordinates. The effect of the polymer is immediately apparent in the wall-normal velocity fluctuations, whose magnitudes are reduced notably by polymer injection, particularly at higher injection concentration. Previous studies in inhomogeneous polymer injected flows [49, 58, 59], as well as homogeneous polymer flows [60, 159], have reported similar find-

ings. The most substantial reduction in vertical fluctuations is observed near the peak value, and the peak location is also shifted away from the wall Fig. 4.12(e). An inset plot in Fig. 4.12(e) shows that the peak location is shifted approximately linearly from $y/\delta_0 \approx 0.2$ to $y/\delta_0 \approx 0.4$ with increasing polymer concentration. The observed upward shift in the peaks is attributed to the suppression of turbulent intensity of small-scale eddies close to the wall by the presence of polymer macromolecules [59, 153].

The dampening effect of polymer injection is also observed in the streamwise velocity fluctuations, but to a lesser extent compared to that on the wall-normal fluctuations. The spatial resolution obtained from sequential-correlation is not sufficient to capture the near wall peak in the streamwise fluctuations (expected at $y/\delta \approx 0.008$, Klebanoff [237]) for the Newtonian flows. However, for the polymer injected cases, the peak fluctuations are observed to be attenuated and shifted away from the wall with increasing polymer concentration, such that they are resolved for the higher concentrations. The magnitudes of u_{rms}/U_∞ below the peak are observed to be attenuated owing to the increased viscous effects close to the wall. However, an increase in the magnitudes of u_{rms}/U_∞ is produced with polymer injection in the region above the peak in each case, while no significant effect is observed in the region $y/\delta_0 > 0.5$. The observed trends agree well with the previous experimental results [49, 59, 60], and corroborate the theoretical description given by Lumley [153] with regards to the observed increase in the magnitudes of u_{rms}/U_∞.

The quadrant plots of velocity fluctuations representative of the earlier identified sub-regimes of *high*, and the onset of *low* drag reduction regimes are examined in Figs. 4.13(a), 4.13(b), and 4.13(c), respectively, at $y^+ \approx 30$. The choice of the wall-normal coordinate for this examination is based on the typical dimensionless wall-normal distance of the turbulent bursts that occur in the buffer region [238, 239]. Note, that the results presented in Fig. 4.13(c) are close to the boundary between low and high drag reduction regimes, and serve to illustrate the gradual relaxation towards near Newtonian flow characteristics expected for lower DR values. The results enable identification of the influence of drag reduction on the turbulent motions of outward interaction, ejection, inward interaction, and sweep, associated with quadrants Q1, Q2, Q3, and Q4, respectively [131, 240]. Elliptical point clouds for the baseline cases (black dots, gray contour) in Fig. 4.13 show a tilted orientation, with the major axis passing through Q2, and Q4, indicating larger magnitudes and more frequent occurrences of the ejection and sweep events. These are known to produce the most significant contribution to the turbulent kinetic energy [131, 240]. The gray ellipses in all the three cases are similar in their orientation and eccentricities, as expected for a pure Newtonian flow. In the high drag reduction regime (Fig. 4.13(a)), the relative magnitudes of the wall-normal fluctuations are observed to decrease significantly in quadrants Q2 and Q4, indicating a significant attenuation of the major turbulent energy contributors. Being accompanied by a slight increase in the streamwise fluctuations at the wall-normal distance con-

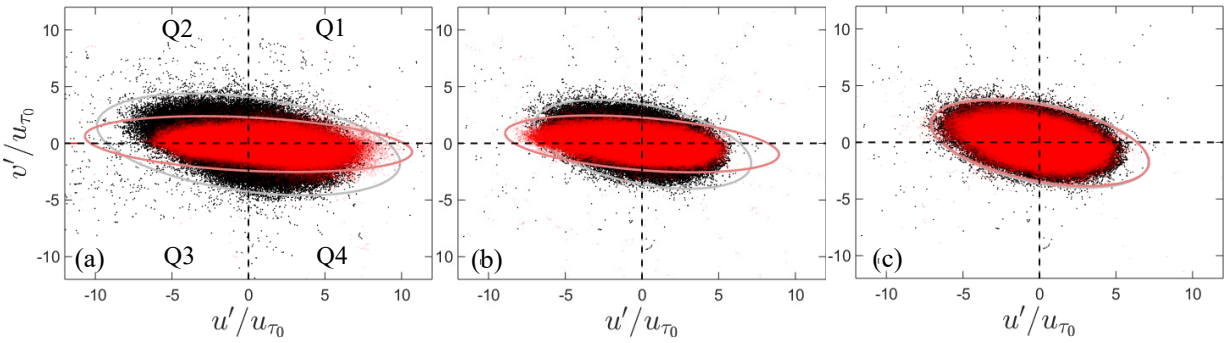

Figure 4.13: Scatter plots showing the effect of polymer drag reduction on the quadrants of velocity fluctuations normalized by the friction velocity for baseline case u_{τ_0} evaluated at $y^+ \approx 30$ for (a) DR = 63%, $x - x_{\text{inj}} = 90\,\text{mm}$, $c_{\text{inj}} = 1000$ ppm ($y/\delta_0 \approx 0.24$), (b) DR = 36%, $x - x_{\text{inj}} = 810\,\text{mm}$, $c_{\text{inj}} = 1000$ ppm ($y/\delta_0 \approx 0.12$), and (c) DR = 16%, $x - x_{\text{inj}} = 810\,\text{mm}$, $c_{\text{inj}} = 100$ ppm ($y/\delta_0 \approx 0.12$). Points corresponding to the baseline cases at each location are shown in black and those corresponding to the respective drag reduced cases are shown in red. Ellipses in gray and red show the iso-contours for 95% confidence intervals of the fluctuations in respective cases. Following White *et al.* [50], velocity fluctuations are normalized with respect to the friction velocity for the baseline case u_{τ_0}.

sidered here, this leads to the reorientation of the ellipse and an increase in its aspect ratio. The observed changes provide further support to the findings of White *et al.* [50] that the polymer molecules play a role in reducing the energy dispersion from the streamwise direction to other directions, directly affecting the self-sustaining mechanism of wall turbulence [130, 241]. With decrease in DR through the linear sub-regime of the *high* (Fig. 4.13(b)) and *low* (Fig. 4.13(c)) drag reduction regimes, the magnitudes of the fluctuations are seen to approach the baseline values, and the orientation of the drag reduced point cloud gradually aligns with that for Newtonian flow.

The polymer effect on the total shear stress profiles is of great importance, as it directly relates to the efficiency of the polymer drag reduction [58]. However, total shear stress in a polymer drag reduced flow (Eq. 2.4) cannot be estimated directly in external flows since the polymer stress τ_P cannot be measured. The procedure employed to estimate the total stress is illustrated in Fig. 4.14, where measured data points correspond to the sum of the viscous shear stress ($\mu d\langle u\rangle/dy$) and the Reynolds shear stress ($-\rho\langle u'v'\rangle$). The total stress distribution for the baseline case agrees well with the typical profiles obtained in a Newtonian boundary layer provided by Thomas and Hasini [68]:

$$\tau_{total}/\tau_{w0} = 1 + 2(y/\delta)^3 - 3(y/\delta)^2. \tag{4.6}$$

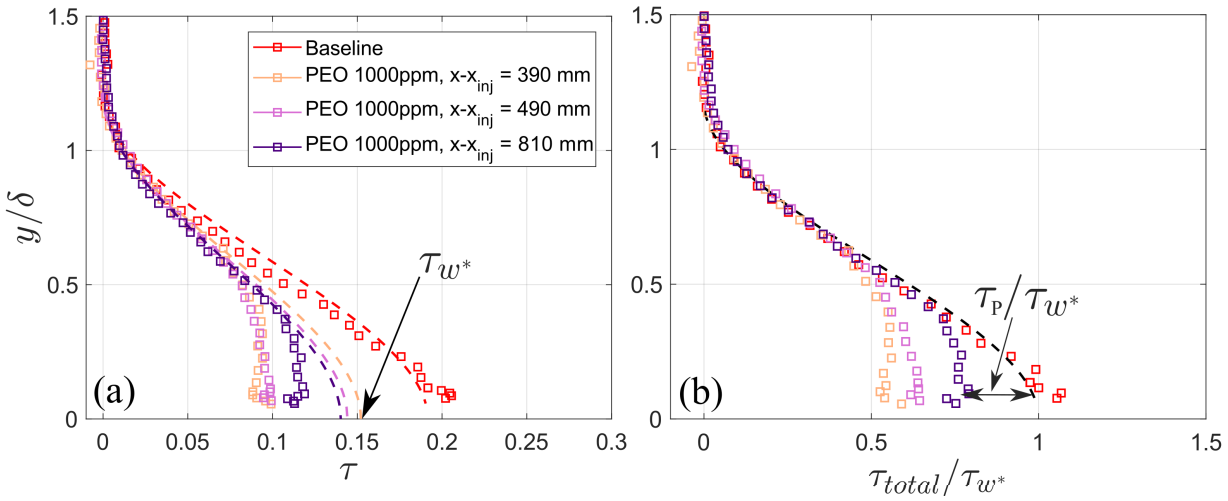

Figure 4.14: Estimation of total and polymer stresses (a) measured data correspond to the sum of viscous and Reynolds shear stresses (b) estimated total stress normalized by τ_w^*. Dashed lines estimate the variation of total shear stress based on fits on the data using Eqs. 4.6 and 4.7 for the Newtonian and drag reduced flow, respectively.

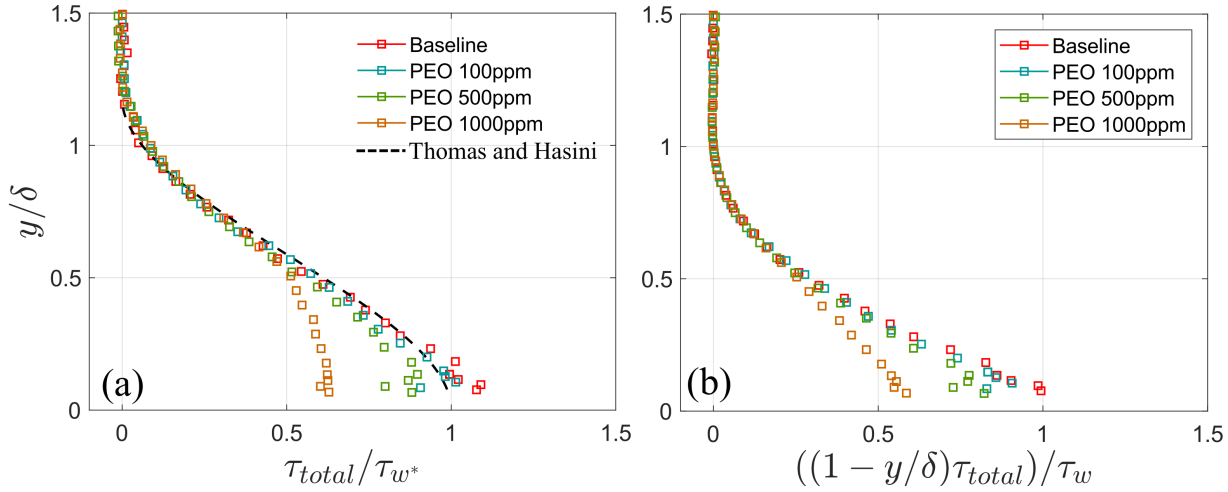

Figure 4.15: (a) Profiles of total shear stress normalized by an estimate of wall shear stress τ_w^* at location $x - x_{\text{inj}} = 490\,\text{mm}$. (b) Profiles of $(1 - y/\delta)\tau_{total})$ normalized by local shear stress τ_w at $x - x_{\text{inj}} = 490\,\text{mm}$. Dashed line in (a) represents the approximation provided by Thomas and Hasini [68].

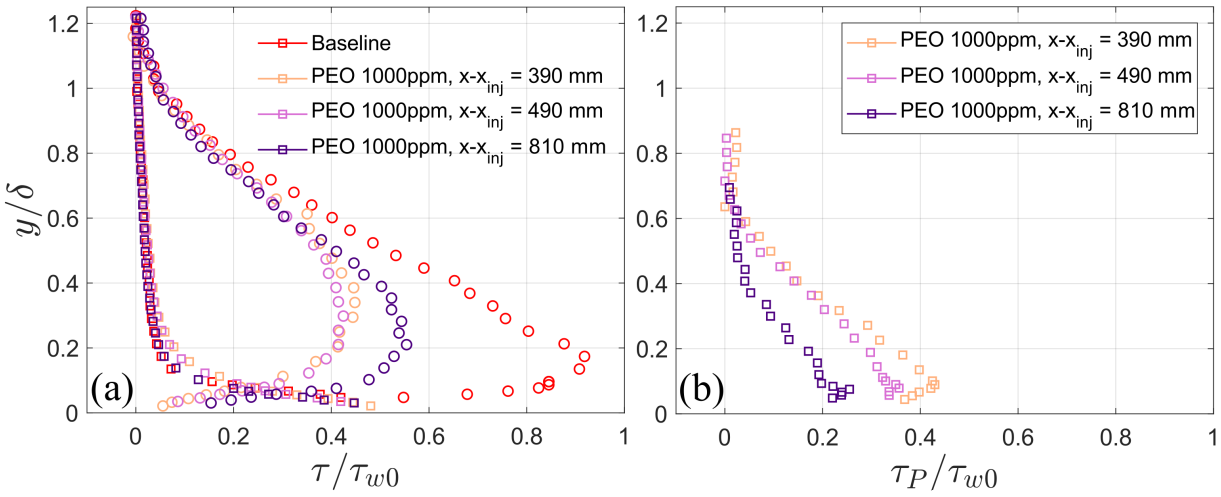

Figure 4.16: Variation of the components of total stress with the streamwise distance from injection slot normalized with the local wall shear stress in the baseline cases (a) Profiles of normalized viscous stress (□) and Reynolds shear stress (○) (b) Profiles of the normalized stress deficit (τ_P).

For the polymer cases, a reduction in the composite viscous and Reynolds shear stresses is immediately apparent, similar to previous observation in drag reduced flows [54, 58, 59]. However, the difference becomes progressively smaller with increasing wall-normal distance, and becomes negligible for $0.7 < y/\delta \leq 1$ where self-similarity is achieved in the polymer data. Thus, similar to internal flow cases [233], it can be assumed that the functional dependence governing the variation of the total stress is similar between drag reduced and Newtonian flows in this region. Consequently, a modified form of Eq. 4.6 can serve to approximate the total stress profile for the polymer case as

$$\tau_{total} = \tau_w^*(1 + 2(y/\delta)^3 - 3(y/\delta)^2). \tag{4.7}$$

where τ_w^* normalization parameter is estimated based on the best fit to data within $0.7 < y/\delta \leq 1$. Note that Yang and Dou [242] employ a similar methodology with a different polynomial approximation that also satisfies physical boundary conditions (see their Eq. 20); however, Eq. 4.6 is found to provide a better approximation to Newtonian data in the present study. Fig. 4.14(b) illustrates the obtained variation of the total stress, which can then be used to estimate polymer stress variation.

The results in Fig. 4.14(b) demonstrate that the stress deficit decreases with increasing distance from the injector. The same trend is observed with decreasing injection concentration in

Fig. 4.15(a), with both trends reflecting the associated decrease in the average polymer concentration. Importantly, a substantial stress deficit is found to be present in the region $y/\delta \lesssim 0.6$, which covers a broader region of the boundary layer than $y/\delta < 0.3$ reported in Refs. [59, 69] A similar observation can be made using $((1-y/\delta)\tau_{total}/\tau_w)$ profiles considered by Hou *et al.* [69] and shown in Fig. 4.15(b). It can be deduced from Fig. 4.14(b) that the affected boundary layer region becomes broader closer to the injection location.

The effect of polymer injection on the components of the total stress is considered in Fig. 4.16 for $c_{\text{inj}} = 1000$ ppm. Fig. 4.16(a) contrasts the Reynolds shear stress ($-\rho\langle u'v'\rangle$) and the viscous stress ($\mu d\langle u\rangle/dy$) in baseline and polymer drag reduced cases. As expected, outside of viscous sublayer, Reynolds stress dominates in the base flow. The Reynolds shear stresses in the corresponding polymer injected cases are dampened notably as compared to the baseline case shown here, whereas changes in the corresponding viscous stresses are less pronounced. Consequently, the significant dampening of the Reynolds shear stress produces a substantial contribution to the stress deficit away from the wall. The corresponding polymer stress profiles are presented in Fig. 4.16(b). The polymer stress peaks at $y/\delta \approx 0.08$, and the magnitude of the polymer stress decays with increasing distance from the injection location.

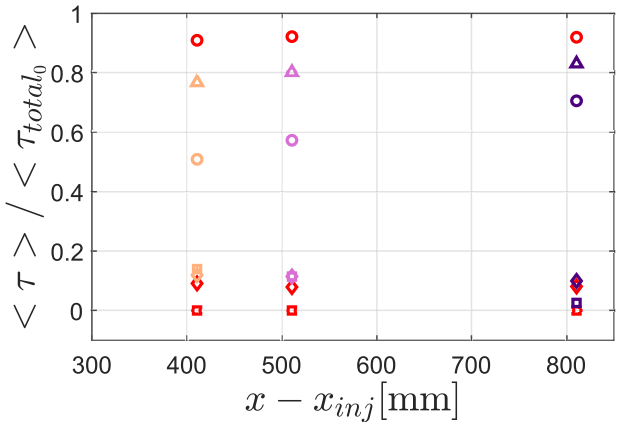

Figure 4.17: Variation of various stress components for $c_{\text{inj}} = 1000$ ppm spatially averaged in wall normal direction over local boundary layer thickness. Results are normalized by the average total shear stress in the corresponding baseline cases. △, ○, ◊, and □ represent the averaged total stress, Reynolds shear stress, viscous shear stress, and polymer stress, respectively. Color coding follows that in Fig. 4.14.

The streamwise variation of the stresses spatially averaged over local boundary layer thickness is presented in Fig. 4.17. The averaged total shear stress in a Newtonian boundary layer flow

is dominated by the Reynolds shear stress ($\sim 90\%$). In the polymer injected flow, the average total shear stress is decreased compared to the corresponding baseline flow, but the contribution of the Reynolds shear stress remains dominant accounting for 60% to 80%. The contribution of the viscous shear stress in the polymer injected case is also found to be relatively constant with the downstream distance and is only slightly increased in magnitude as compared with the baseline cases. The key role played by polymer additives in the Reynolds stress reduction is reflected in the polymer stress values that are seen to exceed the average viscous stress and account for the observed changes in the average Reynolds stress. The streamwise decrease in the polymer stress is attributed to the progressive decrease in the polymer content in the near wall region (Fig. 4.8). These observations are found to be in agreement with the results of Willmarth *et al.* [233] for an internal channel flow, where the polymer stress was shown to be responsible for reduction in the Reynolds shear stress.

4.4 Concluding remarks

An experimental investigation was conducted to characterize the evolution of the turbulent boundary layer in water under a polymer drag-reduced state. Solutions of polyethylene oxide (PEO) were injected into a turbulent boundary layer through a two-dimensional inclined slot at an injection rate equivalent to 8.6% of the flow rate in the viscous sublayer. The effect of the polymer injection was evaluated for three injection concentrations of 100, 500, and 1000 ppm over a region downstream of the injection location. Flow development was characterized by means of two-component PIV and PLIF measurements. The results allowed for a detailed, quantitative analysis of drag reduction in conjunction with the variation in polymer concentration and boundary layer parameters.

The PLIF images revealed the attenuation of turbulent mixing in a polymer injected boundary layer flow, leading to the reduction in local boundary layer thicknesses and increased shape factors in polymer injected cases. The mean velocity profiles in inner coordinates show that the polymer injection effects are most pronounced in the buffer and inertial sublayers, increasing the slope of the latter with increasing injection concentrations. The degree of the observed changes is found to depend on the near-wall polymer concentration.

Close to the injection location, near MDR conditions are observed at the highest concentration investigated, with local drag reduction (DR) of about 60%. The DR was found to decrease approximately linearly with the streamwise distance from the injection slot which is attributed to a steady decrease in the active polymer content within the near wall region. A progressive increase in the polymer density in the region of most energetic motions of the turbulent boundary layer indicates a natural robustness associated with this control strategy allowing for a sustained

performance over relatively long streamwise distances. An empirical linear relation between DR and the slope of the inertial layer (k) was established in the range $15\% <$ DR $< 50\%$ and was shown to apply over a range of data from various studies at comparable Reynolds numbers. While the boundaries and the intercept of the proposed linear correlation vary at higher Reynolds numbers, the established slope is shown to be relevant over a wide range of Reynolds numbers. The following distinctions in the drag reduction regimes are proposed based on the trends in drag reduction and associated flow characteristics: *Low Drag Reduction* regime occurs at lower DR values (DR $< 15 - 35\%$), where the inertial sublayer is displaced parallel to the original Newtonian profile due to increasing buffer layer thickness, *High Drag Reduction* regime takes place at higher DR values, where the effect of polymer action propagates into the inertial layer, progressively increasing its slope with increasing DR. Within this regime, two sub-regimes can be identified at lower Reynolds numbers ($Re_\theta \leq 2400$): i) inertial sub-regime ($\sim 15\%$ <DR<$\sim 50\%$), where the linear relationship between DR and k is applicable but the extent of the log layer progressively diminishes with increasing DR, and ii) viscous sub-regime (DR $> 50\%$), where the extent of the buffer layer essentially overtakes the log layer and the flow behaves similar to that at near MDR conditions. The demarcation between the two regimes is associated with a critical k value of $k \approx 6$. The extent of the viscous sub-regime is argued to be reduced at higher Reynolds numbers due to the increase in the relative extent of the log layer, with the critical k values reached at near MDR conditions. However, a significant scatter in the existing high Reynolds number data hinder quantitative analysis, and further investigations are required for a more detailed characterization of the Reynolds effect.

The polymer injection was shown to induce a significant decrease in wall-normal fluctuations in the boundary layer and to attenuate maximum streamwise fluctuations in the near-wall region. The quadrant analysis revealed that polymer additives attenuated the magnitudes of ejection and sweep motions consequently dampening Reynolds shear stress. Further, the results show that the energy dispersion from the streamwise direction to the wall-normal directions was impeded due to the presence of polymer macromolecules.

The total shear stress in the outer region $0.7 < y/\delta < 1$ was observed to be self-similar for both Newtonian and polymer-injected boundary layer, allowing the use of polynomial fit approximations typical to Newtonian flows to be used for the estimation of total and polymer stresses. The results reveal that polymer injection affects stress distributions over a significant portion of the boundary layer ($y/\delta \lesssim 0.6$). The Reynolds shear stress is shown to be the main contributor to the total stress in the polymer-injected flow, and its decrease is accounted by the polymer stress. The magnitude of the polymer stress increases with increasing local near-wall polymer concentration.

Chapter 5

Effect of polymer injection on coherent structures and Reynolds shear stress

Experimental investigation is conducted using planar and tomographic particle image velocimetry (PIV) measurements spanning the inner layer of Newtonian and drag-reduced zero-pressure gradient turbulent boundary layers. Low to moderate drag reduction is achieved by injecting two different concentrations of drag-reducing polymer solutions through an inclined slot. Instantaneously, both Newtonian and drag reduced flows show regions of high and near-zero Reynolds shear stress (RSS) which are termed as the high-RSS, and low-RSS regions, respectively. The high-RSS regions indicate the passing of near-wall coherent structures and are predominantly present within the cores of the low- and high-speed streaks, whereas the low-RSS regions mainly occupy the regions surrounding the streaks. The magnitude of RSS and size of the high-RSS regions decrease significantly with polymer injection. Canonical coherent structures within the near-wall region, including ejections and sweeps, hairpin-like vortices, meandering low-speed streaks, and precursors of streak breakdown are considered for the evaluation of polymer effect on high- and low-RSS regions. Besides the attenuation of the high-RSS regions, the quasi-streamwise vortices are found to weaken, and low-RSS regions are seen to enlarge around these vortices. In addition, the high-RSS regions within the coherent structures coincide with strong extensional structures which are also found to dampen with polymer injection, indicating potential interactions of the polymer with extensional motions.

Parts of this chapter have been adapted from Y. Shah, S. Ghaemi, and S. Yarusevych, "Three-dimensional characterization of reynolds shear stress in near-wall coherent structures of polymer drag reduced turbulent boundary layers," *Experiments in Fluids*, vol. 62, no. 8, pp. 1–21, 2021.

5.1 Introduction

The discussion in Sec. 2.2.3 highlight two of the most distinguished, but rivaling, theories of polymer based drag reduction which primarily revolve around the factors of increased extensional viscosity [65] and the transfer of turbulent energy into the elastic energy of the polymer [53]. Notably, the underlying mechanisms for both theories involve interactions of long and flexible polymer molecules with near-wall coherent structures, which has been studied in several recent investigations [54–57, 244]. In this effort the contemporary studies have focused on the modification of the near-wall coherent structures by the polymer chains. Besides the reduction in turbulent bursting events [52, 176], polymers have been shown to significantly modify the near-wall streaks [50]. A recent investigation by Pereira *et al.* [56] has shown that polymer stretching due to mean shear in the near-wall region is considerable. However, the mean-shear does not fully explain the observed levels of polymer stretching outside the viscous sublayer where the mean shear decreases significantly. Pereira *et al.* [56] attribute the additional polymer stretching to extensional turbulent motions ($u_i' u_i'$) in the buffer layer. Due to the transfer of the streamwise kinetic energy to the polymer, there is a decreased level of streamwise fluctuations within the viscous and buffer layers [49, 59–61], leading to an increased coherence of the streak structure [174, 244] and increased streak-spacing [50]. In addition, a notable weakening of both rotational (elliptical) and extensional (hyperbolic) motions was observed and attributed to polymer stretching [56].

The discussed mechanisms of polymer interaction with turbulent boundary layers based on the extensional motions are closely aligned with Lumley's hypothesis of extensional viscosity [65]. In contrast, Min *et al.* [54] performed numerical simulations based on the elastic model of de Gennes [53] and proposed a different mechanism involving the near-wall quasi-streamwise vortical motions. It is suggested that the polymer chains stretched by the mean shear in the near-wall regions are lifted up by the quasi-streamwise vortical structures into the lower log-layer where they release the stored elastic energy. This release of energy is shown to primarily occur in the streamwise direction resulting in the observed increase in the streamwise fluctuations in the lower-log region [49, 59–61]. Other numerical studies employing the FENE-P (finitely extensible nonlinear elastic - Peterlin) model have shown a significant dampening of near-wall vorticity in the buffer layer [55, 245]. It is proposed that the counter-torques responsible for this vortex damping are generated as a result of the polymer stretching in the quasi-streamwise vortices [57, 183, 193]. Furthermore, the dampening of the near-wall vorticity results in a significant reduction in the Reynolds shear stress leading to an expanded buffer layer. Li and Graham [194] noted that even with a strong enough viscoelasticity, a non-negligible instantaneous Reynolds shear stress is still observed [54, 195, 196], limiting the drag reduction by the so-called Maximum Drag Reduction (MDR) asymptote [48]. The asymptotic drag reduction limit has been shown to

hold regardless of the polymer, or even the type of the drag reducer [17, 197].

Xi and Graham [195, 246] considered the intermittent dynamics of drag reduction in viscoelastic flows through numerical simulations in minimal flow units (MFU). They highlighted that all flows, Newtonian and drag reduced alike, show intermittent periods of low and high drag events. A high drag event, termed an *active event*, is coupled with increased streamwise vorticity and RSS, whereas a low drag event, or a *hibernating event*, is associated with a damped RSS and a velocity profile similar to the asymptotic profile at MDR. Succeeding numerical works in both MFU and large domains have provided further evidence of these hibernating events and characterized their spatial and temporal aspects [247–249]. The time-scales of the hibernating events increase with increasing Weissenberg number (Wi $= t_{\text{rel}}\dot{\gamma}$, where t_{rel} is the polymer relaxation time and $\dot{\gamma}$ is the characteristic shear rate of the flow), and, at MDR, the flow primarily exhibits hibernating state with infrequent excursions to the active states. The results suggest that similar to the non-Newtonian flows, distinct hibernating and active states are also present in a Newtonian channel flow at Re_τ of 70 to 100, with regions of the latter prevailing over the former in both time and space. In a non-Newtonian flow (Wi > 1), the frequency of occurrence and size of the hibernating events increase leading to an overall decrease in the RSS as well as the time-averaged drag. Consistent with the results found in the channel flows [195, 247], the DNS simulations of Tamano *et al.* [250] also show the existence of the active and hibernating states in a zero-pressure gradient turbulent boundary layer.

Despite the growing evidence that polymer drag reduction might be a stochastic process, almost all of the relevant studies were performed computationally. These studies distinguish the active and hibernating states based on the instantaneous skin friction or the polymer stretching, which are not typically available in experimental flow measurements to a desired accuracy and are yet to be clearly linked to changes in the near-wall flow topology. Thus, the present study explores the effect of polymer additives on typical coherent structures in near-wall turbulent flows. The structures are related to extreme RSS events, which are known to be a robust indicator of the production of turbulent kinetic energy and can be reliably estimated in both experiments and numerical simulations.

The main objective of the present study is to characterize the predominant coherent structures in the near-wall layer of Newtonian and drag-reduced turbulent boundary layers. This is achieved by performing planar and volumetric PIV extending from the wall to the lower-log layer. Spatial manifestations of the high- and low-RSS regions are considered for the ejections (Q2) and sweep (Q4) events, hairpin-like vortices, meandering low-speed streaks, and precursors of streak-breakdown events. Finally, the effect of the polymer on extreme extensional motions within the ejection and sweep structures is analyzed in order to explore their significance to the overall mechanism of drag reduction.

5.2 Experimental setup

Planar and tomographic PIV measurements were conducted using the experimental setup described in Sec. 3.2.1 at the streamwise location presented in Table 5.1. A constant freestream velocity of $U_\infty = 0.3 \pm 0.003\,\mathrm{m\,s^{-1}}$ was used for the present investigation. The boundary layer was tripped with a zigzag trip attached to the flat surface parallel to the leading edge at $x/L \approx 0.14$ where the laminar boundary layer thickness is estimated to be $\delta_{tr} = 5.3$ mm and the Reynolds number based on the height of the trip is estimated to be approximately 650, which falls within the range suggested by Braslow and Knox [112]. The local three-dimensional trip effects are expected to be negligible beyond $15\delta_{tr}$, or $x/L \approx 0.18$ based on the findings of Elsinga and Westerweel [115]. Thus, the position of the injection slot and the measurement domain were selected to be sufficiently far downstream of the trip ($29\delta_{tr}$ and $57\delta_{tr}$, respectively).

The polymer used in this work was polyethylene oxide (PEO, Sigma Aldrich, Inc.) with an average molecular weight of 8×10^6 g/mol. Two different solution concentrations have been considered in this work (500 and 1500 ppm), each of which was prepared using the same protocol verified to produce consistent results for different batches as established in Ch. 4. In order to achieve uniform seeding density in the particle images, seeding particles were stirred along with the polymer solutions with approximately the same concentration as the seeded flow in the tunnel. The injection was performed according to the procedure outlined in Sec. 3.1.3 and the employed mean injection velocity of $u_{\text{inj}} =$ was shown to produce negligible effects of benign injection on the turbulent boundary layer beyond $x - x_{\text{inj}} = 87$ mm, or $(x - x_{\text{inj}})/L \approx 0.04$ in Ch. 4.

In addition to the streamwise location shown in Table 5.1, the present study considered measurements at four other streamwise stations covering $x - x_{\text{inj}} = -8$ mm to 840 mm. Measurements at all the locations included baseline measurement without injection, water injection, and four different polymer concentrations $c_{\text{inj}} = 500$ ppm, 750 ppm, 1000 ppm, and 1500 ppm. The drag reduction (DR) obtained in all the investigated cases pertain to the *Low Drag Reduction* regime (DR $\leq 30\%$). Results are reported for the measurements at one streamwise station corresponding to $x - x_{\text{inj}} = 150$ mm to 190 mm, and two limiting polymer concentrations ($c_{\text{inj}} = 500$ ppm and 1500 ppm). The results corresponding to other streamwise stations and the intermediate polymer concentration cases ($c_{\text{inj}} = 750$ ppm and 1000 ppm) were found to follow the same trends as those illustrated by the drag-reduced cases considered in this study, and thus, were omitted for brevity. Acquisition and processing of particle images was performed using the procedure outlined in Secs. 3.2.1 and 3.2.2, respectively, and the parameters provided in Table 3.1.

Experimental Parameters		
$c_{\text{inj}} = 0^{\dagger}$, 500, 1500 ppm, $U_{\infty} = 0.3\,\text{m}\,\text{s}^{-1}$		
Parameters	Planar PIV	Tomographic PIV
x/L	[0.274, 0.292]	[0.274, 0.296]
$x - x_{VO}$ (mm)	[761, 801]	[761, 810]
$x - x_{\text{inj}}$ (mm)	[150, 190]	[150, 199]
$Re_{x-x_{VO}} \times 10^{-5}$	2.157	
Re_{θ_0}	519	
δ_0 (mm)	17.7	
λ_0 µm	74	

Table 5.1: Test matrix. Coordinate ranges identify the streamwise extent of each field of view and boundary layer parameters are given for the baseline case measured at the centre of the FOV. † indicates water injection. $\lambda_0 = \nu/u_{\tau_0}$, where u_{τ_0} is the friction velocity in baseline case. x_{VO} denotes the virtual origin estimated based on the best fit to the streamwise variation of the displacement thickness in the baseline case.

5.2.1 Conditional sampling technique

The analysis presented in this chapter examines the effect of polymer injection on various canonical coherent structures in the near-wall region, such as ejection (Q2) and sweep (Q4) events, hairpin-like structures, meandering low-speed streaks, and streak breakdown events. These events are conditionally sampled and averaged based on their characteristic Reynolds shear stress (RSS) signatures and velocity fluctuations seen in the buffer and the lower-log regions. This follows the methodology employed by previous studies [131, 136, 138] which have produced conditionally-averaged structures in the log-region. In order to improve the robustness of the algorithm, the Reynolds stresses and velocity fluctuations are first spatially averaged in the range $15 \leq y/\lambda_0 \leq 50$ and denoted by subscript $15 - 50$. Further, noting the higher uncertainty in the out-of-plane component (v') at lower velocity magnitudes, the conditional samples are confined to the extreme RSS events exhibiting relatively large magnitudes of v' ($|v'| > 0.5u_{\tau_0}$). Fig. 5.1 schematically shows the thresholding scheme used for sampling ejections and sweeps, hairpin-

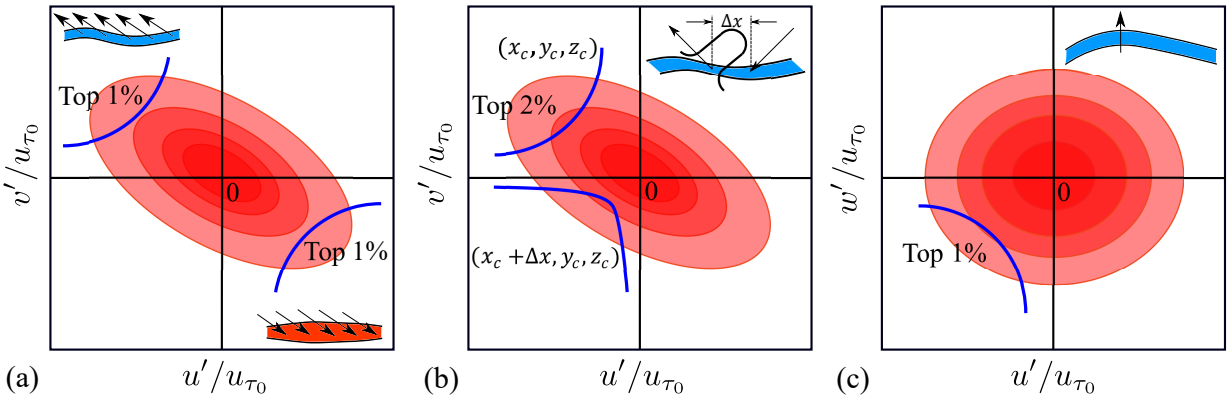

Figure 5.1: Schematic of the thresholding scheme for conditional averaging of (a) ejections (Q2) and sweeps (Q4), (b) hairpin-like structures, and (c) meandering low-speed streaks. Contours in red show schematic joint probability distribution functions of the indicated velocity components, and contours in blue show the threshold of corresponding Reynolds shear stresses (hyperbolas of constant $\langle u_i' u_j' \rangle / u_{\tau_0}^2$) used for conditional sampling in each case. Respective coherent motions sampled via these schemes are schematically illustrated in the insets.

like structures, and meandering low-speed streaks. The sub-figures show schematic joint probability distribution functions (red contours) of velocity fluctuations normalized with the baseline friction velocity (u_{τ_0}). The conditional sampling is performed by identifying the high Reynolds shear stress events as shown with the blue contours. Note that the thresholds identify the location of the centre ($\widetilde{x_c}$, $\widetilde{z_c}$) of the sampling box, where '$\sim$' denotes the conditional averaged quantities.

Ejections (Q2), and sweeps (Q4) are typically coupled with low- and high-speed streaks, respectively, and produce negative Reynolds shear stress ($u'v' < 0$). This is illustrated in Fig. 5.1 (a), and the associated events are sampled as the highest 1% of Reynolds shear stress ($-\overline{u'v'}|_{15-50}$) in the respective quadrants. The bar denotes spatial average in the wall-normal direction. For each identified extreme $u'v'|_{15-50}$, the algorithm samples instantaneous data within a volume equivalent to $200\lambda_0 \times 80\lambda_0 \times 160\lambda_0$, which is then averaged across all the detected events to reconstruct the characteristic structures.

Hairpin-like structures include an ejection motion (Q2) and feature a spanwise vortical connection (head) between the two streamwise oriented vortices (legs). These vortices typically occur as packets of vortices flanking the low-speed streak [120]. Traditionally, the hairpin vortices are typically identified using the stagnation points associated with Q4 and Q2 motions on the shear layer formed upstream of the hairpin [136]. Owing to the limited wall-normal extent of the current measurements, the method of hairpin identification used here follows a slightly different approach. The spanwise section of the vortex induces a negative wall-normal veloc-

ity downstream of the head (Fig. 5.1 (b)) resulting in a Q3 motion close to the wall. Such Q3 motions can be observed under the head, downstream of the hairpin in the quantitative visualizations of such vortices in previous studies at comparable Reynolds numbers [56, 136, 138]. Thus, the current method of identifying these vortices utilizes these Q3 motions following an ejection as a signature of hairpin-like events. This is achieved by imposing an additional criterion for detection of Q3 motions $30\lambda_0$ ($\sim$ diameter of hairpin head, as also seen from the results of Adrian *et al.* [136] at a comparable Reynolds number) downstream of the detected location ($\widetilde{x_c}$, $\widetilde{z_c}$) of strong ejections. The dimensions of the sampling volume are kept the same as those for the ejections. Although this secondary criterion imposes a sufficient condition to sample the ejections of hairpins, the number of samples decreases. Therefore, to collect more samples, the primary threshold for detecting ejections is slightly relaxed to detect the highest 2% of RSS events. In addition, thresholds are employed to reject the samples exhibiting $|u'|/U_\infty < 2\%$ and/or $|v'|/U_\infty < 2\%$ to discard noisy samples.

Meandering of the low-speed streaks ($u' < 0$) is identified by detecting Q2 or Q3 motions in the u'-w' quadrant plot, shown in Fig. 5.1 (c). Here, the meandering of low-speed streak is detected using the threshold corresponding to the highest 1% of Reynolds shear stress ($\overline{u'w'}|_{15-50}$) in Q3. Since the streaks are expected to meander positively ($w' > 0$) and negatively ($w' < 0$) with equal probability, only one case is considered in this study. In order to completely capture the dynamics of the meandered streaks in the streamwise direction, the streamwise length of the sampled volume is increased, resulting in a volume of $300\lambda_0 \times 80\lambda_0 \times 160\lambda_0$ around the detected location ($\widetilde{x_c}$, $\widetilde{z_c}$).

5.3 Results and Discussion

5.3.1 Boundary layer characterization

The turbulent boundary layer for Newtonian and drag reduced cases is first assessed using the time-averaged velocity profiles shown in Fig. 5.2. The results in Fig. 5.2 (a) confirm that the effect of benign momentum injection (i.e., water injection) into the boundary layer is negligible, which is attributed to the low injection rates employed in this study. Further, there is a clear reduction in the near-wall wall-normal gradient of the streamwise velocity in polymer injected cases compared to the baseline. The figure also serves to compare planar and tomographic PIV results, showing that velocity magnitudes from the latter are smaller in the near-wall region due to the use of larger interrogation volumes. While the tomographic measurements do not allow accurate quantification of the changes in the profile slopes near the wall [226], they capture the overall trend shown by the planar measurements. The inner scaling is evaluated based on planar

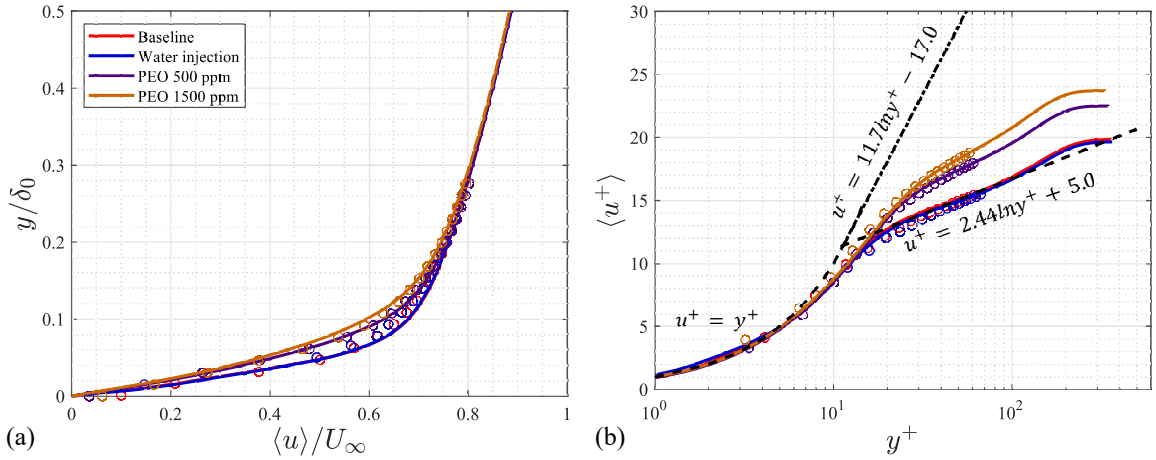

Figure 5.2: Profiles of spatial and time-averaged streamwise velocity ($\langle u \rangle$) at $x - x_{\text{inj}} = 150$ mm to 190 mm in (a) outer coordinates, and (b) inner coordinates. Solid lines show results from planar PIV using ensemble of correlation and $\circ$ show results from tomographic PIV spatially averaged over its streamwise and spanwise directions. Dashed black lines show the classical Newtonian trends in the viscous sublayer, and log-region, respectively. Dash-dot line shows the MDR asymptote [48].

PIV data using the methodology implemented in Ch. 4, and the non-dimensionalized profiles are shown in Fig. 5.2 (b). In particular, the wall shear stress was estimated based on the expected linear variation of $d\langle u \rangle / dy$ within $y^+ \leq 4$, containing at least 12 velocity vectors. The profiles in the Newtonian cases are seen to agree well with the classical trends shown using dashed lines, and those corresponding to the drag reduced cases feature an extended buffer layer and an approximate vertical shift in the log-layer, as expected from previous studies [49,59,61,162,175]. Further, the slope of the log-layer ($k = 1/\kappa$, where κ is the von Kármán constant) is seen to increase towards MDR value ($k = 11.7$) with increasing polymer concentration. The results from tomographic PIV are seen to follow the profiles from planar measurements in the upper-buffer and lower-log layers in all cases. The obtained drag reduction based on the wall-shear stress estimates is within the range of $20\% - 30\%$ for the considered polymer concentrations.

Polymer injection effects on the turbulent boundary layer statistics are further characterized by considering profiles of root-mean-square (RMS) velocity fluctuations and Reynolds shear stress shown in Fig. 5.3. Normalized profiles of the RMS of the streamwise velocity fluctuations ($\sqrt{\langle u'u' \rangle}$) in Fig. 5.3 (a) resolve the near-wall peak at $y/\lambda_0 \approx 15$ for the Newtonian cases. Its position is shifted away from the wall to $y/\lambda_0 \approx 20 - 25$ due to the polymer injection, and the peak magnitude is decreased. The corresponding RMS profiles from tomographic PIV are

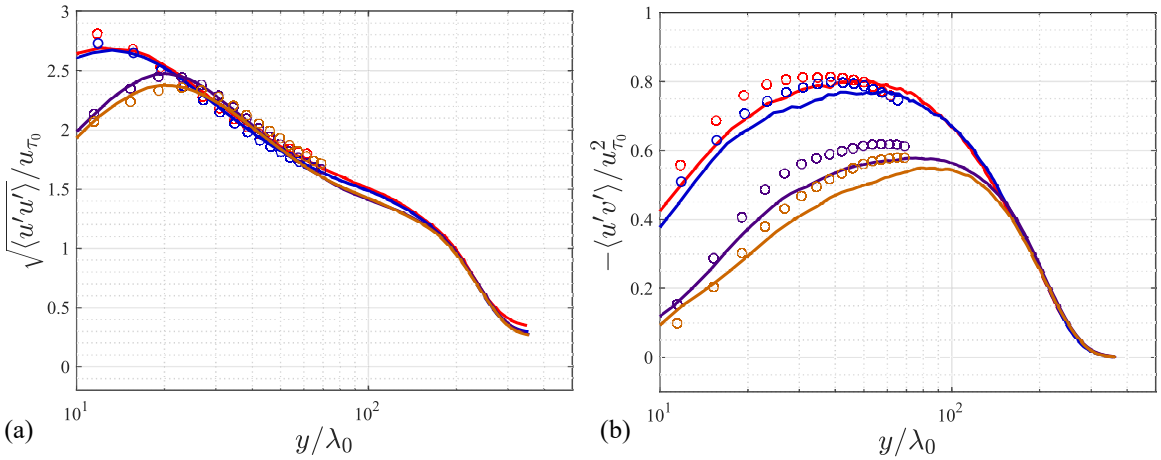

Figure 5.3: Time and space averaged profiles of (a) RMS of streamwise velocity fluctuations ($\sqrt{\langle u'u' \rangle}$), and (b) Reynolds shear stress ($\langle u'v' \rangle$) at $x - x_{\text{inj}} = 150$ mm to 190 mm. Solid lines show results from planar PIV using sequential correlation and ∘ show results from tomographic PIV spatially averaged over its streamwise and spanwise directions. Results are normalized using the inner scaling in the baseline case. Color coding follows that in Fig. 5.2

seen to closely follow the planar PIV data. The profiles of Reynolds shear stress ($\langle u'v' \rangle$) in Fig. 5.3 (b), which are of particular significance in the present study, show the characteristic peak in the upper-buffer/lower-log layer in all the cases. There is a significant attenuation of $\langle u'v' \rangle$ with increasing polymer concentration which is indicative of the expansion of the buffer layer previously noted from Fig. 5.2 (b). The estimates of $\langle u'v' \rangle$ from tomographic PIV are seen to agree with the planar data, while exhibiting a marginally higher magnitude as a result of the higher uncertainty in estimating the out-of-plane velocity component [214, 251].

5.3.2 High and low Reynolds shear stress events

The effect of polymer on Reynolds shear stress is first explored through instantaneous realizations shown in Fig. 5.4. The contours of streamwise velocity fluctuations illustrating the near-wall streak structure are also shown in the figure for reference. Figs. 5.4(a) and (b) show that the near-wall streaky structure is notably different in the case of the polymer injected flow. In general, the polymer injection leads to the formation of wider streaks, and the regions with extreme magnitudes of fluctuations become more sparse. This is aligned with the results in Fig. 5.3 (a) which show a decreased peak magnitude in the polymer cases at the same wall-normal distance

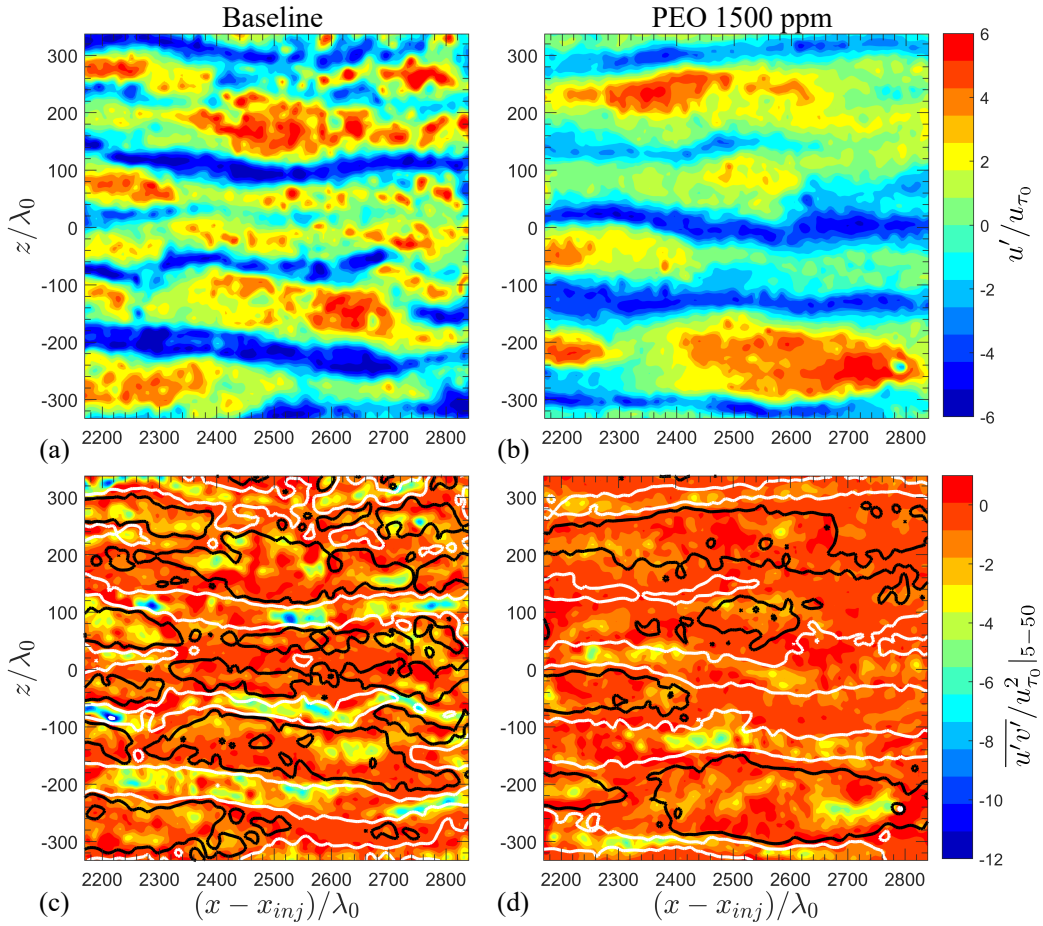

Figure 5.4: Instantaneous visualizations of (a, b) streamwise velocity fluctuations u'/u_{τ_0} at $y^+ \approx 15$, and (c, d) averaged Reynolds shear stress $\overline{u'v'}/u^2_{\tau_0}|_{5-50}$. Left column (sub-figures (a) and (c)) show the near-wall streak structure for baseline case, and right column (sub-figures (b) and (d)) show that for the PEO 1500 ppm case. Contours corresponding to regions with $u'/u_{\tau_0} > 1.5$ (black) and $u'/u_{\tau_0} < -1.5$ (white) are overlaid in sub-figures (c) and (d) to indicate the high- and low-speed streaks.

($y/\lambda_0 \approx 15$). Figs. 5.4(c) and (d) illustrate that the distribution of spatially averaged Reynolds shear stress $-\overline{u'v'}/u^2_{\tau_0}|_{5-50}$ is also significantly affected by the polymer. These distributions are complemented with the contours of u' corresponding to high- (black lines) and low-speed (white lines) streaks. The results show that the regions with large magnitudes of Reynolds shear stress $-\overline{u'v'}/u^2_{\tau_0}|_{5-50}$ are largely confined within the low- and high-speed streaks in both Newtonian and polymer-injected flows. This may be expected since the low- and high-speed streaks are

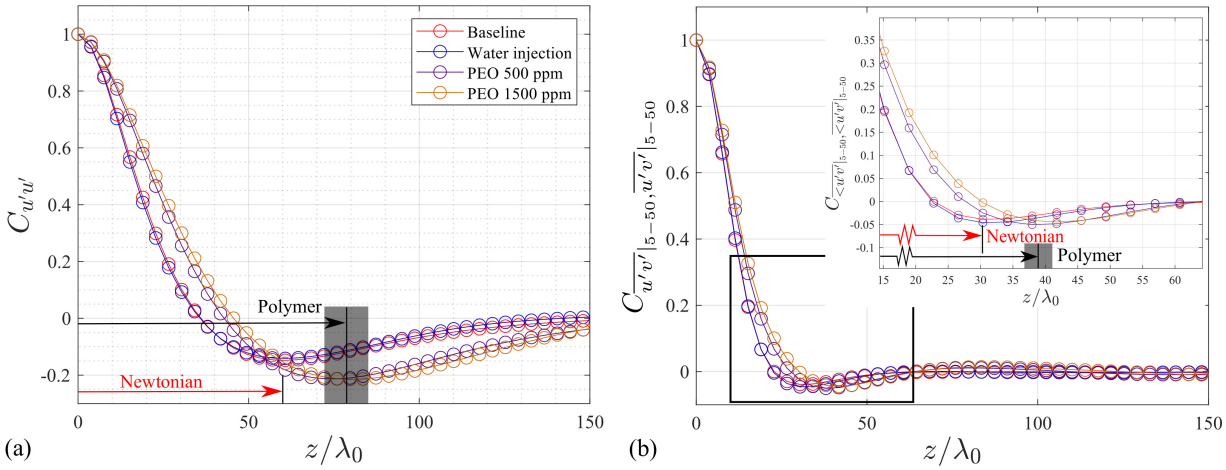

Figure 5.5: Two-point correlation coefficients for (a) streamwise velocity fluctuations (u') at $y/\lambda_0 \approx 15$, and (b) $\overline{u'v'}|_{5-50}$. Spanwise coordinates corresponding to the minima of the coefficients are shown using vertical black lines. Minima for polymer cases vary monotonously with polymer concentration in the region shown in gray.

known to be linked to ejection (Q2) and sweep (Q4) events, respectively [120, 131, 136], each of which contributes substantially to the production of the turbulent kinetic energy. The high-RSS regions ($\overline{u'v'}/u_{\tau_0}^2|_{5-50} < -0.5$) dominate more in the baseline case (Fig. 5.4(c)) in comparison to those in the polymer injected case (Fig. 5.4(d)). Further, the low-RSS ($|\overline{u'v'}/u_{\tau_0}^2|_{5-50}| < 0.5$) regions are scattered non-uniformly in the baseline case, whereas they occupy much larger areas in the polymer-injected case. The reduction in the number density and magnitudes of the high-RSS regions is attributed to the reduction in the frequency of turbulence-producing coherent structures passing through the domain, which enlarges the low-RSS regions.

In order to further elucidate the polymer effect on the near-wall structures, the two-point correlation of the streamwise velocity fluctuations (u') at $y/\lambda_0 \approx 15$ and spatially-averaged Reynolds shear stress $\overline{u'v'}|_{5-50}$ are considered in Figs. 5.5(a) and 5.5(b), respectively. The Reynolds shear stress is averaged within the near-wall region in order to capture the resultant effect of all the coherent structures passing through the near-wall region. In Fig. 5.5(a), the correlation coefficient ($C_{u'u'} = \langle u'(z)u'(z+\Delta z)\rangle / \sqrt{\langle u'(z)^2\rangle\langle u'(z+\Delta z)^2\rangle}$) is seen to decrease below zero to a minimum at $z/\lambda_0 \approx 60$ in the baseline case. This is consistent with the typical half streak spacing values reported by previous studies [50, 123] in Newtonian boundary layers at the considered wall-normal distance. The half streak spacing in polymer cases increases to $z/\lambda_0 \approx 72-84$, with higher spacing achieved at higher concentrations. The obtained range is in good agreement with the empirical correlation provided by White *et al.* [50]. Two-point correla-

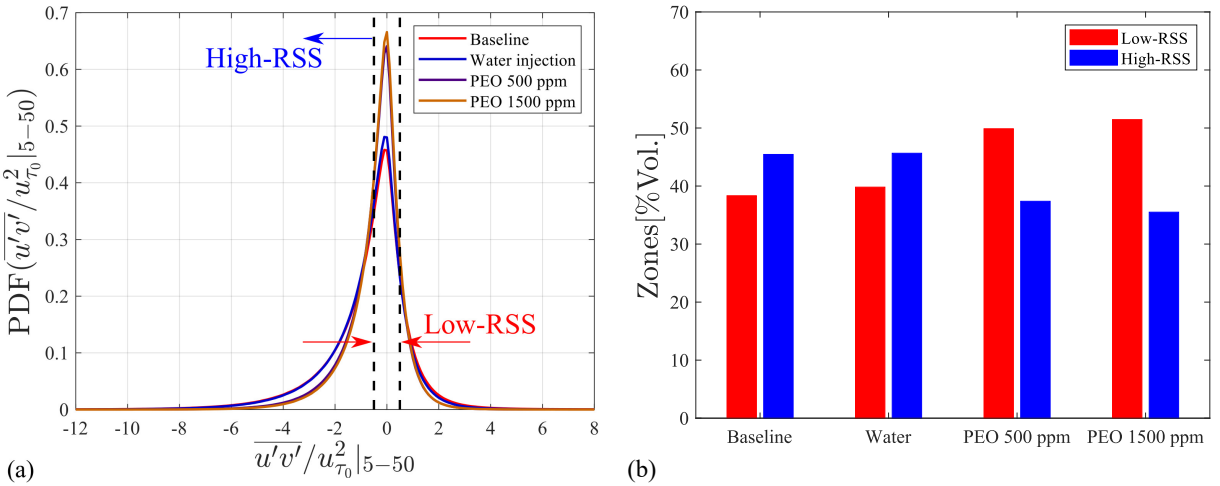

Figure 5.6: Effect of polymer injection on high- and low-RSS events shown through (a) probability distribution functions of $\overline{u'v'}/u^2_{\tau_0}|_{5-50}$, and (b) percentage of volume occupied by these events within the measurement domain.

tion coefficients of the $\overline{u'v'}|_{5-50}$ in Fig. 5.5 (b) show a similar trend with their minimas located at nearly half of the spanwise locations of the corresponding minima in $C_{u'u'}$. Specifically, the extrema for Newtonian cases are located at $z/\lambda_0 \approx 30$, and those for the polymer cases vary in the range $z/\lambda_0 \approx 37 - 42$. This provides a statistical confirmation that high-RSS producing events are predominantly located in the low- and high-speed streaks in both Newtonian and drag reduced cases.

Strong Q2 and Q4 events in the near-wall region are present in both Newtonian and polymer injected cases, as evident from the skewed PDFs of average Reynolds shear stress in the buffer layer in Fig. 5.6(a). Fig. 5.6(a) shows that a significant portion of the population, containing the distribution peak in each case, corresponds to the low-RSS occurrences demarcated by $|\overline{u'v'}/u^2_{\tau_0}|_{5-50}| < 0.5$ for presentation purposes. The peak magnitude increases with increasing polymer concentration correlating with the increase in the size of low RSS regions seen in Fig. 5.4, where turbulence suppression is expected [195, 246, 250]. Another significant portion of the PDF constitutes the high-RSS events, $\overline{u'v'}/u^2_{\tau_0}|_{5-50} < -0.5$, whose magnitude and number are reduced in the polymer cases. A comparison of the relative flow volumes occupied by the low- and high-RSS regions identified using the same thresholds is presented in Fig. 5.6(b). While subjective to the choice of the threshold values, the results indicate that the high-RSS regions occupy larger flow volumes in the Newtonian cases, but their volume fraction diminishes significantly due to the polymer injection.

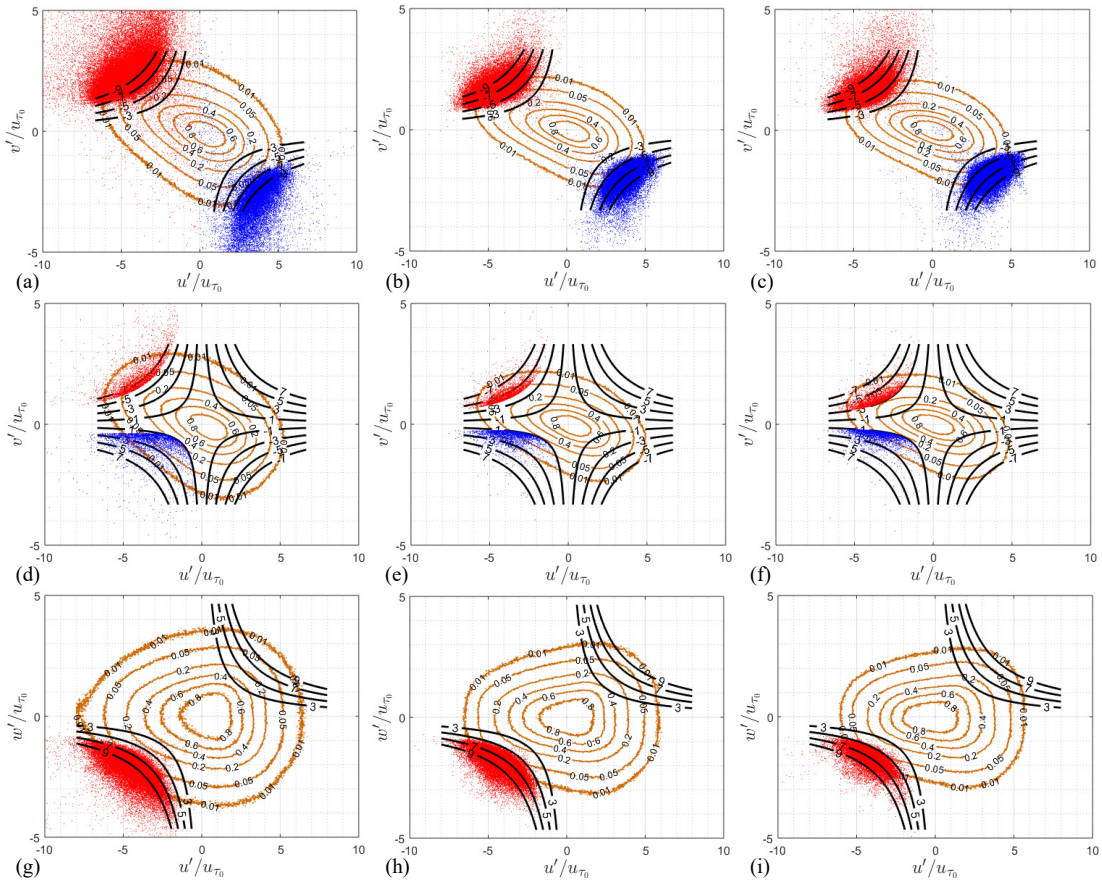

Figure 5.7: Thresholding scheme for conditional averaging of (a-c) ejections (Q2) and sweeps (Q4), (d-f) hairpin-like structures, and (g-i) meandering low-speed streaks. Contours in orange show joint probability distribution functions of the indicated velocity components normalized with their respective peak magnitudes in each case. Contours in black show the constants of corresponding Reynolds shear stresses in inner scaling for reference. Sub-figures in left column (a, d, g): baseline, middle column (b, e, h): PEO 500 ppm, and right column (c, f, i): PEO 1500 ppm. (a-c): Data-points in red and blue correspond to the highest 1% of the averaged Reynolds shear stress ($-\overline{u'v'}|_{15-50}$). (d-f) Data-points in red (upstream, $\widetilde{x}_c$) and blue (downstream, ($\widetilde{x} - \widetilde{x}_c \approx 30\lambda_0$)) correspond to the identified instances of hairpin-like structures with averaged Reynolds shear stress ($-\overline{u'v'}|_{15-50}$) in the highest 2%. (g-i): Data-points in red correspond to the highest 1% of the averaged Reynolds shear stress ($\overline{u'w'}|_{15-50}$) indicating negatively yawed low-speed streaks.

5.3.3 Reynolds shear stress distribution in near-wall coherent structures

Various near-wall coherent motions are characterized by large magnitudes of Reynolds shear stress $-u'v'/u_{\tau_0}^2$ leading to the formation of distinct high-RSS regions, which are associated with Q2 and Q4 motions. These motions are opposing in nature which warrants their independent evaluation. The average three-dimensional topology of such coherent motions is considered here to characterize extreme RSS events, and shed light on some widely debated mechanisms of polymer-turbulence interactions [54, 65]. In this regard, the polymer effect on coherent motions of ejections (Q2) and sweeps (Q4), hairpin-like vortical structures, meandered low-speed streaks, and the precursor events of streak breakdowns is considered.

Ejections (Q2) and sweeps (Q4), categorized on the basis of quadrant analysis [131], are sampled according to the methodology outlined in section 5.2.1. Figs. 5.7 (a-c) show the joint probability distribution functions (J-PDFs) of u'/u_{τ_0} and v'/u_{τ_0} with increasing polymer concentration, and the population distributions of extreme RSS events for conditional sampling and identification of the associated structures. With increasing polymer concentration, the J-PDFs (orange contours) are seen to become narrower and the anticorrelation between u'/u_{τ_0} and v'/u_{τ_0} weakens. This is marked by the decrease in the inclination angle of the distributions, signifying the weakening of the ejections and sweeps. The distributions of extreme RSS events (coloured points), show a decrease in the magnitude of such events with polymer injection and increase in polymer concentration. However, the selected threshold values result in sufficient convergence of conditional averages for both Newtonian and polymer-injected cases. Each conditional average is based on around 6000 to 8000 samples with a maximum overlap of 50% between consecutive samples from the same low-speed streak.

Fig. 5.8 (a-c) shows the conditionally-averaged ejection (Q2) structure for the baseline flow and two polymer injection cases. The vortical structures within the conditionally averaged flow fields are illustrated using the Q-criterion [252]. The ejection events coincide with low-speed streaks, shown on the $\widetilde{x} - \widetilde{z}$ slice at $\widetilde{y}/\lambda_0 \approx 10$, which are located along the spanwise centre of the sampled volume. Further, they form between streamwise oriented counter-rotating vortical structures as indicated by the $\widetilde{y} - \widetilde{z}$ slice at $\widetilde{x}/\lambda_0 \approx 0$ and the corresponding insets. It is noted from the insets that the vortex centres of the streamwise vortices represented by the Q-criterion are slightly biased towards the high shear regions at the centre of the volume [253]. The strongest point of the ejection motions (peak at $\widetilde{u'v'}/u_{\tau_0}^2 \approx -12$ in Newtonian case) is observed at the centre of the sampled volume ($\widetilde{x}/\lambda_0 = 0$). Such strong ejections typically indicate turbulent burst-like events [132, 133], leading to turbulent momentum transport away from the wall. The centres of the counter-rotating streamwise vortices have a spanwise spacing of nearly half the streak-spacing which agrees well with previous findings [254]. With the addition of polymer (insets of Figs. 5.8 (b) and (c)), the same topology is observed, but the spacing between the

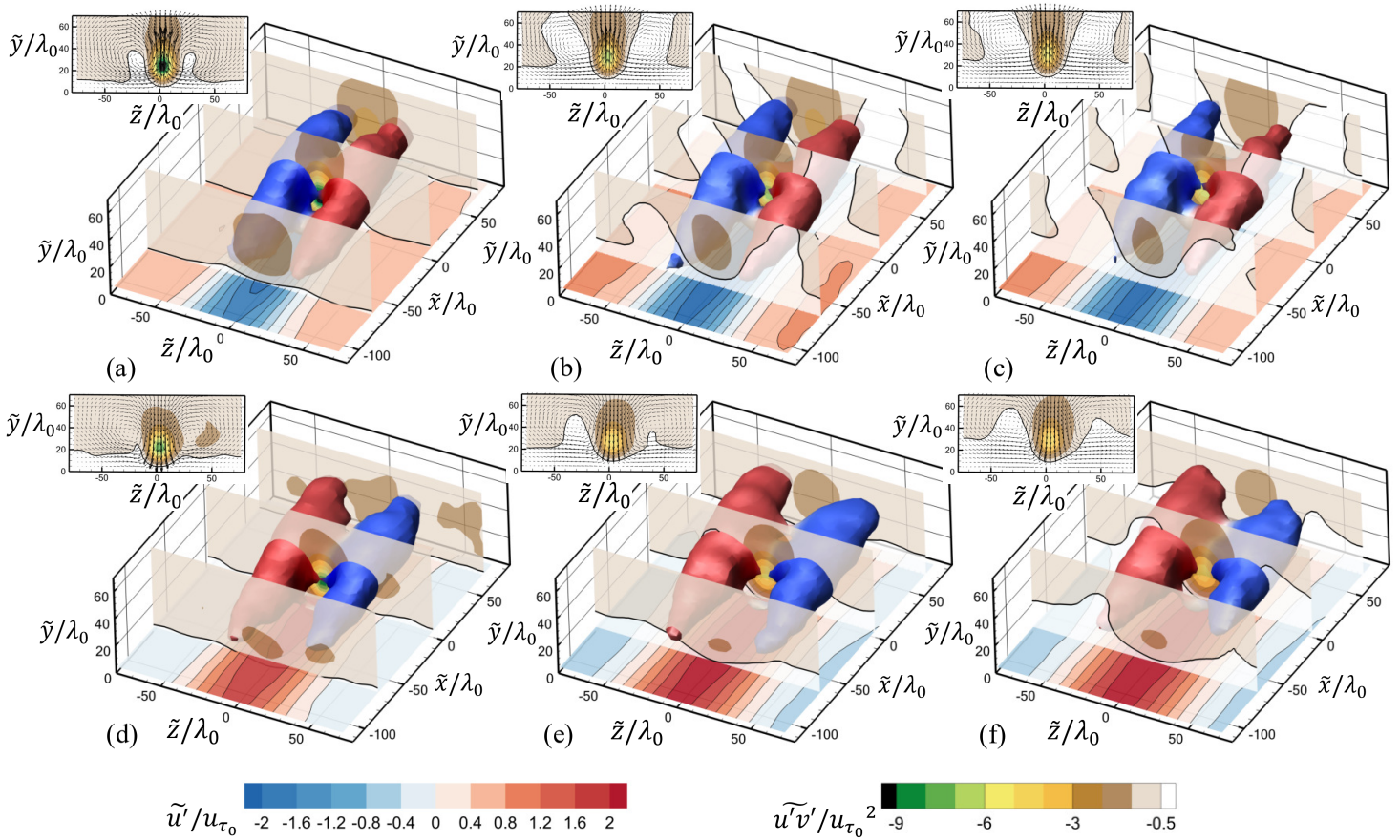

Figure 5.8: Conditionally averaged coherent structures showing (a-c) ejection motions (Q2), and (d-f) sweep motions (Q4). Sub-figures in left column (a, d): baseline, middle column (b, e): PEO 500 ppm, and right column (c, f): PEO 1500 ppm. The quasi-streamwise vortices are identified using the Q-criterion ($\widetilde{Q} = 25$) colored with streamwise vorticity ($\widetilde{\omega_x}$); red color shows $\widetilde{\omega_x} > 0$, and blue shows $\widetilde{\omega_x} < 0$. $\widetilde{y} - \widetilde{z}$ slices at $\widetilde{x}/\lambda_0 = -75, 0$, and 60 show contours of conditionally averaged Reynolds shear stress $\widetilde{u'v'}/u_{\tau_0}^2$. Black contours on $\widetilde{y} - \widetilde{z}$ slices indicate the boundary of the low-RSS regions $\widetilde{u'v'}/u_{\tau_0}^2 = -0.5$. $\widetilde{x} - \widetilde{z}$ slice at $\widetilde{y}/\lambda_0 \approx 10$ shows contours of conditionally averaged streamwise velocity fluctuations $\widetilde{u'}/u_{\tau_0}$. Insets show the slice $\widetilde{x}/\lambda_0 = 0$ overlaid with in-plane velocity vectors.

centres of the vortices is observed to increase in accordance with the increase in streak-spacing (Fig. 5.5 (a)). Further, the strength of the vortices decreases in polymer-injected cases, with normalized circulation $\Gamma/U_\infty\delta_0$ evaluated on a contour corresponding to $Q \approx 50$ decreasing from 4.85 in the baseline case to 3.36 and 1.90 for the PEO 500 and 1500 ppm cases, respectively. This is also accompanied by the decrease in the magnitude of Reynolds shear stresses, as the turbulent burst at the centre of the volume produces only about half of the corresponding Newtonian RSS in the PEO 1500 ppm case.

Despite a significant, but localized, reduction in the Reynolds shear stresses in the high-RSS regions, a notable difference in the near-wall ejection structure arises in the regions containing the streamwise vortices. Figs. 5.8 (b) and (c) illustrate the increase in the extent of low-RSS regions surrounding the main streamwise vortices, with the low-RSS regions qualitatively demarcated by the black contours of $\widetilde{u'v'}/u_{\tau_0}^2 = -0.5$. These low-RSS regions are seen confined between the black contours and the wall. In polymer injected cases, the low-RSS regions begin to encompass the cores of the vortices extending significantly in the wall-normal direction. This contrasts with the Newtonian case of Fig. 5.8 (a), where the contour of $\widetilde{u'v'}/u_{\tau_0}^2 = -0.5$ is situated primarily within the viscous sublayer ($\widetilde{y}/\lambda_0 < 10$) and barely reaches the vortex cores. These observations lend some support to the polymer-vortex interaction mechanism suggested by Min *et al.* [54]. They proposed that the decrease in turbulent kinetic energy production in the lower buffer layer is attributed to the wall-normal transport of the stretched polymer molecules from the near-wall high-shear regions to upper layers, where the polymers relax. This requires a strong wall-normal velocity which is present within the high-RSS regions as observed in the present results. However, it does not explain the formation of low-RSS regions within the vortical structures where the wall-normal motions are weaker compared to those within the core of the high-RSS regions. Thus, it is hypothesized that the near-wall vortical motions may also play a role in stretching the polymer macromolecules. As a consequence of this energy transfer, the strength of the vortices decreases, as seen in the present results as well as some previous studies [56, 57].

Sweep motions (Figs. 5.8 (d-f)) occurring within the high-speed streaks also feature the counter-rotating streamwise vortical structures whose directions are opposite to those seen in ejection events. The resultant wallward motions are associated with high-RSS close to the wall (peak at $\widetilde{y}/\lambda_0 < 20$) in the Newtonian cases (Fig. 5.8 (d)). Similar to the behaviour seen in the ejections, the spacing between the streamwise vortices increases and their strength decreases with the addition of polymer and increase in polymer concentration, but the overall topology remains similar. The peak magnitudes of the high-RSS regions within the high-speed streak at the spanwise centre of the sampled volumes are $\widetilde{u'v'}/u_{\tau_0}^2 \approx -8$ in the Newtonian case and it reduces to $\widetilde{u'v'}/u_{\tau_0}^2 \approx -5$ in the PEO 1500 ppm case. In general, the peak magnitudes of these shear stresses are smaller than those generated in ejection events. This is expected from the slightly skewed distributions of the joint PDFs in Figs. 5.7 (a-c). The low-RSS regions confined within

contours of $\widetilde{u'v'}/u_{\tau_0}^2 = -0.5$ do not change as appreciably as in the ejection cases (Figs. 5.8(a-c)). This suggests a weakening of the polymer effect generated due to the polymer-vortex interaction noted in the ejections, and can be explained by considering the polymer transport in each of these motions. Since the sweeps are characterized by a wallward transport of the fluid from the outer layers, they are likely to contain a lower polymer concentration. This may result in a reduction of the local polymer concentration in the near-wall region. Further, a spanwise transport of the polymer in the near-wall region due to induction by the streamwise vortices may limit the polymer flux into the vortical regions, inhibiting the formation of large low-RSS regions.

Given the fundamental significance of the low-speed streaks for self-sustaining turbulence cycle [127, 128, 130], further discussion is focused on other coherent motions found to occur in them, exploring the polymer-vortex interaction in each of these cases. Previous studies have shown the existence of hairpin-like structures flanking the low-speed streaks in a wide range of Reynolds numbers encompassing those considered in the current case [120, 136, 139, 255, 256]. Fig. 5.9 shows conditionally-averaged hairpins flanking a typical low-speed streak shown at the spanwise centre of the sampled volume on a $\widetilde{x} - \widetilde{z}$ slice at $\widetilde{y}/\lambda_0 \approx 10$. The inclination angle of the legs of the hairpin is estimated by considering the most upstream and downstream loci of the isosurfaces of Q. These angles are found to be in the range $19^\circ - 22^\circ$ in the Newtonian case for different thresholds of Q, and a least squares fit is considered through all the loci to estimate the average inclination of the hairpin legs, which is $\approx 21^\circ$ (inset in Fig. 5.9 (a)). This is in agreement with previous studies [120] at a comparable relative wall-normal location ($y/\delta < 0.3$). With the addition of the polymer, the vortices are significantly weakened and their inclination angles decrease, as seen in the inset plots in Figs. 5.9(b) and 5.9(c). The decrease in the inclination angles of the legs is in accordance with the decreased magnitudes of the wall-normal velocities within the Q2 event upstream of the head (spanwise vortex) of the hairpin, and agrees with the results of Kim *et al.* [57]. As expected, the Q2 motions upstream of the hairpin head produce large magnitudes of Reynolds stress at the centre of the sampled volume, which are seen to decrease in the polymer-injected cases. Additionally, the low-RSS regions ($\widetilde{u'v'}/u_{\tau_0}^2 = -0.5$) are observed to protrude into the legs of the hairpins in the polymer-injected cases. Interestingly, the enlarged low-RSS regions continue to persist in the streamwise direction even beyond the streamwise position of the head of the hairpin. This suggests that the polymer effect produced due to the polymer-vortex interaction is not confined to the strong vortical regions, since the activated polymer may be convectively transported alongside the low-speed streak and affect adjacent flow regions.

Typical coherent structures observed in meandered low-speed streaks and related flow phenomena are illustrated in Fig. 5.10. These coherent structures pertain to the highest 1% of the spatially averaged Reynolds shear stress $\overline{u'w'}|_{15-50}$ shown in Figs. 5.7 (g-i), resulting in a negatively yawed low-speed streak. The results suggest that the meandering of the streak is strongly

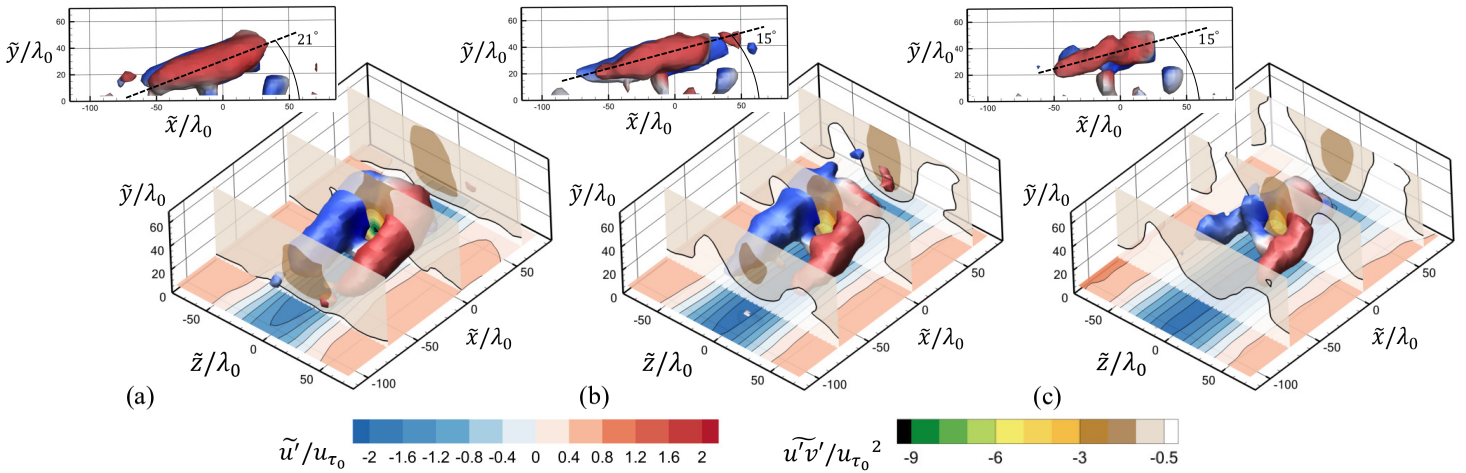

Figure 5.9: Conditionally averaged hairpin-like structures for (a) baseline, (b) PEO 500 ppm, and (c) PEO 1500 ppm. Sub-figures show averaged vortical structures identified using Q-criterion ($\widetilde{Q} = 25$) colored with streamwise vorticity ($\widetilde{\omega_x}$); red color shows $\widetilde{\omega_x} > 0$, and blue shows $\widetilde{\omega_x} < 0$. $\widetilde{y} - \widetilde{z}$ slices at $\widetilde{x}/\lambda_0 = -75, 0$, and 60 show contours of conditionally averaged Reynolds shear stress $\widetilde{u'v'}/u_{\tau_0}^2$. Black contour indicates the boundary of the low-RSS regions $\widetilde{u'v'}/u_{\tau_0}^2 = -0.5$. $\widetilde{x} - \widetilde{z}$ slice at $\widetilde{y}/\lambda_0 \approx 10$ shows contours of conditionally averaged streamwise velocity fluctuations $\widetilde{u'}/u_{\tau_0}$. Insets shows the sideview of the legs of the hairpin-like structure highlighting their nominal inclination angles.

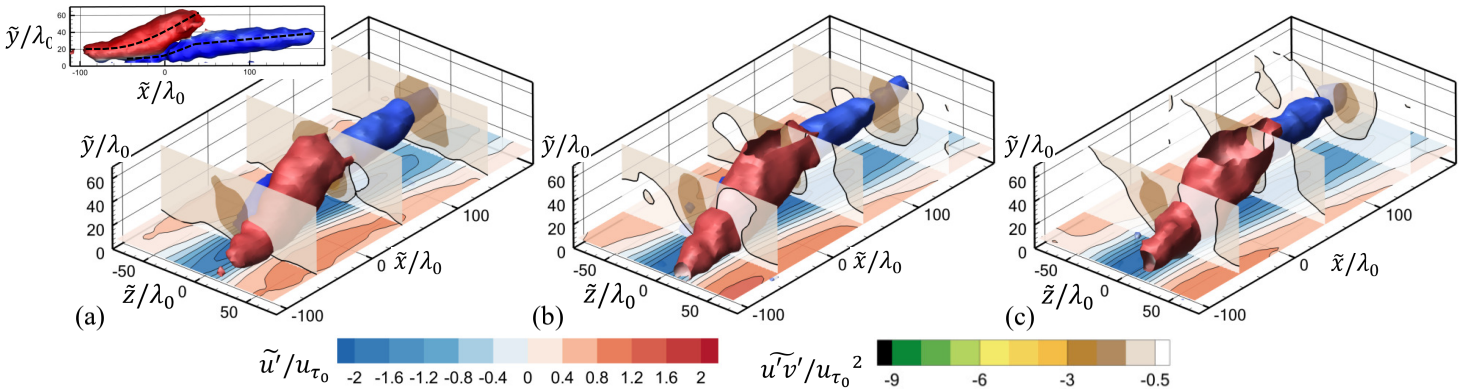

Figure 5.10: Conditionally averaged structures corresponding to meandering low-speed streaks for (a) baseline, (b) PEO 500 ppm, and (c) PEO 1500 ppm. Sub-figures show averaged vortical structures alongside a low-speed streak meandered in the negative z direction. Vortices are identified using Q-criterion ($\widetilde{Q} = 25$) colored with streamwise vorticity ($\widetilde{\omega_x}$); red color shows $\widetilde{\omega_x} > 0$, and blue shows $\widetilde{\omega_x} < 0$. $\widetilde{y} - \widetilde{z}$ slices at $\widetilde{x}/\lambda_0 = -60, 40$, and 140 show contours of conditionally averaged Reynolds shear stress $\widetilde{u'v'}/u_{\tau_0}^2$. Black contour indicates the boundary of the low-RSS regions $\widetilde{u'v'}/u_{\tau_0}^2 = -0.5$. $\widetilde{x} - \widetilde{z}$ slice at $\widetilde{y}/\lambda_0 \approx 10$ shows contours of conditionally averaged streamwise velocity fluctuations $\widetilde{u'}/u_{\tau_0}$. Inset in (a) shows the sideview of the vortical structures highlighting their asymmetric nature with black dashed lines indicating their respective cores.

influenced by the asymmetrically positioned streamwise vortices that flank the streak in both Newtonian (Fig. 5.10 (a)) and polymer-injected cases (Figs. 5.10 (b) and (c)). This is in accordance with the streak-vortex interaction mechanism proposed by Jeong *et al.* [257].

Besides the positional asymmetry, the vortices on either side have different inclination angles resulting in varying magnitudes of negative spanwise velocity within the core of the low-speed streak in the fore portion of the sampled volume. This is confirmed by the negatively-yawed contours of streamwise velocity fluctuations ($\widetilde{u'}/u_{\tau_0}$) on the $\widetilde{x}-\widetilde{z}$ slice at $\widetilde{y}/\lambda_0 \approx 10$. The black dashed lines showing the spines of the vortices obtained using local maxima of Q are included in the inset in Fig. 5.10 (a) for reference. The differences in the inclination angles of these vortices affect their downstream evolution due to the variation in the strengths of their mutual induction along the streamwise direction [257]. This causes the positive vortex to lift-up more substantially compared to the negative vortex, which in turn causes the streak to yaw negatively in the fore portion ($\widetilde{x}/\lambda_0 < 40$), and positively in the aft portion ($\widetilde{x}/\lambda_0 > 40$) of the sampled volume.

The effect of the polymer on the meandering of low-speed streaks can also be deduced from the joint PDFs shown in Figs. 5.7 (g-i). The distributions are seen to become narrower in w'/u_{τ_0} direction with increasing polymer concentration, indicating a decrease in the magnitudes and the frequency of the extreme meandering events. Although the core of the meandered streaks produce relatively low $\widetilde{u'v'}/u_{\tau_0}^2$ as compared to that in the turbulent bursts (Figs. 5.8(a-c)), the polymers result in the notable expansion of low-RSS regions alongside the streak.

This low-RSS region is attributed to the wall-normal transport of the stretched polymer within the core of the streak by the flanking vortices and is consistent with the mechanisms in the case of upwash events discussed earlier. Similar to the hairpin-like structures, the newly formed low-RSS regions persist alongside the positively meandered low-speed streaks beyond the lift-up of the positive vortex.

The meandering of the low-speed streak resulting from various modes of instabilities eventually leads to the breakdown of the streak [99, 128], and thus play an important role in the self-sustenance of the turbulence cycle [127–130]. Consequently, such events can shed light on the critical mechanisms of turbulence control in the polymer drag reduced flows. The streak-breakdown events are characterized by necessary precursor events involving the tail of a low-speed streak in a close contact with the head of an incoming high-speed streak, resulting in a near-zero streamwise fluctuation in the vicinity of breakdown [129]. The produced three-dimensional shear layers have been shown to undergo high frequency perturbations eventually leading to the breakdown of the low-speed streak [129, 258, 259]. Although such perturbations are not captured in the current study due to the use of a non-time-resolved data, the average streak structure corresponding to the precursor events can be captured. The sampling methodology for streak-breakdown events follows a different approach than the joint PDF based sampling

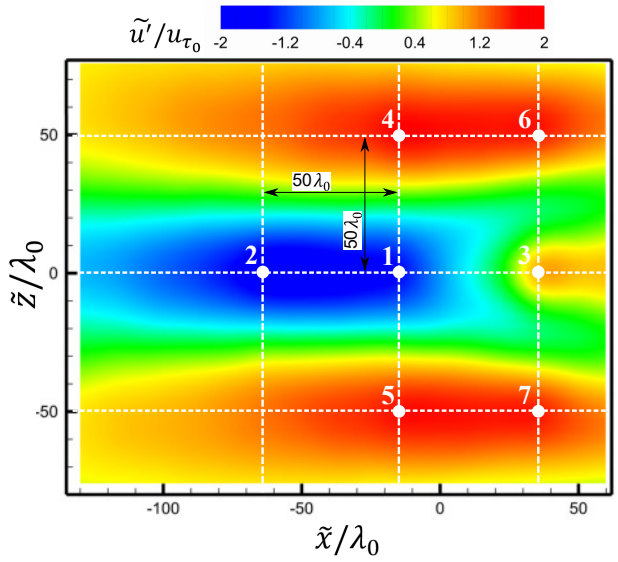

Figure 5.11: Conditional sampling methodology for precursors of streak breakdown events. Locations of grid points 1 to 7 surrounding an average streak breakdown structure are shown in conditionally averaged coordinates normalized with baseline wall units. Thresholds for the grid points 1 to 7 are: $u'_1 < -0.5u_{\tau_0}$, $u'_2 < -0.1u_{\tau_0}$, $u'_3 > 0.5u_{\tau_0}$, $u'_4 > 0.1u_{\tau_0}$, $u'_5 > 0.1u_{\tau_0}$, $u'_6 > 0.1u_{\tau_0}$, $u'_7 > 0.1u_{\tau_0}$.

procedure used in the previous cases. Fig. 5.11 showing an average structure of the precursor of the symmetric breakdown event is used to illustrate the sampling procedure. It is seen that the low-speed streak breaks down ($\widetilde{x}/\lambda_0 \approx 0$) between grid points 1 ($u'_1 < -0.5u_{\tau_0}$) and 3 ($u'_3 > 0.5u_{\tau_0}$), following which the high-speed streak begins. In addition to these conditions, the surrounding flow-field pattern is used by employing minimal thresholds at highlighted grid points 2 ($u' < -0.1u_{\tau_0}$), and 4 to 7 ($u' > 0.1u_{\tau_0}$). The spacing between the adjacent points is $\approx 50\lambda_0$ which corresponds to half of the typical streak-spacing in the baseline case. The employed grid pattern is found to be robust to changes in grid spacing of up to $\pm 20\%$, which allows the same pattern to be employed on polymer-injected cases which have a slightly larger streak-spacing (Fig. 5.5 (a)).

Fig. 5.12 shows that the topology of the conditionally averaged coherent structures of the precursor events of the streak-breakdown event are largely similar for the Newtonian and the polymer-injected cases, but the vortices are found to weaken in polymer-injected cases. As noted earlier, the weaker vortices indicate a significant polymer stretching effect which causes the low-RSS regions to envelope the vortical structures in the wall-normal direction (Figs. 5.12(b) and 5.12(c)). In the Newtonian cases, these low-RSS regions are largely submerged in the viscous

sublayer, barring the region surrounding the streak-breakdown where they rise to the upper buffer layer due to the change in sign of $\widetilde{u}'$. The weakening of the vortices in the breakdown event directly affects the resulting quasi-streamwise vortical structures which are crucial for the streak regeneration process [128, 254].

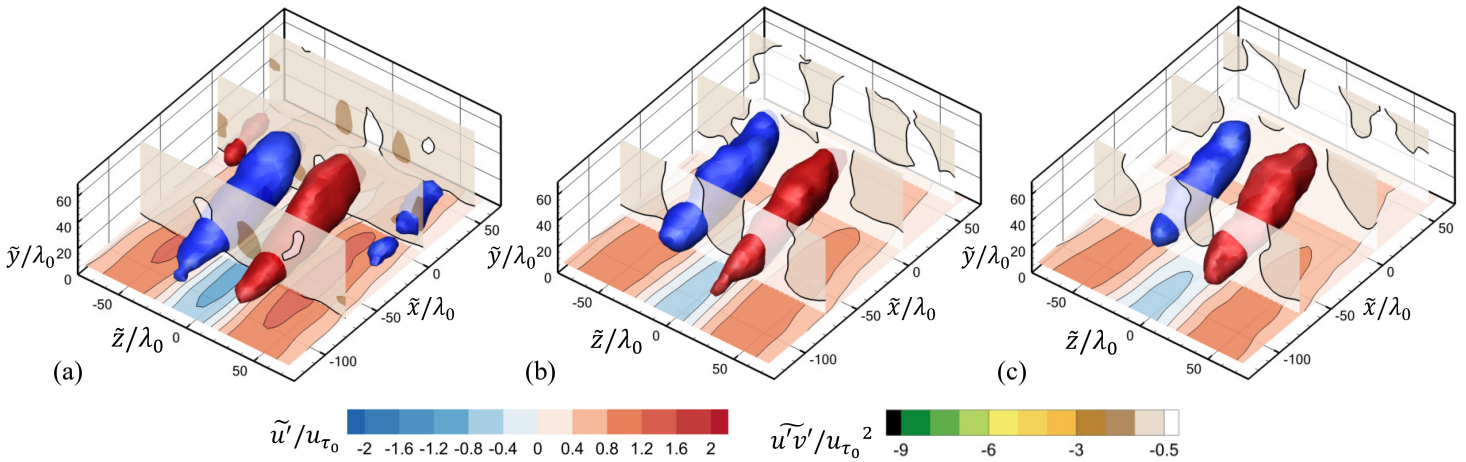

Figure 5.12: Conditionally averaged structures of low-speed streak breakdown events for (a) baseline, (b) PEO 500 ppm, and (c) PEO 1500 ppm. Sub-figures show averaged vortical structures alongside the breakdown event of a low-speed streak identified using Q-criterion ($\widetilde{Q} = 25$) colored with streamwise vorticity ($\widetilde{\omega_x}$); red color shows $\widetilde{\omega_x} > 0$, and blue shows $\widetilde{\omega_x} < 0$. $\widetilde{y} - \widetilde{z}$ slices at $\widetilde{x}/\lambda_0 = -75, 0$, and 50 show contours of conditionally averaged Reynolds shear stress $\widetilde{u'v'}/u_{\tau_0}^2$. $\widetilde{x} - \widetilde{z}$ slice at $\widetilde{y}/\lambda_0 \approx 10$ shows contours of conditionally averaged streamwise velocity fluctuations $\widetilde{u'}/u_{\tau_0}$.

5.3.4 Polymer effects on extensional motions in near-wall region

In contrast to the purely elastic model [53,54,196], previous studies [65,260,261] have attributed the polymer action to the anisotropic behaviour of the extensional viscosity which has led to another branch of contemporary modelling techniques based on the FENE-P model [55, 191, 192, 262]. While the recent experimental study by Shaban *et al.* [60] shows the global effect of extensional viscosity on DR, polymer effect on extensional motions within the near-wall coherent structures is yet to be verified experimentally. The discussion in section 5.3.3 only considered the interaction of the polymer with the quasi-streamwise vortical structures occurring within the ejection and sweep events which were identified using the Q-criterion [252] ($Q > 0$). In this section, the effect of the polymer on extensional motions ($Q < 0$) is considered. The use of the Q-criterion ($Q = 1/2(\|\mathbf{W}\|^2 - \|\mathbf{D}\|^2)$) to identify extensional motions stems from the methodology employed in [56, 263], where a normalized Q-criterion (Eq. 5.1) was employed.

$$Q_{\text{norm}} = \frac{1}{\pi} \cos^{-1} \left(\frac{\|\mathbf{W}\|^2 - \|\mathbf{D}\|^2}{\|\mathbf{W}\|^2 + \|\mathbf{D}\|^2} \right). \tag{5.1}$$

In Eq. 5.1, $\mathbf{W}$ and $\mathbf{D}$ are rates of rotation and strain, respectively, and $\|...\|$ denotes the Euclidean norm operator for each of the two tensors. As discussed in Refs. [56, 263], $0 \leq Q_{\text{norm}} < 0.5$ represent rotational (elliptical) motions, $0.5 < Q_{\text{norm}} \leq 1$ represent extensional (hyperbolic) motions, and $Q_{\text{norm}} = 0.5$ represent shear (parabolic) regions where $\mathbf{W}$ and $\mathbf{D}$ balance each other. Since $\|\mathbf{W}\|^2 + \|\mathbf{D}\|^2 > 0$ (Eq. 5.1), the negative Q-criterion ($Q = 1/2(\|\mathbf{W}\|^2 - \|\mathbf{D}\|^2)$) can be directly utilized to identify local extensional ($Q < 0$) motions.

The near-wall streak structure presents extensional, rotational, and shear deformations within distinct locations as illustrated in Fig. 5.14. The figure shows the spread of the population distributions coloured with their respective Q-values. While all three types of flow deformations are observed in all four quadrants, the spread of the distribution of strong extensional motions (blue points) is the largest. This is followed by the shear motions ($Q_{\text{norm}} = 0.5$, $Q = 0$, white points) whose spread is between that of the extensional and rotational motions, and the strong rotational motions (red points) whose spread is the narrowest. Such a distribution suggests that the extreme quadrant motions, which are likely to appear within the cores of the streaks where the magnitudes of u' and/or v' are the highest, correspond to strong extensional motions ($Q < 0$) as shown in Fig. 5.14. On the other hand, lower magnitudes of u' are more likely to appear within the quasi-streamwise vortices ($Q > 0$). However, such vortices are produced rather intermittently, and the confluence of the adjoining low and high-speed streaks is largely of shearing nature ($Q \approx 0$). Figs. 5.14(b) and (c) show that although the spread of the individual distributions decrease with polymer-injection, the relationship between the flow deformations and streaks is

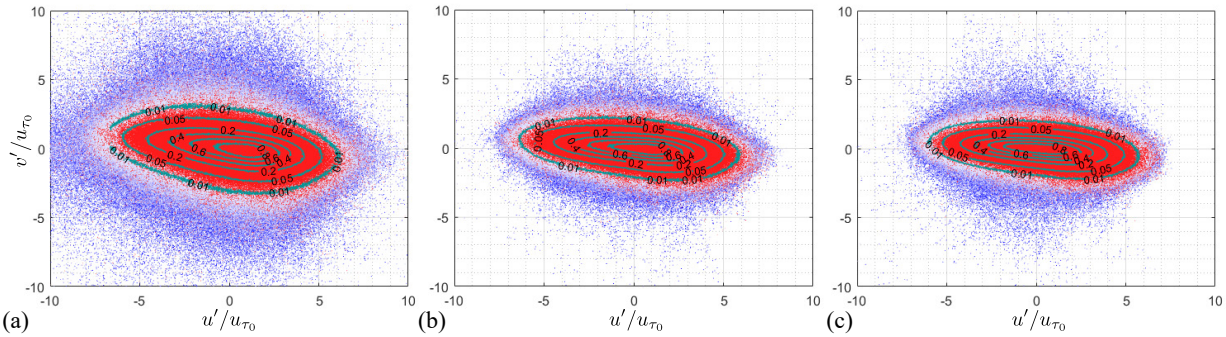

Figure 5.14: Population distributions of the near-wall motions on quadrant plots for (a) baseline, (b) PEO 500 ppm, and (c) PEO 1500 ppm. Velocity fluctuations are normalized with the friction velocity in the baseline case (u_{τ_0}). Samples are averaged between $15 < y^+ < 50$ and colored with their respective averaged Q-values with blue, and red corresponding to strong extensional motions ($Q|_{15-50} < 0$), and rotational motions ($Q|_{15-50} > 0$), respectively, whereas white represents shear motions ($Q|_{15-50} \approx 0$). Contours in green show the joint probability distribution functions of the indicated velocity components normalized with their peak magnitudes in each case similar to those in Fig. 5.7.

not affected significantly, i.e. the strongest fluctuations occurring within the cores of the streaks are attenuated, but predominantly they remain extensional in nature.

The association of strong extensional motions with extreme quadrant events noted in Fig. 5.14 enables the use of the conditional sampling approach described in section 5.2.1 to illustrate the average structure of these events. Fig. 5.15 shows the conditionally-averaged structure of the extensional motions based on the highest 1% of the ejection (Figs. 5.15(a-c)) and sweep events (Figs. 5.15(d-f)). Each subfigure shows the counter-rotating vortical structures ($\widetilde{Q} = 25$) present on the outboard sides of the low- and high-speed streaks (not shown) and the extensional structure ($\widetilde{Q} = -15$) present within the core of those streaks. For both the ejections and the sweeps, the extensional structure is seen to gradually increase in size in the wall-normal direction as the spanwise vortical connection is approached. From the insets in Fig. 5.15, it is observed that the extensional structure upstream of $\widetilde{x}/\lambda_0 = 0$ is weaker within the viscous sublayer in the case of ejections as compared to that in the sweeps, which is a consequence of their respective wall-normal motions. With increasing concentration of the polymer, the size of these extensional structures upstream of the spanwise vortical head ($\widetilde{x}/\lambda_0 < 20$) is seen to decrease in the case of the ejections. This decrease in size is seen despite the increased coherence and broadening of the corresponding streaks as shown in Fig. 5.4. As the viscous effects strengthen with increasing polymer concentration within the viscous and expanded buffer layers, the extensional motions weaken closer to the wall, leading to an apparent displacement of the extensional structures in the

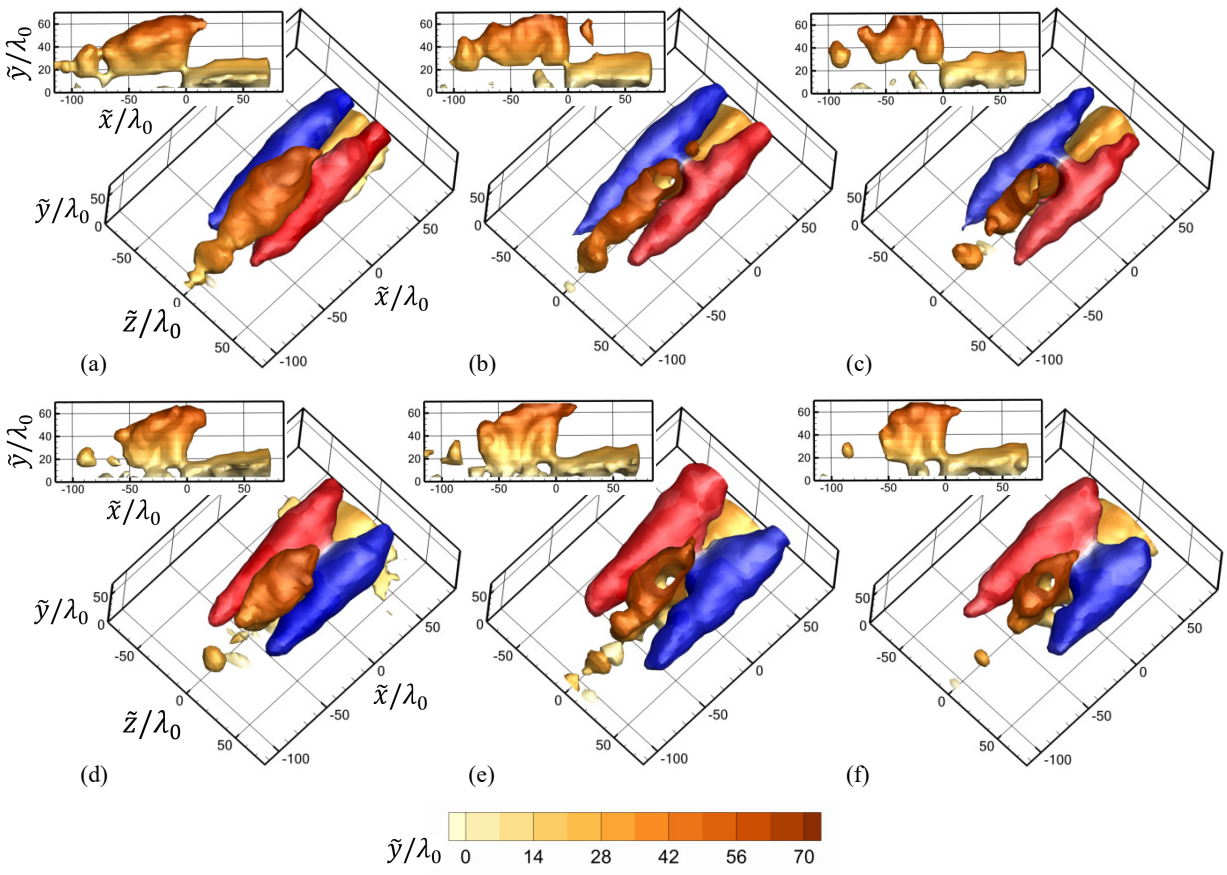

Figure 5.15: Conditionally averaged coherent structures showing (a-c) ejection motions (Q2), and (d-f) sweep motions (Q4). Sub-figures in left column (a, d): baseline, middle column (b, e): PEO 500 ppm, and right column (c, f): PEO 1500 ppm. Sub-figures show averaged quasi-streamwise vortices identified using Q-criterion ($\widetilde{Q} = 25$) colored with streamwise vorticity ($\widetilde{\omega_x}$); red color shows $\widetilde{\omega_x} > 0$, and blue shows $\widetilde{\omega_x} < 0$. Isosurface corresponding to $\widetilde{Q} = -15$ colored with wall-normal distance $\widetilde{y}/\lambda_0$ indicates the structure of the extensional motions with these events. Insets show the side-views of the extensional structure in each case.

wall-normal direction (insets). However, such a considerable effect is not observed in the case of the sweeps, where the extensional structures are only marginally reduced in their streamwise and spanwise extents, and are negligibly affected in their wall-normal extent. The extensional structures in both the ejections and sweeps partially coincide with the high-RSS regions (Fig. 5.8, $\widetilde{x}/\lambda_0 = 0$) where magnitudes of Reynolds shear stresses decrease in the polymer cases. Furthermore, the low-RSS regions downstream of the lifted vortices in the meandered low-speed streak

(Fig. 5.10) and streak-breakdown (Fig. 5.12) were also found to coincide with strong extensional structures, but, the results are not included here for brevity. Thus, in addition to the polymer-vortex interaction highlighted earlier, the reductions in RSS may be partially associated with the polymer uncoiling and stretching caused by these extensional motions [56].

5.4 Concluding remarks

Planar and volumetric PIV measurements conducted within the buffer and lower-log layers of a flat-plate turbulent boundary layer have been used to examine the modifications to the near-wall coherent structures and Reynolds shear stresses in a polymer (PEO) drag reduced flow. The results are reported for the highest (1500 ppm) and the lowest (500 ppm) concentrations considered at a baseline friction Reynolds number of $Re_{\tau_0} = 240$ and a time-averaged drag reduction of 20% to 30%, pertaining to the *low drag reduction* regime. Due to the relatively narrow range of the produced DR, the results show a relatively low effect the polymer concentration. The three-dimensional measurements allow for an analysis of the polymer injection effect on canonical coherent structures associated with extreme RSS events known to play a crucial role in the self-sustaining mechanism of the wall-bounded turbulent flows.

Instantaneous quantitative visualizations of the near-wall drag reduced flows show an increased streak-spacing and reduced magnitudes of $\overline{u'v'}_{5-50}/u^2_{\tau_0}$ as compared to those seen in the Newtonian flow. The injection of the polymer is shown to significantly decrease the magnitude of RSS and diminish the size of the associated high-RSS regions predominantly centred at the low-speed streaks. In contrast, the relative volume fraction of low-RSS regions, localized primarily at the periphery of low-speed streaks, increased significantly with the addition of the polymer and increase in polymer concentration.

The reconstruction of extreme RSS events based on the quadrant analysis revealed similar topologies in Newtonian and drag reduced flows. However, the polymer is shown to play a significant role in the reduction of the magnitudes of the RSS within the characteristic regions of these events. For ejections and sweeps, the counter-rotating vortices are found to be weakened, although the average size of these vortices based on the chosen value of Q is found to remain comparable in all the cases. This lends support to the hypothesis of the generation of counter-torques within the quasi-streamwise vortices in drag reduced flows [56, 57]. A more significant effect is observed in the distribution of the low-RSS regions. Being mainly submerged within the viscous sublayer in a Newtonian flow, low-RSS regions extend significantly in the wall-normal direction in polymer-injected cases, protruding into the streamwise vortical structures formed during the extreme ejection events. This provides indirect support to the polymer-vortex interaction mechanisms [54]. The low-RSS regions around similar streamwise vortical structures

formed in the sweep events are notably smaller compared to those for the ejections, which is attributed to the wallward transport of lower concentration polymer during the sweeps. In this regard, the ejections are more effective as compared to the sweeps in generating low-RSS regions, and perhaps in the activation of the polymer.

Conditionally-averaged structures prevalent within the low-speed streaks, such as hairpin-like vortices, meandered low-speed streaks, and the precursors of streak-breakdown events have been analysed to uncover other potential effects of the polymer-vortex interactions. For these structures, the injection of polymer produced similar enlargements of the low-RSS regions enveloping the streamwise vortices present in each of these events. In addition, the effect of the polymers appear to extend outside these events, as the generated low-RSS regions are seen to persist beyond the lift-up of the characteristic streamwise vortical structures. This is partially attributed to the convective transport of the activated polymer from these extreme events.

To explore the dampening of the high-RSS regions by polymer injection, the extensional motions have been considered. The results indicate that extreme RSS events, which are significantly affected by the polymers, coincide with significant extensional motions in core regions of the streaks. Using conditional sampling of extreme RSS events, it has been shown that the reduction of high-RSS regions in extreme events is accompanied with the dampening of the collocated extensional motions, indicating a potential accumulation of the polymer stresses. The combined observation of the increase in low-RSS regions around dominant vortical structures and the dampening of the high-RSS regions in the core of the streaks suggests that both rotational ($Q > 0$) and extensional ($Q < 0$) deformations play an important role in the overall mechanism of the polymer drag reduction.

Chapter 6

Effect of polymer on extreme skin friction events

An experimental investigation is conducted using planar and tomographic particle image velocimetry (PIV) measurements in the near-wall region of drag-reduced zero-pressure-gradient turbulent boundary layers. Drag reductions of approximately 20% *and* 30% *were achieved using injection of two different concentrations of polymer solutions into the boundary layer via a two-dimensional inclined slot. The PIV measurements are utilised for evaluating the effect of the polymers on the near-wall flow fields associated with extreme skin-friction events, which are identified by proxy of fluctuating streamwise velocity at the edge of the viscous sublayer. A binary scale decomposition technique is employed to investigate the dampening of small-scale motions in drag reduced flows using the three-dimensional measurements. The scale decomposed results highlight a range of small-scale structures (*$<\sim \delta/2$*) with negligible contribution to the Reynolds shear stresses (RSS) in the polymer-injected flows, while the effect of the polymer on the large-scale motions (*$>\sim \delta/2$*) remains negligible. Furthermore, conditional averaging of the near-wall flow field elucidates the topology within the buffer and lower-log regions associated with extreme large-scale low and high wall-shear stress events. The results highlight the effect of polymer injection on the phase differences between the extreme wall-shear stress events and the RSS producing large-scale coherent structures.*

Parts of this chapter have been adapted from Y. Shah, S. Ghaemi, and S. Yarusevych, "Experimental investigation of extreme skin friction events in polymer drag-reduced turbulent boundary layers [**In Review**]."

6.1 Introduction

The results of Chapter 5 provide an enhanced understanding of the effect of polymers on various coherent structures such as ejections, sweeps, quasi-streamwise vortices, and hairpin-like vortices which directly influence the local skin friction [50, 54–57]. A more detailed discussion of previous investigations and open questions in regard to the effect of turbulence on skin friction is presented in Sec. 2.1.4. Some of the previous investigations have highlighted the role of viscoelasticity of the flexible polymers in dampening the small-scale turbulence in wall-bounded flows [53, 65, 152, 157]. Although, being largely motivated by the ongoing debate between various theories of polymer based drag reduction, including the elastic and molecular extension theories (*e.g.,* Tabor and de Gennes [53] and Lumley [65]), most of the previous studies have focused on the interactions of polymers and coherent structures in the buffer and log-regions, while the effect of these interactions on the local skin-friction induced by the coherent structures has received much less attention.

The previous studies on turbulent boundary layers suggest that the near-wall dynamics pertaining to the extreme wall-shear stress events involves complex multiscale interactions. To untangle the multiscale characteristics of the flow associated with extreme shear stress events, [147] employed a scale-decomposition using spatial-averaging with a kernel of δ. This approach allowed them to carefully examine the contributions of large- and small-scale motions to the Reynolds shear stress using

$$\langle u'v' \rangle = \langle u'_l v'_l \rangle + \langle u'_l v'_s \rangle + \langle u'_s v'_l \rangle + \langle u'_s v'_s \rangle, \tag{6.1}$$

where u' and v' are the fluctuating velocity components in the streamwise and wall-normal directions, respectively, and $\langle . \rangle$ is the time-averaging operator. The subscripts l and s indicate *large*- and *small*-scale contributions, respectively. Gomit *et al.* [147] observed that the extreme shear stress events were strongly correlated with an increased Reynolds shear stress, and that the Reynolds shear stress activity was primarily associated with large-scale motions ($u'_l v'_l$).

Given that the addition of drag-reducing polymers has a profound effect on the wall-shear stress, polymer-based drag reduction has been subjected to a number of investigations with a major portion of the existing body of work focused on understanding the control mechanism. Reviews by White and Mungal [154] and Xi [265] provide an excellent overview of the current understanding of drag-reduced flows. The polymer molecules have been shown to reduce turbulence production by interacting with near-wall coherent structures and reducing their strengths [55–57]. Attenuation of near-wall vortices through viscoelastic mechanisms highlighted by Min *et al.* [54] is accompanied by a reduction in wall-normal velocity fluctuations and Reynolds shear stress [49, 58, 59], increased spanwise spacing of near-wall streaks [50, 51],

and decreased magnitudes of ejections and sweeps [60,61]. Recent studies [56,243] have shown the interaction of polymers with extensional motions, which is hypothesized to play an important role in the drag reduction process [65]. However, these studies also show that the effect of polymers on the extensional motions is localized within the core of the coherent structures, where a significant accumulation of extensional stresses is expected. On the other hand, a significant polymer effect seen on the rotational motions in these studies can be attributed to the elastic mechanisms proposed by Tabor and de Gennes [53] and Min *et al.* [54].

The effect of polymer drag reduction on wall-shear stress in turbulent boundary layers has been studied at a relatively low Reynolds number ($Re_\tau = 70$ to 100) through DNS simulations [195,246]. These studies show that both Newtonian and drag-reduced flows feature distinct phases of high and low turbulent kinetic energy, which they termed as *active* and *hibernating*-states, respectively. Coincidentally, these active and hibernating states are shown to be coupled with high- and low-C_f events, respectively, where C_f is the skin friction coefficient. The hibernating states in both Newtonian and drag-reduced flows were observed to have an MDR-like (Maximum Drag Reduction) velocity profile, which is typically attributed to higher polymer concentrations and near-zero RSS [51, 60]. Succeeding numerical works [247, 248, 250] have provided further evidence for the intermittent characteristics of the active and hibernating states. The results of Wang *et al.* [249] show an increase in the conditionally-averaged RSS during a high-C_f (active) event, and a decrease during a low-C_f (hibernating) event. It is interesting to note that the results of Tamano *et al.* [250] at a comparable Reynolds number suggest a phase lag between the regions of low-C_f and low-RSS, which is speculated to depend on the relaxation time of the polymer (t_{rel}). This may contradict the assumed concurrence of the low-C_f and the low-RSS events in the above studies (*e.g.*, Wang *et al.* [249] and Kushwaha *et al.* [248]).

In addition to wall-shear stress, several studies have investigated the role of polymers in dampening small-scale motions at the dissipative end of the turbulent energy cascade through detailed DNS simulations [62–64]. At the same time, de Angelis *et al.* [266] observed that the energy contained in the most energetic modes increased in the viscoelastic flows in comparison to the Newtonian flows, suggesting a redistribution of the turbulent kinetic energy across the range of scales. This is aligned with the perspective of the elastic theory of polymer drag reduction which suggests the existence of critical length scales that depend on polymer concentration (or, more accurately, the Weissenberg number (Wi)) below which the turbulent energy cascade is disrupted by the polymer [157]. Although a number of numerical studies have confirmed various features of the elastic theory [54, 55, 193, 194], the critical length scales, which have a foundational importance for this theory, have not been verified through experiments.

The present study explores the effect of polymer injection on extreme skin-friction events in a turbulent boundary layer at Reynolds numbers of $Re_\tau \approx 240$. Following recent observations, the footprints in the wall-shear stress at this relatively low Reynolds number are expected

to be strongly associated with the coherent structures in the inner layer [147, 149]. Thus, three-dimensional particle image velocimetry (PIV) measurements are employed to elucidate the complex mechanisms in the buffer and lower-log regions associated with the extreme skin-friction events. A scale decomposition technique is employed to determine the association of the wall-shear stress with the large-scale flow topology within these extreme events, as well as to provide a quantitative measure of the dampening of the small-scale motions [53, 157]. Further, the conditional flow fields corresponding to the extreme skin friction events are utilized to investigate the correlation and phase difference between the skin friction and RSS in the near-wall region in both Newtonian and drag-reduced flows.

6.2 Experimental setup

As discussed in Sec. 3.2, the experimental setup for the present investigation is the same as the one employed in Ch. 5. Thus, the reader is referred to Secs. 3.2 and 5.2 for the details of the planar and tomographic PIV setup. This section discusses the employed data reduction and analysis techniques used in the present study.

6.2.1 Wall-shear stress estimation

The measurement of instantaneous wall-shear stress (τ_w) through optical flow measurement techniques, such as those used in the present study, is a challenging task due to the larger measurement uncertainty of these techniques close to the wall [214]. Notably, Alfredsson *et al.* [267] have shown that the noted complications in the near-wall velocity measurement are not limited to PIV, and the erroneous data associated with near-wall measurement are often diagnosed using a well established near-wall relationship within $y^+ < 5$ given by

$$\frac{\tau'_{w,\text{rms}}}{\langle \tau_w \rangle} = \lim_{y \to 0} \frac{u_{\text{rms}}}{\langle U \rangle}, \tag{6.2}$$

where $\langle \tau_w \rangle$ and $\tau'_{w,\text{rms}}$ are the mean and root-mean-square (rms) of the estimated wall-shear stress, and $\langle U \rangle$ and u_{rms} are the mean and root-mean-square of the streamwise velocity. Other studies have confirmed the applicability of Eq. 6.2 in the region $y^+ < 10$ and have shown that the fluctuating intensity of the wall-shear stress ($\tau'_{w,\text{rms}}/\langle \tau_w \rangle$) remains nearly constant at about 0.4 for $Re_\tau > 400$ [268, 269], but decreases at lower Reynolds numbers [270]. Nevertheless, noting the strong correlation between the streamwise velocity fluctuations (u') with the wall-shear stress,

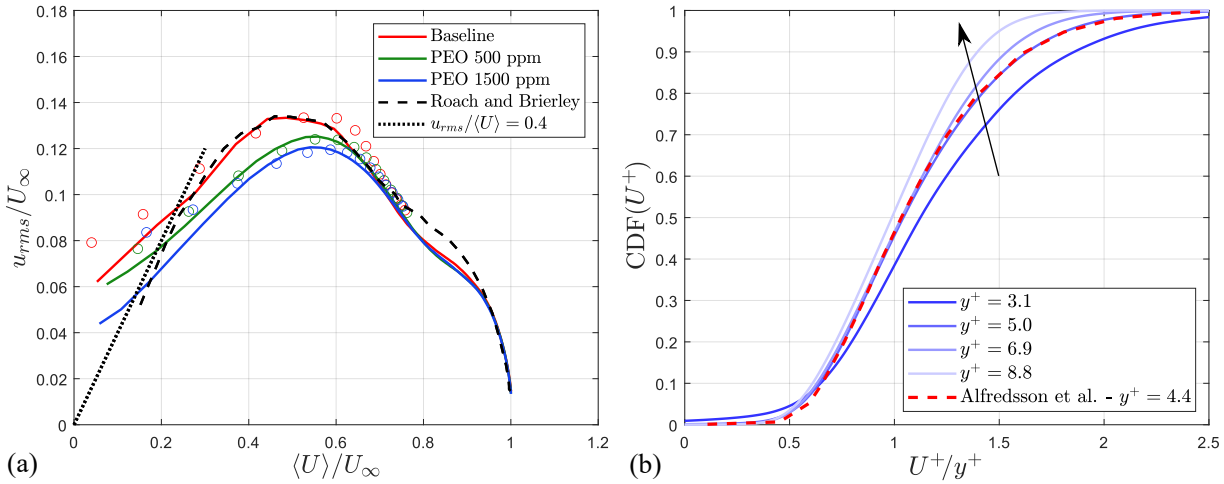

Figure 6.1: (a) Diagnostic plot showing the rms of streamwise velocity fluctuations (u_{rms}) vs. mean streamwise advection velocity ($\langle U \rangle$). Solid lines show planar PIV data and ∘ shows tomographic (tomo) PIV data. Dashed line shows data from the T3A case [78] at fully turbulent stage ($Re_\tau = 300$). Dotted line indicates the expected linear trends with a slope of 0.4 suggested by Alfredsson *et al.* [269]. (b) Cumulative distribution functions (CDF) of u^+ near the wall within $3 < y^+ < 9$ for baseline case using planar PIV. Dashed red line indicates the self-similar result obtained by Alfredsson *et al.* [269] for $y^+ < 5$. Arrow shows the trend with increasing y^+.

the fluctuations in the wall-shear stress can be estimated by proxy of a streamwise velocity signal in the region $y^+ < 10$. A diagnostic plot has been proposed by Alfredsson and Örlü [268] which utilizes the near-wall relationship in Eq. 6.2 to identify the data points affected by the measurement errors in the viscous layer, causing the data to deviate from the linear relationship.

Following the procedure outlined by Alfredsson and Örlü [268], the data points prone to measurement errors close to the wall are identified using the diagnostic plot illustrated in Fig. 6.1(a) where both planar and tomographic PIV results are complemented with the linear relation in Eq. 6.2 ($u_{\text{rms}}/\langle U \rangle = 0.4$). The figure also includes the results of Roach and Brierley [78] at a comparable Reynolds number obtained using a hot wire for reference. Based on the velocity measurements, the location for estimating wall-shear stress fluctuations is selected as that where the turbulent intensity ($u_{\text{rms}}/\langle U \rangle$) is the closest to the expected estimate of 0.4. In cases where the expected value is found to lie between two consecutive data points near the wall ($y^+ < 7$), an average of the two signals at these data points is used. This procedure results in obtaining the surrogate u' signals at $y^+ = 5 - 6$ in the Newtonian cases and at $y^+ = 5 - 7$ in the drag reduced cases.

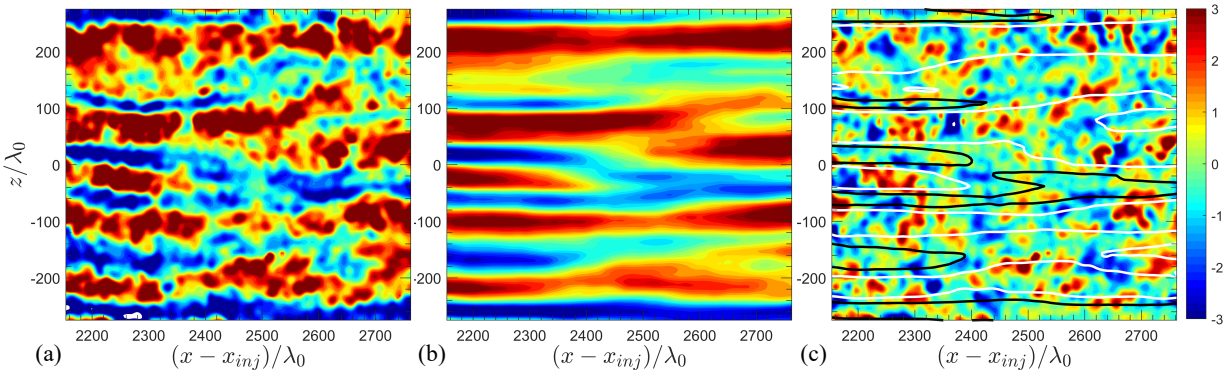

Figure 6.2: Scale decomposition technique applied to a tomo PIV snapshot showing streamwise velocity fluctuations corresponding to (a) unfiltered velocity field (u'/u_{τ_0}), (b) large-scales (u'_l/u_{τ_0}) , and (c) small-scales (u'_s/u_{τ_0}) on an $x - z$ plane at $y^+ \approx 5$. Black and white contours in (c) correspond to $u'_l/u_{\tau_0} = -1$ and $u'_l/u_{\tau_0} = 1$, respectively.

The reliability of the chosen surrogate signals of u' is evaluated by considering the corresponding cumulative distribution functions (CDF) of U^+ illustrated in Fig. 6.1(b). Using both DNS and experimental data, Alfredsson *et al.* [269] have noted that the CDFs of U^+ in the region $y^+ < 5$ are self-similar when normalized by their wall-normal distance. The results show that the CDF at $y^+ = 5.0$ closely agrees with the self-similar distribution. In contrast, progressive deviations are observed closer to the wall due to the higher measurement uncertainty of PIV. Similarly, the results at $y^+ > 5$ also progressively deviate from the self-similar fit, which is aligned with the observations of Alfredsson *et al.* [269]. The CDFs of U^+ in the case of polymer-injected flows (omitted for brevity) were verified to agree with the self-similar distribution for a larger wall-normal distance (i.e., for $4 < y^+ < 7$) which enables the usage of the corresponding u' signals as surrogates for wall-shear stress in these cases.

6.2.2 Scale decomposition technique

The main objective of the present study is to evaluate the effect of polymer injection on both large and small-scale fluctuations in the vicinity of extreme wall-shear stress events. This is achieved by the scale decomposition of the velocity fluctuations from both planar and tomographic PIV measurements. The scale decomposition technique used for this purpose follows the methodology of Gomit *et al.* [147] which involves the extraction of large-scale velocity field by employing a moving-average filter with a kernel of size δ in the streamwise direction. The computed large-scale velocity components (u'_l, v'_l, w'_l) are then subtracted from the original fluctuating velocity

field (u', v', w') to estimate the small-scale fluctuations (u'_s, v'_s, w'_s). Fig. 6.2 illustrates the result of this procedure on a tomo-PIV snapshot of the $x-z$ plane at $y^+ \approx 5$. The velocity statistics of the resulting large- and small-scale flow fields have been shown to be relatively robust to minor variations in the filter length around the chosen value of δ at high Reynolds numbers [147, 271]. Further, the effect of the near-wall modulation by very large scale motions occurring farther away from the wall, which could potentially affect the robustness of the filtering technique at the employed filter lengths, is not expected at the investigated Reynolds numbers [149, 150].

6.2.3 Conditional sampling technique

The decomposed velocity fields are used to examine the effect of polymer injection on the large- and small-scale velocity statistics as well as topologies of large-scale wall-shear stress events. In this regard, a large-scale decomposed signal $(u'_l|_w)$ corresponding to the surrogate of τ'_w obtained within $y^+ = 5-7$ as described in Sec. 6.2.1 is computed according to the decomposition procedure discussed in Sec. 6.2.2. Conditional samples corresponding to the lowest and the highest quartiles of $u'_l|_w$ are collected with a sampling volume of $300\lambda_0 \times 80\lambda_0 \times 150\lambda_0$ around the detected location $(\widetilde{x}_c, \widetilde{z}_c)$, where '$\sim$' denotes the conditionally averaged quantities. Each data set collected with this procedure contains more than 4000 samples which produce statistically converged conditional flow fields.

6.3 Results and discussion

6.3.1 Mean flow field

The time-averaged profiles of the streamwise velocity and Reynolds stresses for the Newtonian and the polymer injected cases have been previously discussed in detail in Ch. 5. This section discusses the characteristics of wall-shear stress in Newtonian and drag reduced flows.

The estimates of wall-shear stress fluctuations from planar and tomographic PIV are also evaluated by considering the probability density functions (PDFs) of u'/U_{rms} at the chosen wall-normal locations ($y^+ = 5-6$) illustrated in Fig. 6.3. As discussed in the previous section, u'/U_{rms} at these locations is a surrogate for $\tau'_w/\tau_{\text{rms}}$. The results are complemented with the PDFs of the wall-shear stress ($\tau'_w/\tau_{\text{rms}}$) from previous literature which show a collapse of the data from the present study for both planar and tomographic measurements. The peaks of the PDFs from the tomographic PIV data are slightly higher than those obtained using planar PIV, which is attributed to an underestimation of velocity fluctuations caused by the use of larger interrogation

Study	Method	Re_τ	Range of y^+ for obtaining τ_w	S_{τ_w}	K_{τ_w}
Present	Planar PIV	240	5.0	0.81	5.32
Present	Tomo PIV	240	5.7	0.87	4.91
Gubian *et al.*	Hot-wire anemometry based shear-stress sensor	232	0	1.13	4.93
Sheng *et al.*	Digital holographic microscopy	1400	0 - 4.5	0.9	5.2
Obi *et al.*	Laser gradient meter	410	0 - 2	0.95	4.56
Lenaers *et al.*	DNS	178.8	0	0.93	4.25
Schlatter and Örlü	DNS	410	0	0.97	4.70
Alfredsson *et al.*	Hot wire anemometry	200	5.0	1.10	4.80

Table 6.1: Skewness (S_{τ_w}) and flatness (K_{τ_w}) of τ_w. Data from the present study is reported for the baseline case utilizing the velocity measurements at the indicated wall-normal locations to estimate τ_w. Data from Refs. [267, 270, 272–275] are presented for comparison.

volumes in tomographic PIV. However, the spatial averaging is seen to have a minor effect on the skewness (S_{τ_w}) and flatness (K_{τ_w}) parameters for the PDFs presented in Table 6.1, which show a good agreement with those obtained by previous studies employing either direct wall-shear measurements or higher-resolution velocity measurements within the viscous sublayer. Further, the results highlight the applicability of Eq. 6.2 just outside the edge of the viscous sublayer and serve to further validate the use of streamwise velocity fluctuations at $y^+ = 5 - 6$ for estimating wall-shear stress fluctuations.

Despite the decrease in the streamwise fluctuations u' seen in Fig. 5.3(a), the effect of polymer injection on the PDFs of u'/u'_{rms} at the considered wall-normal locations is found to be negligible in Fig. 6.3. The decreased level of the streamwise fluctuation results in a decrease in u'_{rms} which causes the PDFs to overlap with their Newtonian counterpart, suggesting a self-similarity of the characteristic PDF of $\tau'_w/\tau_{w,\text{rms}}$ in the low drag reduction regime investigated in the present study.

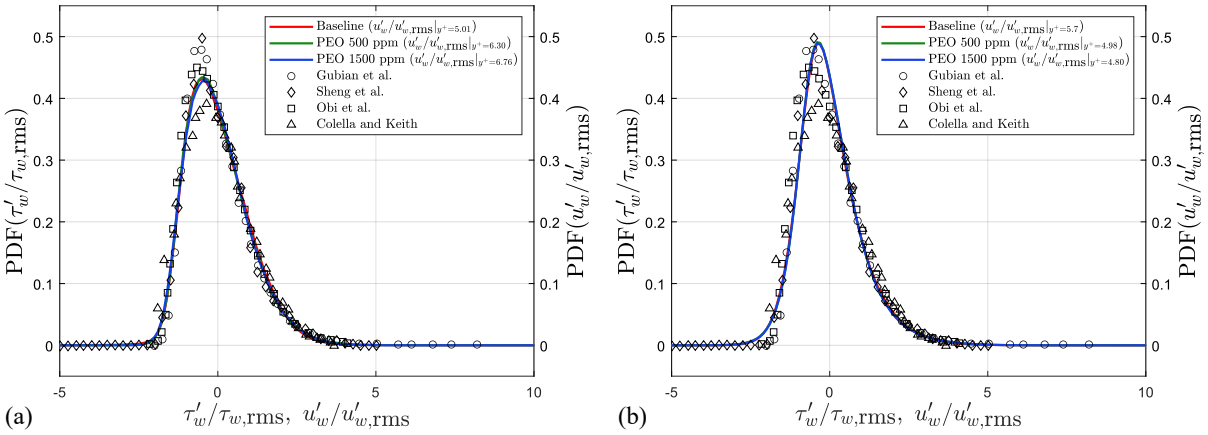

Figure 6.3: Probability density functions (PDFs) of u'/u'_{rms} at the chosen data points from (a) planar PIV, and (b) tomographic PIV. PDFs of wall-shear stress ($\tau'_w/\tau'_{w,\mathrm{rms}}$) from previous studies [270, 272, 273, 276] are included for comparison.

6.3.2 Polymer effect on large- and small-scale motions

The scale decomposition technique described in Sec. 6.2.2 is applied to planar PIV data to examine the effect of polymer injection on large- and small-scale motions and the associated wall-shear stress fluctuations. The effect of the polymer in decreasing the streamwise fluctuations close to the edge of the viscous sublayer, as noted in Sec. 5.3.1, is further examined by considering the rms of the scale decomposed u' signals at the near-wall locations in Fig. 6.4(a). The figure illustrates the aforementioned decrease in the rms of the unfiltered velocity fluctuations with increasing polymer concentration, whereas the unfiltered u'_{rms} in the water injection case is seen to be similar to the baseline flow considering the uncertainty based on 95% confidence intervals. The decreased u'_{rms} at the edge of the viscous sublayer is representative of the decreased wall-shear stress fluctuations in the drag reduced cases. It is observed that the rms of u' for the large scales ($u'_{l,\mathrm{rms}}$) is sightly larger than the rms of u' for the small scales ($u'_{s,\mathrm{rms}}$) in the Newtonian cases. In addition, the $u'_{l,\mathrm{rms}}$ (large-scales) in the polymer-injected flows remains nearly equal to the corresponding $u'_{l,\mathrm{rms}}$ in Newtonian flows. In contrast, a notable reduction is seen in the $u'_{s,\mathrm{rms}}$ of small scales with increasing polymer concentration.

The variation of the rms of the scale-decomposed u' with the filter length (l) as a fraction of the rms of the unfiltered u' in the respective cases is considered in Fig. 6.4(b). The figure shows similar differences in the trends of the large- and small-scale components of the u'_{rms} in both baseline and polymer injected cases as the filter length is increased within $0 < l^+ \leq \delta_0^+$ range.

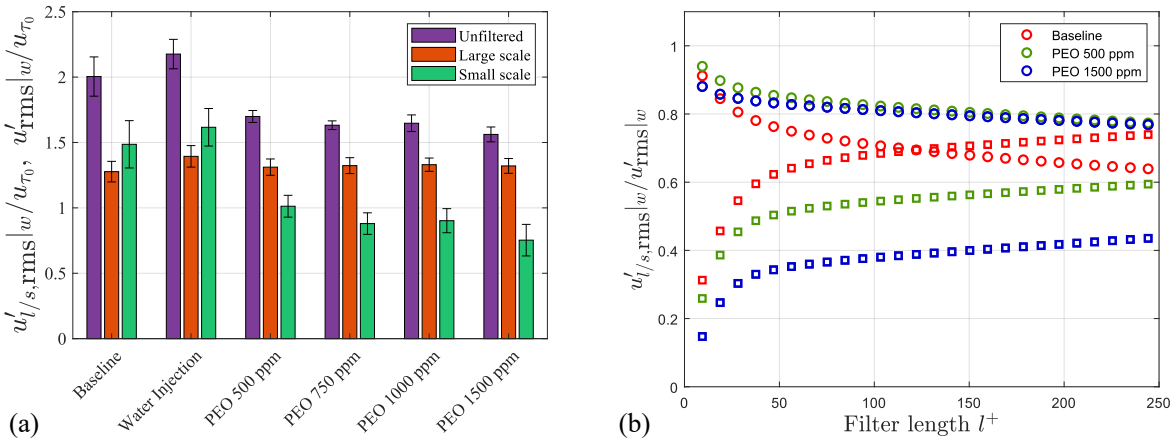

Figure 6.4: (a) Comparison of rms of unfiltered and scale-decomposed streamwise velocity for the data-points chosen for wall-shear stress estimation between different cases with a filter length $l^+ = \delta_0^+$. (b) Variation of rms of streamwise velocity in unfiltered ($u'_{\text{rms}}|_w$), large- and small-scale filtered data ($u'_{l/s,\text{rms}}|_w$) with increasing filter length (l^+). $\circ$ and $\square$ correspond to $u'_{l,\text{rms}}|_w$ and $u'_{s,\text{rms}}|_w$, respectively. The filter length is normalized by λ_0. Error bars in (a) show 95% confidence intervals. Results are obtained from planar PIV.

As expected, the contribution of the large-scale streamwise velocity ($u'_{l,\text{rms}}$) to the total rms (u'_{rms}) progressively decreases with a corresponding increase in the small-scale contribution ($u'_{s,\text{rms}}$) as the filter length is increased. In the baseline case, the contributions of the large and small scales to the total rms are nearly equal for a filter length of approximately half of the boundary layer thickness, and the small-scale streamwise fluctuations surpass those due to large scales for a larger filter length. This indicates that the streamwise velocity component in the Newtonian flow near the wall is largely dominated by relatively small-scale motions which are also likely to be incoherent in nature as seen in Fig. 6.2(c). In contrast, the small-scale contribution to the total rms of u' is significantly decreased in the polymer-injected cases throughout the range of filter lengths investigated ($l^+ \leq \delta_0^+$). Consistent with the results in Fig. 6.4(a), the large-scale rms contributions in the polymer-injected cases are similar for both polymer-injected cases for $l^+ > \delta_0^+/2$, and differ only marginally for smaller filter lengths. The decreased $u'_{s,\text{rms}}$ for the small scales is in accordance with the dampening of small-scale motions expected from the elastic mechanism of polymer drag reduction [62, 63]. It also suggests that the wall-shear stress events, which are significantly influenced by the incoherent small-scale motions within the viscous sublayer in the Newtonian cases, are more coherent in the drag reduced cases. Further, the large-scale motions ($> \delta_0/2$) in the near-wall region are rather insensitive to the polymer

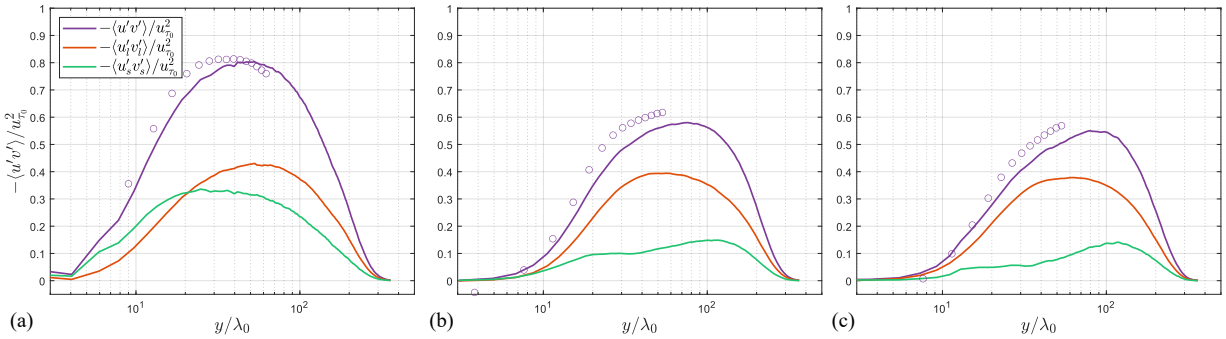

Figure 6.5: Time-averaged unfiltered ($-\langle u'v'\rangle/u_{\tau_0}^2$), and large- ($-\langle u_l'v_l'\rangle/u_{\tau_0}^2$) and small-scale ($-\langle u_s'v_s'\rangle/u_{\tau_0}^2$) filtered Reynolds shear stress corresponding to (a) baseline, (b) PEO 500 ppm, and (c) PEO 1500 ppm. Solid lines show planar PIV data and ∘ shows tomo PIV data. The profiles are averaged over the length of the field of view.

injection in the low drag reduction regime, which aligns with the results of de Angelis *et al.* [266].

To further examine the polymer effect on the large- and small-scale motions, the scale-decomposed Reynolds shear stresses are considered in Fig. 6.5. The presented scale-decomposed, time-averaged results for the large- ($-\langle u_l'v_l'\rangle/u_{\tau_0}^2$) and small-scales ($-\langle u_s'v_s'\rangle/u_{\tau_0}^2$) are the major contributors of the total RSS ($-\langle u'v'\rangle/u_{\tau_0}^2$) in Eq. 6.1 according to the findings of both Gomit *et al.* [147] and the present study. The profiles of unfiltered time-averaged RSS ($-\langle u'v'\rangle/u_{\tau_0}^2$) from planar PIV data in Figs. 6.5(a) - 6.5(c) show that RSS increases and peaks within the inner layer, subsequently decreasing in the outer layer. The peak magnitudes of $-\langle u'v'\rangle/u_{\tau_0}^2$ in the polymer-injected cases decrease with increasing polymer concentration, and the locations of the peaks are shifted farther away from the wall (Figs. 6.5(b) and 6.5(c)). Although the peaks are not fully captured in the present tomographic PIV results, the time-averaged results are in reasonable agreement with the planar PIV data in all the cases. In addition, the planar PIV results illustrate that the RSS remains nearly zero for an extended distance from the wall in the polymer-injected cases (up to $y^+ = 6 - 7$), indicating a negligible turbulent production in this region. This is one of the main reasons for the applicability of Eq. 6.2 over an extended wall normal distance in polymer-injected cases as seen earlier.

The scale-decomposed RSS profiles show similar characteristic trends but with lower peak magnitudes and different peak locations in the baseline flow (Fig. 6.5(a)). The time-averaged large-scale RSS ($-\langle u_l'v_l'\rangle/u_{\tau_0}^2$) peaks slightly farther away from the wall ($y/\lambda_0 \approx 55$) in comparison to the total RSS. On the other hand, the profile of the small-scale RSS ($-\langle u_s'v_s'\rangle/u_{\tau_0}^2$) shows a peak within the buffer layer ($y\lambda_0 \approx 25$) at a lower magnitude than that of the large-scale RSS peak. However, it can be seen that the small-scale contribution exceeds that of the large scales at

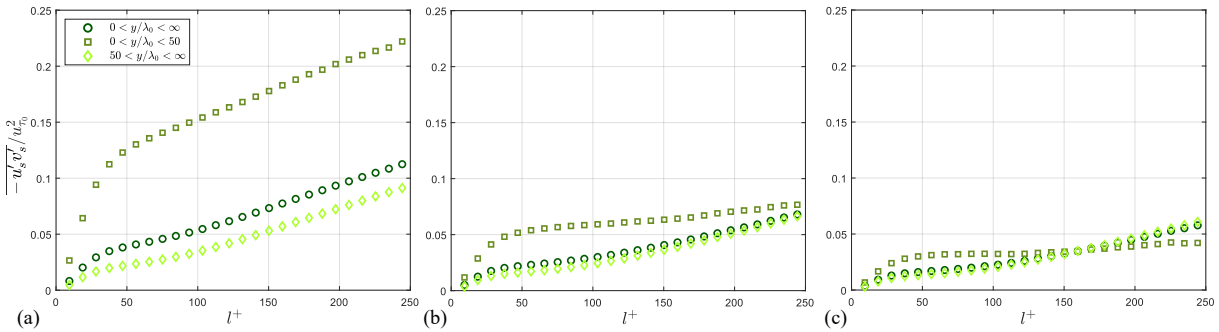

Figure 6.6: Spatially averaged small-scale contribution of the Reynolds shear stress ($\overline{-u_s' v_s'}/u_{\tau_0}^2$) within inner layer ($0 < y^+ \leq 50$), outer layer ($50 < y^+ < \infty$), and the total boundary layer ($0 < y^+ < \infty$) for (a) baseline, (b) PEO 500 ppm, and (c) PEO 1500 ppm with increasing filter length (l). The filter length is normalized by λ_0, and varied in the range $0 < l^+ < \delta_0^+$. Results are obtained using planar PIV data.

$y\lambda_0 < 20$ showing the significance of the small-scale motions in the buffer layer in a Newtonian flow.

With the addition of the polymer, a notable reduction is seen in the small-scale RSS throughout the boundary layer thickness, but particularly within the inner layer (Figs. 6.5(b) and 6.5(c)). The near-wall peak in the small-scale RSS profile of the Newtonian case vanishes in the polymer-injected cases, leading to a substantial decrease in the magnitudes ($-\langle u_s' v_s' \rangle / u_{\tau_0}^2 \leq 0.1$) in the buffer and lower-log layers. In contrast, the profiles of the large-scale RSS are not affected as substantially by polymer injection, with peak magnitudes being reduced only marginally compared to the baseline Newtonian flow. While the present results support that the small-scale motions are dampened by polymers [53], they also highlight that the large-scale motions, which primarily dominate in the log and outer layers, are not influenced significantly.

Noting the pronounced effect of polymers on the small-scale motions within the inner layer ($0 < y^+ \leq 50$), Fig. 6.6 considers the variation of the spatial mean of small-scale RSS over the inner ($0 < y^+ \leq 50$), outer ($50 < y^+ < \infty$), and total ($0 < y^+ < \infty$) boundary layer with increasing spatial filter length (l^+). The results show that the spatial means in the outer layer and the total boundary layer increase with increasing l^+ in all the cases as expected due to the addition of small-scale RSS. However, a plateau seen within $50 < l^+ < 150$ in the variation of $-\overline{u_s' v_s'}/u_{\tau_0}^2$ in the inner layer (squares) for the polymer-injected cases suggests a negligible contribution to RSS within this range of scales.

To further explore the damping of small-scale RSS, normalization of the spatially averaged small-scale RSS within the inner layer by the respective values at $l^+ = \delta_0^+$ is considered in

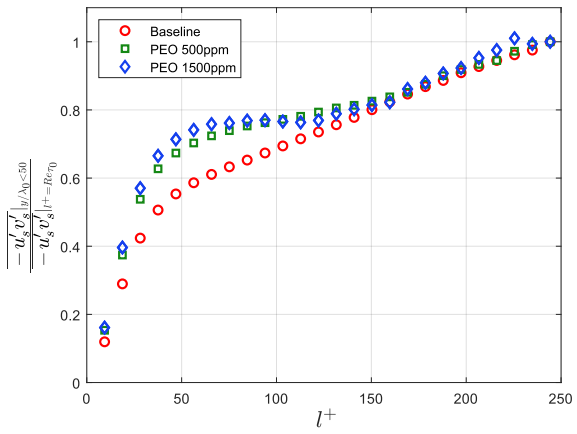

Figure 6.7: Spatially averaged small-scale contribution of the Reynolds shear stress ($\overline{-u_s'v_s'}$) within inner layer ($0 < y^+ < 50$) normalized by its value at $l^+ = \delta_0^+$. Results are obtained using planar PIV data.

Fig. 6.7. The results indicate a collapse of the data in the range $150 < l^+ < \delta_0^+$ on a linear trend which is attributed to a self-similar increase in the small-scale contribution within the inner layer despite the dampening of the small-scale RSS throughout the range of l^+ seen in Fig. 6.6. The self-similar increase in the RSS at the higher end of the range of investigated l^+ is further attributed to the increasing coherence of the motions and the similarity of the coherent structures associated with the buffer layer. On the other hand, the normalized data for the polymer-injected cases elucidate the aforementioned plateau in the range $50 < l^+ < 150$, while highlighting that the critical length scale below which the small-scale RSS contribution is subdued increases with increasing polymer concentration. This critical length scale is observed to be approximately $100\lambda_0$ and $120\lambda_0$ for the PEO 500 ppm and 1500 ppm, respectively.

6.3.3 Association of large-scale wall-shear stress events with near-wall flow events

While the foregoing discussion suggests that the effect of the polymer is mainly observed on the incoherent small-scale motions, the average scale decomposed results do not provide information with regards to possible phase differences between RSS and wall-shear stress events in polymer-injected flows expected from the results of Tamano *et al.* [250]. These phase differences, if present, are expected to occur in the large-scale motions in the near-wall region based on the findings of Gomit *et al.* [147] in Newtonian flows. Furthermore, considering that the near-wall

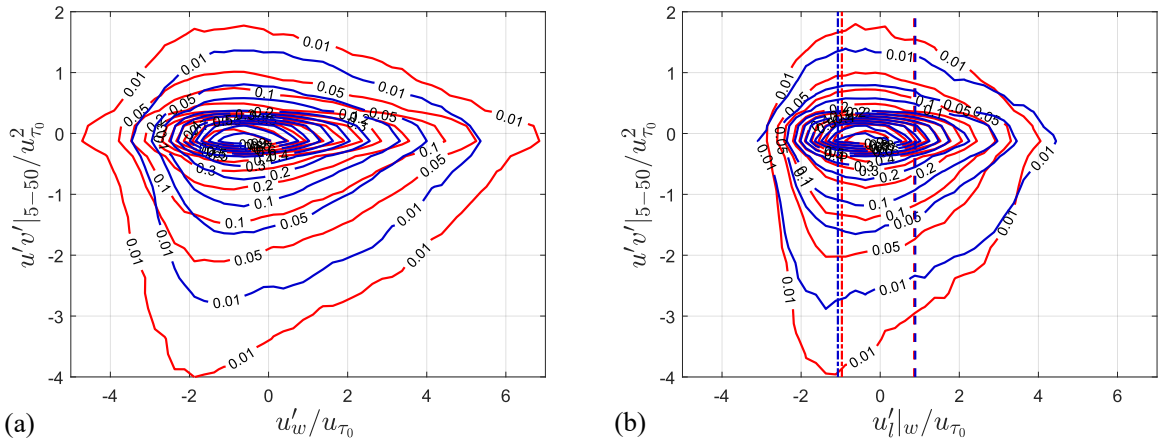

Figure 6.8: Joint probability distribution functions (JPDFs) of the spatially averaged Reynolds shear stress $(u'v'|_{5-50}/u_{\tau_0}^2)$ within $5 \leq y^+ \leq 50$ and (a) streamwise velocity fluctuations (u'_w/u_{τ_0}), and (b) large-scale streamwise velocity fluctuations $(u'_l|_w/u_{\tau_0})$ at $y^+ \approx 5$ obtained from tomo PIV. Red and blue contours show the results for the baseline and PEO 1500 ppm cases, respectively. Dash-dotted and dashed lines in (b) indicate the thresholds for the lowest and the highest quartiles of $u'_l|_w/u_{\tau_0}$.

small-scale activity is strongly correlated with the large-scale motions in both inner and outer layers [145,277–279], it is of interest to investigate the near-wall large-scale topology associated with the extreme wall-shear stress events. To this end, the tomographic PIV results are utilised to explore the connection between the high- and low-wall-shear stress events and the average Reynolds shear stress within the buffer and lower-log region $(u'v'|_{5-50})$ by considering their joint probability distribution functions (JPDFs) in Fig. 6.8, with the spatial averaging being performed in the range $5 \leq y^+ \leq 50$. The spatially averaged RSS accounts for all the coherent structures passing in the buffer and lower-log regions. The JPDFs in Fig. 6.8(a) show that large magnitudes of average RSS $(-u'v'|_{5-50})$, which are greater than the peak time-averaged RSS (Fig. 6.5), are produced during both low and high wall-shear stress events (*i.e.,* u'_w extremes), likely attributable to the ejections and sweeps, respectively. The figure also suggests that the magnitudes of the averaged RSS are close to zero at the extreme values of u'_w, suggesting a possible phase delay between the extreme skin-friction events and the near-wall RSS producing coherent structures. These results are found to be similar in the polymer-injected case but with lowered magnitudes of both u'_w and the averaged RSS. On the other hand, the JPDFs of the averaged RSS and the large-scale decomposed streamwise velocity fluctuations $u'_l|_w$ considered in Fig. 6.8(b) show that the horizontal extents of the distributions are decreased notably in comparison to the distributions corresponding to u'_w considered in Fig. 6.8(a), confirming that the extreme fluctuations in u'_w are

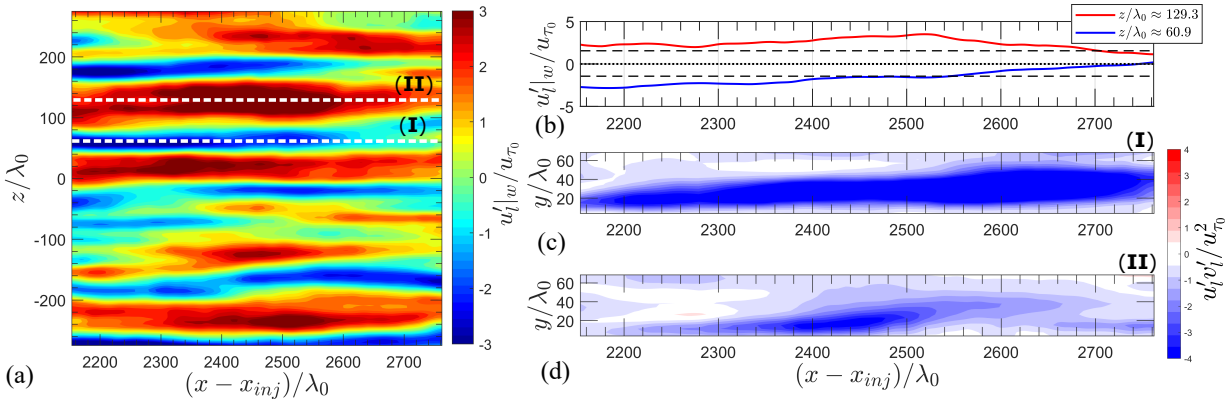

Figure 6.9: Representative instantaneous snapshot from Tomo PIV data for the baseline case showing (a) large-scale streamwise velocity fluctuations ($u_l'|_w/u_{\tau_0}$) at $y/\lambda_0 \approx 5$, (b) variation of ($u_l'|_w/u_{\tau_0}$) in the streamwise direction at $z/\lambda_0 \approx 60.9$ and 129.3, (c, d) contours of ($u_l'v_l'/u_{\tau_0}^2$) in the slices considered in (b). Slices considered in (b) are demarcated by (I) and (II), respectively, in (a). Dashed lines in (b) indicate values corresponding to top and bottom 10% of $u_l'|_w/u_{\tau_0}$.

produced due to the small-scale motions. It is further noted that the horizontal extents of the distributions for $u_l'|_w$ (Fig. 6.8(b)) in both baseline and polymer-injected flows are similar, as expected from Fig. 6.4(a). As observed in Fig. 6.8(a), the average RSS at the extreme values of $u_l'|_w$ are close to zero, however, the proportion of the population within the extreme large-scale wall-shear events with such low RSS magnitudes is marginal. The distributions also indicate that the largest magnitudes of average RSS ($-u'v'|_{5-50}$) fall within the lowest quartile of $u_l'|_w$ as indicated by the thresholds (dash-dotted lines) in both baseline and polymer cases, while the largest magnitudes of $-u'v'|_{5-50}$ also exceed the peak time-averaged RSS in the highest quartile of $u_l'|_w$.

To further explore the relation between the large-scale decomposed surrogate $u_l'|_w$ and the average RSS in the buffer layer, an instantaneous snapshot of the large-scale decomposed streamwise velocity is presented in Fig. 6.9(a), along with the large-scale component of the RSS ($u_l'v_l'/u_{\tau_0}^2$) corresponding to two distinct spanwise locations (z/λ_0) in Figs. 6.9(c) and 6.9(d.) A one-dimensional representation of the streamwise variation of $u_l'|_w$ is considered in Fig. 6.9(b) where the indicated z/λ_0 locations coincide with a large-scale low- and high-wall-shear stress event as seen in Fig. 6.9(a). Accordingly, the $u_l'|_w$ is seen to remain consistently high and low in the respective slices, indicating the occurrence of a large-scale wall-shear stress event. The corresponding $x - y$ slices showing the instantaneous large-scale RSS ($u_l'v_l'\rangle/u_{\tau_0}^2$) in Figs. 6.9(c) and 6.9(d) show large structures with RSS magnitudes significantly larger than the peak time-averaged RSS (see Fig. 6.5) present in the vicinity of the wall-shear stress event. Moreover, the

core of the large-scale RSS structure is seen to occur downstream (*i.e.,* $2400 < (x - x_{\text{inj}})/\lambda_0 < 2700$) of the low-wall-shear stress event which peaks in the range $2150 < (x - x_{\text{inj}})/\lambda_0 < 2400$. At the same time, the core of the large-scale RSS occurs slightly upstream (*i.e.,* $2400 < (x - x_{\text{inj}})/\lambda_0 < 2500$) of the high-wall-shear stress event which peaks at $(x - x_{\text{inj}})/\lambda_0 \approx 2530$). This is aligned with the distributions in Fig. 6.8 which show that the peak RSS magnitudes are not obtained in the extreme wall-shear stress events, suggesting the presence of a phase shift between the wall-shear stress and the RSS in the buffer layer.

It is also noted that, while the cores of the instantaneous large scale RSS structures appear to be slightly displaced in the streamwise direction with respect to the peak wall-shear stress events, the RSS magnitudes directly above the extreme wall-shear stress event are still larger than the peak time-averaged RSS magnitudes, in accordance with the observations made in Fig. 6.8(b). Such large-scale RSS signatures are attributed to the large-scale ejections and sweeps occurring in the near-wall region, which are associated with the low- and high-speed streaks, respectively [146, 243].

The association between the RSS structures and the extreme large-scale wall-shear stress events is further analyzed by considering conditionally averaged velocity fields using the methodology described in Sec. 6.2.3 corresponding to the lowest (top row) and the highest (bottom row) quartile of $u_l'|_w$ in Fig. 6.10. Figs. 6.10(a) and 6.10(d) show extreme large-scale low and high wall-shear stress events, respectively, in the baseline flow, where the extreme event at the wall is seen to be confined within the respective low- and high-speed streaks. Notable large-scale counter-rotating vortices (in gray), identified using the Q-criterion [252], are present adjacent to the streaks in both low- and high-wall-shear stress events. The sense of rotation of the counter-rotating vortices changes inducing an upwash in the former and a downwash in the latter event in the centre of the domain. The overall topology for low and high wall-shear stress events matches those of ejections (Q2) and sweeps (Q4), respectively [121, 133, 243]. Accordingly, the $\widetilde{x} - \widetilde{y}$ slice at $\widetilde{z}/\lambda_0 = 0$ show large-scale RSS structures with core magnitudes exceeding the peak time-averaged RSS. The cores of the RSS structures in the high wall-shear stress event form closer to the wall in comparison to those in the low wall-shear stress event, as expected from the relative wall-normal motion in each of these events. The spanwise topology of the RSS structure is illustrated on the $\widetilde{y} - \widetilde{z}$ slice at $\widetilde{x}/\lambda_0 = 0$, which shows a low RSS signature ($-\widetilde{u'^+v'^+} < 0.5$) within the viscous sublayer ($\widetilde{y}/\lambda_0 < 10$) in both low and high wall-shear stress conditional structures. In the low wall-shear stress structure, the low RSS regions are also seen to be elevated under the cores of the vortices, similar to the previous findings by Shah *et al.* [243].

The conditional fields in the polymer-injected cases present a similar topology to their Newtonian counterparts, with Figs. 6.10(b-c) and Figs. 6.10(e-f) corresponding to the low- and high wall-shear stress events, respectively. The figures illustrate a significant dampening of the vor-

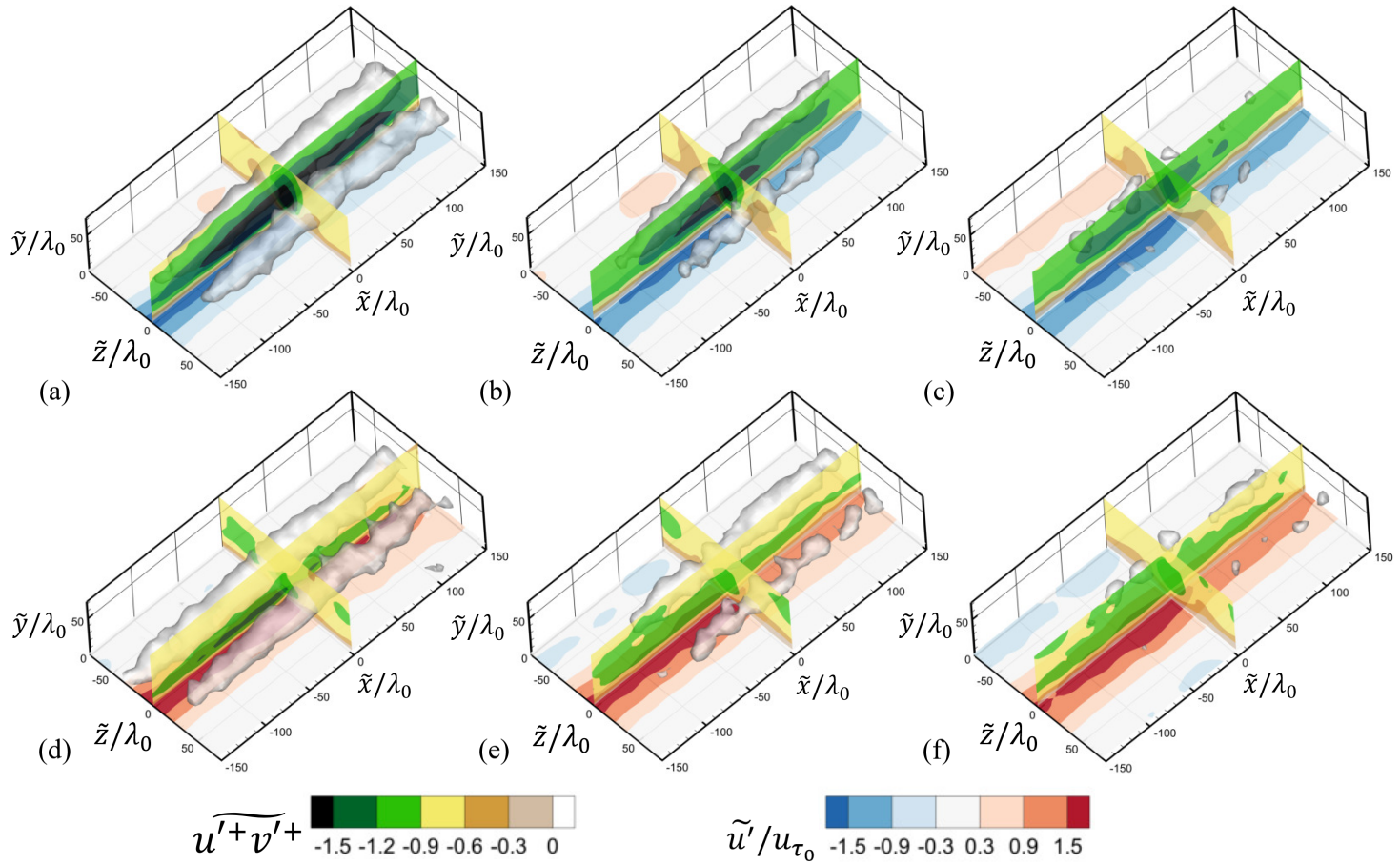

Figure 6.10: Conditionally averaged coherent structures corresponding to the lowest (a-c) and highest (d-f) quartile of $u_l'|_w$. Sub-figures in left column (a, d) baseline, middle column (b, e) PEO 500 ppm, and right column (c, f) PEO 1500 ppm. The quasi-streamwise vortices in gray are identified using Q-criterion ($Q = 10$). $\widetilde{y}-\widetilde{z}$ slice at $\widetilde{x}/\lambda_0 \approx 0$ and $\widetilde{x}-\widetilde{y}$ slice at $\widetilde{z}/\lambda_0 \approx 0$ show contours of conditionally averaged Reynolds shear stress ($\widetilde{u'^+v'^+}$). $\widetilde{x}-\widetilde{z}$ slice at $\widetilde{y}/\lambda_0 \approx 5$ shows the contours of conditionally averaged streamwise velocity fluctuations.

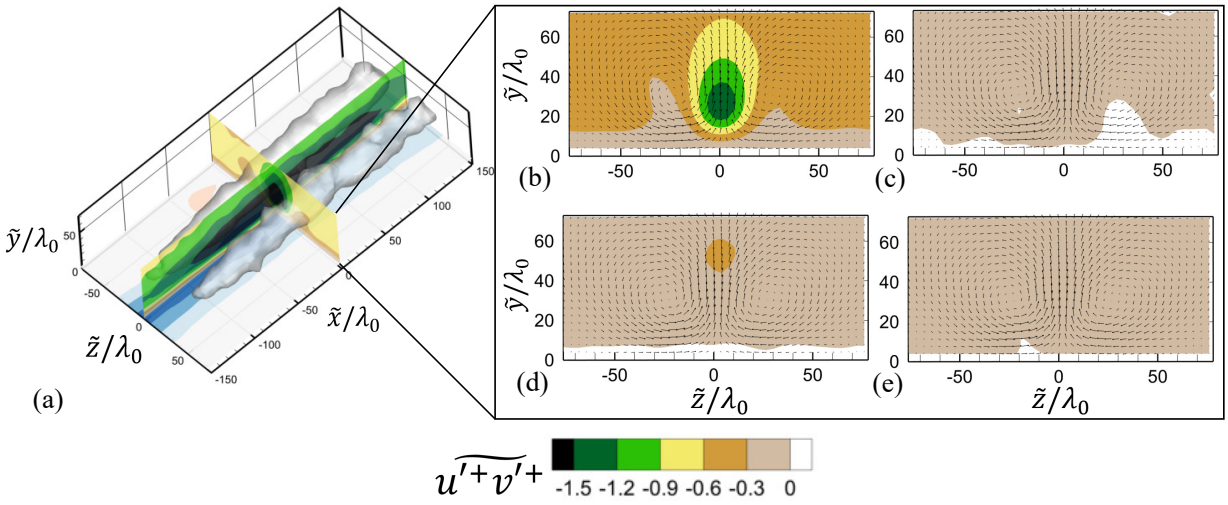

Figure 6.11: Scale decomposition of the conditionally averaged Reynolds shear stress ($-\widetilde{u'v'}/u_{\tau_0}^2$) within $0 < y^+ < 70$. (a) shows the conditionally averaged coherent structure corresponding to the lowest quartile of $u_l'|_w$. Panels b - e show components of the conditional RSS on the $\widetilde{y} - \widetilde{z}$ plane at $\widetilde{x} = 0$ where (b) $-\widetilde{u_l'v_l'}/u_{\tau_0}^2$, (c) $-\widetilde{u_l'v_s'}/u_{\tau_0}^2$, (d) $-\widetilde{u_s'v_s'}/u_{\tau_0}^2$, and (e) $-\widetilde{u_s'v_l'}/u_{\tau_0}^2$.

tices and a reduction in the magnitudes of RSS within the core regions for the polymer-injected cases. The sizes of the vortices decrease with increasing polymer concentration, which is in agreement with the production of the counter-torques within the vortices noted in numerical simulations [57, 183] following the elastic theory [53, 54]. Despite the notable reduction in the RSS magnitudes above the wall-shear stress event, the RSS magnitudes still surpass the time-averaged peak RSS in the respective cases.

Given the strong association of the large-scale wall-shear stress events with the turbulence producing coherent quadrant motions, albeit with the noted phase shift in Fig. 6.8, their connection with the RSS contributed by various length scales is further explored by considering the scale-decomposed fields of RSS in Fig. 6.11. The scale decomposition of RSS follows the methodology used by Gomit *et al.* [147] (Eq. 6.1) as outlined in Sec. 6.2.2. Representative fields of the individual terms in the total RSS in Eq. 6.1 are illustrated in Figs. 6.11(b-e) corresponding to the baseline conditional structure shown in Fig. 6.11(a). It is observed from Figs. 6.11(b-e) that the large-scale motions ($-\widetilde{u_l'v_l'}/u_{\tau_0}^2$) are the dominant contributors of the total RSS, and are mainly responsible for defining the topology of the RSS structure. In comparison, the RSS contributions of the small-scale motions ($-\widetilde{u_s'v_s'}/u_{\tau_0}^2$) and the cross-terms ($-\widetilde{u_l'v_s'}/u_{\tau_0}^2$, $-\widetilde{u_s'v_l'}/u_{\tau_0}^2$) are negligible, even within the core of the RSS structure. Considering this result in combina-

tion with the previous findings of the small-scale activity being correlated with the large-scale motion in the near-wall region (*e.g.,* Mathis *et al.* [145] and Schlatter and Örlü [278]), also apparent from the tomo PIV results in Fig.6.2(c), the large-scale component of the RSS is used for establishing a statistical correlation with the wall-shear stress signatures in both Newtonian and polymer-injected cases. Additionally, a significant dampening of the small-scale activity and a relatively stable character of the large-scale RSS component (Fig. 6.5) with polymer injection further justifies this consideration.

Three-dimensional two-point correlations between the conditionally sampled surrogate signal of the wall-shear stress ($\widetilde{u'}$) and the large-scale component of RSS ($-\widetilde{u'_l v'_l}$) are performed, and their two-dimensional $\widetilde{x}-\widetilde{y}$ slices at $\widetilde{z}/\lambda_0 = 0$ are presented in Fig. 6.12. Similar to the conditionally averaged results in Figs. 6.10 and 6.11, the conditional samples considered for these correlations correspond to the highest and the lowest quartile of $u'_l|_w$, leading to a segregation of the correlation structures corresponding to the $\widetilde{u'} > 0$ (high-speed streak) and $\widetilde{u'} < 0$ (low-speed streak), respectively. A correlation coefficient which varies between -1 and 1 is defined as

$$C_{\widetilde{u'},-\widetilde{u'_l v'_l}} = \frac{\widetilde{\widetilde{u'}}(\widetilde{x},\widetilde{y}=y_w,\widetilde{z}) \cdot (-\widetilde{\widetilde{u'_l v'_l}}(\widetilde{x'},\widetilde{y'},\widetilde{z'}))}{\sigma_{\widetilde{\widetilde{u'}}(\widetilde{x},\widetilde{y}=y_w,\widetilde{z})} \cdot \sigma_{-\widetilde{\widetilde{u'_l v'_l}}(\widetilde{x'},\widetilde{y'},\widetilde{z'})}}, \tag{6.3}$$

where $\widetilde{\widetilde{(\cdot)}}$ denotes the fluctuation of the conditional signal with respect to the conditional average, $(\widetilde{x},\widetilde{y}=y_w,\widetilde{z})$ are the coordinates of the reference location with y_w being the wall-normal location where the surrogate signal $u'_l|_w$ is considered, $(\widetilde{x'},\widetilde{y'},\widetilde{z'})$ are the coordinates where the large-scale RSS signal is considered, and σ denotes the standard deviation. This form of the correlation coefficient has been employed by a number of previous studies to investigate the correlations between various quantities in turbulent flows (*e.g.,* [280–283]).

The correlation structures corresponding to the lowest quartile of $u'_l|_w$ presented in the left column of Fig. 6.12 show negative values of the correlation coefficient ($C_{\widetilde{u'},-\widetilde{u'_l v'_l}}$), which suggests that the magnitude of the fluctuation of the large-scale RSS signal ($-\widetilde{\widetilde{u'_l v'_l}}$) is positive in an extreme low wall-shear stress event (*i.e.,* $\widetilde{\widetilde{u'}} < 0$). On the other hand, the correlation coefficients for the highest quartile of $u'_l|_w$ (right column) show positive values, which also suggest an increase in the large-scale RSS close to the wall with respect to the corresponding conditional average. Further, the results indicate that, while the correlation peak lies within the buffer layer, the correlated/anticorrelated structures are confined within the relative proximity of the wall. This is aligned with the presence of RSS producing ejection and sweep motions during the extreme wall-shear stress events observed in Fig. 6.10.

The effect of polymer injection on the correlation between the large-scale RSS component

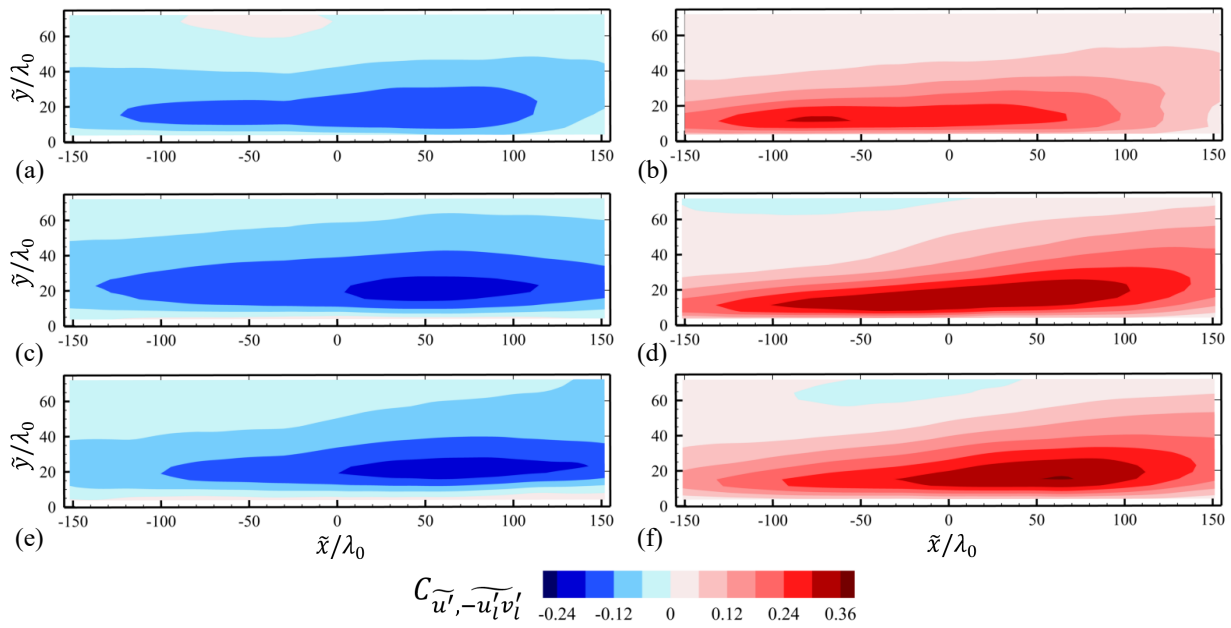

Figure 6.12: Slices of the three-dimensional correlation of conditionally sampled surrogate signal of the wall-shear stress (*i.e.,* $\widetilde{u'}$ at $y^+ < 6$) and large-scale filtered Reynolds shear stress $-\widetilde{u_l'v_l'}$. Left and right columns correspond to the lowest and highest quartile of $u_l'|_w$, respectively. Rows show different cases corresponding to (a, b) baseline, (c, d) PEO 500 ppm, and (e, f) PEO 1500 ppm.

and the wall-shear stress is evaluated by comparing the correlation coefficients ($C_{\widetilde{u'},-\widetilde{u_l'v_l'}}$) between the baseline and the drag-reduced cases in Fig. 6.12. In both types of wall-shear stress events, the strength of the correlation coefficient is seen to increase with an increase in the size of the core of the correlated/anticorrelated structures with increasing polymer concentration. Furthermore, a notable streamwise shift in the location of the correlation peaks is seen with increasing polymer concentration in both types of correlation structures. The peak correlation magnitude in the low wall-shear stress event (Fig. 6.12, left column), seen to occur at $\widetilde{x}/\lambda_0 \approx 26$ in the baseline case, is displaced by approximately $27\lambda_0$ and $35\lambda_0$ for the PEO 500 ppm and PEO 1500 ppm cases, respectively. More dramatic changes are elicited in the high wall-shear stress event (Fig. 6.12, right column) where the correlation structure presents a forward-leaning shape with the peak correlation coefficient located upstream of the reference location in the baseline case (*i.e.,* at $\widetilde{x}/\lambda_0 \approx -84$). A higher magnitude of the correlation coefficient upstream of the reference location is expected in this case as seen from the instantaneous realization presented in Fig. 6.9(d). With the addition of the polymer, the correlation structures become more well-

defined in shape and the correlation peaks are observed to move downstream of the reference location with their positions at $\widetilde{x}/\lambda_0 \approx 11$ and $\widetilde{x}/\lambda_0 \approx 65$ for the PEO 500 ppm and PEO 1500 ppm cases, respectively. The results for the correlation structures support the presence of a phase delay in the response of the near-wall RSS to drag-reduction observed by Tamano *et al.* [250] in a drag-reduced boundary layer.

6.4 Concluding remarks

The present study examines three-dimensional flow fields in the vicinity of high and low wall-shear stress events in zero-pressure-gradient Newtonian and drag reduced turbulent boundary layers at relatively low Reynolds numbers. Planar and tomographic PIV measurements conducted in the near-wall region of the boundary layers are utilized to estimate the fluctuating wall-shear stress based on the streamwise velocity fluctuations in the viscous sublayer [268], and allow for an evaluation of the polymer effect on the extreme skin-friction events. In addition, a binary scale decomposition technique is employed to investigate the effect of the polymer on various turbulent length scales and the corresponding Reynolds shear stress contributions.

The wall-shear stress estimation methodology applied to Newtonian and drag reduced boundary layer PIV measurements reveals a self-similarity in the PDFs of u'/u'_{rms} in the viscous sublayer, which is attributed to the decreased u'_{rms} in the polymer-injected cases. Scale decomposition of the streamwise velocity signal (u'), which is used for the estimation of wall-shear stress fluctuations, highlights that the decrease in u'_{rms} is attributed primarily to the dampening of the small-scale fluctuations in u', whereas the effect on large-scale fluctuations ($> \delta_0/2$) is relatively minor.

The time-averaged profiles of the scale-decomposed RSS show similar results, with the polymer-effect being primarily observed in the damping of the small-scale RSS contribution within the inner layer ($y^+ < 50$) for the investigated flow. Further examination of the small-scale RSS component within the inner layer with a variation in the length of the spatial filter elucidates that the length scales in the range $50\lambda_0$ to $120\lambda_0$ contribute negligibly to the average RSS in polymer-injected flows. While this damping of the RSS contribution is an indication of the critical length scales in polymer-injected flows below which the small-scale RSS contribution is subdued, the results also suggest a self-similarity in the variation of the small-scale RSS within the inner layer for length scales greater than $150\lambda_0$, which is attributed to the similarity of the coherent structures associated with these larger scales.

The JPDFs of the average RSS within the inner layer and the surrogate u' indicate that both low and high wall-shear stress events produce large magnitudes of RSS which are linked to the

passage of ejections and sweeps within these respective events. However, most of the extreme u' events are associated with the small-scale motions that occur within these relatively large-scale coherent structures. Further, the observed near-zero magnitudes of RSS at the extreme $u_l'|_w$ point to a phase delay between the large-scale wall-shear stress events and the cores of the RSS structures in the buffer layer.

Conditionally sampled large-scale skin friction events from tomographic PIV data show that relatively large structures ($\mathcal{O}(\delta)$) of RSS occur in the near-vicinity of these extreme events, and are attributed to the ejection and sweep motions. Increasing polymer concentration leads to a reduction in the magnitude of the RSS, the size of the RSS structures, and the strength of the quasi-streamwise vortices which occur alongside the conditionally sampled wall-shear stress event. Furthermore, the scale decomposition of conditionally sampled RSS shows a negligible contribution of the small-scale dependent components of the RSS, and the majority of the topology and the corresponding energy of the RSS structure is recovered from the large-scale RSS component. In light of this result, the correlations between the conditionally sampled large-scale component of the RSS and wall-shear stress fluctuations provide a proxy for the association between the RSS in the inner layer and the wall-shear stress. Besides confirming the increased magnitude of the large-scale RSS within the inner layer in comparison to the conditional averaged magnitudes of RSS in the vicinity of both low and high wall-shear stress events, the correlation results indicate that the correlated/anticorrelated structures are seen to be strengthened and progressively shifted downstream from the reference points with increasing polymer concentration. This confirms the presence of a phase delay between the occurrences of the large-scale wall-shear stress events and the large-scale coherent structures in the inner layer. Further, the phase delay of the high-C_f events with respect to the high-RSS producing coherent structures is larger in comparison to the low-C_f events.

Overall, the results show that, while the time-averaged statistics of large-scale components of the wall-shear stress and RSS remain equivalent between Newtonian and drag reduced cases, dynamic changes in the large-scale RSS within the inner layer are present near the extreme skin-friction events. While this has important implications for the understanding of the polymer effect derived based on the characteristics of the intermittent low- and high-drag regions, the present findings provide evidence for a relatively large-scale viscoelastic phenomenon at play in the vicinity of both types of extreme wall-shear stress events.

Chapter 7

Effect of polymer on bypass-transitioning boundary layers

An experimental investigation is conducted to evaluate the effect of polymer injection on the development of a zero-pressure-gradient bypass transitioning boundary layer on a flat plate. Planar PIV and PLIF measurements conducted at multiple streamwise stations allow for a characterization of the development of the bypass transition process in both Newtonian and polymer-injected flow, which is induced by a two-dimensional trip wire. Two different trip placements with respect to the injection slot are considered to study the effect of polymer injection within the wake of the trip wire and within the laminar boundary layer upstream of the trip. The transition process is initiated in a separated shear layer downstream of the trip wire, where a rapid amplification of the velocity perturbations via an inflectional Kelvin-Helmholtz (K-H) instability leads to vortex shedding and subsequent breakdown to turbulence. A similar transition process is observed with polymer injection, but an earlier amplification and more rapid initial growth of perturbations is observed. This is attributed to elasto-inertial instabilities, which also modify salient characteristics of the primary disturbances and lead to earlier breakdown to turbulence. Nonetheless, an onset of polymer effect is seen in the late transition stages and leads to significant levels of drag reduction in the developing turbulent boundary layer.

Parts of this chapter have been adapted from Y. Shah and S. Yarusevych, "Effect of polymer injection on the development of a bypass transitioning boundary layer [**In Review**]."

7.1 Introduction

Chapters 4 - 6 have highlighted the polymer's ability to suppress turbulence within the boundary layer resulting in decrease in skin friction as also shown by a number of previous investigations [65, 152, 154, 265]. Further, recent studies, including those reported in this thesis, have exploited both advanced measurement techniques like particle image velocimetry (PIV) [50, 51, 60] and computational simulations [54–57] to highlight the interactions of polymer and turbulent motions. In contrast, very few studies have considered the effect of polymer additives on the laminar-to-turbulent transition, where potential benefits could be derived by suppressing turbulent motions, which are discussed in detail in Sec. 2.1.2, and thereby delaying transition.

The effect of polymer injection on laminar-to-turbulent transition has been explored in pipe flows [204, 285–289] where the later stages of transition involve intermittent formation of turbulent puffs and slugs following the amplification of the local perturbations [290–292]. These investigations produced inconsistent results, potentially due to significant differences in experimental setups. In most investigations, no distinct effect of polymers on the transition process was observed. Draad *et al.* [204] noted that this can be potentially attributed to common experimental setup issues, namely, high inlet disturbances from the pumps and the use of relatively large-diameter pipes in which the onset shear stress [163] for the polymers could not be achieved within the laminar regime. Coiled polymer conformations, low molecular weights ($\mathcal{O}(10^5)$), and polymer degradation due to metallic meshes used to condition the pipe flow in the above studies have also been attributed to cause an increase in the onset shear stress which may have prevented polymer action and led to a premature transition [204]. However, a distinct delay in transition has been observed in a few studies where the above factors were carefully controlled in addition to employing higher molecular weight polymers ($\mathcal{O}(10^6)$) and helical conformations with both low and high concentration solutions [158, 293, 294].

The recent viscoelastic numerical simulations in channel flows have investigated the mechanisms of polymer drag reduction at transitional Reynolds numbers ($Re_\tau = 70 - 130$) [195, 248, 249], which have been previously discussed in Chapter 5. These studies have shown that the near-wall flow dynamics resulting from intermittent regions of high and low turbulence activity are significantly modified by the introduction of viscoelasticity. While such localized regions of low turbulence, or *hibernating* regions, are also found in Newtonian channel flows [246, 247, 295], they are shown to expand with increasing Weissenberg number (Wi), leading to drag reduction within the transitional regime. Similar expansions of the hibernating regions were noted within the buffer layer of polymer injected fully developed turbulent boundary layers in Chapter 5 and the results of Tamano *et al.* [250].

Despite an enhanced understanding of the mechanisms of polymer drag reduction in turbulent boundary layers and exploratory studies on polymer effect on transition in channel flows, to the

best of the authors' knowledge, the polymer effect on laminar-to-turbulent transition in boundary layers has yet to be investigated. Thus, the present work studies the effect of slot-injected polymer solutions in bypass transitioning flat-plate boundary layers with the goal to examine the development of salient flow features via two-dimensional particle image velocimetry (PIV) and planar laser induced fluorescence (PLIF) measurements. The measurements are conducted at multiple stations within an extended length of the transitional flat-plate boundary layer which is produced by a two-dimensional spanwise trip-wire. Furthermore, two different injection slot locations with respect to the trip-wire are considered providing important insights for the practical implementation of this flow control approach as well as a holistic understanding of the polymer effect on the transitioning flow.

7.2 Experimental setup

Planar PIV and PLIF measurements were conducted in the $x-y$ plane at the mid-span of the flat-plate model using a similar experimental setup as the one described in Sec. 3.2.1. The tunnel was operated at a freestream velocity of $0.3\,\mathrm{m\,s^{-1}}$ for all the cases studied in the present work, resulting in a laminar boundary layer thickness of $\delta_{\text{slot}} = 5.80\,\mathrm{mm}$ at the injection slot. Bypass transition over an extended length on the flat plate was achieved using a two-dimensional spanwise round trip wire with a diameter of $1.65\,\mathrm{mm}$ as shown in Fig. 7.1. Two different configurations were considered based on the trip location relative to the slot, with the trip wire placed $8\,\mathrm{mm}$ upstream and $15\,\mathrm{mm}$ downstream of the injection slot, which correspond to local laminar boundary layer thicknesses of $5.50\,\mathrm{mm}$ and $6.05\,\mathrm{mm}$, respectively. These configurations are denoted as the trip-upstream and the trip-downstream configurations in the present study. For these trip positions, the polymer is injected within the recirculating region formed downstream of the trip wire in the trip-upstream configuration, whereas it is injected in the laminar boundary layer upstream of the trip wire in the trip-downstream configuration. The use and sizing of a two-dimensional trip follows a well-established practice from prior experiments (*e.g.* Refs. [111, 114, 296]). For a given trip geometry, its efficiency depends on the Reynolds number based on the height (r) of the roughness element ($Re_r = rU_r/\nu$, where U_r is the streamwise velocity in the laminar boundary layer at the height r from the wall) [112]. For the two configurations investigated in the present study, the trip locations and the wire diameter were chosen such that Re_r, estimated to be 229 and 210, at the upstream and downstream trip locations respectively, falls in the range of the critical Reynolds numbers required to produce a transitional flow [296]. Based on preliminary experiments, for $Re_r < 180$, the flow did not fully transition over the length of the flat-plate, while for $Re_r > 300$, a rapid transition effectively localized at the trip wire is expected [296].

Solutions of polyethylene oxide (PEO, Sigma Aldrich, Inc.) with an average molecular

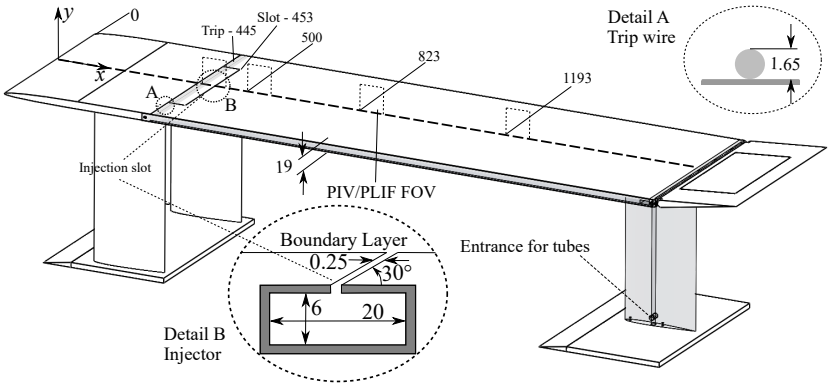

Figure 7.1: Schematic of the flat-plate model showing the coordinate system, polymer injection setup, and details of the trip wire. All dimensions are in mm but are not to scale. For clarity, only four PIV measurement stations are shown here corresponding to the trip-upstream case.

weight of 8×10^6 g/mol and a concentration of 1000 ppm were prepared and injected using the protocols outlined in Sec. 3.1.3. The injection parameters used in the previous works reported in this thesis were shown to produce negligible effects of benign injection in a turbulent boundary layer, and did not produce a significant effect on bypass-transition process in the present investigation.

Planar PIV measurements were conducted at multiple streamwise stations at the mid-span of the plate (Table 7.1), with the specifications of the instrumentation used outlined in Sec. 3.2.1. The camera imaged a field of view (FOV) of $38.4 \times 32.4\,\mathrm{mm}^2$ with a resolution of $66.7\,\mathrm{pixel/mm}$. For each experimental condition, 4500 double-frame image pairs were acquired with a time separation $\Delta t = 1000\,\mu\mathrm{s}$ and an acquisition frequency of 15 Hz. This corresponded to a mean particle displacement of approximately 20 pixels in the freestream. The uncertainty due to random errors in instantaneous vector fields was estimated to be less than 0.5% of U_∞ with 95% confidence limits. Prior to the measurements of the two bypass transition cases with the trip wire, PIV measurements were performed in the laminar boundary layer to establish the baseline boundary layer development on the flat plate. In each of the three cases, injection of water and polymer with $c_{\mathrm{inj}} = 1000$ ppm were included along with the baseline Newtonian flow. Measurements were performed at nine and six downstream stations in the trip-upstream and trip-downstream cases, respectively, in addition to the measurement station around the trip.

The image pre-processing and PIV processing were performed according to the protocols outlined in Sec. 3.2.2. Accordingly, the pre-processed images were first processed using the ensemble-of-correlation algorithm [207, 208] to produce a time-averaged velocity vector field with a final window size of 4×4 pixels and an overlap of 50%. The mean vector fields result-

Experimental parameters							
Trip - upstream ($x_{\text{trip}} - x_{\text{inj}} = -8$, $U_\infty = 0.3\,\text{m}\,\text{s}^{-1}$, $c_{\text{inj}} = 0^\dagger$, 1000 ppm)							
x/L	$x - x_{\text{inj}}$	$x - x_{\text{trip}}$	δ_0	λ_0 (µm)	Re_{τ_0}	Re_{δ^*}	PLIF (Yes/No)
[0.201, 0.220]	[-10, 30]	[-2, 38]	6.13	...	...	923	Yes
[0.227, 0.245]	[47, 87]	[55, 95]	6.99	139.8	50	734	Yes
[0.238, 0.256]	[70, 110]	[78, 118]	7.30	102.8	71	634	Yes
[0.265, 0.283]	[130, 170]	[138, 178]	8.00	69.5	115	555	Yes
[0.292, 0.310]	[190, 230]	[198, 238]	11.05	60.7	182	504	Yes
[0.329, 0.347]	[270, 310]	[278, 318]	12.24	63.4	193	553	Yes
[0.374, 0.392]	[370, 410]	[378, 418]	14.74	65.2	226	679	No
[0.420, 0.438]	[470, 510]	[478, 518]	16.77	66.3	253	770	Yes
[0.465, 0.483]	[570, 610]	[578, 618]	17.98	68.6	262	812	No
[0.542, 0.560]	[740, 780]	[748, 788]	21.53	68.6	314	997	No
Trip - downstream ($x_{\text{trip}} - x_{\text{inj}} = 15$, $U_\infty = 0.3\,\text{m}\,\text{s}^{-1}$, $c_{\text{inj}} = 0^\dagger$, 1000 ppm)							
[0.204, 0.222]	[-5, 35]	[-20, 20]	6.14	...	...	872	Yes‡
[0.240, 0.258]	[75, 115]	[60, 100]	7.45	149.0	50	762	Yes
[0.265, 0.283]	[130, 170]	[115, 155]	7.70	113.2	68	725	Yes
[0.292, 0.310]	[190, 230]	[175, 215]	7.90	77.5	102	661	Yes
[0.338, 0.360]	[290, 330]	[275, 315]	10.08	62.2	162	551	Yes
[0.429, 0.447]	[490, 530]	[475, 515]	14.62	62.7	233	668	Yes
[0.542, 0.560]	[740, 780]	[725, 765]	19.58	65.7	298	913	No
Laminar - No trip ($U_\infty = 0.3\,\text{m}\,\text{s}^{-1}$, $c_{\text{inj}} = 0^\dagger$, 1000 ppm)							
[0.201, 0.220]	[-10, 30]	...	5.91	111.7	53	581	No
[0.292, 0.310]	[190, 230]	...	7.62	120.3	63	724	No
[0.383, 0.401]	[390, 430]	...	8.83	129.5	68	828	No
[0.451, 0.470]	[540, 580]	...	10.03	134.5	75	921	No
[0.542, 0.560]	[740, 780]	...	10.89	134.0	81	981	No

Table 7.1: Test matrix. Coordinate ranges corresponding to the streamwise extent of the field of view and the boundary layer parameters measured for the baseline case at the centre of each FOV are provided. † indicates water injection. ‡ indicates that PLIF measurements were performed at two locations $x - x_{\text{inj}} = [-1, 39]$ and $[15, 55]$. $\lambda_0 = \nu/u_{\tau_0}$, where u_{τ_0} is the friction velocity.

ing from this procedure have a vector pitch of $30\,\mu\mathrm{m}$ and were used as an initial displacement predictor for a sequential-correlation algorithm used to obtain instantaneous velocity fields. The employed iterative correlation with window deformation had a final window size of 24×24 pixels and 75% overlap resulting in a vector pitch of $90\,\mu\mathrm{m}$.

For the bypass transition cases, planar-laser induced fluorescence (PLIF) measurements were conducted according to the procedure outlined in Sec. 3.2.3 with both water and polymer injection at selected streamwise stations indicated in Table 7.1. In this case, 2000 images were acquired in the single frame mode at an acquisition frequency of $50\,\mathrm{Hz}$ for each experimental condition. Time-averaged local concentrations relative to a reference concentration (c_{ref}) at each measurement station were estimated based on the expected linear relationship between the light intensity and the concentration of the weakly excited dye [216].

7.3 Results and discussion

7.3.1 Transitional flow visualization and concentration diffusion

The development of the transitioning boundary layer induced by the trip-wire is firstly studied using flow visualization and concentration of the injected dye obtained from the PLIF measurements. Representative instantaneous flow visualization images for both the trip position upstream and downstream of the injection slot are presented in Figs. 7.2(a) and 7.2(b), respectively, with the cases corresponding to water (passive tracer) and polymer injection shown in rows marked (i) and (ii), respectively, for each trip position. The initial development of the tripped boundary layer flow in both cases show that the injected fluid is concentrated in a separated shear layer forming due to flow separation from the trip. The separated shear layer is highly unstable and the attendant Kelvin-Helmholtz (K-H) instability rapidly manifests in the growth of perturbations and roll-up visualized by the entrained dye. The distinct evidence of the periodically shed vortices can be seen within $10 < (x - x_{\mathrm{trip}})/\delta_{\mathrm{slot}} < 16$ in all the cases considered. Consecutively shed co-rotating vortices undergo merging downstream, resulting in doubling of the primary wavelength, as indicated in Figs. 7.2(a)(i) and 7.2(b)(i), consistent with the vortex merging in free shear layers (*e.g.,* Ho and Huerre [297]) and near-wall separating-reattaching flows (*e.g.,* Kurelek *et al.* [298]). An instantaneous snapshot of the vortex merging is seen at $(x - x_{\mathrm{trip}})/\delta_{\mathrm{slot}} \approx 14$ in Fig. 7.2(b)(i). Moreover, an occasional merging of multiple consecutive vortices is also observed within this streamwise range in all the cases. As these spanwise oriented vortical structures convect downstream, they are seen to lift-up and eventually breakdown due to secondary three-dimensional instabilities that lead to the formation of Λ vortices, transitional-turbulent spots, and hairpin-like vortices [114, 299].

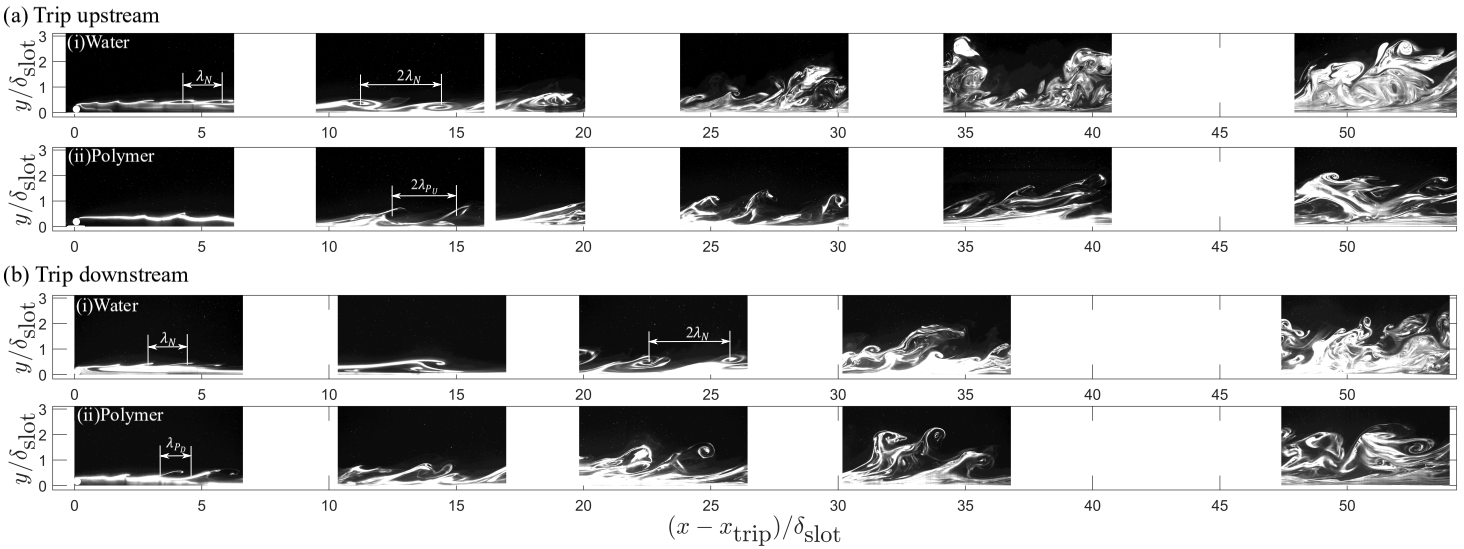

Figure 7.2: Instantaneous flow visualization of the injected fluid in (a-i, a-ii) trip upstream and (b-i, b-ii) trip downstream case. (a-i) and (b-i) show injected flow development with water injection (passive tracer), whereas (a-ii) and (b-ii) show the development with polymer injection for each of the transition cases, respectively. The coordinate axes are normalized by the laminar boundary layer thickness measured at the injection slot (δ_{slot}). The injection slot is located at $(x - x_{\text{trip}})/\delta_{\text{slot}} \approx 1.38$ in (a-i) and (a-ii) whereas it is located at $(x - x_{\text{trip}})/\delta_{\text{slot}} \approx -2.6$ in (b-i) and (b-ii), and thus, not shown.

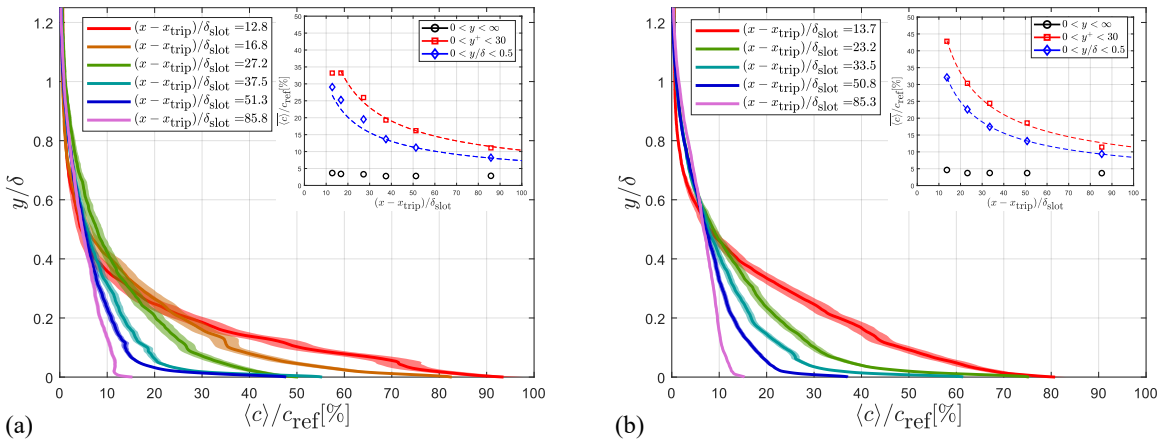

Figure 7.3: Profiles of concentration normalized by the concentration of the injected polymer at various downstream distances from the trip-wire in (a) trip-upstream and (b) trip-downstream case. Insets show the variation of spatially averaged concentration ($\overline{\langle c \rangle}/c_{\mathrm{ref}}$) within different regions of the boundary layer with best-fits of $\overline{\langle c \rangle}/c_{\mathrm{ref}} \sim (x - x_{\mathrm{trip}})^b$ shown by dashed lines. Variation of $\overline{\langle c \rangle}/c_{\mathrm{ref}}$ computed over the height of the FOV ($0 < y/\delta < \infty$), which exceeds 1.9δ at each location, is shown for reference.

Despite the similarities in the transition process, the flow visualizations for the polymer-injected flow cases considered in Figs. 7.2(a)(ii) and 7.2(b)(ii) show notable differences close to the trip wire in comparison to the Newtonian flow. While the transition process initiates with formation of the K-H instabilities, the primary streamwise wavelength associated with vortex shedding is observed to decrease from $\lambda_N \approx 1.5\delta_{\mathrm{slot}}$ in the baseline flow to approximately $\lambda_{P_U} \approx 1.25\delta_{\mathrm{slot}}$ in the polymer-injected trip-upstream case. Furthermore, while notable cycle-to-cycle variations exist, on the average, the shear layer roll-up tends to take place closer to the trip-wire in the polymer-injected trip-downstream configuration ($(x-x_{\mathrm{trip}})/\delta_{\mathrm{slot}} \approx 2-3$) in comparison to the corresponding trip-upstream case, suggesting an increased amplification of velocity perturbations. This leads to an earlier onset of vortex breakdown at $10 < (x-x_{\mathrm{trip}})/\delta_{\mathrm{slot}} < 15$ in the trip-downstream case. In contrast, the breakdown in both cases considered in the trip-upstream configuration is observed within approximately $25 < (x - x_{\mathrm{trip}})/\delta_{\mathrm{slot}} < 30$, further suggesting a relatively minor effect of the polymer on the transition process in this configuration.

For a quantitative evaluation of the diffusion of injected polymer in the transitioning boundary layer, time averaged profiles of normalized polymer concentration are considered in Fig. 7.3. For consistency, the reference concentration c_{ref} is evaluated immediately downstream of the recirculating region downstream of the trip ($(x - x_{\mathrm{trip}})/\delta_{\mathrm{slot}} \approx 10.5$) to minimize inaccuracies

caused by the insufficient penetration of the laser sheet through the highly concentrated dye in the separated shear layer. While the polymer concentrations at the chosen reference location are expected to be different in the two cases precluding a quantitative comparison of the near-wall concentration, the normalized concentration profiles in both transitioning cases show a peak in polymer concentration at the wall similar to previous observations in turbulent boundary layers [61, 182, 220, 221]. As expected, the peak magnitudes decrease with increasing streamwise distance due to the wall-normal transport of the polymer noted in Fig. 7.2.

To aid the quantitative analysis of the effect of the polymer solutions on flow transition, variation of the spatially averaged polymer concentration in the near-wall region is considered in the insets of Figs. 7.3(a) and 7.3(b). Spatial averaging is considered in both near-wall viscous region ($0 < y^+ < 30$) and the lower half of the boundary layer ($0 < y/\delta < 0.5$) to account for the strongly decreasing frictional length scales in the initial portion of the tripped boundary layer (with the scaling parameters estimated using PIV). Results show that the spatially-averaged concentrations in the lower half of the boundary layer decrease with the streamwise distance from the trip location according to a power law $\langle c \rangle / c_{\text{inj}} \sim (x - x_{\text{trip}})^b$, with the exponent $b = -0.62$ and -0.67 in the trip-upstream and trip-downstream cases, respectively. The difference between the two cases decreases when the near-wall range ($0 < y^+ < 30$) is considered for spatial averaging, signifying a diminished effect of the trip position on the evolution of the average concentration in the near-wall region.

7.3.2 Flow past trip-wire

The flow dynamics in the region downstream of the trip-wire in each of the cases seen in Fig. 7.2 is further investigated to offer more quantitative insights into the initial development of the transitional boundary layer. The time averaged velocity vector field in Fig. 7.4 confirm the laminar flow separation over the trip wire and the subsequent recirculating region downstream of the trip, as evidenced by the negative streamwise velocity near the wall. The contour corresponding to $\langle u \rangle = 0$, which separates the recirculating region from the streamwise flow, is observed to be aligned with the trip height. Measurements at a downstream location (omitted for brevity) show that the mean flow-field reattaches at approximately $10\delta_{\text{slot}}$ downstream of the trip wire. Similar results are obtained in the baseline flow corresponding to the trip downstream case.

Time averaged profiles of streamwise velocity immediately downstream of the trip-wire are considered in Fig. 7.5 to investigate the effect of the polymer on the separated shear layer formed above the recirculating bubble. The results averaged over $0.2 < (x - x_{\text{trip}})/\delta_{\text{slot}} < 1.2$ in each of the presented cases show that, while the recirculating bubble persists in the polymer-injected cases, the magnitude of the negative streamwise velocities within the bubble is notably reduced.

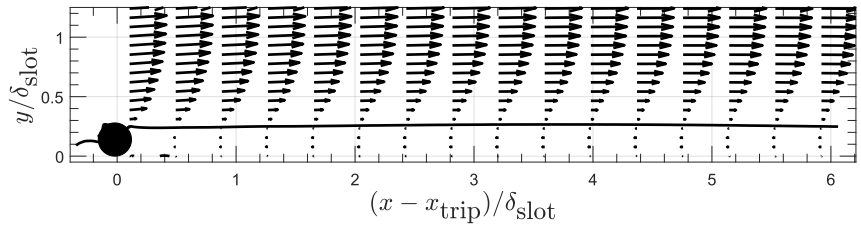

Figure 7.4: Time averaged velocity vectors for the baseline flow showing the recirculation bubble downstream of the trip-wire.

This is attributed to the presence of the higher viscosity polymer solutions within the bubble. The results further show that polymer injection in the trip-upstream configuration has a negligible effect on the height of the bubble. In contrast, an increased bubble height and, thus, the wall-normal distance of the separated shear layer is seen to be increased in the trip-downstream configuration, illustrated by the maxima of the normalized wall-normal gradient of the mean streamwise velocity. The difference between the two polymer-injected scenarios may be explained based on the concentration of the polymer contained within the separated shear layer. In the trip-downstream configuration, the highly concentrated polymer solution surrounding the upstream portion of the trip-wire experiences relatively strong normal stresses, which are stored within the polymers and are released in the wall-normal (radially-outward) direction as they flow past the trip wire into the separated shear layer. This behaviour is consistent with the expansion of the wake [300] and earlier separation [301] observed in polymer laden flows over cylinders. Such an imbalance in the normal stresses is not expected to the same degree in the trip-upstream configuration since the polymers are released within the recirculating bubble where significantly lower wall-normal stresses are observed.

To further investigate the development of the separated shear layer formed due to the trip-wire and the polymer effect on the resulting transition process, root-mean-square (rms) fields for the streamwise and wall-normal velocities downstream of the trip-wire are considered in Fig. 7.6. The results show relatively large magnitudes of both u_{rms}/U_∞ and v_{rms}/U_∞ confined within the boundary layer above the recirculation bubble which is attributed to the rapid growth of perturbations in the separated shear layer. Polymer injection within the recirculation bubble in the trip-upstream configuration marginally lowers the streamwise velocity fluctuations (Fig. 7.6(b)), while at the same time, increases considerably the wall-normal fluctuations (Fig. 7.6(e)) within the transitioning shear layer. This effect is notably changed in the polymer-injected trip-downstream configuration which shows substantial magnitudes of u_{rms}/U_∞ within the shear layer even before it separates from the trip-wire along with the region of increased v_{rms}/U_∞ forming closer to the trip-wire in comparison to the former case. The increased stream-

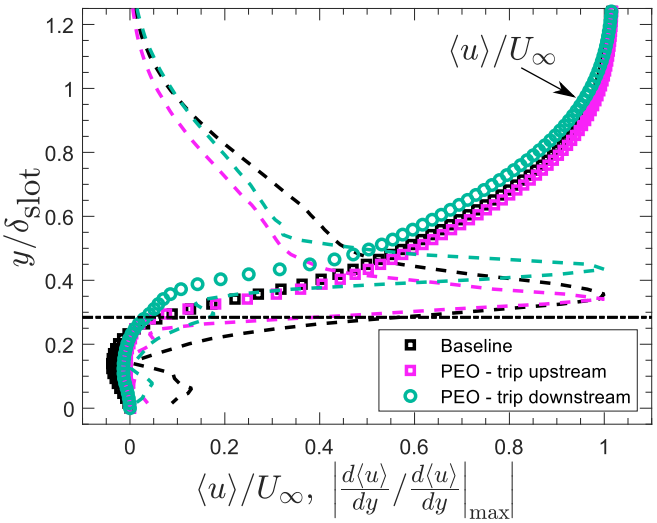

Figure 7.5: Time averaged profiles of streamwise velocity and its gradient with respect to the wall-normal coordinate. Results are averaged within a window of length δ_{slot} downstream of the trip-wire. Dash-dot line shows the height of the trip-wire.

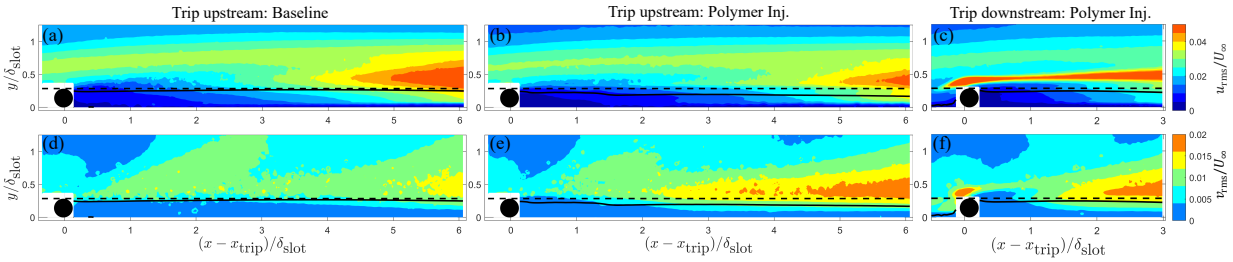

Figure 7.6: Normalized rms of the (a-c) streamwise velocity (u_{rms}/U_∞), and (d-f) wall-normal velocity (v_{rms}/U_∞) downstream of the trip. Results corresponding to the trip upstream configuration are shown for (a, d) baseline, and (b, e), whereas those for the polymer-injected flow in the trip downstream configuration are shown in (c, f). Dashed lines show the height of the trip and solid lines show the contour corresponding to $\langle u \rangle = 0$.

wise fluctuations within the region confined to the layer of the highly concentrated polymer flow suggests the onset of elastic instabilities which are noted to occur at large Wi and subsequently lead to elasto-inertial turbulence [302, 303]. While this phenomenon is not observed in the polymer-injected trip-upstream case, the increased wall-normal fluctuations are indicative of the increased amplification rate of the K-H instability.

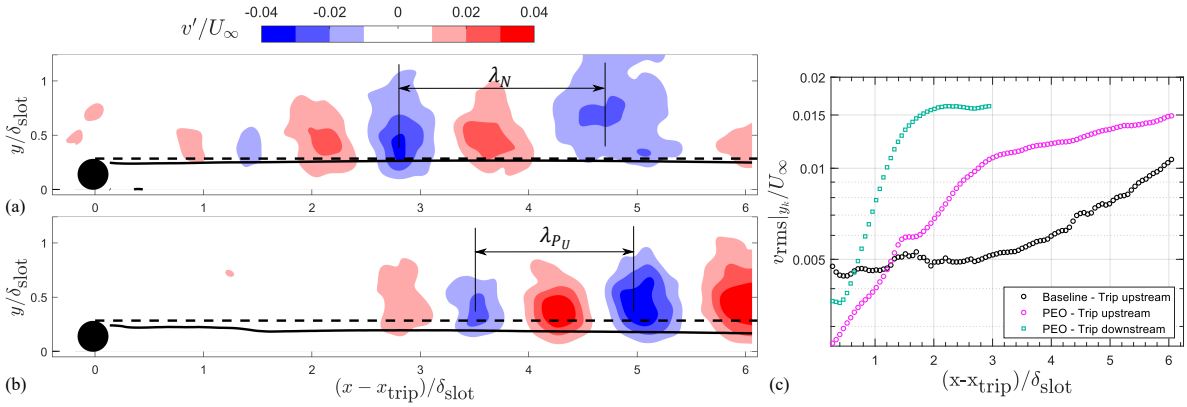

Figure 7.7: Representative instantaneous realizations showing vortex shedding in (a) baseline, and (b) polymer-injected trip-upstream cases. Contours are smoothed with a two-dimensional Gaussian window ($0.25\delta_{\text{slot}} \times 0.25\delta_{\text{slot}}$). Black dashed lines show the height of the trip and solid lines show the contour corresponding to $\langle u \rangle = 0$. (c) shows the variation of v_{rms} with $(x - x_{\text{trip}})/\delta_{\text{slot}}$ at the height of the trip y_k.

The amplification of the shear layer perturbations is further illustrated in Fig. 7.7. Figs. 7.7(a) and 7.7(b) present instantaneous snapshots of wall-normal velocity fluctuations showing a distinct periodicity characteristic of K-H instability, with the streamwise wavelength (λ_N) corresponding to that seen in Fig. 7.2(a)(i). Further, this wavelength is noted to decrease in the polymer-injected flow substantiating the changes in the transition process. Fig. 7.7(c) shows the streamwise variation in rms of the wall-normal fluctuations $v_{\text{rms}}|_{y_k}$ sampled along the trip height. The results suggest that polymer-injected flows feature higher growth rates compared to the baseline flow within $(x - x_{\text{trip}})/\delta_{\text{slot}} < 2$. In addition, for the polymer injected flow in the trip-downstream configuration, velocity fluctuations reach similar levels within a shorter streamwise distance compared to that in the trip-upstream configuration, which highlights a more pronounced effect of the elastic instabilities in the former case.

7.3.3 Transitional flow development

The quantitative description of the development of the transitional boundary layer induced by the trip is first considered through the variation in the boundary layer parameters in the streamwise direction in Fig. 7.8. Results are complemented with the variation in the boundary layer parameters corresponding to the no-trip configuration (laminar flow) in the left column of Fig. 7.8 for reference. Fig. 7.8(a) shows the expected variation in both boundary layer thickness (δ) and displacement thickness (δ^*) in the baseline flow, and the effect of water injection is seen to

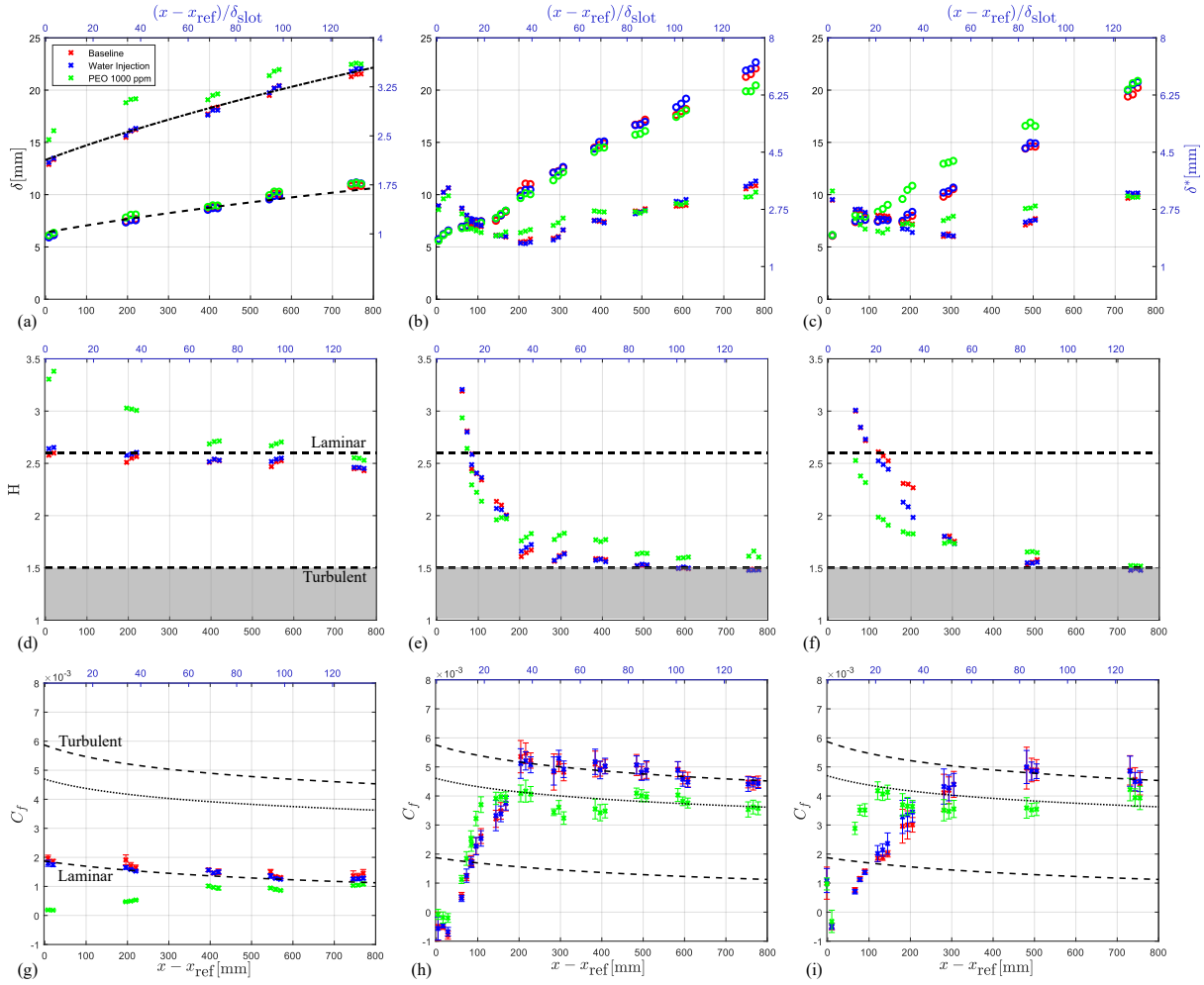

Figure 7.8: Variation of the boundary layer parameters in (a, d, g) no-trip (laminar), (b, e, h) trip-upstream, and (c, f, i) trip-downstream configurations. Left axis in the top row shows the variation of boundary layer thickness (δ) marked by $\circ$ and right axis shows displacement thickness (δ^*) marked by $\times$. Middle row shows the shape factor $H - \delta^*/\theta$ and bottom row shows the skin friction coefficient C_f. Black dashed and dash-dotted lines in (a) show the typical variation in laminar boundary layers from Blasius' relations and dashed in (d)-(i) indicate typical values of H and C_f in laminar and turbulent boundary layers as indicated. Dotted line in (g)-(i) shows 20% reduction in C_f from the Prandtl-Kármán (turbulent) law. Reference location x_{ref} is considered at the injection slot (x_{inj}) in the no-trip configuration and at the trip-wire (x_{trip}) in the tripped boundary layer cases.

be negligible on these parameters. Similar results are noted for the shape factor (H) for these two cases, with H remaining close to the expected value of 2.6 in the laminar boundary layer and decreasing marginally with increasing streamwise distance. The marginal decrease in H is attributed to the natural amplification of the disturbances within the laminar boundary layer expected to occur at Re_{δ^*} greater than $Re_{\text{crit}} = 520$ (Table 7.1). The polymer injection produces a notable increase in all the boundary layer parameters close to the injection slot, but this effect is seen to progressively decrease with increasing streamwise coordinate. The increase in δ^*, and consequently H, close to the injection slot is consistent with the observations in polymer-injected turbulent boundary layers (*e.g.,* Fig. 4.5), and is attributed to the decreased near-wall streamwise velocity due to the higher viscosity within the concentrated layer of polymer formed close to the wall (Fig. 7.3).

As expected, the introduction of the trip wire results in a significant increase in the boundary layer thickness compared to the laminar flow in both transitional cases (Figs. 7.8(b) and 7.8(c)). On the other hand, the displacement thickness decreases initially in the range $(x-x_{\text{trip}})/\delta_{\text{slot}} < 50$ ($x - x_{\text{trip}} < 300$ mm) before increasing monotonically. This initial decrease in δ^* has also been noted by Dhawan and Narasimha [98] in transitional boundary layers and is attributed to the increased mass flow rate within the boundary layer caused by the increased mixing of the outer flow by growing perturbations. Compounded by the increase in the momentum thickness (θ), the shape factor decreases sharply within $(x - x_{\text{trip}})/\delta_{\text{slot}} < 50$ from the value of 2.6, followed by a more gradual decrease until the boundary layer becomes fully turbulent (Figs. 7.8(e) and 7.8(f)). The decrease in H in the latter portion of the transition region ($(x - x_{\text{trip}})/\delta_{\text{slot}} > 50$) is mainly driven by the increase in the momentum thickness, as δ^* increases in this range. It is further observed that the boundary layer thickness in the trip-downstream case is lower than the case where the trip is positioned upstream of the injection slot. This is attributed to a decreased effectiveness of the trip in the former case as a result of the lower Re_r at the trip wire. Furthermore, these trends are seen to hold with the injection of water, indicating that the effect of benign injection is negligible.

In the trip-upstream configuration, the polymer injection is seen to produce a minor effect on the development of the boundary layer thickness with more notable changes seen in the latter portion of transition and in the turbulent regimes (Fig. 7.8(b)). In contrast, the δ^* is reduced below the corresponding Newtonian values immediately downstream of the trip, while it is increased at the locations near the minimum in δ^* ($(x - x_{\text{trip}})/\delta_{\text{slot}} \approx 35$), indicating reduced turbulent mixing by the polymers leading to a decreased mass flow rate within the boundary layer. This is further seen from the sharper reduction of H in the region $(x - x_{\text{trip}})/\delta_{\text{slot}} < 35$ in comparison to the corresponding Newtonian values. For $(x - x_{\text{trip}})/\delta_{\text{slot}} > 35$, the decrease in the shape factor saturates and progresses at a rate lower than that in the Newtonian flow indicating the activation of the polymer effect.

Unlike the results seen with the trip-upstream configuration, the boundary layer thickness for the polymer injected transitional boundary layer in the trip-downstream case (Fig. 7.8(c)) is notably increased in comparison to the corresponding Newtonian flows at $(x - x_{\text{trip}})/\delta_{\text{slot}} < 35$. This is attributed to the increased amplification of the instabilities closer to the trip-wire, which results in an earlier breakdown to turbulence as previously shown in Figs. 7.2 and 7.6. These effects are confirmed by the significantly decreased values of δ^* and H in $(x - x_{\text{trip}})/\delta_{\text{slot}} < 35$. Beyond this range, both δ^* and H are seen to be higher than the corresponding values in the Newtonian cases, suggesting the polymer action to be effective in controlling turbulence. However, H is seen to progressively decrease to typical values in turbulent Newtonian flows towards the end of the measurement domain which is attributed to the progressive depletion of the near-wall polymer concentration (Fig. 7.3).

In order to elucidate the associated changes in the skin friction, the streamwise variation in the estimated mean skin friction coefficient ($C_f = \tau_w/(0.5\rho U_\infty^2)$) is considered in Figs. 7.8(g-i). These data are obtained by computing the wall-normal gradient of the mean streamwise velocity ($d\langle u\rangle/dy|_w$) over 10 to 16 velocity vectors obtained from ensemble-of-correlation results in the near-wall region where the near-wall law $u^+ = y^+$ is expected to be applicable, *i.e.,* within $y^+ \leq 5$ [155]. C_f is estimated by utilizing this linear trend within the viscous sublayer with the fluid properties of water at the measured freestream temperature. Further, to reduce measurement errors, a sliding average operation on the local estimates of C_f is performed over a window of 2 mm in the x-direction (equivalent to 68 velocity vectors), similar to the procedure used in turbulent boundary layers by previous studies employing optical techniques [61, 273]. It should be noted that the estimates of C_f in the polymer-injected cases are obtained by utilizing the fluid properties of the base medium (water) due to the lack of measurements for the local viscosity of the polymer. This procedure is expected to produce reliable estimates of C_f in the later stages of transition and the turbulent regimes where sufficient mixing of polymer with the base media has occurred leading to the maximum concentrations to be within the limits of overlap concentration for the employed polymer ($c^* = 330$ ppm, using Mark-Houwink relationship [222]).

The results for the no-trip case in Fig. 7.8(g) confirm that the variation of C_f follows the canonical trends in laminar boundary layers. As expected, the relatively viscous layer formed by the injected polymer solution close to the wall results in a decreased gradient of the streamwise velocity at the wall ($d\langle u\rangle/dy|_w$) as noted from the figure. However, it must be noted that the actual C_f is higher than that for the baseline flow of water given that the polymer solutions exhibit a shear viscosity that is an order of magnitude higher than the viscosity of water at the employed shear rates [60,61]. With the addition of the trip-wire (Figs. 7.8(h) and 7.8(i)) and the subsequent creation of the recirculating bubble, negative values of C_f are observed immediately downstream of the trip. As the flow develops downstream, the C_f is seen to monotonically increase and then converge on the trend predicted by the Prandtl-Kármán law for the fully turbulent boundary layer,

in accordance with previous studies on bypass transition [78, 98, 102]. The location where the peak in C_f is obtained is usually denoted as the *transition point* [304]. As observed in Fig. 7.8, the differences in the transitional flows between the two trip position cases considered here are also seen in the variation of C_f, highlighting the sensitivity of the trip effectiveness to Re_r. Due to a lower Re_r, the transition point is noted to occur later in the trip-downstream configuration, *i.e.,* in the range $70 < (x - x_{\text{trip}})/\delta_{\text{slot}} < 85$, whereas it occurs in the range $30 < (x - x_{\text{trip}})/\delta_{\text{slot}} < 40$ in the trip-upstream configuration. Further, consistent with the results for other boundary layer parameters, on the average, water injection is not seen to significantly alter the flow development.

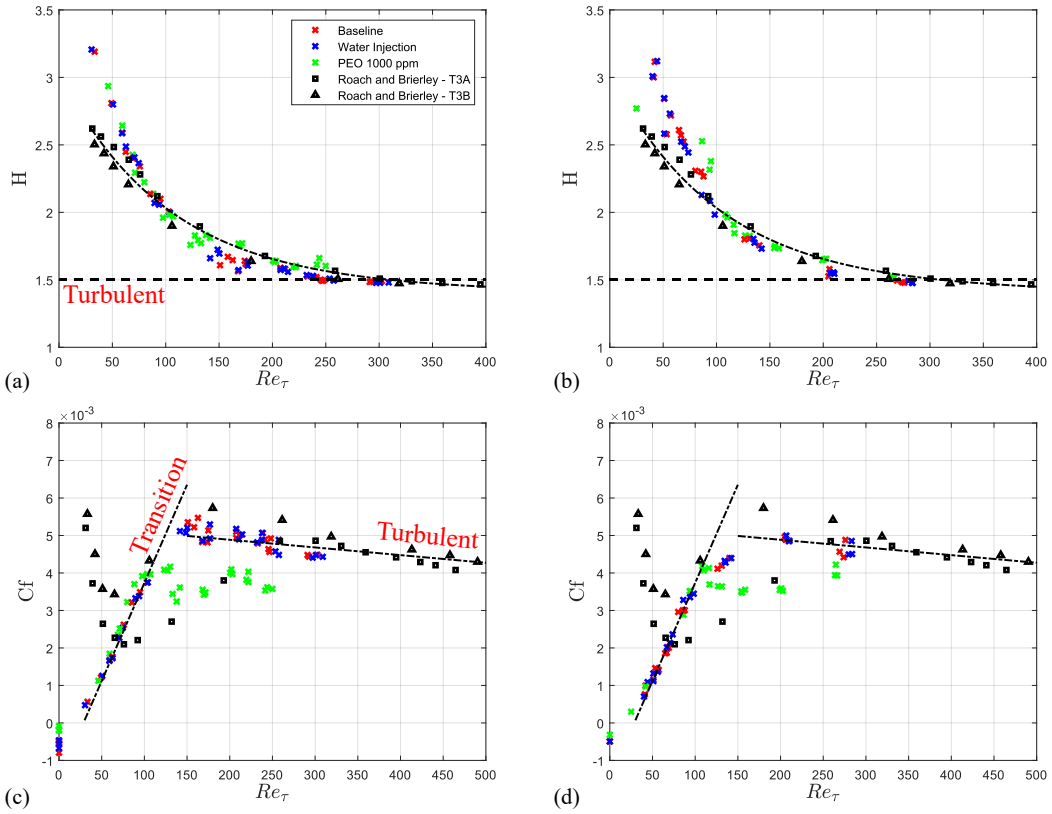

Figure 7.9: Variation of the shape factor (H) and the skin friction coefficient (C_f) in (a, c) trip-upstream, and (b, d) trip-downstream cases with Re_τ. Data corresponding to the T3A and T3B cases from the study of Roach and Brierley [78] are included for reference. Dash-dotted lines in (a) and (b) show best-fits to the T3A and T3B cases and dashed line indicates the typical value in fully developed turbulent boundary layers. Dash-dotted lines in (c) and (d) show linear fits to the data corresponding to the transition and turbulent regimes as indicated.

Figs. 7.8(h) and 7.8(i) show a notable effect of polymer injection on the variation of C_f in the transitional flows. While the general trend in the variation of C_f agrees with the Newtonian cases, the C_f is noted to be significantly higher than the corresponding Newtonian values in the initial part of the transition process. This agrees with the earlier observations of the enhanced transition by the polymer injection and the associated trends in C_f are attributed to the insufficient activation of the polymers in this region. The C_f is seen to peak at similar values in both polymer-injected transitional flows, but at lower values than the peak in the corresponding Newtonian flows. The decreased magnitude of the peak C_f is attributed to the *onset* of polymer activation, which likely occurs upstream of the peak leading to a progressively increasing suppression of the turbulent motions, as expected from previous studies in drag reduced internal flows [152]. This leads to an earlier saturation in the initially more rapid growth of C_f in the polymer-injected cases. Similar to that in the Newtonian flows, the location where the peak C_f occurs in the polymer-injected cases may be regarded as the transition point, however, in contrast to Newtonian flows, the polymer-laden flow beyond this point is not expected to be representative of a fully developed turbulent flow. This point is found to occur at a similar distance from the trip in comparison to the corresponding Newtonian flow in the trip-upstream configuration, *i.e.,* in the range $25 < (x - x_{\text{trip}})/\delta_{\text{slot}} < 40$, whereas it is notably advanced closer to the trip in the polymer-injected trip-downstream configuration, *i.e.,* in the range $15 < (x - x_{\text{trip}})/\delta_{\text{slot}} < 30$ in comparison to the corresponding Newtonian flow.

In both trip configurations, the skin friction growth saturates at the values lower than those for the corresponding baseline Newtonian flows and show drag reduction in the developing turbulent boundary layer. For example, Fig. 7.8(h) shows that the local drag reductions (DR) are at least 20% for a considerable distance beyond the transition point for the trip-upstream configuration, where DR is given as

$$\text{DR}[\%] = 100 \times \frac{C_{f_N} - C_{f_P}}{C_{f_N}}, \tag{7.1}$$

with C_{f_N} and C_{f_P} being the local skin friction coefficients in the baseline Newtonian and polymer-injected cases, respectively. Due to the diffusion of the near-wall polymer (Fig. 7.3), the DR progressively decreases, and the C_f values are seen to gradually return towards to the corresponding Newtonian values within the drag-reduced regime of the transitional flow. Similar results are noted in the case with the trip positioned downstream of the injector (Fig. 7.8(i)), however, the effect is seen to diminish at a higher rate which is partially attributed to the relatively higher diffusion rate of the average near-wall polymer concentration (Fig. 7.3).

In order to facilitate a more effective comparison between the two different trip placement configurations, variation of H and C_f with the frictional Reynolds number (Re_τ) is considered in Fig. 7.9. The figure also reproduces data from the T3A and T3B cases from Roach and Brier-

ley [78] as a reference. Although their study was performed in transitioning boundary layers bypassed using high freestream turbulence intensities, the Re_τ obtained by Roach and Brierley are similar to the ones employed in the present study. Figs. 7.9(a) and 7.9(b) show an excellent agreement in the shape factor data of the present results and the reference in the later stages of transition, while the differences in the earlier transition stages are attributed to the different methods used to induce the bypass transition in the two studies. The collapse between the tripped cases considered in the present study with those from Roach and Brierley [78] highlights the universality of the variation in H in the late transitional stages. As suggested by Dhawan and Narasimha [98], this universality is associated with the late transition stages being dominated by turbulent spots, independent of the mechanism by which transition has been initiated. Furthermore, the results for the polymer-injected flows are also found to be in agreement with the Newtonian flows, highlighting self-similarity between these flows in terms of Re_τ. This self-similarity facilitates extrapolations for the streamwise distances required for the drag-reduced transitional flows to reach fully-turbulent states expected at $H = 1.5$ or $Re_\tau \approx 300$, and the present results exhibit an effective delay in reaching the fully-turbulent state in the polymer-injected flows. A similar result is noted in the variation of C_f (Figs. 7.9(c) and 7.9(d)), which shows a collapse of both Newtonian and polymer-injected flows with the T3B case in the transition regime. Furthermore, the rate of increase of C_f with Re_τ is found to be approximately equal between the two trip configurations investigated in the present study, despite the noted differences in the trip effectiveness and polymer performance between these cases.

To further aid the understanding of the transitional flow development, time averaged profiles of the streamwise velocity are considered in inner coordinates in Fig. 7.10. An equivalent Re_{τ_0} in the baseline flow in each of the cases is indicated to aid the comparisons between the two tripped configurations. The figure shows that beyond the initial region of decreased near-wall streamwise momentum caused by the wake of the trip-wire ($Re_{\tau_0} < 150$), the baseline and water-injected Newtonian cases exhibit the expected progression towards a logarithmic profile in the fully developed turbulent flow seen at $Re_\tau \approx 300$. A similar development is seen in the polymer-injected cases as the flow develops past the initial trip-effects. The profiles at $Re_{\tau_0} > 150$ closely follow the expected trends in a drag reduced turbulent boundary layer with the developed logarithmic region shifted vertically from the Newtonian log-law depending on the achieved DR as shown by previous studies [17, 59, 61]. The disparities in the development of the velocity profiles in the earlier stages of the transition between the two configurations are attributed to the earlier noted differences in the initial transition process and near-wall polymer distribution between the two cases.

Time-averaged profiles of Reynolds normal and shear stresses in inner coordinates are considered in Fig. 7.11 with increasing Re_{τ_0}. Close to the trip-wire, *i.e.,* at $Re_{\tau_0} < 100$, the results show substantial magnitudes for all the Reynolds stresses within $y^+ < 30$ which is attributed to

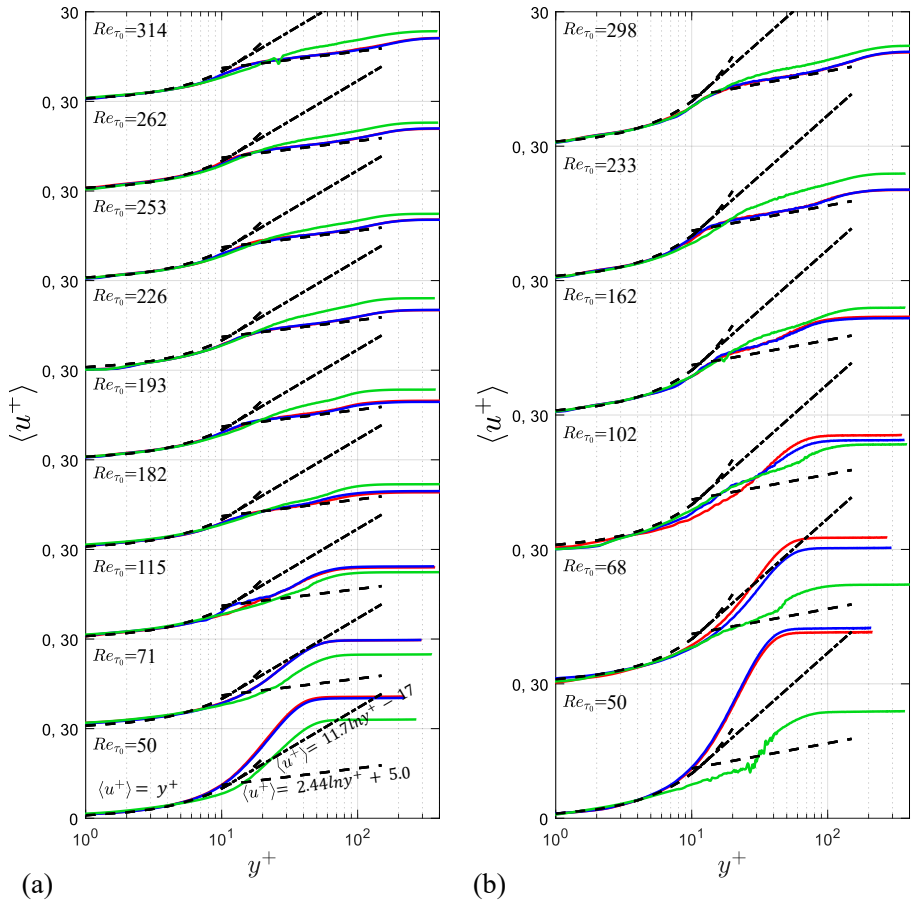

Figure 7.10: Mean streamwise velocity profiles in inner coordinates for (a) trip-upstream and (b) trip-downstream case. Profiles are displaced vertically to distinguish the streamwise positions marked by Re_{τ_0}. Color coding for the various cases follows the one shown in Fig. 7.9. Black-dashed lines indicate the near-wall and logarithmic laws in turbulent boundary layers and dash-dotted lines show Virk's MDR profile.

the amplification of K-H instability and the subsequent shedding of vortical structures in this region. Comparatively lower peak magnitudes are observed in this region for the trip-downstream configuration due to a lower tripping efficiency (lower Re_r) in this tripping scenario. As the vortices breakdown farther downstream ($Re_\tau > 100$), a peak in $\langle u'u' \rangle$ develops at $y^+ \approx 15$ and grows in both transitional scenarios, aligned with the results expected in the limiting case of fully developed turbulent boundary layers. Similarly, both $\langle v'v' \rangle$ and $-\langle u'v' \rangle$ peak farther away from the wall from a relatively early stage of transition in both configurations and reach their

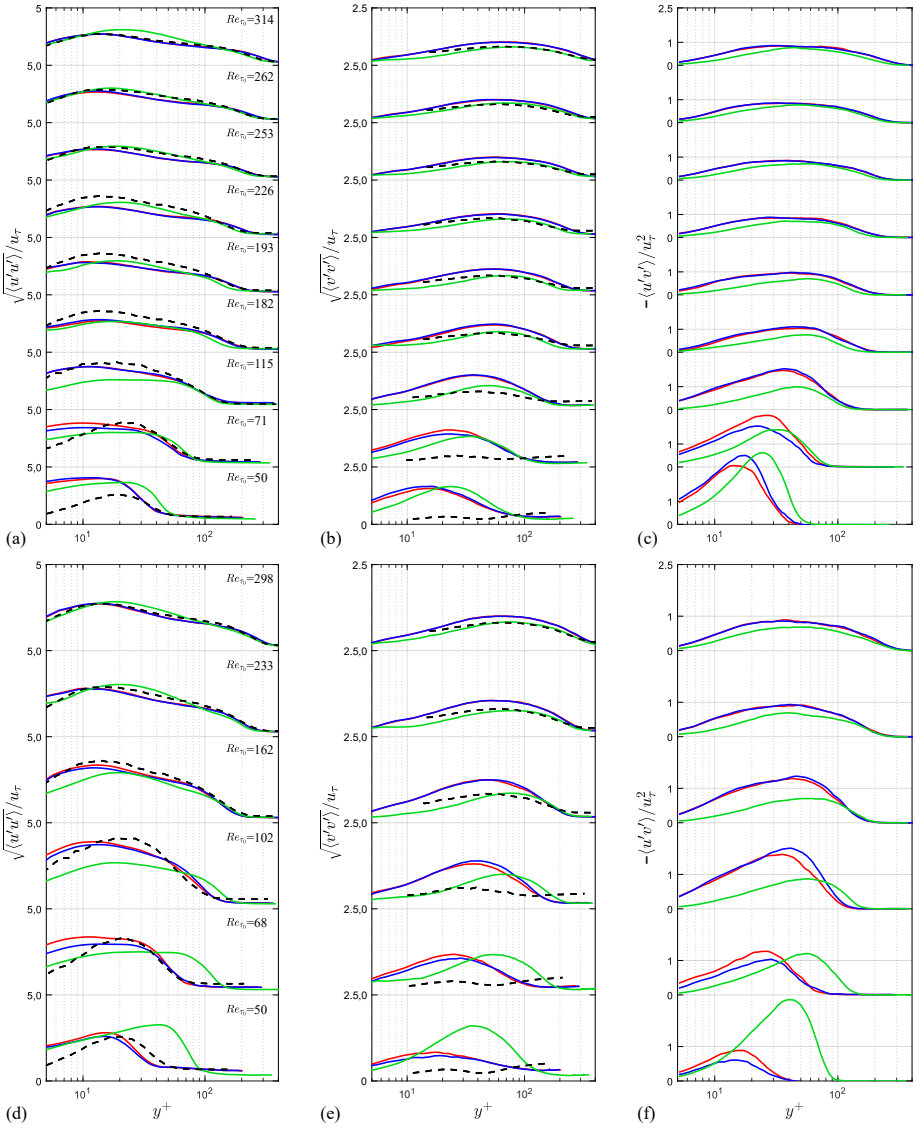

Figure 7.11: Reynolds normal and shear stresses in inner coordinates for (a-c) trip-upstream and (d-f) trip-downstream case. Profiles are displaced vertically to distinguish the streamwise positions marked by Re_{τ_0} in the left column. Color coding for the various cases follows the one shown in Fig. 7.9. Black dashed profiles are shown at equivalent friction Reynolds numbers from the T3A case of Roach and Brierley [78].

respective expected peak values in the limiting case by $Re_{\tau_0} \approx 200$. Furthermore, the profiles of both $\langle u'u' \rangle$ and $\langle v'v' \rangle$ corresponding to the Newtonian flow agree with the results of the T3A case from Roach and Brierley [78] in the late transition stages, signifying the aforementioned universality in the flow development.

Although a similar development of the profiles of the Reynolds stresses is seen in the polymer-injected transitional flows, notable differences in the peak magnitudes and locations are seen with respect to the corresponding Newtonian profiles. Moreover, the differences are considerable in the early transition stages ($Re_{\tau_0} < 100$) between the two transitional flows. The latter is attributed to a rapid transition process due to a relatively high shear and the resulting amplification of the instabilities within the separated shear layer in the trip-downstream configuration. As the flow proceeds towards the late transition stages ($Re_{\tau_0} > 100$), the polymer effect is seen to reduce the near-wall turbulent fluctuations in all Reynolds stresses, while increasing the $\langle u'u' \rangle$ above the Newtonian values in the buffer and lower-log regions ($20 < y^+ < \delta^+/2$), in alignment with the behaviour expected in drag reduced turbulent boundary layers [49,59,61]. Further, following the behaviour in the limiting case of turbulent boundary layers, the peaks in all the Reynolds stresses appear to shift in the wall-normal direction in the late transition stages, indicating the formation of a thicker buffer layer.

The efficiency of the polymers within the boundary layer is directly observed by considering the normalized profiles of the total shear stress (τ_{total}) which is composed of the Reynolds shear stress ($-\rho\langle u'v' \rangle$) and the viscous stress ($\mu d\langle u \rangle / dy$) as illustrated in Fig. 7.12. Since the normalized stress components are significantly higher in the early transition stages, and they develop towards their limiting values in the late transitional stages, as illustrated in Figs. 7.12(a) and 7.12(c), the normalized profiles of τ_{total} are considered for $Re_{\tau_0} > 100$. Following the approach of Hou *et al.* [69], the normalization by the local wall-shear stress ($\tau_w = \rho u_\tau^2$) and weighting by $(1 - y/\delta)$ allows for an evaluation of the polymer stress (τ_P). The results in Figs. 7.12(b) and 7.12(d) corresponding to the two transitional cases investigated in this study indicate a collapse of the weighted data on a linear trend within $0 < y/\delta < 0.6$ as expected in turbulent Newtonian flows. Further, the weighted profiles for the polymer-injected flow are also seen to collapse on the same trend in the outer layer of the boundary layer with a progressively decreasing stress deficit which is attributed to the decreasing polymer concentration in the near-wall region. While the self-similar linear trend of the weighted total stress profiles is not observed in the early-mid transitional regime precluding a quantitative assessment of the polymer stresses in this region, the results qualitatively show a significant accumulation of the polymer stresses throughout the boundary layer thickness. Comparison of the stress deficits between the two tripping configurations suggests that considerable polymer stresses are accumulated and maintained farther away from the wall in the trip-downstream case owing to a relatively larger wall-normal polymer transport close to the trip (Fig. 7.3) leading to a broader polymer-affected region.

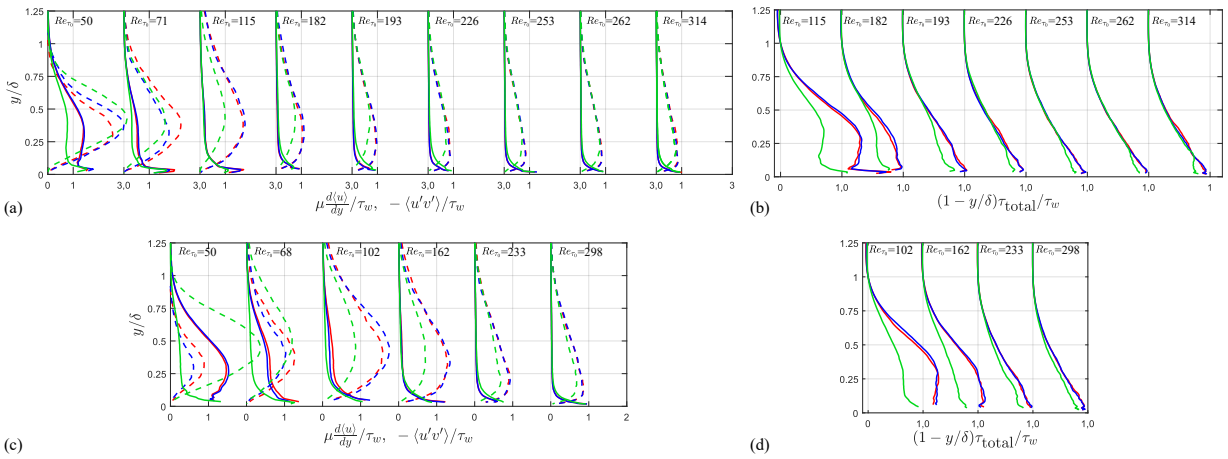

Figure 7.12: Variation of the viscous ($\mu d\langle u\rangle/dy$) and Reynolds shear stress ($-\rho\langle u'v'\rangle$) in outer coordinates for (a) trip-upstream and (c) trip-downstream case. Variation of the total stress multiplied by $(1-y/\delta)$ for the respective cases in shown in (b) and (d) following Hou *et al.* [69]. Stresses are normalized by the respective wall-shear stress (τ_w) in each of the cases. Profiles are displaced horizontally to distinguish the streamwise positions marked by Re_{τ_0}. Dashed lines in (a) and (c) represent Reynolds shear stress and solid lines show the viscous stress. Total stress profiles ($(1-y/\delta)\tau_{\text{total}}$) are shown only for the later stages of the transitioning boundary layer as indicated by the top axis.

7.4 Concluding remarks

The present study experimentally investigates the effect of slot-injected polymer (1000 ppm of polyethylene oxide) on laminar-to-turbulent transition in flat-plate tripped boundary layers using a two-dimensional trip wire. The resulting transitioning boundary layer is characterized using planar PIV and PLIF measurements which allow for a detailed study of the streamwise development of the bypass transition process. Further, the study explores the effectiveness of polymer injection for two different trip placements relative to the injection slot. For the trip positions upstream of the slot ($Re_r = 229$ based on the trip height), the polymer is injected within a recirculating bubble formed downstream of the trip wire (trip-upstream configuration). On the other hand, with the trip positioned downstream of the injector ($Re_r = 210$), the polymer is injected in the laminar boundary layer upstream of the trip (trip-downstream configuration). The results provide a detailed understanding of the salient flow features and the potential advantages and drawbacks of polymer injection in the considered configurations which are critical for the practical implementation of this flow control technique on various marine vehicles.

The mean flow in the region downstream of the trip elicits an inflectional streamwise velocity profile due to the formation of a long recirculating region (approximately $10\delta_{\text{slot}}$). Accordingly, this leads to a relatively rapid amplification of Kelvin-Helmholtz instabilities within the separated shear layer which is illustrated using both flow visualization and quantitative measurements. In both trip-slot configurations, a more accelerated transition is induced by the polymer injection in comparison to the corresponding Newtonian base flow. The polymer injection within the laminar flow region upstream of the trip wire (trip-downstream case) results in more rapid amplification of perturbations and consequently an earlier breakdown to turbulence compared to the trip-upstream case. This is likely a result of more pronounced elasto-inertial instabilities resulting from higher polymer deformations induced in the higher strain regions around the trip wire. Additionally, the confinement of the polymer solution within the separated shear layer in conjunction with the larger wall-normal fluctuations closer to the trip-wire in the trip-downstream case results in a discernible increase in polymer diffusion in the lower half of the boundary layer.

While the results highlight a counterproductive effect of the polymer injection on the bypass transition, reflected in the decreased shape factors (H) and increased C_f, the peak C_f attained at the transition point is lower than that in the corresponding Newtonian flow. The ensuing flow downstream of the transition point elicits drag reduction related to the near-wall polymer concentration, highlighting the onset of the drag reduction phenomenon within the late transition stages. In this regard, the critical shear stress corresponding to the onset of drag reducing effect is observed to be nearly equal in the two tripped cases considered in the present study while the drag reduced regime persists over a longer streamwise distance in the trip-upstream scenario due to a relatively higher near-wall polymer concentration. Although the differences in the tripping efficiency in the considered cases result in varying trends in the outer coordinates, consideration of the variation of both H and C_f with Re_τ is observed to be in excellent alignment with the results of Roach and Brierley [78], illustrating a universal behaviour in the late transition stages irrespective of polymer injection or the mechanism by which bypass transition is initiated.

In accordance with the noted universality in the late transition stages, the time-averaged profiles of streamwise velocity and Reynolds stresses show a consistent progression towards those expected in the limiting fully developed turbulent flow from the mid-to-late stages of transition regime ($Re_{\tau_0} > 150$). Barring the differences in the early stages of transition, similar progression is seen in the polymer injected flow relative to the corresponding expectations in the drag reduced turbulent boundary layer flow. Further, the development of the profiles of total stress elicits a self-similar behaviour in the outer layer in both Newtonian and drag reduced flow. A progressively decreasing stress deficit in both magnitude and wall-normal coverage is observed in the polymer-injected cases which is attributed to the declining drag reduction and polymer stress accumulation closer to the wall.

Chapter 8

Conclusions and Recommendations

The main findings from various works reported in the result chapters are summarized and recommendations for future studies are provided.

8.1 Conclusions

This thesis experimentally investigated the effect of polymer injection on turbulent and bypass transitioning flat plate boundary layers in pursuit of the key objectives presented in Sec. 1.1, which are essential for a fundamental understanding of polymer based drag reduction and its practical application on marine vehicles. These research objectives were systematically formulated to answer the research questions with regards to the polymer effect on (i) development of transitioning and turbulent boundary layers; (ii) various coherent structures in the near-wall region; (iii) skin friction; and (iv) various turbulent scales. The experimental investigations conducted using planar and tomographic PIV and PLIF techniques provide important insights into the various interactions of polymers and turbulent motions which directly affect the drag reduction effected by the polymer, while supplementing the extensive body of work mainly derived from numerical simulations. Furthermore, unlike the vast majority of previous studies that considered homogeneously distributed polymer-laden channel and pipe flows, the present investigation considers the boundary layer subjected to inhomogeneously distributed polymer additives injected via a two-dimensional slot, which is more representative of possible practical applications on marine vehicles.

The investigations reported in Chapters 4 and 7 highlight that injection of polymer solutions at relatively low Reynolds numbers ($100 < Re_{\tau_0} < 300$) produce a substantial, albeit waning, drag reduction over an extensive length of the flat plate depending on the polymer concentration in the near-wall region. Higher drag reduction is obtained in turbulent boundary layers with increasing injected polymer concentration within the range 100 ppm $< c_{\text{inj}} <$ 1000 ppm, in alignment with the universal variation of DR with K [59]. Various sub-regimes of drag reduction are distinguished by the variation of the slope of the time-averaged streamwise velocity profiles in the logarithmic layer (k) which is found to be well-correlated with DR at comparable Reynolds numbers. The sub-regimes defined using this parameter reflect the dominance of the inertial and viscous effects at moderate and high levels of drag reduction, respectively. Further, the velocity fluctuations and Reynolds shear stress are observed to be dampened with increasing drag reduction, and this dampening is most notable for the turbulence producing ejection and sweep motions occurring within the buffer layer.

The Reynolds shear stress, being relevant to turbulence production, was further investigated in Chapter 5 by means of three-dimensional PIV measurements in the buffer and lower log layers in Newtonian and drag reduced boundary layer flows. The RSS producing coherent structures in these layers were shown to be significantly modified even in low to moderate drag reduction states. The three-dimensional reconstructions of the conditionally sampled ejections and sweeps corresponding to the extreme RSS production were utilized to elucidate the average distribution of the RSS within the coherent structures. The results highlighted a significant dampening of

the RSS within the cores of the coherent structures and enlarged regions of low-RSS, particularly in the vicinity of the rotational structures in polymer injected flows, directly pointing to an elastic mechanism previously discussed by Min *et al.* [54]. Various mechanisms of polymer transport within these near-wall coherent structures and other structures associated with the low-speed streaks were elucidated through conditional sampling and reconstruction. These conditional flow fields demonstrated weakened counter-rotating and hairpin-like vortices in addition to the dampening of structures corresponding to extensional motions in the core regions of the low- and high-speed streaks, providing support for the widely debated theories involving the elastic mechanism [53] and extensional viscosity [65].

The polymer effect on the extreme skin friction events and the associated flow fields was evaluated using both planar and tomographic PIV measurements in the turbulent boundary layer in Chapter 6. The fluctuations in the wall-shear stress obtained by proxy of the fluctuating streamwise velocity at the edge of the viscous sublayer allowed for a characterization and conditional sampling of the extreme low and high wall shear stress events, which demonstrated the presence of large scale ejections and sweeps within these extreme events. Accordingly, large structures of RSS were found within the cores of these extreme events. The effect of various turbulent scales on the extreme events was evaluated by means of a scale decomposition technique employed on both planar and tomographic PIV data. While the results highlighted the dampening of small-scale motions ($< \delta/2$) and the corresponding RSS, which is generally associated with incoherent motions within the large scale coherent structures, they illustrated the relative robustness of the large scale coherent motions ($> \delta/2$) to polymer injection. The conditionally sampled large scale skin friction events further demonstrated the dominant contributions of the large scale RSS to the total RSS, and were, thus, used for a quantitative investigation of the association of the large scale RSS with the wall-shear stress by means of a three-dimensional two-point correlation. The correlation structures confirmed the presence of large-scale RSS with magnitudes substantially exceeding the peak time-averaged RSS in both low and high wall-shear stress events, while highlighting a significant phase delay in the RSS with respect to the extreme wall-shear stress.

Considering the notable effect of the polymers on various turbulent motions, the effect of polymer injection on bypass transitioning boundary layers was investigated in Chapter 7 by considering two positions of polymer injection with respect to a trip wire. The transition process initiated via the amplification of perturbations in a separated shear layer formed downstream of the trip wire, leading to an inflectional K-H instability followed by vortex shedding and breakdown to turbulence. This process was shown to be accelerated in the polymer injected flow, which resulted in an earlier breakdown to turbulence. Further, the injection of polymer solution upstream of the trip wire led to a more significant upstream advancement of the transition point, which was attributed to significant elasto-inertial instabilities compared to the case when the polymer was injected downstream of the trip. However, an onset of the drag reducing effect

of the polymer was noted to occur within the late transition stages with substantial levels of DR reached in both polymer injected cases. The DR was observed to decay more rapidly in the case with the trip positioned downstream of the injection slot which is attributed to the relatively lower near-wall polymer concentration sustained in this case. The effect of drag reduction in the late transition stages was also observed to be reflected in the reduction of velocity fluctuations and the Reynolds shear stresses, as expected from the investigations in drag reduced turbulent flows reported in this thesis.

Overall, in the context of a practical implementation of this flow control strategy on marine vehicles, the results of Chapters 4 and 7 highlight the important considerations required for the optimization of the location of polymer injection. These studies show that an increase in the local skin friction is expected up to varying streamwise distances close to the injection slot depending on the regime of the flow, which is attributed to the relatively high viscosity layer of the polymer solution formed downstream of the injection slot. While the higher turbulent intensity in late transition and fully turbulent regimes causes an effective mixing of this viscous polymer layer with the base medium and activates the polymer effect leading to drag reduction within a relatively short streamwise distance (*i.e.,* within $x - x_{\text{trip}} < 20\delta_{\text{tr}}$, Chapter 4), the streamwise distances required for the onset of drag reduction with the injection in earlier transition stages are notably larger ($x - x_{\text{trip}} > 40\delta_{\text{tr}}$, Chapter 7) due to a delayed activation of the polymer. In this regard, a critical shear stress is observed to be applicable for the activation of the polymer effect, which is reached late in the transition process. Furthermore, the results in Chapter 4 illustrate that the High Drag Reduction (HDR) states are rapidly attained downstream of the onset of drag reduction in fully turbulent flow. In contrast, the injection of similar concentrations of polymer solutions in early transition stages result in the drag reduction to be limited within the Low Drag Reduction (LDR) regime, while declining rapidly in the late transition and turbulent regimes, as shown in Chapter 7. Thus, the injection of polymer solutions at the location corresponding to the late stages of transition in the base flow is more preferable than the injection earlier upstream.

8.2 Recommendations

1. The investigation of bypass transition in Chapter 7 demonstrated the drag reducing effect of the polymer in the late transition stages, while its onset was noted to occur slightly upstream of the transition point. Further studies using three-dimensional measurements are required in the late transition regime, particularly in the vicinity of the transition point, to investigate the onset phenomenon in transitioning boundary layer flow. Polymer effect on the generation of turbulent spots and the resulting intermittency are of particular interest. The understanding gained from such a study is expected to be useful for the imple-

mentation of polymer injection in naturally transitioning boundary layers, given the noted universality in the late transition stages.

2. The present work has highlighted the effect of polymer injected via a two-dimensional slot in the bypass-transitioning and fully turbulent regimes of a flat-plate boundary layer flow. A notable limitation of slot injection is the progressive decrease of the near-wall polymer concentration, limiting the region where high levels of drag reduction can be sustained over the hull of a ship. To overcome this limitation, recent studies have considered distributed dosing of polymer solutions [218, 305] and use of polymer releasing antifouling paints [306], which maintains a consistent near-wall polymer concentration. In addition, multiple tangential injection slots can be considered for this purpose with the streamwise spacing between the slots related to the achievable extent of high drag reduction. Detailed investigations using advanced measurement techniques, such as PIV and PLIF, should be conducted to evaluate the drag reduction performance using these control strategies to provide optimal parameters for practical implementation.

3. Further, for a practical application of polymer drag reduction on large marine vehicles, such as cargo ships, the effect of polymer should be considered at large Reynolds numbers. Previous studies have shown a remarkable Reynolds number effect in turbulent boundary layer flows [307, 308] at Reynolds numbers such as those obtained on large marine vehicles. While Elbing *et al.* [162] and Winkel *et al.* [182] have considered polymer based drag reduction at such high Reynolds numbers, further detailed investigations are required for the characterization of the drag reduced boundary layers given the high data scatter in these studies. In addition, the utility of the above control strategies of wall-dosing and polymer releasing paint should be explored at high Reynolds numbers.

4. The present investigation considered the effect of polymer injection in a flat-plate boundary layer. In practice, the design of the marine vehicles leads to both favourable and adverse pressure gradient regions on the fore and aft-body, hydrofoils, and control surfaces. Furthermore, pressure gradients are also encountered during various maneuvers as well as in the presence of locally misaligned oceanic currents. Thus, investigating the effect of polymer injection within regions of non-zero pressure gradients is of practical interest. The study by Koskie and Tiederman [232] showed that the effectiveness of the polymer solutions in external boundary layers under adverse pressure gradients was greatly reduced. Further investigations in this area are warranted with the advanced measurement techniques for a detailed understanding of the effect of polymer injection in regions of non-zero pressure gradient.

References

[1] International Maritime Organization, 2014. Third imo greenhouse gas study 2014. (accessed: 26.05.2021). [Online]. Available: https://gmn.imo.org/wp-content/uploads/2017/05/GHG3-Executive-Summary-,-Report_web.pdf

[2] Olmer, N., Comer, B., Roy, B., Mao, X., Rutherford D. International council on clean transportation: Greenhouse gas emissions from global shipping, 2013-2015. (accessed: 26.05.2021). [Online]. Available: https://theicct.org/sites/default/files/publications/Global-shipping-GHG-emissions-2013-2015_ICCT-Report_17102017_vF.pdf

[3] International Energy Agency, 2020. International shipping. (accessed: 26.05.2021). [Online]. Available: https://www.iea.org/reports/international-shipping

[4] Cames, M., Graichen, J., Siemons, A., Cook, V. Emission reduction targets for international aviation , shipping. european parliament. (accessed: 26.05.2021). [Online]. Available: https://www.europarl.europa.eu/RegData/etudes/STUD/2015/569964/IPOL_STU(2015)569964_EN.pdf

[5] United Nations, 2015. Paris agreement. (accessed: 26.05.2021). [Online]. Available: https://unfccc.int/sites/default/files/english_paris_agreement.pdf

[6] International Energy Agency, 2020. Energy technology perspectives, 2020. (accessed: 26.05.2021). [Online]. Available: https://iea.blob.core.windows.net/assets/7f8aed40-89af-4348-be19-c8a67df0b9ea/Energy_Technology_Perspectives_2020_PDF.pdf

[7] Maddox Consulting. (2012). Long-term potential for increased shipping efficiency through the adoption of industry-leading practices. (accessed: 26.05.2021). [Online]. Available: https://ec.europa.eu/clima/sites/clima/files/transport/shipping/docs/market_barriers_2012_en.pdf

[8] Y. Cho, K. H. Jeon, S. B. Lee, H. Park, and I. Lee, "Evaluation of in-service speed performance improvement by means of fdr-af (frictional drag reducing anti-fouling) marine coating based on iso19030 standard," *Scientific Reports*, vol. 11, no. 1, pp. 1–11, 2021.

[9] B. R. Elbing, "Skin-friction drag reduction within turbulent flows," Ph.D. dissertation, Ph. D. dissertation, University of Michigan, Ann Arbor, 2009.

[10] S. H. Park and I. Lee, "Optimization of drag reduction effect of air lubrication for a tanker model," *International Journal of Naval Architecture and Ocean Engineering*, vol. 10, no. 4, pp. 427–438, 2018.

[11] S. Deck, N. Renard, R. Laraufie, and P.-É. Weiss, "Large-scale contribution to mean wall shear stress in high-reynolds-number flat-plate boundary layers up to 13650," *Journal of Fluid Mechanics*, vol. 743, p. 202, 2014.

[12] M. Ibrahim, S. Amran, Y. Yunos, M. Rahman, M. Mohtar, L. Wong, and A. Zulkharnain, "The study of drag reduction on ships inspired by simplified shark skin imitation," *Applied bionics and biomechanics*, vol. 2018, 2018.

[13] K.-S. Choi, X. Yang, B. Clayton, E. Glover, M. Atlar, B. Semenov, and V. Kulik, "Turbulent drag reduction using compliant surfaces," *Proceedings of the Royal Society of London. Series A: Mathematical, Physical and Engineering Sciences*, vol. 453, no. 1965, pp. 2229–2240, 1997.

[14] S. Mizokami, C. Kawakita, Y. Kodan, S. Takano, S. Higasa, and R. Shigenaga, "Experimental study of air lubrication method and verification of effects on actual hull by means of sea trial," *Mitsubishi Heavy Industries Technical Review*, vol. 47, no. 3, pp. 41–47, 2010.

[15] C. Hoang, Y. Toda, Y. Sanada *et al.*, "Full scale experiment for frictional resistance reduction using air lubrication method," in *The Nineteenth International Offshore and Polar Engineering Conference*. International Society of Offshore and Polar Engineers, 2009.

[16] S. L. Ceccio, "Friction drag reduction of external flows with bubble and gas injection," *Annual Review of Fluid Mechanics*, vol. 42, pp. 183–203, 2010.

[17] S. Tamano, M. Itoh, T. Inoue, K. Kato, and K. Yokota, "Turbulence statistics and structures of drag-reducing turbulent boundary layer in homogeneous aqueous surfactant solutions," *Physics of Fluids*, vol. 21, no. 4, p. 045101, 2009.

[18] B. A. Toms, "Some observations on the flow of linear polymer solutions through straight tubes at large reynolds numbers," *Proc. of In. Cong. On Rheology, 1948*, vol. 135, 1948.

[19] K. J. Mysels, "Flow of thickened fluids," Dec. 27 1949, uS Patent 2,492,173.

[20] R. Sellin, J. Hoyt, and O. Scrivener, "The effect of drag-reducing additives on fluid flows and their industrial applications part 1: basic aspects," *Journal of Hydraulic Research*, vol. 20, no. 1, pp. 29–68, 1982.

[21] R. Sellin, J. Hoyt, J. Poliert, and O. Scrivener, "The effect of drag reducing additives on fluid flows and their industrial applications part 2: present applications and future proposals," *Journal of Hydraulic Research*, vol. 20, no. 3, pp. 235–292, 1982.

[22] S. Vossoughi and F. Seyer, "Pressure drop for flow of polymer solution in a model porous medium," *Can. J. Chem. Eng*, vol. 52, pp. 666–669, 1974.

[23] F. Durst, R. Haas, and B. Kaczmar, "Flows of dilute hydrolyzed polyacrylamide solutions in porous media under various solvent conditions," *Journal of Applied Polymer Science*, vol. 26, no. 9, pp. 3125–3149, 1981.

[24] V. Belokon', N. Bespalova, V. Vdovin, S. Vlasov, V. Kalashnikov, and N. Ushakov, "Reduction of the hydrodynamic friction of hydrocarbons by means of small additions of certain organosilicon polymers," *Journal of Engineering Physics and Thermophysics*, vol. 36, no. 1, pp. 1–3, 1979.

[25] M. Brod, B. Deane, and F. Rossi, "Field experience with the use of additives in the pipeline transportation of waxy crudes," *Journal Institute of Petroleum*, vol. 57, no. 554, pp. 110–116, 1971.

[26] E. Burger, L. Chorn, and T. Perkins, "Studies of drag reduction conducted over a broad range of pipeline conditions when flowing prudhoe bay crude oil," *Journal of Rheology*, vol. 24, no. 5, pp. 603–626, 1980.

[27] E. Burger, "Flow increase in the transoalaska pipeline using a polymeric drag reducing additive," SPE9419, 1980: 1O7, Tech. Rep.

[28] A. Evans, "A new drag-reducing polymer with improved shear stability for nonaqueous systems," *Journal of Applied Polymer Science*, vol. 18, no. 7, pp. 1919–1925, 1974.

[29] A. Ram, E. Finkelstein, and C. Elata, "Reduction of friction in oil pipelines by polymer additives," *Industrial & Engineering Chemistry Process Design and Development*, vol. 6, no. 3, pp. 309–313, 1967.

[30] H. Canham, J. Catchpole, and R. Long, "Boundary layer additives to reduce ship resistance," *Naval Architect*, no. 2, 1971.

[31] H. Dove, "The effect on resistance of polymer additives injected into a boundary layer of a frigate model," in *Proc. 11th Int. Towing Tank Conf., Tokyo*, 1966.

[32] B. Doherty, "Investigation of drag reduction obtained through boundary layer injection of dilute solutions of poly (ethylene-oxide)," NAVAL ACADEMY ANNAPOLIS MD, Tech. Rep., 1965.

[33] R. Jones and S. Thurston, "Experimental model studies of non-newtonian soluble coatings for drag reduction," *Journal of Aircraft*, vol. 2, no. 2, pp. 122–126, 1965.

[34] W. Vogel and A. Patterson, *An experimental investigation of the effect of additives injected into the boundary layer of an underwater body*. Pacific Naval Laboratory, Defence Research Board of Canada, 1964.

[35] A. G. Fabula, "Fire-fighting benefits of polymeric friction reduction," *Journal of Basic Engineering*, vol. 93, no. 3, pp. 453–455, 1971.

[36] N. C. Franz, "Fluid aditives for improving high velocity jet cutting," in *Proc. 1st Int. Symp. Jet Cut. Technol.*, vol. 7, 1972.

[37] J. Zakin and D. A. Summers, "The effect of viscoelastic additives on jet structures," 1976.

[38] R. Sellin, "Drag reduction in sewers: First results from a permanent installation," *Journal of Hydraulic Research*, vol. 16, no. 4, pp. 357–371, 1978.

[39] R. Sellin and M. Ollis, "Polymer drag reduction in large pipes and sewers: Results of recent field trials," *Journal of Rheology*, vol. 24, no. 5, pp. 667–684, 1980.

[40] J. Overfield, H. Crawford, J. Baxter, L. Harrington, and I. Santry Jr, "Increasing wastewater flow velocity by using chemical additives," *Journal (Water Pollution Control Federation)*, pp. 1570–1585, 1969.

[41] V. Elias and J. Vocel, "'application of polymer additives in sprinkler irrigation," *Vodohospodarsky cas*, vol. 26, pp. 610–621, 1978.

[42] H. Greene, L. Thomas, R. Mostardi, and R. Nokes, "Potential biomedical applications of drag reducing agents," in *Proc. Int. Conf. Drag Reduction*, 1974, pp. H2–17.

[43] H. Greene, R. Nokes, and L. Thomas, "Drag reduction in pulsed flow of blood," *Medical Research Engineering*, vol. 9, no. 5, p. 19, 1970.

[44] H. L. Greene, R. F. Mostardi, and R. F. Nokes, "Effects of drag reducing polymers on initiation of atherosclerosis," *Polymer Engineering & Science*, vol. 20, no. 7, pp. 499–504, 1980.

[45] W. White and J. Hoyt, "The effect of linear-high molecular weight polymers on the turbulent flow properties of human blood," in *Proceedings of the 8th International Conference on Medical and Biological Engineering, Chicago*, 1969, pp. 11–11.

[46] W. J. Han and H. J. Choi, "Role of bio-based polymers on improving turbulent flow characteristics: materials and application," *Polymers*, vol. 9, no. 6, p. 209, 2017.

[47] L. C. Edomwonyi-Otu, M. M. Gimba, and N. Yusuf, "Drag reduction with biopolymer-synthetic polymer mixtures in oil-water flows: Effect of synergy," *Engineering Journal*, vol. 24, no. 6, pp. 1–10, 2020.

[48] P. Virk, H. S. Mickley, and K. Smith, "The ultimate asymptote and mean flow structure in toms' phenomenon," *Journal of Applied Mechanics*, vol. 37, no. 2, pp. 488–493, 1970.

[49] H. Petrie and A. A. Fontaine, "Comparison of turbulent boundary layer modifications with slot-injected and homogeneous drag-reducing polymer solutions," *American Society of Mechanical Engineers, Fluids Engineering Division (Publication) FED*, vol. 237, pp. 205–208, 1996.

[50] C. White, V. Somandepalli, and M. Mungal, "The turbulence structure of drag-reduced boundary layer flow," *Experiments in Fluids*, vol. 36, no. 1, pp. 62–69, 2004.

[51] M. Warholic, D. Heist, M. Katcher, and T. Hanratty, "A study with particle-image velocimetry of the influence of drag-reducing polymers on the structure of turbulence," *Experiments in fluids*, vol. 31, no. 5, pp. 474–483, 2001.

[52] W. G. Tiederman, T. S. Luchik, and D. Bogard, "Wall-layer structure and drag reduction," *Journal of Fluid Mechanics*, vol. 156, pp. 419–437, 1985.

[53] M. Tabor and P. De Gennes, "A cascade theory of drag reduction," *EPL (Europhysics Letters)*, vol. 2, no. 7, p. 519, 1986.

[54] T. Min, J. Y. Yoo, H. Choi, and D. D. Joseph, "Drag reduction by polymer additives in a turbulent channel flow," *Journal of Fluid Mechanics*, vol. 486, pp. 213–238, 2003.

[55] Y. Dubief, C. M. White, V. E. Terrapon, E. S. Shaqfeh, P. Moin, and S. K. Lele, "On the coherent drag-reducing and turbulence-enhancing behaviour of polymers in wall flows," *Journal of Fluid Mechanics*, vol. 514, pp. 271–280, 2004.

[56] A. S. Pereira, G. Mompean, L. Thais, and R. L. Thompson, "Statistics and tensor analysis of polymer coil–stretch mechanism in turbulent drag reducing channel flow," *Journal of Fluid Mechanics*, vol. 824, pp. 135–173, 2017.

[57] K. Kim, C.-F. Li, R. Sureshkumar, S. Balachandar, and R. J. Adrian, "Effects of polymer stresses on eddy structures in drag-reduced turbulent channel flow," *Journal of Fluid Mechanics*, vol. 584, pp. 281–299, 2007.

[58] M. Warholic, H. Massah, and T. Hanratty, "Influence of drag-reducing polymers on turbulence: effects of reynolds number, concentration and mixing," *Experiments in fluids*, vol. 27, no. 5, pp. 461–472, 1999.

[59] Y. Hou, V. Somandepalli, and M. Mungal, "Streamwise development of turbulent boundary-layer drag reduction with polymer injection," *Journal of Fluid Mechanics*, vol. 597, pp. 31–66, 2008.

[60] S. Shaban, M. Azad, J. Trivedi, and S. Ghaemi, "Investigation of near-wall turbulence in relation to polymer rheology," *Physics of Fluids*, vol. 30, no. 12, p. 125111, 2018.

[61] Y. Shah and S. Yarusevych, "Streamwise evolution of drag reduced turbulent boundary layer with polymer solutions," *Physics of Fluids*, vol. 32, no. 6, p. 065108, 2020.

[62] L. Zhu, H. Schrobsdorff, T. M. Schneider, and L. Xi, "Distinct transition in flow statistics and vortex dynamics between low-and high-extent turbulent drag reduction in polymer fluids," *Journal of Non-Newtonian Fluid Mechanics*, vol. 262, pp. 115–130, 2018.

[63] S. Sibilla and C. P. Beretta, "Near-wall coherent structures in the turbulent channel flow of a dilute polymer solution," *Fluid dynamics research*, vol. 37, no. 3, p. 183, 2005.

[64] K. D. Housiadas and A. N. Beris, "Polymer-induced drag reduction: Effects of the variations in elasticity and inertia in turbulent viscoelastic channel flow," *Physics of Fluids*, vol. 15, no. 8, pp. 2369–2384, 2003.

[65] J. L. Lumley, "Drag reduction by additives," *Annual review of fluid mechanics*, vol. 1, no. 1, pp. 367–384, 1969.

[66] S. A. Vanapalli, "Polymer chain scission in extensional and turbulent flows and implications for friction drag technologies," 2006.

[67] H. Schlichting, K. Gersten, E. Krause, H. Oertel, and K. Mayes, *Boundary-layer theory*. Springer, 1955, vol. 7.

[68] L. Thomas and S. Hasani, "Supplementary boundary-layer approximations for turbulent flow," *Journal of fluids engineering*, vol. 111, no. 4, pp. 420–427, 1989.

[69] Y. Hou, V. S. Somandepalli, and M. Mungal, "A technique to determine total shear stress and polymer stress profiles in drag reduced boundary layer flows," *Experiments in fluids*, vol. 40, no. 4, pp. 589–600, 2006.

[70] W. S. Saric, H. L. Reed, and E. J. Kerschen, "Boundary-layer receptivity to freestream disturbances," *Annual review of fluid mechanics*, vol. 34, no. 1, pp. 291–319, 2002.

[71] W. M. Orr, "The stability or instability of the steady motions of a perfect liquid and of a viscous liquid. part ii: A viscous liquid," in *Proceedings of the Royal Irish Academy. Section A: Mathematical and Physical Sciences*. JSTOR, 1907, pp. 69–138.

[72] A. Sommerfeld, "Ein beitrag zur hydrodynamischen erklärung der turbulenten flüssigkeitsbewegung. g. castelnuovo, ed," in 4^{th} *Int. Congr. Math. III, Rome, Italy*, pp. 116–124.

[73] H. L. Reed, W. S. Saric, and D. Arnal, "Linear stability theory applied to boundary layers," *Annual review of fluid mechanics*, vol. 28, no. 1, pp. 389–428, 1996.

[74] G. B. Schubauer and H. K. Skramstad, "Laminar-boundary-layer oscillations and transition on a flat plate," National Aeronautics and Space Administration, Washington D.C., Tech. Rep., 1948.

[75] W. S. Saric, J. A. Hoos, and R. H. Radeztsky, "Boundary-layer receptivity of sound with roughness," *Boundary layer stability and transition to turbulence*, pp. 17–22, 1991.

[76] W. S. Saric, "Physical description of boundary-layer transition: Experimental evidence," *In AGARD*, 1994.

[77] M. V. Morkovin, "Bypass-transition research: issues and philosophy," in *Instabilities and Turbulence in Engineering Flows*. Springer, 1993, pp. 3–30.

[78] P. Roach and D. Brierley, "The influence of a turbulent free-stream on zero pressure gradient transitional boundary layer development: Part 1 - Test cases T3A and T3B," in *ERCOFTAC Workshop, Lausanne*, 1990.

[79] M. Matsubara and P. H. Alfredsson, "Disturbance growth in boundary layers subjected to free-stream turbulence," *Journal of Fluid Mechanics*, vol. 430, p. 149, 2001.

[80] F. Lundell, "Experimental studies of bypass transition and its control," Ph.D. dissertation, KTH, 2003.

[81] E. Reshotko, "Disturbances in a laminar boundary layer due to distributed surface roughness," *Turbulence and chaotic phenomena in fluids*, pp. 39–46, 1984.

[82] M. Tadjfar and R. Bodonyi, "Receptivity of a laminar boundary layer to the interaction of a three-dimensional roughness element with time-harmonic free-stream disturbances," *Journal of Fluid Mechanics*, vol. 242, pp. 701–720, 1992.

[83] M. Choudhari, "Boundary-layer receptivity due to distributed surface imperfections of a deterministic or random nature," *Theoretical and Computational Fluid Dynamics*, vol. 4, no. 3, pp. 101–117, 1993.

[84] J. Crouch, "Localized receptivity of boundary layers," *Physics of Fluids A: Fluid Dynamics*, vol. 4, no. 7, pp. 1408–1414, 1992.

[85] A. K. Yusim and I. Utama, "An investigation into the drag increase on roughen surface due to marine fouling growth," *IPTEK The Journal for Technology and Science*, vol. 28, no. 3, 2017.

[86] M. Schultz, J. Bendick, E. Holm, and W. Hertel, "Economic impact of biofouling on a naval surface ship," *Biofouling*, vol. 27, no. 1, pp. 87–98, 2011.

[87] P. Klebanoff, "Effect of free-stream turbulence on a laminar boundary layer," in *Bulletin of the American Physical Society*, vol. 16, no. 11. American Inst. Physics, 1971, pp. 1323–+.

[88] J. Kendall, "Experimental study of disturbances produced in a pre-transitional laminar boundary layer by weak freestream turbulence," in *18th Fluid Dynamics and Plasmadynamics and Lasers Conference*, 1985, p. 1695.

[89] A. Boiko, K. Westin, B. Klingmann, V. Kozlov, and P. Alfredsson, "Experiments in a boundary layer subjected to free stream turbulence. part 2. the role of ts-waves in the transition process," *Journal of Fluid Mechanics*, vol. 281, pp. 219–245, 1994.

[90] J. Mans, H. De Lange, and A. Van Steenhoven, "Sinuous breakdown in a flat plate boundary layer exposed to free-stream turbulence," *Physics of Fluids*, vol. 19, no. 8, p. 088101, 2007.

[91] J. Mans, "Streak development and breakdown during bypass transition," 2007.

[92] P. Schlatter, L. Brandt, H. De Lange, and D. S. Henningson, "On streak breakdown in bypass transition," *Physics of fluids*, vol. 20, no. 10, p. 101505, 2008.

[93] K. Westin, A. Boiko, B. Klingmann, V. Kozlov, and P. Alfredsson, "Experiments in a boundary layer subjected to free stream turbulence. part 1. boundary layer structure and receptivity," *Journal of Fluid Mechanics*, vol. 281, pp. 193–218, 1994.

[94] K. Westin, A. Bakchinov, V. Kozlov, and P. Alfredsson, "Experiments on localized disturbances in a flat plate boundary layer. part 1. the receptivity and evolution of a localized free stream disturbance," *European Journal of Mechanics-B/Fluids*, vol. 17, no. 6, pp. 823–846, 1998.

[95] A. Bakchinov, K. Westin, V. Kozlov, and P. Alfredsson, "Experiments on localized disturbances in a flat plate boundary layer. part 2. interaction between localized disturbances and ts-waves," *European Journal of Mechanics-B/Fluids*, vol. 17, no. 6, pp. 847–873, 1998.

[96] G. Balamurugan and A. Mandal, "Experiments on localized secondary instability in bypass boundary layer transition," *Journal of Fluid Mechanics*, vol. 817, p. 217, 2017.

[97] H. W. Emmons, "The laminar-turbulent transition in a boundary layer-part i," *Journal of the Aeronautical Sciences*, vol. 18, no. 7, pp. 490–498, 1951.

[98] S. Dhawan and R. Narasimha, "Some properties of boundary layer flow during the transition from laminar to turbulent motion," *Journal of Fluid Mechanics*, vol. 3, no. 4, pp. 418–436, 1958.

[99] M. Asai, M. Minagawa, and M. Nishioka, "The instability and breakdown of a near-wall low-speed streak," *Journal of Fluid Mechanics*, vol. 455, pp. 289–314, 2002.

[100] C. K. Tam, "Excitation of instability waves in a two-dimensional shear layer by sound," *Journal of Fluid Mechanics*, vol. 89, no. 2, pp. 357–371, 1978.

[101] X. Wu, R. G. Jacobs, J. C. Hunt, and P. A. Durbin, "Simulation of boundary layer transition induced by periodically passing wakes," *Journal of Fluid Mechanics*, vol. 398, pp. 109–153, 1999.

[102] R. Jacobs and P. Durbin, "Simulations of bypass transition," *Journal of Fluid Mechanics*, vol. 428, p. 185, 2001.

[103] P. R. Voke and Z. Yang, "Numerical study of bypass transition," *Physics of Fluids*, vol. 7, no. 9, pp. 2256–2264, 1995.

[104] O. Marxen and T. A. Zaki, "Turbulence in intermittent transitional boundary layers and in turbulence spots," *Journal of Fluid Mechanics*, vol. 860, pp. 350–383, 2019.

[105] J. Steelant and E. Dick, "Modelling of bypass transition with conditioned navier–stokes equations coupled to an intermittency transport equation," *International journal for numerical methods in fluids*, vol. 23, no. 3, pp. 193–220, 1996.

[106] T. Corke, A. Bar-Sever, and M. Morkovin, "Experiments on transition enhancement by distributed roughness," *The Physics of fluids*, vol. 29, no. 10, pp. 3199–3213, 1986.

[107] R. S. Downs III, E. B. White, and N. A. Denissen, "Transient growth and transition induced by random distributed roughness," *AIAA journal*, vol. 46, no. 2, pp. 451–462, 2008.

[108] A. E. Von Doenhoff and E. A. Horton, "A low-speed experimental investigation of the effect of a sandpaper type of roughness on boundary-layer transition," *NACA Report 1349*, 1956.

[109] F. G. Ergin and E. B. White, "Unsteady and transitional flows behind roughness elements," *AIAA journal*, vol. 44, no. 11, pp. 2504–2514, 2006.

[110] N. A. Denissen and E. B. White, "Roughness-induced bypass transition, revisited," *AIAA journal*, vol. 46, no. 7, pp. 1874–1877, 2008.

[111] P. Klebanoff, W. Cleveland, and K. Tidstrom, "On the evolution of a turbulent boundary layer induced by a three-dimensional roughness element," *Journal of Fluid Mechanics*, vol. 237, pp. 101–187, 1992.

[112] A. L. Braslow and E. C. Knox, "Simplified method for determination of critical height of distributed roughness particles for boundary-layer transition at mach numbers from 0 to 5," 1958.

[113] F. R. Hama, J. D. Long, and J. C. Hegarty, "On transition from laminar to turbulent flow," *Journal of Applied Physics*, vol. 28, no. 4, pp. 388–394, 1957.

[114] A. Perry, T. Lim, and E. Teh, "A visual study of turbulent spots," *Journal of Fluid Mechanics*, vol. 104, pp. 387–405, 1981.

[115] G. Elsinga and J. Westerweel, "Tomographic-PIV measurement of the flow around a zigzag boundary layer trip," *Experiments in Fluids*, vol. 52, no. 4, pp. 865–876, 2012.

[116] C. Lyon, M. Selig, A. Broeren, C. Lyon, M. Selig, and A. Broeren, "Boundary layer trips on airfoils at low reynolds numbers," in *35th aerospace sciences meeting and exhibit*, 1997, p. 511.

[117] P. Lavoie, A. Naguib, and J. F. Morrison, "Transient growth induced by surface roughness in a blasius boundary layer," *XXII ICTAM, Adelaide, Australia*, 2008.

[118] S. K. Robinson, "Coherent motions in the turbulent boundary layer," *Annual Review of Fluid Mechanics*, vol. 23, no. 1, pp. 601–639, 1991.

[119] D. J. Dennis, "Coherent structures in wall-bounded turbulence," *Anais da Academia Brasileira de Ciências*, vol. 87, no. 2, pp. 1161–1193, 2015.

[120] D. J. Dennis and T. B. Nickels, "Experimental measurement of large-scale three-dimensional structures in a turbulent boundary layer. part 1. vortex packets," *Journal of Fluid Mechanics*, vol. 673, p. 180, 2011.

[121] J. Jiménez, "Coherent structures in wall-bounded turbulence," *Journal of Fluid Mechanics*, vol. 842, 2018.

[122] C. Smith and S. Metzler, "The characteristics of low-speed streaks in the near-wall region of a turbulent boundary layer," *Journal of Fluid Mechanics*, vol. 129, pp. 27–54, 1983.

[123] J. Kim, P. Moin, and R. Moser, "Turbulence statistics in fully developed channel flow at low reynolds number," *Journal of fluid mechanics*, vol. 177, pp. 133–166, 1987.

[124] C. J. Kähler, "The significance of turbulent eddies for the mixing in boundary layers," in *IUTAM Symposium on One Hundred Years of Boundary Layer Research*. Springer, 2006, pp. 405–414.

[125] ——, "The significance of coherent flow structures for the turbulent mixing in wall-bounded flows," Ph.D. dissertation, Citeseer, 2004.

[126] G. Offen and S. Kline, "A proposed model of the bursting process in turbulent boundary layers," *Journal of Fluid Mechanics*, vol. 70, no. 2, pp. 209–228, 1975.

[127] W. Schoppa and F. Hussain, "Coherent structure generation in near-wall turbulence," *Journal of fluid Mechanics*, vol. 453, pp. 57–108, 2002.

[128] J. M. Hamilton, J. Kim, and F. Waleffe, "Regeneration mechanisms of near-wall turbulence structures," *Journal of Fluid Mechanics*, vol. 287, no. 1, pp. 317–348, 1995.

[129] L. Brandt and H. De Lange, "Streak interactions and breakdown in boundary layer flows," *Physics of fluids*, vol. 20, no. 2, p. 024107, 2008.

[130] J. Jiménez and A. Pinelli, "The autonomous cycle of near-wall turbulence," *Journal of Fluid Mechanics*, vol. 389, pp. 335–359, 1999.

[131] W. Willmarth and S. Lu, "Structure of the Reynolds stress near the wall," *Journal of Fluid Mechanics*, vol. 55, no. 1, pp. 65–92, 1972.

[132] T. Luchik and W. Tiederman, "Timescale and structure of ejections and bursts in turbulent channel flows," *Journal of Fluid Mechanics*, vol. 174, pp. 529–552, 1987.

[133] J. Kim, "Turbulence structures associated with the bursting event," *The Physics of fluids*, vol. 28, no. 1, pp. 52–58, 1985.

[134] C. Kähler, "Investigation of the spatio-temporal flow structure in the buffer region of a turbulent boundary layer by means of multiplane stereo piv," *Experiments in Fluids*, vol. 36, no. 1, pp. 114–130, 2004.

[135] M. Head and P. Bandyopadhyay, "New aspects of turbulent boundary-layer structure," *Journal of fluid mechanics*, vol. 107, pp. 297–338, 1981.

[136] R. J. Adrian, C. D. Meinhart, and C. D. Tomkins, "Vortex organization in the outer region of the turbulent boundary layer," *Journal of fluid Mechanics*, vol. 422, pp. 1–54, 2000.

[137] Z.-Q. Tang, N. Jiang, A. Schröder, and R. Geisler, "Tomographic piv investigation of coherent structures in a turbulent boundary layer flow," *Acta Mechanica Sinica*, vol. 28, no. 3, pp. 572–582, 2012.

[138] J. Zhou, R. J. Adrian, S. Balachandar, and T. Kendall, "Mechanisms for generating coherent packets of hairpin vortices in channel flow," *Journal of fluid mechanics*, vol. 387, pp. 353–396, 1999.

[139] B. Ganapathisubramani, E. K. Longmire, and I. Marusic, "Characteristics of vortex packets in turbulent boundary layers," *Journal of Fluid Mechanics*, vol. 478, no. 35-46, pp. 35–46, 2003.

[140] X. Wu and P. Moin, "Direct numerical simulation of turbulence in a nominally zero-pressure-gradient flat-plate boundary layer," *Journal of Fluid Mechanics*, vol. 630, p. 5, 2009.

[141] D. Bogard and W. Tiederman, "Burst detection with single-point velocity measurements," *Journal of Fluid Mechanics*, vol. 162, pp. 389–413, 1986.

[142] N. Hutchins and I. Marusic, "Evidence of very long meandering features in the logarithmic region of turbulent boundary layers," 2007.

[143] N. Hutchins, J. P. Monty, B. Ganapathisubramani, H. C.-H. Ng, and I. Marusic, "Three-dimensional conditional structure of a high-reynolds-number turbulent boundary layer," *Journal of Fluid Mechanics*, vol. 673, p. 255, 2011.

[144] D. J. Dennis and T. B. Nickels, "Experimental measurement of large-scale three-dimensional structures in a turbulent boundary layer. part 2. long structures," *Journal of Fluid Mechanics*, vol. 673, p. 218, 2011.

[145] R. Mathis, N. Hutchins, and I. Marusic, "Large-scale amplitude modulation of the small-scale structures in turbulent boundary layers," 2009.

[146] J. Sheng, E. Malkiel, and J. Katz, "Buffer layer structures associated with extreme wall stress events in a smooth wall turbulent boundary layer," *Journal of Fluid Mechanics*, vol. 633, p. 17, 2009.

[147] G. Gomit, R. De Kat, and B. Ganapathisubramani, "Structure of high and low shear-stress events in a turbulent boundary layer," *Physical Review Fluids*, vol. 3, no. 1, p. 014609, 2018.

[148] H. Abe, H. Kawamura, and H. Choi, "Very large-scale structures and their effects on the wall shear-stress fluctuations in a turbulent channel flow up to $\mathrm{Re}_\tau = 640$," *J. Fluids Eng.*, vol. 126, no. 5, pp. 835–843, 2004.

[149] J. Wang, C. Pan, and J. Wang, "Characteristics of fluctuating wall-shear stress in a turbulent boundary layer at low-to-moderate reynolds number," *Physical Review Fluids*, vol. 5, no. 7, p. 074605, 2020.

[150] P. Schlatter, R. Örlü, Q. Li, G. Brethouwer, J. H. Fransson, A. V. Johansson, P. H. Alfredsson, and D. S. Henningson, "Turbulent boundary layers up to $\mathrm{Re}_\theta = 2500$ studied through simulation and experiment," *Physics of Fluids*, vol. 21, no. 5, p. 051702, 2009.

[151] K. Fukagata, K. Iwamoto, and N. Kasagi, "Contribution of reynolds stress distribution to the skin friction in wall-bounded flows," *Physics of Fluids*, vol. 14, no. 11, pp. L73–L76, 2002.

[152] P. S. Virk, "Drag reduction fundamentals," *AIChE Journal*, vol. 21, no. 4, pp. 625–656, 1975.

[153] J. L. Lumley, "Drag reduction in turbulent flow by polymer additives," *Journal of Polymer Science: Macromolecular Reviews*, vol. 7, no. 1, pp. 263–290, 1973.

[154] C. M. White and M. G. Mungal, "Mechanics and prediction of turbulent drag reduction with polymer additives," *Annu. Rev. Fluid Mech.*, vol. 40, pp. 235–256, 2008.

[155] F. M. White and I. Corfield, *Viscous fluid flow*. McGraw-Hill New York, 2006, vol. 3.

[156] M. T. Landahl, "Drag reduction by polymer addition," in *Theoretical and Applied Mechanics*. Springer, 1973, pp. 177–199.

[157] K. R. Sreenivasan and C. M. White, "The onset of drag reduction by dilute polymer additives, and the maximum drag reduction asymptote," *Journal of Fluid Mechanics*, vol. 409, pp. 149–164, 2000.

[158] M. Escudier, F. Presti, and S. Smith, "Drag reduction in the turbulent pipe flow of polymers," *Journal of non-newtonian fluid mechanics*, vol. 81, no. 3, pp. 197–213, 1999.

[159] M. Escudier, A. Nickson, and R. Poole, "Turbulent flow of viscoelastic shear-thinning liquids through a rectangular duct: Quantification of turbulence anisotropy," *Journal of Non-Newtonian Fluid Mechanics*, vol. 160, no. 1, pp. 2–10, 2009.

[160] R. Benzi, E. De Angelis, V. L'vov, I. Procaccia, and V. Tiberkevich, "Maximum drag reduction asymptotes and the cross-over to the newtonian plug," *Journal of Fluid Mechanics*, vol. 551, pp. 185–195, 2006.

[161] B. E. Owolabi, D. J. Dennis, and R. J. Poole, "Turbulent drag reduction by polymer additives in parallel-shear flows," *Journal of Fluid Mechanics*, vol. 827, 2017.

[162] B. R. Elbing, M. Perlin, D. R. Dowling, and S. L. Ceccio, "Modification of the mean near-wall velocity profile of a high-reynolds number turbulent boundary layer with the injection of drag-reducing polymer solutions," *Physics of Fluids*, vol. 25, no. 8, p. 085103, 2013.

[163] P. Virk, E. Merrill, H. Mickley, and K. Smith, "The critical wall shear stress for reduction of turbulent drag in pipe flow," *Mechanics of Continua*, pp. 37–52, 1966.

[164] P. De Gennes, "Coil-stretch transition of dilute flexible polymers under ultrahigh velocity gradients," *The Journal of Chemical Physics*, vol. 60, no. 12, pp. 5030–5042, 1974.

[165] P. Virk and D. Wagger, "Aspects of mechanisms in type b drag reduction," in *Structure of Turbulence and Drag Reduction*. Springer, 1990, pp. 201–213.

[166] A. Vaas, "Naval underwater weapons research and engineering station, newport, rhode island, technical document" investigation of methods for acoustic location hydrophones", parts 1, 2, 3," in *A technical paper presented during the US Navy Mathematics Workshop, Colorado State University*, 1967.

[167] A. Fabula, "The Toms phenomenon in the turbulent flow of very dilute polymer solutions," in *Proc. of* 4^{th} *Int. Congr. of Rheology*. E.H. Lee Ed. Interscience Publishers, New York, 1965.

[168] G. T. Pruitt and H. R. Crawford, "Effect of molecular weight and segmental constitution on the drag reduction of water soluble polymers." Western Co. of North America, Dallas, Tech. Rep., 1965.

[169] A. Metzner and M. G. Park, "Turbulent flow characteristics of viscoelastic fluids," *Journal of Fluid Mechanics*, vol. 20, no. 2, pp. 291–303, 1964.

[170] W. White, "Drag-reduction measurements for three polymers at 4° c," in *Viscous Drag Reduction*. Springer, 1969, pp. 173–182.

[171] N. F. Whitsitt, L. J. Harrington, and H. R. Crawford, "Effect of wall shear stress on drag reduction of viscoelastic fluids," WESTERN CO OF NORTH AMERICA RICHARDSON TX RESEARCH DIV, Tech. Rep., 1968.

[172] P. S. Virk, E. Merrill, H. Mickley, K. Smith, and E. Mollo-Christensen, "The toms phenomenon: turbulent pipe flow of dilute polymer solutions," *Journal of Fluid Mechanics*, vol. 30, no. 2, pp. 305–328, 1967.

[173] K. Harder and W. Tiederman, "Drag reduction and turbulent structure in two-dimensional channel flows," *Philosophical Transactions of the Royal Society of London. Series A: Physical and Engineering Sciences*, vol. 336, no. 1640, pp. 19–34, 1991.

[174] M. Mohammadtabar, R. Sanders, and S. Ghaemi, "Turbulent structures of non-newtonian solutions containing rigid polymers," *Physics of Fluids*, vol. 29, no. 10, p. 103101, 2017.

[175] J. R. Elsnab, J. P. Monty, C. M. White, M. M. Koochesfahani, and J. C. Klewicki, "High-fidelity measurements in channel flow with polymer wall injection," *Journal of Fluid Mechanics*, vol. 859, pp. 851–886, 2019.

[176] G. Donohue, W. Tiederman, and M. Reischman, "Flow visualization of the near-wall region in a drag-reducing channel flow," *Journal of Fluid Mechanics*, vol. 56, no. 3, pp. 559–575, 1972.

[177] D. Oldaker and W. Tiederman, "Spatial structure of the viscous sublayer in drag-reducing channel flows," *Physics of Fluids*, vol. 20, no. 10, pp. S133–S144, 1977.

[178] D. Walker and W. Tiederman, "Turbulent structure in a channel flow with polymer injection at the wall," *Journal of Fluid Mechanics*, vol. 218, pp. 377–403, 1990.

[179] A. Fontaine, H. Petrie, and T. Brungart, "Velocity profile statistics in a turbulent boundary layer with slot-injected polymer," *Journal of Fluid Mechanics*, vol. 238, pp. 435–466, 1992.

[180] D. Walker and W. Tiederman, "The concentration field in a turbulent channel flow with polymer injection at the wall," *Experiments in Fluids*, vol. 8, no. 1-2, pp. 86–94, 1989.

[181] V. Somandepalli, Y. Hou, and M. Mungal, "Concentration flux measurements in a polymer drag-reduced turbulent boundary layer," *Journal of Fluid Mechanics*, vol. 644, pp. 281–319, 2010.

[182] E. Winkel, G. Oweis, S. Vanapalli, D. Dowling, M. Perlin, M. Solomon, and S. Ceccio, "High-reynolds-number turbulent boundary layer friction drag reduction from wall-injected polymer solutions," *Journal of Fluid Mechanics*, vol. 621, pp. 259–288, 2009.

[183] Y. Dubief, V. E. Terrapon, C. M. White, E. S. Shaqfeh, P. Moin, and S. K. Lele, "New answers on the interaction between polymers and vortices in turbulent flows," *Flow, turbulence and combustion*, vol. 74, no. 4, pp. 311–329, 2005.

[184] J. Oldroyd, "A suggested method of detecting wall-effects in turbulent flow through tubes," *Int. Rheol. Congr*, vol. 2, p. 130, 1948.

[185] ——, "Non-newtonian flow of liquids and solids," in *Rheology, Volume 1*. Elsevier, 1956, pp. 653–682.

[186] M. Poreh and K.-S. Hsu, "Diffusion of drag reducing polymers in a turbulent boundary layer (diffusion rate of diluted drag reducing polymers in turbulent boundary layer)," *Journal of Hydronautics*, vol. 6, no. 1, pp. 27–33, 1972.

[187] G. Davies and A. Ponter, "Turbulent flow properties of dilute polymer solutions," *Nature*, vol. 212, no. 5057, pp. 66–66, 1966.

[188] R. G. Shaver and E. W. Merrill, "Turbulent flow of pseudoplastic polymer solutions in straight cylindrical tubes," *AIChE Journal*, vol. 5, no. 2, pp. 181–188, 1959.

[189] A. Fabula and J. Hoyt, "The effect of additives on fluid friction," *National Technical Information Service: Columbus, OH, USA*, 1964.

[190] J. Savins, "Drag reduction characteristics of solutions of macromolecules in turbulent pipe flow," *Society of Petroleum Engineers Journal*, vol. 4, no. 03, pp. 203–214, 1964.

[191] R. Sureshkumar, A. N. Beris, and R. A. Handler, "Direct numerical simulation of the turbulent channel flow of a polymer solution," *Physics of Fluids*, vol. 9, no. 3, pp. 743–755, 1997.

[192] J. Den Toonder, F. Nieuwstadt, and G. Kuiken, "The role of elongational viscosity in the mechanism of drag reduction by polymer additives," *Applied scientific research*, vol. 54, no. 2, pp. 95–123, 1995.

[193] P. A. Stone, A. Roy, R. G. Larson, F. Waleffe, and M. D. Graham, "Polymer drag reduction in exact coherent structures of plane shear flow," *Physics of Fluids*, vol. 16, no. 9, pp. 3470–3482, 2004.

[194] W. Li and M. D. Graham, "Polymer induced drag reduction in exact coherent structures of plane poiseuille flow," *Physics of Fluids*, vol. 19, no. 8, p. 083101, 2007.

[195] L. Xi and M. D. Graham, "Intermittent dynamics of turbulence hibernation in newtonian and viscoelastic minimal channel flows," *Journal of Fluid Mechanics*, vol. 693, p. 433, 2012.

[196] V. Dallas, J. C. Vassilicos, and G. F. Hewitt, "Strong polymer-turbulence interactions in viscoelastic turbulent channel flow," *Physical Review E*, vol. 82, no. 6, p. 066303, 2010.

[197] P. R. Bandyopadhyay, "Stokes mechanism of drag reduction," *Journal of applied mechanics*, vol. 73, no. 3, pp. 483–489, 2006.

[198] D. F. James and N. Yogachandran, "Filament-breaking length—a measure of elasticity in extension," *Rheologica acta*, vol. 46, no. 2, pp. 161–170, 2006.

[199] P. Bradshaw and R. Mehta. Wind tunnel design. (accessed: 20.05.2005). [Online]. Available: http://vonkarman.stanford.edu/tsd/pbstuff/tunnel/index.html

[200] G. Derbunovich, A. Zemskaya, E. Repik, and Y. P. Sosedko, "Use of screens for controlling the structure of flow turbulence in wind tunnels," *Uch. Zap. TsAGI*, vol. 13, no. 11, 1982.

[201] R. E. Hanson, H. P. Buckley, and P. Lavoie, "Aerodynamic optimization of the flat-plate leading edge for experimental studies of laminar and transitional boundary layers," *Experiments in fluids*, vol. 53, no. 4, pp. 863–871, 2012.

[202] D. Walker, W. Tiederman, and T. Luchik, "Optimization of the injection process for drag-reducing additives," *Experiments in fluids*, vol. 4, no. 2, pp. 114–120, 1986.

[203] W. A. Rowin, R. S. Sanders, and S. Ghaemi, "A recipe for optimum mixing of polymer drag reducers," *Journal of Fluids Engineering*, vol. 140, no. 11, p. 111402, 2018.

[204] A. A. Draad, G. D. C. Kuiken, and F. T. M. Nieuwstadt, "Laminar–turbulent transition in pipe flow for newtonian and non-newtonian fluids," *Journal of Fluid Mechanics*, vol. 377, p. 267–312, 1998.

[205] J. Wu and M. Tulin, "Drag reduction by ejecting additive solutions into pure-water boundary layer," *Journal of Basic Engineering*, vol. 94, no. 4, pp. 749–754, 1972.

[206] M. Raffel, C. E. Willert, F. Scarano, C. J. Kähler, S. T. Wereley, and J. Kompenhans, *Particle image velocimetry: a practical guide*. Springer, 2018.

[207] C. D. Meinhart, S. T. Wereley, and J. G. Santiago, "A piv algorithm for estimating time-averaged velocity fields," *Journal of Fluids Engineering*, vol. 122, no. 2, pp. 285–289, 2000.

[208] A. Sciacchitano, F. Scarano, and B. Wieneke, "Multi-frame pyramid correlation for time-resolved PIV," *Experiments in fluids*, vol. 53, no. 4, pp. 1087–1105, 2012.

[209] S. Scharnowski, R. Hain, and C. J. Kähler, "Reynolds stress estimation up to single-pixel resolution using piv-measurements," *Experiments in fluids*, vol. 52, no. 4, pp. 985–1002, 2012.

[210] F. Avallone, S. Discetti, T. Astarita, and G. Cardone, "Convergence enhancement of single-pixel piv with symmetric double correlation," *Experiments in Fluids*, vol. 56, no. 4, p. 71, 2015.

[211] B. Wieneke, "Volume self-calibration for 3d particle image velocimetry," *Experiments in fluids*, vol. 45, no. 4, pp. 549–556, 2008.

[212] C. Atkinson and J. Soria, "An efficient simultaneous reconstruction technique for tomographic particle image velocimetry," *Experiments in Fluids*, vol. 47, no. 4-5, p. 553, 2009.

[213] F. Scarano and M. L. Riethmuller, "Advances in iterative multigrid piv image processing," *Experiments in Fluids*, vol. 29, no. 1, pp. S051–S060, 2000.

[214] C. Atkinson, S. Coudert, J.-M. Foucaut, M. Stanislas, and J. Soria, "The accuracy of tomographic particle image velocimetry for measurements of a turbulent boundary layer," *Experiments in fluids*, vol. 50, no. 4, pp. 1031–1056, 2011.

[215] A. Sciacchitano, "Uncertainty quantification in particle image velocimetry," *Measurement Science and Technology*, vol. 30, no. 9, p. 092001, 2019.

[216] J. Crimaldi, "Planar laser induced fluorescence in aqueous flows," *Experiments in fluids*, vol. 44, no. 6, pp. 851–863, 2008.

[217] J. E. Koskie and W. G. Tiederman, "Polymer drag reduction of a zero-pressure-gradient boundary layer," *Physics of Fluids A: Fluid Dynamics*, vol. 3, no. 10, pp. 2471–2473, 1991.

[218] M. Motozawa, S. Ishitsuka, K. Iwamoto, H. Ando, T. Senda, and Y. Kawaguchi, "Experimental investigation on turbulent structure of drag reducing channel flow with blowing polymer solution from the wall," *Flow, turbulence and combustion*, vol. 88, no. 1-2, pp. 121–141, 2012.

[219] M. Motozawa, T. Sawada, S. Ishitsuka, K. Iwamoto, H. Ando, T. Senda, and Y. Kawaguchi, "Experimental investigation on streamwise development of turbulent structure of drag-reducing channel flow with dosed polymer solution from channel wall," *International Journal of Heat and Fluid Flow*, vol. 50, pp. 51–62, 2014.

[220] V. S. R. Somandepalli and M. Mungal, "Combined PIV and PLIF meaurements in a polymer drag reduced turbulent boundary layer," Ph.D. dissertation, 2006.

[221] T. A. Brungart, H. Petrie, W. Harbison, and C. Merkle, "A fluorescence technique for measurement of slot injected fluid concentration profiles in a turbulent boundary layer," *Experiments in Fluids*, vol. 11, no. 1, pp. 9–16, 1991.

[222] F. Bailey Jr and R. Callard, "Some properties of polyethylene oxide in aqueous solution," *Journal of applied polymer science*, vol. 1, no. 1, pp. 56–62, 1959.

[223] A. Vdovin and A. Smol'Yakov, "Diffusion of polymer solutions in a turbulent boundary layer," *Journal of Applied Mechanics and Technical Physics*, vol. 19, no. 2, pp. 196–201, 1978.

[224] ——, "Turbulent diffusion of polymers in a boundary layer," *Journal of Applied Mechanics and Technical Physics*, vol. 22, no. 4, pp. 526–531, 1981.

[225] R. W. Balluffi, S. Allen, and W. C. Carter, *Kinetics of materials*. John Wiley & Sons, 2005.

[226] C. J. Kähler, U. Scholz, and J. Ortmanns, "Wall-shear-stress and near-wall turbulence measurements up to single pixel resolution by means of long-distance micro-PIV," *Experiments in fluids*, vol. 41, no. 2, pp. 327–341, 2006.

[227] A. Segalini, R. Örlü, and P. H. Alfredsson, "Uncertainty analysis of the von Kármán constant," *Experiments in Fluids*, vol. 54, no. 2, p. 1460, 2013.

[228] H. M. Nagib and K. A. Chauhan, "Variations of von Kármán coefficient in canonical flows," *Physics of Fluids*, vol. 20, no. 10, p. 101518, 2008.

[229] A. Smits, N. Matheson, and P. Joubert, "Low-Reynolds-number turbulent boundary layers in zero and favorable pressure gradients," *Journal of ship research*, vol. 27, no. 03, pp. 147–157, 1983.

[230] W. McComb and L. Rabie, "Local drag reduction due to injection of polymer solutions into turbulent flow in a pipe. Part I: Dependence on local polymer concentration," *AIChE Journal*, vol. 28, no. 4, pp. 547–557, 1982.

[231] M. Reischman and W. Tiederman, "Laser-doppler anemometer measurements in drag-reducing channel flows," *Journal of Fluid Mechanics*, vol. 70, no. 2, pp. 369–392, 1975.

[232] J. E. Koskie and W. G. Tiederman, "Turbulence structure and polymer drag reduction in adverse pressure gradient boundary layers," Purdue University Lafayette in School of Mechanical Engineering, Tech. Rep., 1991.

[233] W. Willmarth, T. Wei, and C. Lee, "Laser anemometer measurements of Reynolds stress in a turbulent channel flow with drag reducing polymer additives," *The Physics of fluids*, vol. 30, no. 4, pp. 933–935, 1987.

[234] H. Petrie, A. Fontaine, M. Moeny, and S. Deutsch, "Experimental study of slot-injected polymer drag reduction," in *Proceedings of the* 2^{nd} *International Symposium on Seawater Drag Reduction. Busan*, vol. 605620, 2005.

[235] C.-F. Li, R. Sureshkumar, and B. Khomami, "Influence of rheological parameters on polymer induced turbulent drag reduction," *Journal of Non-Newtonian Fluid Mechanics*, vol. 140, no. 1-3, pp. 23–40, 2006.

[236] K.-S. Choi, "Near-wall structure of a turbulent boundary layer with riblets," *Journal of fluid mechanics*, vol. 208, pp. 417–458, 1989.

[237] P. Klebanoff, "Characteristics of turbulence in a boundary layer with zero pressure gradient," National Bureau of Standards Gaithersburg MD, Tech. Rep., 1955.

[238] S. J. Kline, W. C. Reynolds, F. Schraub, and P. Runstadler, "The structure of turbulent boundary layers," *Journal of Fluid Mechanics*, vol. 30, no. 4, pp. 741–773, 1967.

[239] H. Kim, S. Kline, and W. Reynolds, "The production of turbulence near a smooth wall in a turbulent boundary layer," *Journal of Fluid Mechanics*, vol. 50, no. 1, pp. 133–160, 1971.

[240] J. M. Wallace, H. Eckelmann, and R. S. Brodkey, "The wall region in turbulent shear flow," *Journal of Fluid Mechanics*, vol. 54, no. 1, pp. 39–48, 1972.

[241] J. Jiménez, "Turbulent flows over rough walls," *Annu. Rev. Fluid Mech.*, vol. 36, pp. 173–196, 2004.

[242] S.-Q. Yang and G. Dou, "Drag reduction in a flat-plate boundary layer flow by polymer additives," *Physics of Fluids*, vol. 17, no. 6, p. 065104, 2005.

[243] Y. Shah, S. Ghaemi, and S. Yarusevych, "Three-dimensional characterization of reynolds shear stress in near-wall coherent structures of polymer drag reduced turbulent boundary layers," *Experiments in Fluids*, vol. 62, no. 8, pp. 1–21, 2021.

[244] Y. Farsiani, Z. Saeed, B. Jayaraman, and B. R. Elbing, "Modification of turbulent boundary layer coherent structures with drag reducing polymer solution," *Physics of Fluids*, vol. 32, no. 1, p. 015107, 2020.

[245] K. Kim and R. Sureshkumar, "Spatiotemporal evolution of hairpin eddies, reynolds stress, and polymer torque in polymer drag-reduced turbulent channel flows," *Physical Review E*, vol. 87, no. 6, p. 063002, 2013.

[246] L. Xi and M. D. Graham, "Active and hibernating turbulence in minimal channel flow of newtonian and polymeric fluids," *Physical Review Letters*, vol. 104, no. 21, p. 218301, 2010.

[247] R. D. Whalley, J. S. Park, A. Kushwaha, D. J. Dennis, M. D. Graham, and R. J. Poole, "Low-drag events in transitional wall-bounded turbulence," *Physical Review Fluids*, vol. 2, no. 3, p. 034602, 2017.

[248] A. Kushwaha, J. S. Park, and M. D. Graham, "Temporal and spatial intermittencies within channel flow turbulence near transition," *Physical Review Fluids*, vol. 2, no. 2, p. 024603, 2017.

[249] S.-N. Wang, A. Shekar, and M. D. Graham, "Spatiotemporal dynamics of viscoelastic turbulence in transitional channel flow," *Journal of Non-Newtonian Fluid Mechanics*, vol. 244, pp. 104–122, 2017.

[250] S. Tamano, M. D. Graham, and Y. Morinishi, "Streamwise variation of turbulent dynamics in boundary layer flow of drag-reducing fluid," *Journal of Fluid Mechanics*, vol. 686, pp. 352–377, 2011.

[251] N. Worth, T. Nickels, and N. Swaminathan, "A tomographic piv resolution study based on homogeneous isotropic turbulence dns data," *Experiments in Fluids*, vol. 49, no. 3, pp. 637–656, 2010.

[252] J. C. Hunt, A. A. Wray, and P. Moin, "Eddies, streams, and convergence zones in turbulent flows," *Studying Turbulence Using Numerical Simulation Databases-I1*, 1988.

[253] V. Kolář, "Vortex identification: New requirements and limitations," *International journal of heat and fluid flow*, vol. 28, no. 4, pp. 638–652, 2007.

[254] R. F. Blackwelder and H. Eckelmann, "Streamwise vortices associated with the bursting phenomenon," *Journal of Fluid Mechanics*, vol. 94, no. 3, pp. 577–594, 1979.

[255] B. Ganapathisubramani, E. K. Longmire, and I. Marusic, "Experimental investigation of vortex properties in a turbulent boundary layer," *Physics of Fluids*, vol. 18, no. 5, p. 055105, 2006.

[256] G. Elsinga, D. J. Kuik, B. Van Oudheusden, and F. Scarano, "Investigation of the three-dimensional coherent structures in a turbulent boundary layer with tomographic-PIV," in 45^{th} *AIAA Aerospace Sci. Meet. and Exhibit*, 2007, p. 1305.

[257] J. Jeong, F. Hussain, W. Schoppa, and J. Kim, "Coherent structures near the wall in a turbulent channel flow," *Journal of Fluid Mechanics*, vol. 332, no. 185-214, p. 188, 1997.

[258] A. V. Johansson, P. H. Alfredsson, and J. Kim, "Evolution and dynamics of shear-layer structures in near-wall turbulence," *Journal of Fluid Mechanics*, vol. 224, pp. 579–599, 1991.

[259] M. Landahl, "On sublayer streaks," *Journal of Fluid Mechanics*, vol. 212, pp. 593–614, 1990.

[260] F. A. Seyer and A. Metzner, "Turbulence phenomena in drag reducing systems," *AIChE Journal*, vol. 15, no. 3, pp. 426–434, 1969.

[261] G. Ryskin, "Turbulent drag reduction by polymers: a quantitative theory," *Physical review letters*, vol. 59, no. 18, p. 2059, 1987.

[262] P. Orlandi, "A tentative approach to the direct simulation of drag reduction by polymers," *Journal of Non-Newtonian Fluid Mechanics*, vol. 60, no. 2-3, pp. 277–301, 1995.

[263] R. S. Martins, A. S. Pereira, G. Mompean, L. Thais, and R. L. Thompson, "An objective perspective for classic flow classification criteria," *Comptes Rendus Mecanique*, vol. 344, no. 1, pp. 52–59, 2016.

[264] Y. Shah, S. Ghaemi, and S. Yarusevych, "Experimental investigation of extreme skin friction events in polymer drag-reduced turbulent boundary layers [**In Review**]."

[265] L. Xi, "Turbulent drag reduction by polymer additives: Fundamentals and recent advances," *Physics of Fluids*, vol. 31, no. 12, p. 121302, 2019.

[266] E. De Angelis, C. M. Casciola, V. S. L'vov, R. Piva, and I. Procaccia, "Drag reduction by polymers in turbulent channel flows: Energy redistribution between invariant empirical modes," *Physical Review E*, vol. 67, no. 5, p. 056312, 2003.

[267] P. H. Alfredsson, A. V. Johansson, J. H. Haritonidis, and H. Eckelmann, "The fluctuating wall-shear stress and the velocity field in the viscous sublayer," *Physics of Fluids*, vol. 31, no. 5, pp. 1026–1033, 1988.

[268] P. H. Alfredsson and R. Örlü, "The diagnostic plot—a litmus test for wall bounded turbulence data," *European Journal of Mechanics-B/Fluids*, vol. 29, no. 6, pp. 403–406, 2010.

[269] P. H. Alfredsson, R. Örlü, and P. Schlatter, "The viscous sublayer revisited–exploiting self-similarity to determine the wall position and friction velocity," *Experiments in Fluids*, vol. 51, no. 1, pp. 271–280, 2011.

[270] P.-A. Gubian, J. Stoker, J. Medvescek, L. Mydlarski, and B. R. Baliga, "Evolution of wall shear stress with reynolds number in fully developed turbulent channel flow experiments," *Physical Review Fluids*, vol. 4, no. 7, p. 074606, 2019.

[271] B. Ganapathisubramani, N. Hutchins, J. Monty, D. Chung, and I. Marusic, "Amplitude and frequency modulation in wall turbulence," *J. Fluid Mech*, vol. 712, no. 61, pp. 064 602–17, 2012.

[272] S. Obi, K. Inoue, T. Furukawa, and S. Masuda, "Experimental study on the statistics of wall shear stress in turbulent channel flows," *International Journal of Heat and Fluid Flow*, vol. 17, no. 3, pp. 187–192, 1996.

[273] J. Sheng, E. Malkiel, and J. Katz, "Using digital holographic microscopy for simultaneous measurements of 3D near wall velocity and wall shear stress in a turbulent boundary layer," *Experiments in Fluids*, vol. 45, no. 6, pp. 1023–1035, 2008.

[274] P. Lenaers, Q. Li, G. Brethouwer, P. Schlatter, and R. Örlü, "Rare backflow and extreme wall-normal velocity fluctuations in near-wall turbulence," *Physics of Fluids*, vol. 24, no. 3, p. 035110, 2012.

[275] P. Schlatter and R. Örlü, "Assessment of direct numerical simulation data of turbulent boundary layers," *Journal of Fluid Mechanics*, vol. 659, p. 116, 2010.

[276] K. J. Colella and W. L. Keith, "Measurements and scaling of wall shear stress fluctuations," *Experiments in Fluids*, vol. 34, no. 2, pp. 253–260, 2003.

[277] J. Jiménez, J. C. Del Alamo, and O. Flores, "The large-scale dynamics of near-wall turbulence," *Journal of Fluid Mechanics*, vol. 505, p. 179, 2004.

[278] P. Schlatter and R. Örlü, "Quantifying the interaction between large and small scales in wall-bounded turbulent flows: a note of caution," *Physics of Fluids*, vol. 22, no. 5, p. 051704, 2010.

[279] M. Bernardini and S. Pirozzoli, "Inner/outer layer interactions in turbulent boundary layers: a refined measure for the large-scale amplitude modulation mechanism," *Physics of Fluids*, vol. 23, no. 6, p. 061701, 2011.

[280] J. A. Sillero, J. Jiménez, and R. D. Moser, "Two-point statistics for turbulent boundary layers and channels at reynolds numbers up to $\delta^+ \approx 2000$," *Physics of Fluids*, vol. 26, no. 10, p. 105109, 2014.

[281] B. Ganapathisubramani, N. Hutchins, W. Hambleton, E. Longmire, and I. Marusic, "Investigation of large-scale coherence in a turbulent boundary layer using two-point correlations," 2005.

[282] D. Tritton, "Some new correlation measurements in a turbulent boundary layer," *Journal of Fluid Mechanics*, vol. 28, no. 3, pp. 439–462, 1967.

[283] A. G. Kravchenko, H. Choi, and P. Moin, "On the relation of near-wall streamwise vortices to wall skin friction in turbulent boundary layers," *Physics of Fluids A: Fluid Dynamics*, vol. 5, no. 12, pp. 3307–3309, 1993.

[284] Y. Shah and S. Yarusevych, "Effect of polymer injection on the development of a bypass transitioning boundary layer [**In Review**]."

[285] R. Hansen and R. Little, "Early turbulence and drag reduction phenomena in larger pipes," *Nature*, vol. 252, no. 5485, pp. 690–690, 1974.

[286] A. Ram and A. Tamir, "Structural turbulence in polymer solutions," *Journal of Applied Polymer Science*, vol. 8, no. 6, pp. 2751–2762, 1964.

[287] M. Ohara, "Triggered laminar-to-turbulent transition in pipe flows of dilute polymer solutions." Ph.D. dissertation, Massachusetts Institute of Technology, 1968.

[288] R. W. Paterson and F. Abernathy, "Turbulent flow drag reduction and degradation with dilute polymer solutions," *Journal of Fluid Mechanics*, vol. 43, no. 4, pp. 689–710, 1970.

[289] W. Castro and W. Squire, "The effect of polymer additives on transition in pipe flow," *Applied Scientific Research*, vol. 18, no. 1, pp. 81–96, 1968.

[290] I. J. Wygnanski and F. Champagne, "On transition in a pipe - Part 1: The origin of puffs and slugs and the flow in a turbulent slug," *Journal of Fluid Mechanics*, vol. 59, no. 2, pp. 281–335, 1973.

[291] C. Van Doorne and J. Westerweel, "Measurement of laminar, transitional and turbulent pipe flow using stereoscopic-PIV," *Experiments in Fluids*, vol. 42, no. 2, pp. 259–279, 2007.

[292] C. Van Doorne, B. Hof, R. Lindken, J. Westerweel, and U. Dierksheide, "Time resolved stereoscopic piv in pipe flow. visualizing 3D flow structures," in *Proceedings of* 5^{th} *International Symposium on Particle Image Velocimetry. Busan, South-Korea, September*, 2003, pp. 22–24.

[293] J. Hand and M. C. Williams, "Effect of secondary polymer structure on the drag-reducing phenomenon," *Journal of Applied Polymer Science*, vol. 13, no. 11, pp. 2499–2503, 1969.

[294] W. White and D. M. McEligot, "Transition of mixtures of polymers in a dilute aqueous solution," *Journal of Basic Engineering*, vol. 92, no. 3, pp. 411–418, 1970.

[295] S. Ryu, E. Davis, J. S. Park, H. Zhang, and J. Y. Yoo, "Wall-shear-stress-based conditional sampling analysis of coherent structures in a turbulent boundary layer," *Journal of Fluids Engineering*, vol. 143, no. 4, p. 041301, 2021.

[296] A. Smith and D. W. Clutter, "The smallest height of roughness capable of affecting boundary-layer transition," *Journal of the Aerospace Sciences*, vol. 26, no. 4, pp. 229–245, 1959.

[297] C.-M. Ho and P. Huerre, "Perturbed free shear layers," *Annual review of fluid mechanics*, vol. 16, no. 1, pp. 365–422, 1984.

[298] J. Kurelek, S. Yarusevych, and M. Kotsonis, "Vortex merging in a laminar separation bubble under natural and forced conditions," *Physical Review Fluids*, vol. 4, no. 6, p. 063903, 2019.

[299] X. Wu, P. Moin, J. M. Wallace, J. Skarda, A. Lozano-Durán, and J.-P. Hickey, "Transitional–turbulent spots and turbulent–turbulent spots in boundary layers," *Proceedings of the National Academy of Sciences*, vol. 114, no. 27, pp. E5292–E5299, 2017.

[300] Y. L. Xiong, C.-H. Bruneau, and H. Kellay, "A numerical study of two dimensional flows past a bluff body for dilute polymer solutions," *Journal of Non-Newtonian Fluid Mechanics*, vol. 196, pp. 8–26, 2013.

[301] J. Kim, "Evolution of a vortical structure associated with the bursting event in a channel flow," in *Turbulent Shear Flows 5*. Springer, 1987, pp. 221–233.

[302] D. Samanta, Y. Dubief, M. Holzner, C. Schäfer, A. N. Morozov, C. Wagner, and B. Hof, "Elasto-inertial turbulence," *Proceedings of the National Academy of Sciences*, vol. 110, no. 26, pp. 10 557–10 562, 2013.

[303] Y. Dubief, V. E. Terrapon, and J. Soria, "On the mechanism of elasto-inertial turbulence," *Physics of Fluids*, vol. 25, no. 11, p. 110817, 2013.

[304] C. Kuan and T. Wang, "Investigation of the intermittent behavior of transitional boundary layer using a conditional averaging technique," *Experimental Thermal and Fluid Science*, vol. 3, no. 2, pp. 157–173, 1990.

[305] M. Motozawa, T. Kurosawa, T. Otsuki, K. Iwamoto, H. Ando, T. Senda, and Y. Kawaguchi, "PLIF measurement of turbulent diffusion in drag-reducing flow with dosed polymer solution from a wall," *Journal of Thermal Science and Technology*, vol. 7, no. 1, pp. 272–287, 2012.

[306] M. Motozawa, T. Ito, A. Matsumoto, H. Ando, T. Ashida, T. Senda, and Y. Kawaguchi, "Turbulent drag reduction by polymer containing paint: Simultaneous measurement of skin friction and release rate," in *International Heat Transfer Conference*, vol. 49378, 2010, pp. 787–795.

[307] I. Marusic, J. P. Monty, M. Hultmark, and A. J. Smits, "On the logarithmic region in wall turbulence," *Journal of Fluid Mechanics*, vol. 716, 2013.

[308] N. Hutchins, K. Chauhan, I. Marusic, J. Monty, and J. Klewicki, "Towards reconciling the large-scale structure of turbulent boundary layers in the atmosphere and laboratory," *Boundary-layer meteorology*, vol. 145, no. 2, pp. 273–306, 2012.

[309] S. Scharnowski, M. Bross, and C. J. Kähler, "Accurate turbulence level estimations using piv/ptv," *Experiments in Fluids*, vol. 60, no. 1, pp. 1–12, 2019.

[310] C. Tropea and A. L. Yarin, *Springer handbook of experimental fluid mechanics*. Springer Science & Business Media, 2007, vol. 1.

[311] A. Sciacchitano and B. Wieneke, "PIV uncertainty propagation," *Measurement Science and Technology*, vol. 27, no. 8, p. 084006, 2016.

[312] S. A. Glantz, B. K. Slinker, and T. Neilands, "Primer of applied regression and analysis of variance. mcgraw-hill," *Inc., New York*, 1990.

Appendix A

Characterization of water tunnel facility

This chapter presents the mean flow fields, uniformity, and turbulence intensities characterized using PIV and LDV measurements. The flow in the tunnel was characterized at freestream velocities in the range $0.27\,\mathrm{m\,s^{-1}}$ to $0.5\,\mathrm{m\,s^{-1}}$ in the test section, which was adjusted by a combination of the settings of the inlet valve and the porosity on the back-gate. The test section has a length of $2.5\,\mathrm{m}$, height of $0.8\,\mathrm{m}$, and a width of $0.5\,\mathrm{m}$.

A.1 Experimental setup

Planar PIV measurements were conducted in the mid-span vertical plane ($x - z$) and spanwise horizontal ($x - y$) planes. The coordinate system used for data presentation is illustrated in Fig. A.1. A FastCam SA4 (Photron Inc.) with a 12 bit CMOS sensor having a pixel pitch of 20 µm and a resolution of 1024 $\times$ 1024 pixels was used for image acquisition. The camera was equipped with a 50 mm fixed focal length Nikkor macro lens set to a numerical aperture of $f_{\#} = 5.6$. For the measurements in the $x - z$ plane, the camera imaged three field of views (FOVs) measuring $220\,\mathrm{mm} \times 220\,\mathrm{mm}$ which were vertically displaced maintaining an overlap of $20\,\mathrm{mm}$ between the subsequent FOVs to aid stitching of the resulting velocity vector fields. The traverse used for this purpose has a resolution of 5 µm and is controlled digitally via a computer. The vector field obtained from the stitching procedure measures $220\,\mathrm{mm} \times 620\,\mathrm{mm}$ and covers the bulk of the flow in the test section. Illumination of the FOVs was achieved by a DM20 single cavity Nd:YLF laser (Photonics Inc.) and hollow glass spheres (Sphericel, Potters Inc.) with an average size of $10\,\mu\mathrm{m}$ were used for seeding the flow. Synchronization between the laser and the camera was achieved using a high-speed timing unit (LaVision Inc.).

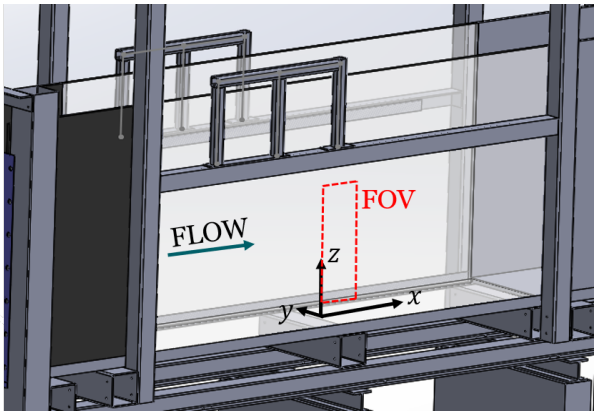

Figure A.1: Sketch of the test section of the water tunnel showing the coordinate system and field of view used for flow characterization using PIV.

Following the measurements in the $x - z$ plane, a FOV of approximately $77\,\mathrm{mm} \times 77\,\mathrm{mm}$ was positioned in the $x - y$ plane at the mid-height of the test section for the characterization of the spanwise uniformity of the streamwise velocity. Each data set containing 5456 images was acquired in a single frame mode at an acquisition frequency of $60\,\mathrm{Hz}$ which was downsampled to $30\,\mathrm{Hz}$ resulting in particle displacements of approximately $90\,\mathrm{pixels}$ at a freestream velocity of $0.5\,\mathrm{m\,s^{-1}}$. These acquisition parameters were chosen to achieve large particle displacements to minimize the effect of the measurement uncertainty on the estimates of turbulence intensity [309]. The image pre-processing included subtraction of the minimum over a kernel of 7 images and normalization of the images to minimize the variations in the background light intensity due to a significant expansion of the laser beam. PIV processing was performed by using a final interrogation window of 64×64 pixels with a 50% overlap.

In addition to the planar PIV measurements, the uniformity of the flow in the test section was further characterized using laser doppler velocimetry (LDV) in the streamwise direction by traversing the LDV probe in both vertical and spanwise directions covering approximately $0.75\,\mathrm{m}$ and $0.3\,\mathrm{m}$, respectively. The spanwise measurements were conducted at three different heights, *i.e.,* $z = 0.25\,\mathrm{m}$, $0.45\,\mathrm{m}$, and $0.65\,\mathrm{m}$ with the measurement duration at each location exceeding $5\,\mathrm{min}$.

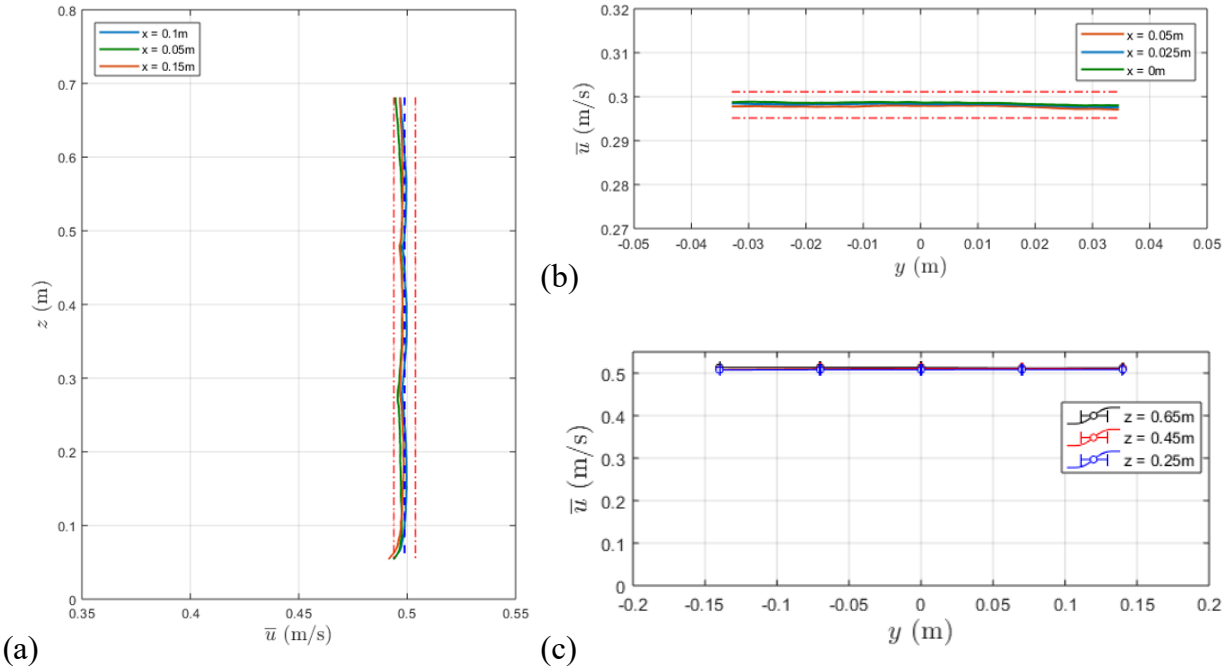

Figure A.2: Profiles of mean streamwise velocity in (a) vertical direction, and (b) spanwise direction using planar PIV. Freestream velocities of 0.5 m s^{-1} and 0.3 m s^{-1} are used in (a) and (b), respectively. (c) shows spanwise profiles of the streamwise velocity at three vertical positions using LDV. Red dash-dot lines in (a) and (b) indicate $\pm 1\%$ limits.

A.2 Results

A.2.1 Flow uniformity

The profiles of mean streamwise velocity are shown in Fig. A.2. The profiles in Figs. A.2(a) and A.2(b) obtained using planar PIV illustrate that the flow in the test section has a non-uniformity of $< 1\%$ within the bulk flow region in both vertical and spanwise directions. Further, the measurements performed at 0.5 m s^{-1} and 0.3 m s^{-1} in these figures show that the flow uniformity is maintained throughout the range of the achievable freestream velocities in the tunnel. Results for the spanwise profiles of the streamwise velocity obtained using LDV measurements acquired within a larger span ($0.15 \leq y \leq 0.15$) demonstrate a non-uniformity of approximately 0.6% (Fig. A.2(c)), which is aligned with the PIV results.

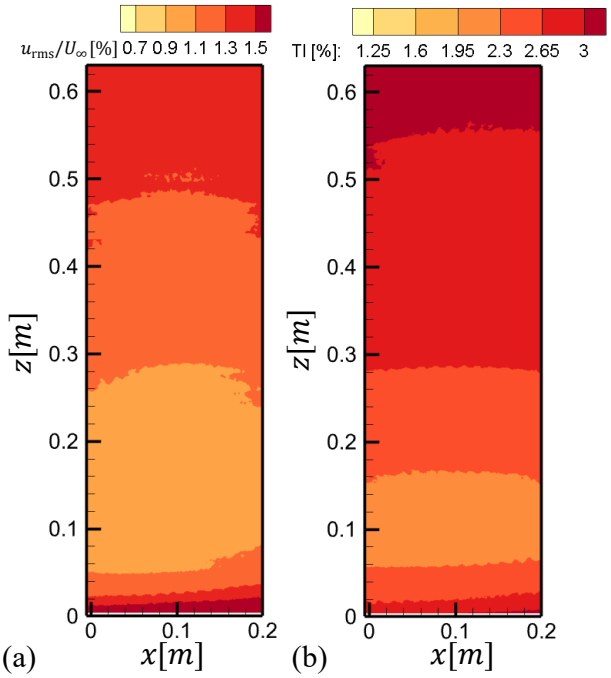

Figure A.3: Turbulence intensities obtained using planar PIV corresponding to (a) streamwise velocity fluctuations, and (b) streamwise and vertical velocity fluctuations.

A.2.2 Turbulence intensity

The PIV measurements performed with the consideration of minimizing the measurement uncertainty are suitable for the characterization of the turbulence intensity in both streamwise and vertical directions. Figs. A.3(a) and A.3(b) illustrate the turbulence intensity in the streamwise and the combined turbulence intensity in both streamwise and vertical directions (TI $= \sqrt{(u_{\text{rms}}^2 + w_{\text{rms}}^2)/2}/U_\infty$), respectively. Results in Fig. A.3(a) depict that the turbulence intensity in the streamwise direction is close to 1% within the bulk of the flow and it decreases closer to the bottom wall, barring the region closest to the wall comprising of the boundary layer. Similar trend is observed in the combined turbulence intensity in Fig. A.3(b), which is seen to be within 2% - 3% in the region $0\,\text{m} < y < 0.5\,\text{m}$.

The effect of the variation of the freestream velocity on the turbulence intensity at the centre of the test section while maintaining the water height at 0.8 m in the test section was investigated by adjusting the porosity on the back gate of the water tunnel which allowed for the freestream velocities to be varied between $0.27\,\text{m}\,\text{s}^{-1}$ to $0.5\,\text{m}\,\text{s}^{-1}$. Results in Fig. A.4 show that the streamwise turbulence intensity (u_{rms}/U_∞) remains at about 1% throughout the range of the freestream

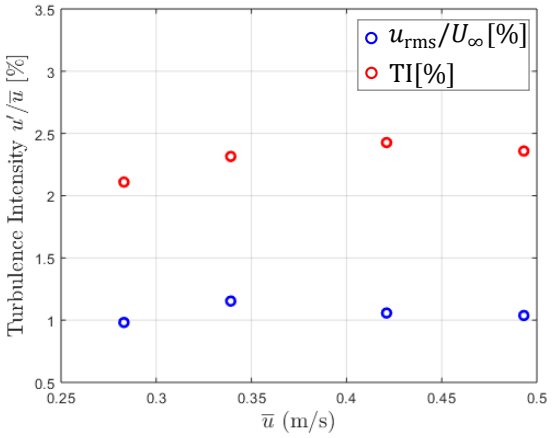

Figure A.4: Variation of the turbulence intensity averaged over a FOV $z = 0.2\,\mathrm{m}$ to $z = 0.42\,\mathrm{m}$ with freestream velocity.

velocities investigated, whereas the total turbulence intensity (TI) increases by approximately 0.3% with increasing freestream velocity. Noting the reduced combined turbulence intensity at lower freestream velocities, the freestream velocities in the range $0.28\,\mathrm{m\,s^{-1}}$ to $0.3\,\mathrm{m\,s^{-1}}$ are used in the various studies reported in this thesis.

Appendix B

Characterization of polymer injector

This chapter presents the characterization results of the outlet velocity from the injection manifold used for the polymer injection throughout this thesis. The chapter briefly describes the design of the injector and the methodology used for the characterization of the outlet velocity before presenting the results. The design of the injector used in the present thesis mainly consists of two parts *viz.,* a manifold created within the flat-plate and an inclined slot from the manifold to the plate surface (see Fig. 3.2). This chapter is aimed at the characterization of the outlet flow through the manifold which itself has a spanwise opening, and is referred to as a slot in this chapter. The outlet velocity profile and the spanwise velocity distribution is of interest in this study to obtain the flow uniformity.

B.1 Injector design

The design of the injector follows the design guidelines provided by Walker *et al.* [202]. Similar designs have been implemented by several preceding studies with a wide range of slot dimensions and inclination angles (*e.g.,* [50, 59, 182]). The slot width in these studies vary between 0.15 mm - 1 mm with the most commonly employed inclination angle of 30° at comparable Reynolds numbers. Previous studies [21, 182] have also used one or more layers of metallic screens within the plenum to equilibrate the pressure drop and mitigate the spanwise non-uniformity in the outlet flow.

The present injector design is shown in Fig. B.1 with the coordinate axes in Fig. B.1(a) used for the presentation of the velocity data in this chapter. The injection manifold is 3D printed in two parts using PC-ABS with the dimensions 400 mm × 25 mm × 9.5 mm. The material of the

injector was chosen to be non-metallic to minimize polymer degradation [21]. The wall thickness is 2 mm, except for the sides connected to the tubes which have a wall thickness of approximately 6 mm. A wire mesh with wire diameter of 0.23 mm and an open area of approximately 70% is sandwiched between the two pieces before they are glued together (Fig.B.1(b)) to enhance flow uniformity. The manifold has two inlet ports on the sides fitted with push-to-connect tube fittings for 4 mm outside diameter tubes. The outlet of the injector is a narrow slot with a slot width (d) of 0.5 mm and a spanwise length of 300 mm.

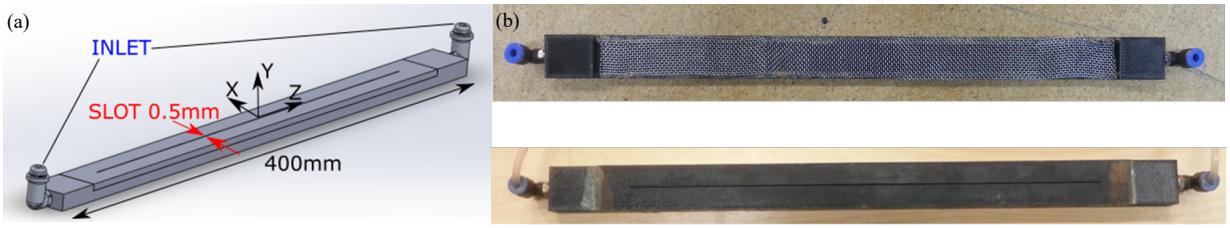

Figure B.1: Design of injection manifold. (a) shows the CAD model of the injector, and (b) shows the metallic mesh sandwiched between the top and bottom parts of the injector plenum.

B.2 Experimental setup

Characterization of the outlet flow was performed using planar PIV and laser doppler velocimetry (LDV) in two different experimental setups shown in Fig. B.2. Firstly, planar PIV measurements were conducted with the injector placed at the bottom of a glass water tank with the dimensions 0.6 m $\times$ 0.4 m $\times$ 0.3 m (Fig. B.2(a)). The tank was filled with water up to a height of at least 0.1 m. The measurements were conducted for the injection of water that was pumped into the injector using a peristaltic pump (Model: AOBL BT101S). The planar PIV measurements were conducted in the spanwise ($y-z$) and cross-span ($x-y$) planes with the high-speed FastCam SA4 (Photron Inc.) having a resolution of 1024 px $\times$ 1024 px and a pixel pitch of 20 µm. To capture the full span of the injection slot, two cameras were placed along the span with each of the cameras imaging a field of view of 160 mm $\times$ 100 mm resulting in an overlap of approximately 10 mm in the spanwise centre of the slot. On the other hand, one camera mounted on an optical rail was used to image the cross-span fields of view at three spanwise stations corresponding to $z = -100$ mm, 0 mm, and 100 mm. The illumination of the field of view was achieved by a Nd:YLF laser (Photonics Inc.) and both injected and ambient water was seeded with the Spherical hollow glass sphere particles (Potters Inc.) with a mean diameter of 10 µm. Particle images were acquired in the single frame mode, and the timing and synchronization between the laser

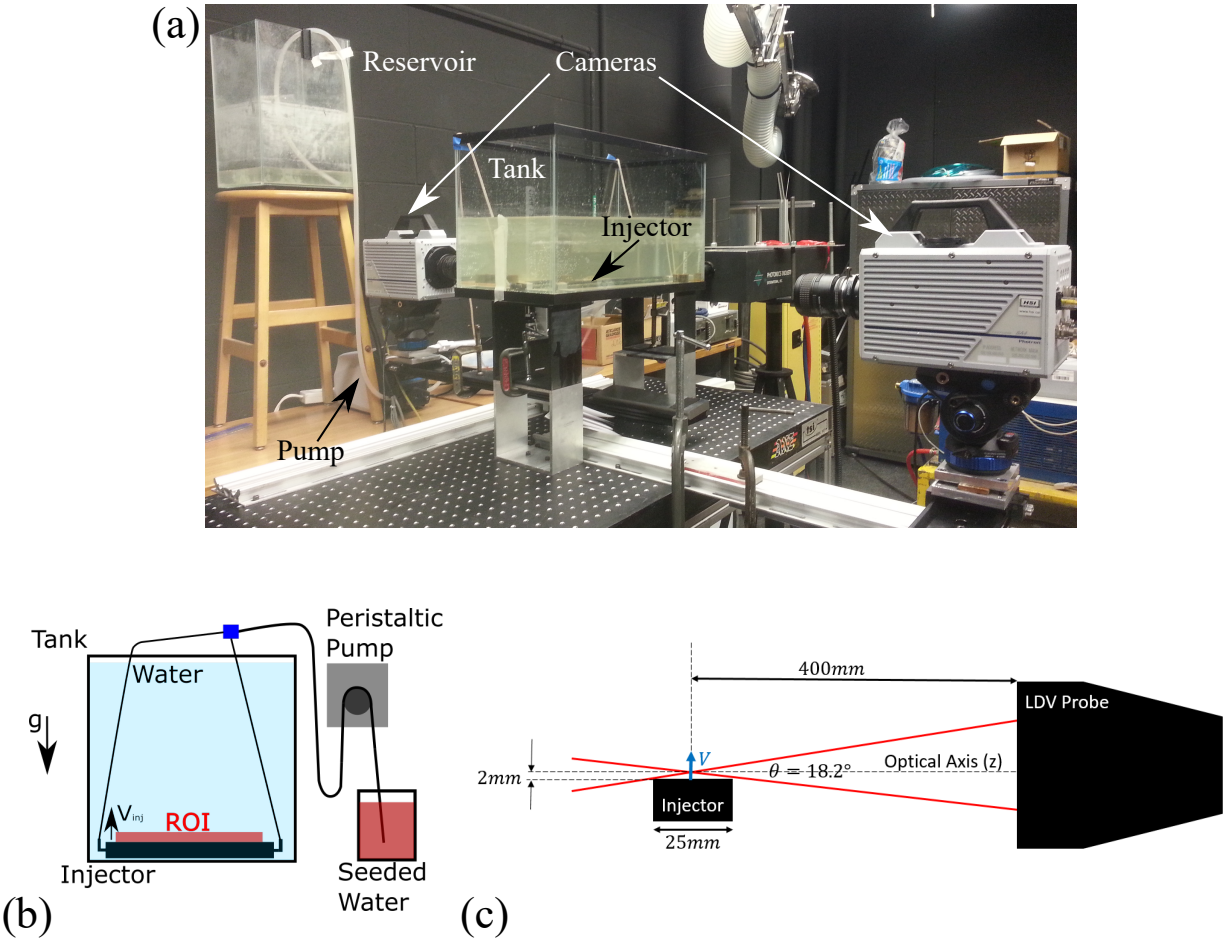

Figure B.2: Experimental setup for characterization of outlet flow through injector. (a) Planar PIV setup with two cameras positioned along the span of the injector, (b) schematic of the setup for LDV measurements along the span, and (c) schematic side-view of the injector and LDV setup showing limitation of optical access below $y = 2\,\text{mm}$.

and cameras was achieved using the LaVision High-Speed controller and DaVis 8.4 software. The PIV parameters used for each of these measurements are provided in Table B.1.

The image processing and vector evaluation was performed in DaVis 8.4. The particle images were first processed using a minimum intensity subtraction time-series filter with a kernel of 15 images. The images for the spanwise measurements were processed using a sequential correlation algorithm with an interrogation window of 24×24 pixel^2 and 75% overlap resulting in instantaneous velocity fields with a vector pitch of 0.93 mm. The velocity fields obtained for

the two cameras were averaged in time and then stitched to produce a single vector field spanning the full length of the injection slot. The cross-span measurements were processed using the ensemble of correlation [208] algorithm with a final window size of 6×6 pixel^2 and no overlap resulting in a time-averaged velocity field with a vector pitch of 0.12 mm, sufficient to resolve the width of the outlet jet.

PIV parameters		
Parameter	Spanwise ($y-z$)	Cross-span ($x-y$)
Cameras	2	1
FOV	160 mm $\times$ 100 mm	25 mm $\times$ 25 mm
Lens	50 mm	200 mm
Numerical aperture ($f_\#$)	16	5.6
Acquisition frequency (Hz)	60	120
Dataset	1500	2400
Velocity evaluation method	Seq. correlation	Ensemble of correlation
Int. window (px) / Overlap	24×24 / 75%	6×6 / 0%
Vector pitch (mm)	0.93	0.12

Table B.1: PIV parameters for characterization of outlet flow through the injector.

Since the laser sheet thickness (1-2 mm) in the planar PIV measurements conducted along the span is larger than the slot width of the jet outlet resulting in the averaging of the velocity data along the width of the jet, the outlet flow was also characterized using the laser doppler velocimetry (LDV) (Fig. B.2(b)). In this case, the injector wass placed at the bottom of a glass water tank (0.46 m $\times$ 0.09 m $\times$ 0.37 m) mounted on a fixed table. A water column of at least 25 mm was maintained above the injector throughout the data acquisition period which was confirmed to produce negligible effects of the surface waves on the outlet jet flow using flow visualization.

The measurements were conducted using the MiniLDV G5L velocimeter (Measurement Science Enterprise) and the acquisition and processing software provided by the same manufacturer. The measurement probe focuses two laser beams at a distance of 400 mm from the plane of the lens of the probe resulting in a measurement volume with a length of 0.9 mm $\times$ 100 µm $\times$ 70 µm. Optical access is limited by the inclination of the bottom beam. The lowest streamwise position

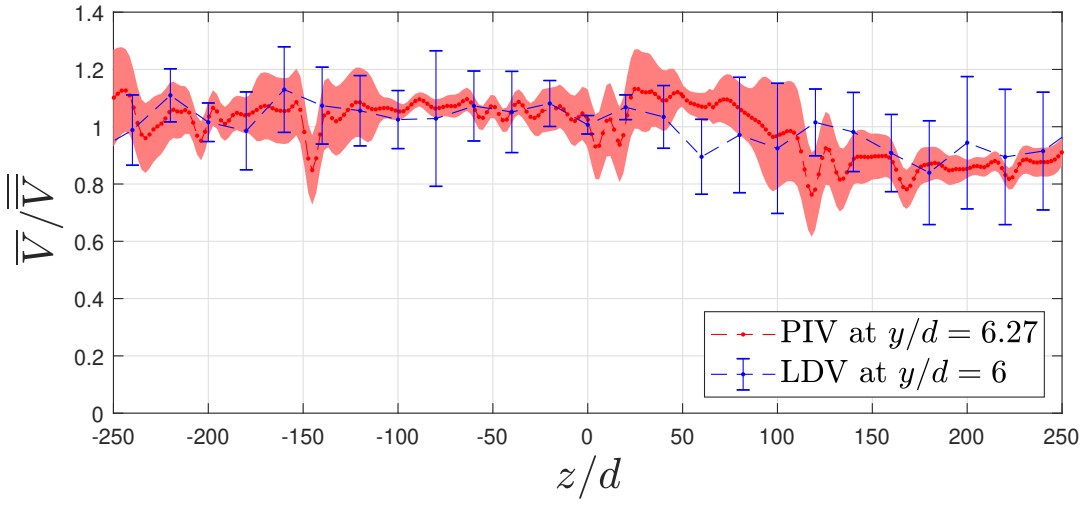

Figure B.3: Spanwise distribution of time-averaged outlet velocity ($\overline{V}$) obtained using planar PIV and LDV. Velocities are normalized by the mean of the measurements at the measured vertical location. Error-bars and shaded regions correspond to 95% confidence intervals.

that is optically accessible, with the measurement volume vertically aligned with the slot, is approximately 2 mm as shown in Fig.B.2(c). The probe was mounted on a traversing system (Velmex BiSlide) to enable measurements along the span. Measurements were performed at a distance of 3 mm from the outlet plane of the slot with a spanwise spacing between the measurement stations of 10 mm.

The data was acquired for at least 60 s with an average data rate of approximately 100 samples/s. This resulted in statistically converged time-averaged velocities confirmed by the convergence of uncorrelated samples at each measurement location, with the correlation time determined using an auto-correlation function of the time-series signal (refer Tropea *et al.* [310] for details).

B.3 Results

The time-averaged outlet velocity ($\overline{V}$) obtained using PIV and LDV along the spanwise direction of the injection slot are presented in Fig. B.4. In order to aid comparisons of the spanwise uniformity from the two measurements considered at slightly different wall-normal locations, the outlet velocities are normalized by the corresponding spatial means of the velocity data at the considered vertical locations ($\overline{\overline{V}}$). The results considered at approximately $y = 3$ mm from

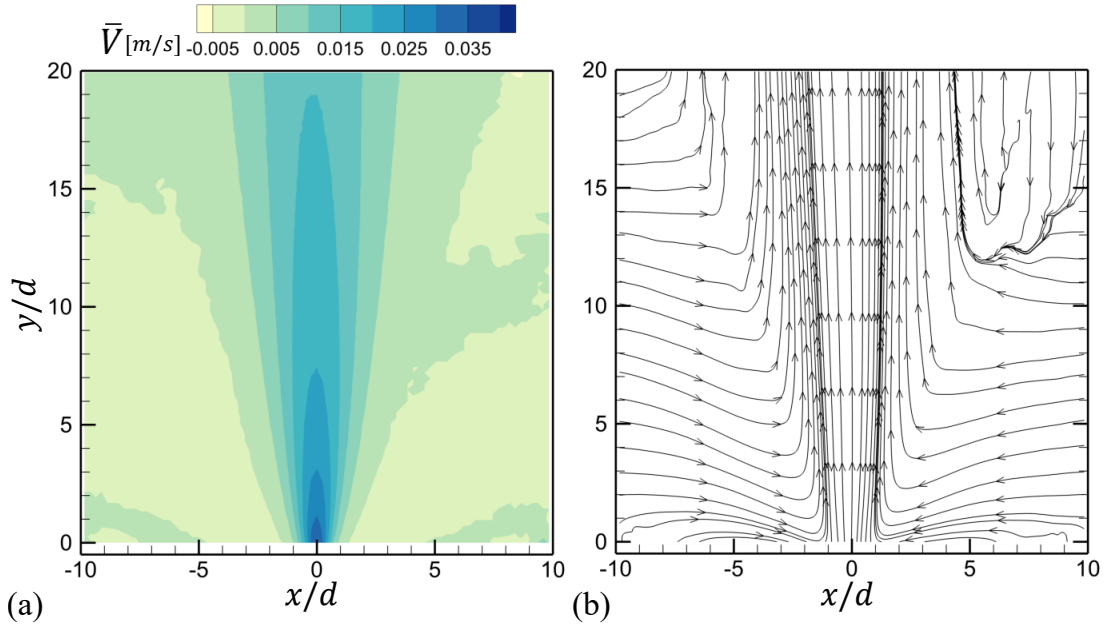

Figure B.4: Spanwise distribution of time-averaged outlet velocity ($\overline{V}$) obtained using planar PIV and LDV. Velocities are normalized by the mean of the measurements at the measured vertical location. Error-bars and shaded regions correspond to 95% confidence intervals.

the outlet plane of the jet using both measurement techniques show comparable distributions of the spanwise velocity within the uncertainty of the measurements. The spanwise uniformity is found to be within $\pm$13% over the full span of the injection slot and it is within $\pm$7.6% over 75% of the centre span. It is further observed from both measurements that the spanwise uniformity improves slightly with the vertical distance.

Both PIV and LDV measurments show notable non-uniformity between the left and right halves of the injection slot which is attributed to the unequal lengths of the tubing used to feed the injector through the inlet ports on either sides. This mismatch of the tubing lengths was eliminated in all the remaining experiments reported in this thesis. Deformations of the 3D printed injector body, particularly under the loads applied by the injected fluid on the inner lips of the upper part containing the slot, is also expected to cause non-uniformity in the outlet flow along the span of the slot. The deformation of the injector body is eliminated in the flat-plate experiments since the injector body is tightly sandwiched between the upper and lower aluminum plates of the flat-plate model and securing its position under the inclined duct (Fig. 3.2). The outlet flow through the inclined duct is expected to further improve the spanwise uniformity of the outlet velocity.

Appendix C

Uncertainty estimation

C.1 Uncertainty in mean velocity

The uncertainty in the estimation of the mean velocity ($\langle u \rangle$) using N independent samples with the assumption of a normally distributed random error is given by Eq. C.1.

$$\epsilon_{\langle u \rangle} = \frac{\sigma_u}{\sqrt{N}}, \tag{C.1}$$

where σ_u is the estimated standard deviation considering both the variance due to true velocity fluctuations ($\sigma_{u,\text{fluct}}$) and the uncertainty in the instantaneous velocity component (ϵ_u) [311].

The PIV data is acquired at $14\,\text{Hz}$ and $15\,\text{Hz}$ in Chapter 4 and Chapters 5 to 7, respectively, leading to spatial separations between the consecutive samples exceeding the boundary thickness (δ) along the streamwise direction. Thus, the acquired datasets, each containing more than 4000 independent samples, lead to an uncertainty in the mean velocity $\epsilon_{\langle u \rangle}$ of less than 0.1% at the peak of the velocity fluctuations within the boundary layer. It is further noted that the uncertainty in the streamwise velocity (ϵ_u) is expected to vary from 0.1 pixels in the freestream to 1.5 pixels at the wall due to the strong velocity gradient closer to the wall, whereas the uncertainty in the wall-normal component (ϵ_v) is expected to be approximately 0.2 pixels [214]. However, this has relatively minor effect in the uncertainty of the mean velocity which is dominated by the variance corresponding to the velocity fluctuations.

C.2 Uncertainty in wall shear stress

The wall-shear stress is estimated by a linear fit to the time averaged PIV data in the viscous sublayer. The goodness of the linear fit (R^2) is estimated to be greater than 0.98 in each of the time averaged datasets with a sliding average operation as described in Sec. 4.3.3. The relative uncertainty in the wall shear stress ($\epsilon_{d\langle u\rangle/dy}$) is derived using Eq. C.2

$$\epsilon_{\frac{d\langle u\rangle}{dy}} = \sqrt{\frac{1/R^2 - 1}{n-2}}, \tag{C.2}$$

where n is the number of data points considered for the linear fit within the viscous sublayer [312]. The uncertainty decreases with an increased magnification in the viscous sublayer increasing the number of data points (n) while also leading to a simultaneous improvement in R^2. Thus, the planar PIV measurements were designed to consider relatively large magnifications to have at least 12 velocity vectors for the linear fit. The resulting uncertainty in the gradient of the time averaged velocity is estimated to be approximately $\pm 5\%$.

C.3 Uncertainty in velocity fluctuations and Reynolds shear stress

The uncertainty in the root-mean-squared velocity (σ_u) and time averaged Reynolds shear stress is estimated using Eq. C.3 and Eq. C.4, respectively,

$$\epsilon_{\sigma_u} = \frac{\sigma_u}{\sqrt{2(N-1)}}, \tag{C.3}$$

$$\epsilon_{\langle u'v'\rangle} = \sigma_u \sigma_v \sqrt{\frac{1+\rho_{uv}^2}{N-1}}, \tag{C.4}$$

where ρ_{uv} is the cross-correlation coefficient between the velocity components u and v. In the case of planar PIV measurements, the maximum uncertainty $\epsilon_{\langle u'v'\rangle}$ with an assumption of $\rho_{uv} = 1$ is negligible due to the collection of large number of samples.

The measurement accuracy of the velocity fluctuations and Reynolds shear stress from tomographic PIV is assessed via a comparison with the planar PIV data in Fig. C.1. Fig. C.1(a) shows that the maximum relative error in the rms of the in-plane component obtained from tomographic PIV is within 7.5% of the local magnitude. On the other hand, the relative error in

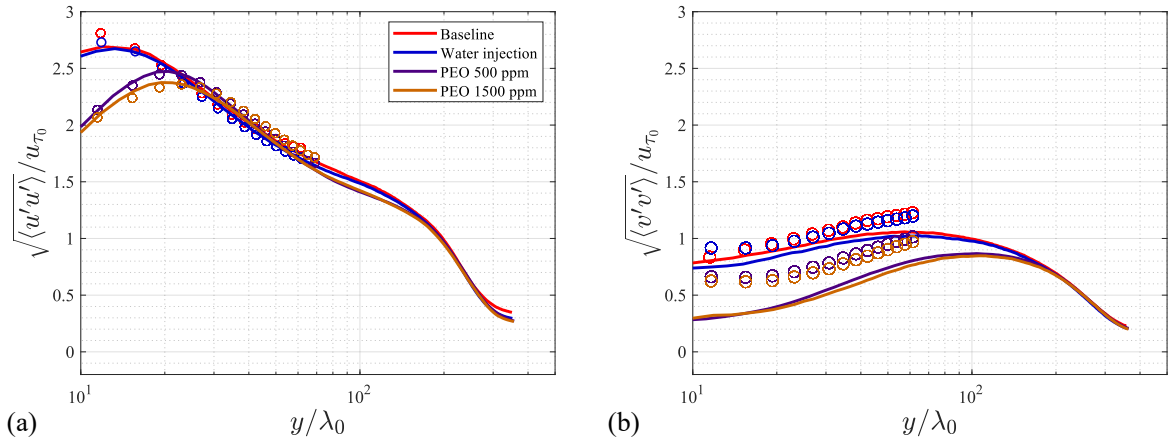

Figure C.1: Time averaged profiles of rms of (a) streamwise $\sqrt{\langle u'u' \rangle}$, and (b) wall-normal $\sqrt{\langle v'v' \rangle}$ velocity fluctuations at $x - x_{\text{inj}} = [150, 190]$mm for the data presented in Chapters 5 and 6. Solid lines show results from planar PIV and $\circ$ show results from tomographic PIV. Results are normalized using the inner scaling in the baseline case.

the wall-normal component, which is the out-of-plane component in the present measurements, varies between 25% and 80% of the local magnitude as shown in Fig. C.1(b). While the tomographic PIV is able to capture the trends in the profiles of wall-normal velocity fluctuations, results show an over-estimation close to the wall, which is attributed to the higher relative error in the measurement of low velocities. However, this uncertainty in the out-of-plane component does not correlate with the errors in the streamwise component leading to a minor overestimation in the time-averaged Reynolds shear stress (Fig. 6.5).